Schweizerische Eidgenossenschaft
Confédération suisse
Confederazione Svizzera
Confederaziun svizra

Eidgenössisches Departement für Umwelt, Verkehr, Energie und Kommunikation UVEK
Département fédéral de l'environnement, des transports, de l'énergie et de la communication DETEC
Dipartimento federale dell'ambiente, dei trasporti, dell'energia e delle comunicazioni DATEC

Bundesamt für Strassen
Office fédéral des routes
Ufficio federale delle Strade

Seismic Safety of Existing Bridges – Cyclic Inelastic Behaviour of Bridge Piers

Erdbebensicherheit bestehender Brücken – Zyklisch-inelastisches Verhalten von Brückenstützen

Sécurité sismique des ponts existants – comportement plastique - cyclique des piles de pont

Earthquake Engineering and Structural Dynamics Laboratory (EESD)
École Polytechnique Fédérale de Lausanne (EFPL)
Pia Hannewald
Katrin Beyer

Forschungsprojekt AGB 2008/001 auf Antrag der Arbeitsgruppe Brückenforschung (AGB)

September 2014 **662**

Schweizerische Eidgenossenschaft
Confédération suisse
Confederazione Svizzera
Confederaziun svizra

Eidgenössisches Departement für Umwelt, Verkehr, Energie und Kommunikation UVEK
Département fédéral de l'environnement, des transports, de l'énergie et de la communication DETEC
Dipartimento federale dell'ambiente, dei trasporti, dell'energia e delle comunicazioni DATEC

Bundesamt für Strassen
Office fédéral des routes
Ufficio federale delle Strade

Seismic Safety of Existing Bridges – Cyclic Inelastic Behaviour of Bridge Piers

Erdbebensicherheit bestehender Brücken – Zyklisch-inelastisches Verhalten von Brückenstützen

Sécurité sismique des ponts existants – comportement plastique - cyclique des piles de pont

Earthquake Engineering and Structural Dynamics Laboratory (EESD)
École Polytechnique Fédérale de Lausanne (EFPL)
Pia Hannewald
Katrin Beyer

Forschungsprojekt AGB 2008/001 auf Antrag der Arbeitsgruppe Brückenforschung (AGB)

September 2014 **662**

Impressum

Forschungsstelle und Projektteam

Projektleitung
Prof. Dr. Katrin Beyer

Mitglieder
Dr. Pia Hannewald

Begleitkommission

Präsident
Dr. Armand Fürst

Mitglieder
Dr. Manuel Alvarez
Heinrich Figi
Dr. Hansrudolf Ganz
Prof. Dr. Aurelio Muttoni
Dr. Dario Somaini

Antragsteller

Arbeitsgruppe Brückenforschung (AGB)

Bezugsquelle

Das Dokument kann kostenlos von http://www.mobilityplatform.ch heruntergeladen werden.

Inhaltsverzeichnis

Zusammenfassung

Viele bestehende Brücken wurden auf der Grundlage von Normen bemessen, die keine oder nur ungenügende Angaben zu Erdbebenlasten enthielten. Besonders in Ländern moderater Seismizität, wie z.B. der Schweiz, sind moderne Erdbebennormen oft erst vor wenigen Jahren eingeführt worden, da die Erdbebengefahr lange unterschätzt wurde. Existierende Brücken haben daher möglicherweise eine geringe Verformungskapazität aufgrund ihrer Bauart und ihrer konstruktiven Details. Um dies zu beurteilen wurde ein zweiteiliges Forschungsprojekt zu bestehenden Brücken initiiert. Der erste Teil dieses Projektes [1], [2] wurde an der ETHZ ausgeführt und diente zur Abschätzung des Verformungsbedarfs von bestehenden Brücken. Er befasste sich eingehend mit der Modellierung von Brücken sowie der Identifizierung kritischer Stützenkonfigurationen. Zu den dabei identifizierten kritischen Details gehören (i) Bewehrungsstösse in der potenziellen plastischen Region über dem Fundament, (ii) geringe Querbewehrungsgrade und (iii) das Fehlen von Umschnürungsbewehrung. Für die Überprüfung dieser Brücken können verformensbasierte Methoden, welche die bei einem Erdbeben aufgebrachten Verformungen mit der Verformungskapazität vergleichen, verwendet werden [1], [2].

Der zweite Teil des Forschungsprojektes, der in dem vorliegenden Bericht behandelt wird, befasst sich mit der Abschätzung der Verformungskapazität gedrungener, wandartiger Stützen (Schlankheit ca. 1 – 3) mit rechteckigem Querschnitt. Da die verformensbasierte Überprüfung von praktisch tätigen Ingenieuren durchgeführt wird und eine grosse Anzahl Brücken zu überprüfen ist, sollten die Modelle zur Abschätzung des Verformungsvermögens relativ einfach anwendbar sein und gleichzeitig gute und nicht zu konservative Resultate liefern. Mit dieser Arbeit soll zur Entwicklung solcher Modelle beigetragen werden. Versuche an Stützen mit den genannten Konstruktionsdefiziten, die im Rahmen beider Teile des Forschungsprojektes an der ETHZ durchgeführt wurden [1], [3], dienen als experimentelle Datenbasis zur Überprüfung und Validierung. Zwei Ansätze wurden auf Basis der genannten Kriterien zum vertieften Studium ausgewählt: die Modellierung mit plastischem Gelenk sowie ein kinematisches Modell für schubkritische Wände.

Der erste Teil dieses Berichtes befasst sich mit der Modellierung mit plastischem Gelenk. Es wird ein Überblick über Gleichungen zur Bestimmung der Länge des plastischen Gelenkes, zur Ermittlung der Biege- und Schubverformung sowie zur Berechnung der Dehnungslimite, die den Versagenszustand definieren, gegeben. Durch Überprüfung mit den experimentellen Daten wird ein Verfahren identifiziert, mit dem die Last-Verformungskurve der Stützen ermittelt werden kann. Der Einfluss der Bewehrungsstösse auf das Verhalten sowie die Schubverformungen werden dabei in einfacher Weise berücksichtigt.

Im zweiten Teil des Berichtes werden die Schubdegradation sowie ein kinematisches Modell zur Vorhersage des Verhaltens von rechteckigen, schubkritischen Stützen behandelt. Das Modell basiert auf der bei Schubrissbildung einsetzenden Kinematik und wurde andernorts entwickelt. In diesem Bericht wird es mit Hilfe einer erweiterten Datenbank validiert. Ausserdem wird der Einfluss einiger wichtigen Charakteristiken, wie zum Beispiel der Bewehrungsgehalte und der Schlankheit, insbesondere im Hinblick auf die Verformungskapazität, anhand dieses Modells dargestellt.

Der Vergleich der Vorhersagen mit den experimentellen Daten zeigte, dass die Modellierung mit plastischem Gelenk, trotz ihrer Einfachheit, gute Ergebnisse für die hier betrachteten nur teilweise biegebestimmten Wände lieferte. Dieser Modellierungsansatz resultiert in einer eher konservativen Abschätzung der Verformungskapazität, die in etwa der Verformung bei Maximallast entspricht. Um auch den zum degradierenden Ast gehörenden Teil der Antwort zu berücksichtigen, sollte das kinematische Modell, mit dem sowohl Querkraft- als auch Axiallastversagen erfasst werden können, verwendet werden.

Gliederung des Berichtes

In den folgenden Abschnitten wird eine Zusammenfassung der wesentlichen Punkte dieses Berichtes gegeben. Zuerst wird die Modellierung mit plastischem Gelenk dargestellt. Dabei werden das prinzipielle Vorgehen und alle zur Modellierung notwendigen Grössen und Formulierungen kurz erläutert. Im Anschluss daran folgt eine Einführung in die Grundlagen eines kinematischen Modells zur Berechnung des Verhaltens schubkritischer Stützen. Diese ausführliche Zusammenfassung wird auf Deutsch und Französisch präsentiert. Danach folgt dann der eigentliche Forschungsbericht in englischer Sprache, in dem sowohl ausführlichere Erläuterungen als auch die Grundlagen der präsentierten Modelle zu finden sind.

Modellierung mit plastischem Gelenk

Einführung

In diesem Abschnitt werden die wesentlichen Punkte zur Modellierung wandartiger, rechteckiger Stützen mit plastischem Gelenk dargestellt. Bei dieser Modellierung wird der plastische Bereich am Fuss der Stütze durch ein sogenanntes plastisches Gelenk abgebildet, in welchem eine konstante plastische Krümmung angenommen wird. Dies ist eine vereinfachte Darstellung des in Experimenten häufig beobachteten näherungsweise linearen Verlaufs der plastischen Krümmungen, siehe Abb. 1. In dieser Darstellung ist ϕ_p die plastische Krümmung, ϕ'_y die Krümmung bei erstmaligem Fliessen der Längsbewehrung, ϕ_b die Krümmung am Fuss der Stütze und ϕ_{sp} die aus der Ausbreitung der Dehnungen in das Fundament resultierende Krümmung. Durch die Integration des Krümmungsprofils ist der Ansatz mit plastischem Gelenk in erster Linie zur Bestimmung der Biegeverformungen geeignet. Die Schubverformungen können jedoch, da sie im inelastischen Bereich im Verhältnis zu den Biegeverformungen stehen, ebenfalls berücksichtigt werden.

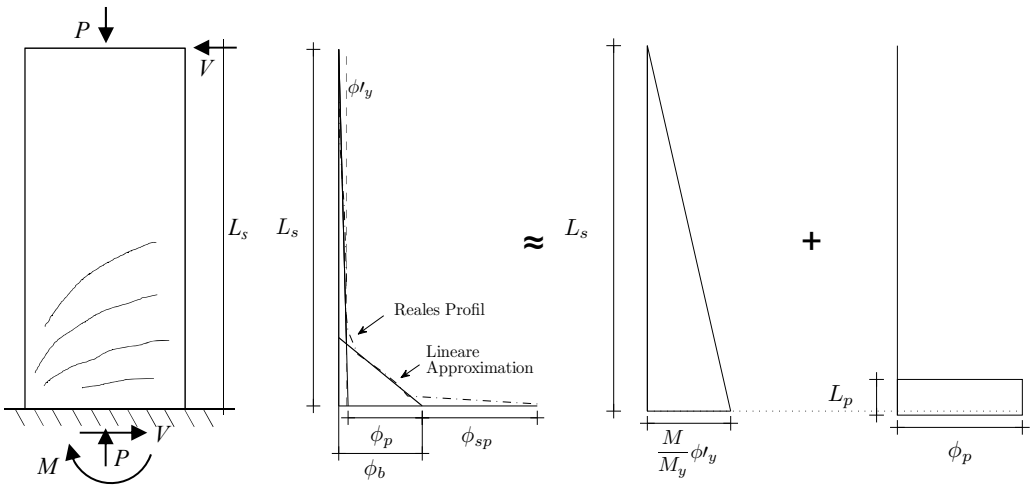

Abb. 1: *Wandartige Stütze unter Belastung, resultierendes reales Krümmungsprofil und näherungsweise Darstellung im plastischen Gelenk Modell.*

Im Folgenden wird zuerst auf die anhand der Versuchsdaten bestimmte Länge des plastischen Gelenkes eingegangen. Danach werden Empfehlungen zur Momenten-Krümmungsanalyse und den Dehnungslimits, mit welchen die Krümmungs- und damit die Verformungskapazitäten der Stützen bestimmt werden, gegeben. Im Anschluss wird auf die Bestimmung der Biege- und Schubverformung eingegangen, aus deren Summe sich die Gesamtverformung bestimmen lässt. Ausserdem werden Hinweise zur Berücksichtigung eines Bewehrungsstosses am Stützenfuss gegeben.

Wahl der Länge des plastischen Gelenkes

Das plastische Gelenk ist eine Modellierungsgrösse, die im Modell den inelastischen Bereich eines Bauteils abbildet. Basierend auf den im Rahmen der in den beiden Teilen dieses Projektes durchgeführten Tests [1] [3], wurden verschiedene Gleichungen zur Ermittlung der Länge des plastischen Gelenkes von Wänden evaluiert. Die beste Übereinstimmung mit den experimentellen Daten wurde mit der folgenden Gelenklänge [4] erzielt:

$$L_p = \left(0.2h + 0.05L_s\right)\left(1 - 1.5\frac{P}{A_g f_c}\right) \leq 0.8h \tag{1}$$

In dieser Gleichung werden neben der Querschnittshöhe h und der Schubspannweite L_s auch ein die Gelenklänge reduzierender Einfluss der Axiallast P berücksichtigt. Letztere ist als bezogene Last $P/(A_g f_c)$ enthalten, berechnet mit der Bruttoquerschnittsfläche der Wand A_g und der Betonfestigkeit f_c. Nicht explizit berücksichtigt wird hingegen ein „Strain Penetration“ Anteil, mit welchem die Ausbreitung der Dehnungen ins Fundament erfasst wird. Der Vergleich mit den experimentellen Daten im inelastischen Bereich hat gezeigt, dass dieser Anteil im allgemeinen vergleichsweise klein ist und die Gesamtverformung der Stützen ohne zusätzliche Berücksichtigung dieses Effektes gut abgeschätzt werden kann.

Momenten-Krümmungsbeziehung und Dehnungslimits

Zur Ermittlung der Momenten-Krümmungsbeziehung wird eine Querschnittsanalyse durchgeführt. Diese basiert auf der Annahme, dass ebene Querschnitte eben bleiben. Abb. 2 stellt die wichtigsten Grundlagen der Querschnittsanalyse dar. Neben der der Querschnittsanalyse zugrunde liegenden Annahme der Dehnungsverteilung und der Momenten-Krümmungsbeziehung für einen der betrachteten Versuchskörper werden die für Beton und Stahl verwendeten Materialgesetze gezeigt. Für den Beton wurde die Spannungs-Dehnungsbeziehung für umschnürten Beton gemäss [5] verwendet. Für den Stahl wurde eine bilineare Spannungs-Dehnungsbeziehung verwendet und Zugversteifung („tension stiffening“) wurde nicht berücksichtigt

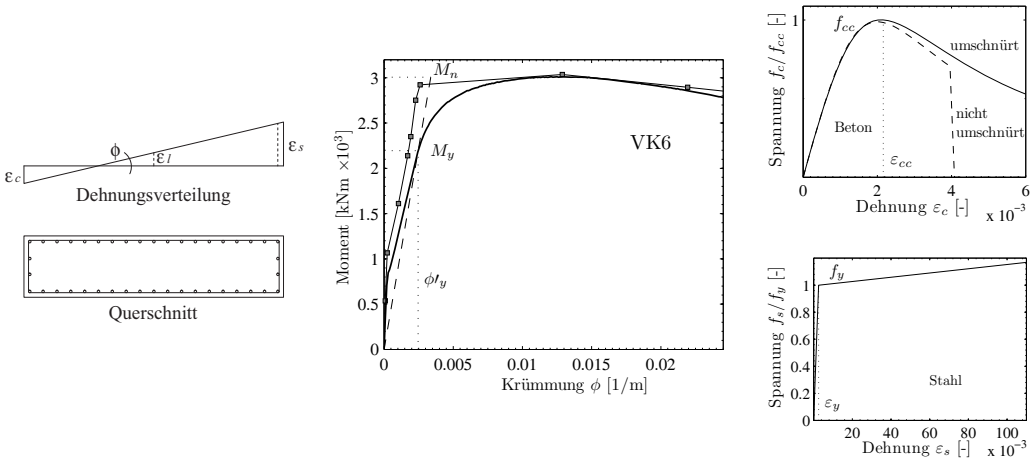

a) Querschnitt und Dehnungsverteilung. *b) Momenten-Krümmungsbeziehung.* *c) Materialgesetze.*

Abb. 2: *Grundlagen der Querschnittsanalyse.*

Die Verformungskapazität des Bauteils wird in der Regel über das Erreichen eines Dehnungslimits im plastischen Gelenk definiert. Bei Überschreiten dieser Dehnung wird angenommen, dass die Schädigung im plastischen Bereich gross genug ist, um zu einem gewissen, als Versagenszustand definierten, Lastabfall zu führen. Ein Verlust der

Querkrafttragfähigkeit von 20% wird häufig als Versagen definiert. Die hier präsentierten Dehnungslimiten für Beton $\varepsilon_{cu,cyc}$ und Stahl $\varepsilon_{su,cyc}$ wurden für diesen Lastabfall entwickelt [6]:

$$\varepsilon_{cu,cyc} = 0.0035 + \left(\frac{1}{x_{c,con}}\right)^{3/2} + 0.4\frac{k_{con}\rho_v f_{yv}}{f_{cc}}$$
$$k_{con} = \left(1 - \frac{s}{2b_{con}}\right)\left(1 - \frac{s}{2h_{con}}\right)\left(1 - \frac{\sum s_{l,c}^2/6}{b_{con}h_{con}}\right) \quad (2)$$
$$\varepsilon_{su,cyc} = 0.375\varepsilon_{su}$$

In den Gleichungen bezeichnen $x_{c,con}$ die Tiefe der umschnürten Druckzone, h_{con} und b_{con} die Dimensionen des umschnürten Querschnittes, ρ_v den Querbewehrungsgrad, f_{yv} die Fliessgrenze der Querbewehrung, f_{cc} die Druckfestigkeit des umschnürten Betons, s den Abstand der Querbewehrung und $s_{l,c}$ den Abstand der Längsbewehrungsstäbe, die durch Haken o.ä. gegen Ausknicken gesichert sind. Bezüglich des Dehnungslimits für den Stahl ist anzumerken, dass dieses experimentell nicht verifiziert werden konnte, da ein Versagen der Längsbewehrung in den Versuchen nicht massgebend war. Die Endbereiche der betrachteten Stützenquerschnitte waren nicht umschnürt. Die Versuche haben gezeigt, dass das elastisch bleibende Fundament jedoch in einer gewissen Umschnürung des Wandfusses resultiert, welche bei der Beurteilung der Dehnungskapazität des Betons berücksichtigt werden sollte. Die Dimensionen des umschnürten Querschnittes wurden hier den Dimensionen des durch die Lage der gesamten Stützenlängsbewehrung definierten Kerns gleich gesetzt. Bei den hier betrachteten wandartigen Stützen wird mit diesen Dehnungslimits eine Verformung als Verformungskapazität definiert, die kurz nach der Verformung bei Maximallast erreicht wird. Eine weiterreichende Berücksichtigung der post-peak Verformungskapazität ist mit dem plastischen Gelenk Modell nicht möglich. Dies liegt unter anderem daran, dass mit zunehmender Schädigung des Bauteils die im plastischen Gelenk Modell getroffene Annahme von eben bleibenden Querschnitten immer weniger gültig ist und ein Teil des Lastabfalls auf eine Degradation des Schubmechanismus, der mit diesem Modell nicht erfasst wird, zurückzuführen ist. Falls eine bessere Anrechnung der post-peak Verformungskapazität notwendig ist, sollte das später erwähnte kinematische Modell angewendet werden.

Berücksichtigung von Bewehrungsstössen

Ein Stoss der Längsbewehrung am Fuss der Stütze, wo sich auch das plastische Gelenk bildet, kann zu einem schnellen Abfall der Querkrafttragfähigkeit führen, sobald das Versagen des Stosses einsetzt. Sofern der Stoss nicht umschnürt ist und lang genug ist, um die sich aus der Stahlzugfestigkeit ergebende Zugkraft aufzunehmen, wird das Stossversagen durch Schädigung des Betons auf Druck eingeleitet. Die Übertragung der Kraft zwischen den gestossenen Stäben wird, falls keine Umschnürungsbewehrung vorhanden ist, einzig durch den Beton sichergestellt. Durch das Entstehen von Betondruckrissen wird die Betonzugfestigkeit und somit die Kapazität der Kraftübertragung herabgesetzt. Unter zyklischer Belastung wird bei einer auf die Druckbelastung folgenden Zugbelastung damit das Entstehen von Spaltrissen begünstigt, was zu einem Verlust der Tragfähigkeit des Stosses führen kann.

Das Dehnungslimit für das Versagen des Betons auf Druck kann gemäss der Gleichung nach [5] für umschnürten Beton abgeschätzt werden:

$$\varepsilon_{cc} = \varepsilon_c\left(1 + 5\left(\frac{f_{cc}}{f_c} - 1\right)\right)$$
$$f_{cc} = f_c\left(1.254 + 2.254\sqrt{1 + \frac{7.94 f_l'(k_{con},\rho_v)}{f_c}} - 2\frac{f_l'(k_{con},\rho_v)}{f_c}\right) \quad (3)$$

k_{con} wird nach Gl. (2) mit einem Bügelabstand s, der dem Abstand zwischen dem Fundament und dem untersten Bügel entspricht, bestimmt. Das heisst das Fundament wird für diesen Fall als Bügel betrachtet. Ausserdem werden zur Ermittlung der Effektivität der Umschnürung (ebenfalls Faktor k_{con}) alle Längsbewehrungsstäbe angerechnet, da diese durch das Fundament in Querrichtung gehalten sind. Der Längsbewehrungsabstand der gegen Knicken gesicherten Stäbe $s_{l,c}$ entspricht somit dem Längsbewehrungsabstand s_l. In Längs- (x) bzw. Querrichtung (y) der Bügel wird eine Spannung $f'_{lx/y}=k_{con}\rho_{vx/y}f_{yv}$ angenommen, die den Beton umschnürt. Die Querbewehrungsgehalte und die Anzahl der berücksichtigten Längsbewehrungsstäbe wurden hier, da bei den Stützen kein umschnürter Endbereich vorhanden war, für einen quadratischen Bereich am Rand des Querschnittes bestimmt. Um die Verformungskapazität bei einsetzendem Stossversagen abzuschätzen, ist das kleinste Dehnungslimit gemäss Gl. (2) – (3) massgebend.

Nach dem Erreichen der zu diesem Limit gehörenden Krümmung wird ein sofortiger Abfall des Querkraftwiderstandes auf eine durch die Exzentrizität der Axiallast bestimmte Restkapazität angenommen. Letztere wird gemäss folgender Gleichung bestimmt:

$$V = \frac{P}{L_s}\frac{h_c - a}{2} \quad \text{mit} \quad a = \frac{P}{0.85 f_c b_c} \tag{4}$$

Hierin bezeichnen h_c und b_c die Dimensionen des durch die Lage der Längsbewehrung definierten Kerns, das heisst die Dimensionen der Stütze ohne Berücksichtigung der Betonüberdeckung.

Biegeverformungen

Die Biegeverformungen können mit dem sogenannten verfeinerten Ansatz nach [7] bestimmt werden. Dieser Ansatz erlaubt eine Bestimmung der gesamten Last-Verformungskurve anstatt der häufig verwendeten bilinearen Approximation. Zwischen dem Nullpunkt und der Biegeverformung bei erstmaligem Fliessen $\Delta'_{y,fl}$ (zugehörige Krümmung ϕ'_y) wird dabei linear interpoliert (siehe auch Abb. 2 b)). Die Krümmung ϕ'_y wird durch erstmaliges Fliessen der äussersten Bewehrungsstäbe (zugehörige Dehnung $\varepsilon_s=f_y/E_s$) oder durch erstmaliges Erreichen der maximalen Druckspannung gehörenden Betonstauchung (typischerweise $\varepsilon_c=0.002$) am äussersten Rand des Querschnittes definiert. Danach werden die Biegeverformungen Δ_{fl} abhängig von der mit der Querschnittsanalyse bestimmten Krümmung ϕ berechnet:

$$\begin{aligned} \Delta'_{y,fl} &= \phi'_y \frac{L_s^2}{3} & F'_y &= \frac{M_y}{L_s} \\ \Delta_{fl} &= \Delta'_{y,fl}\frac{M}{M_y} + \left(\phi - \phi'_y \frac{M}{M_y}\right) L_p L_s & F &= \frac{M}{L_s} \end{aligned} \tag{5}$$

Mit diesen Gleichungen können die Biegeverformungen bis zu dem Punkt bestimmt werden, der durch die von den Dehnungslimits in Gl. (2) – (3) abhängige maximale Krümmung ϕ_u definiert ist. Diese Biegeverformung entspricht, wie bereits erwähnt, der durch das plastische Gelenk Modell definierten Verformungskapazität.

Mit Gl. (1) – (5) lassen sich die Biegeverformungen bestimmen, die in Abb. 3 exemplarisch für eine Stütze mit duchgängiger Bewehrung (VK6) sowie für die zugehörige Stütze mit Stoss (VK5) dargestellt sind. Zum Vergleich sind die experimentell gemessenen Biegeverformungen sowie die Punkte, bei denen im Versuch erstmals die Dehnungslimits gemäss Gl. (2) – (3) überschritten wurden, dargestellt. Die Biegeverformungen werden als Drift, das heisst mittlere Schiefstellung $\delta=\Delta_{fl}/L_s$ in Prozent, dargestellt.

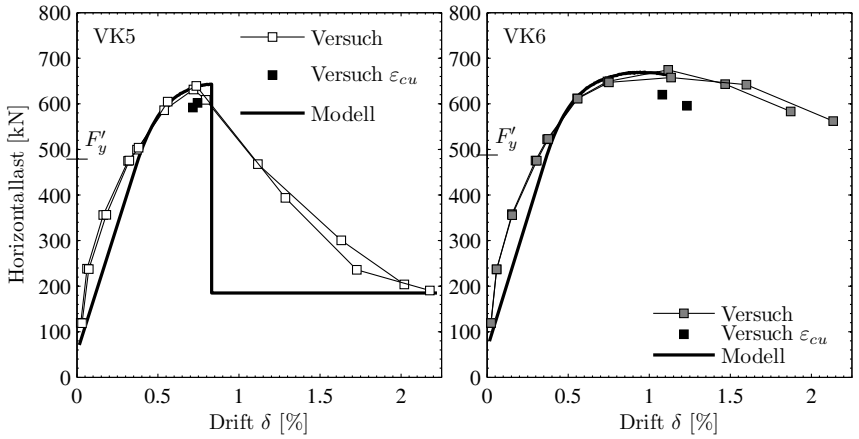

Abb. 3: *Berechnete und experimentell bestimmte Biegeverformungen je eines Versuchskörpers mit (VK5) und ohne (VK6) Stoss [3].*

Schubverformungen

Wie im ersten Abschnitt dargestellt ist die Modellierung mit plastischem Gelenk primär dazu gedacht, die Biegeverformungen eines Bauteils vorherzusagen. Da die Schubverformungen jedoch im inelastischen Bereich in der Regel zu den Biegeverfomungen in Relation stehen, können sie in der Modellierung über diese Relation berücksichtigt werden. Die im Rahmen dieses Projektes durchgeführten Experimente haben gezeigt, dass bei Erreichen der Fliesslast F'_y die Schubverformungen noch relativ klein sind und nicht berücksichtigt werden müssen. Im inelastischen Bereich wurden jedoch bei den schubkritischen Stützen Schubverformungen bestimmt, die über 30% der Biegeverformungen entsprechen. Eine Vernachlässigung dieser Verformungen würde daher zu einer Unterschätzung der Verformungskapazität führen.

Für die hier betrachteten Versuchskörper wurde eine gute Abschätzung des Schub- zu Biegeverformungsverhältnisses mit einem modifizierten Ansatz nach [8] erreicht. Mit dieser Gleichung werden die Schubverformungen über die Krümmung und die Axialdehnung zu den Biegeverformungen in Relation gesetzt. Mit diesen beiden Werten können für die Biegeverformungen im plastischen Bereich die korrespondierenden Schubverformungen bestimmt werden. Weiterhin hängen die Schubverformungen von dem erwarteten Risswinkel θ ab; je steiler dieser Winkel ist, d.h. je mehr Schubrissbildung auftritt, desto grösser sind die Schubverformungen. Der Risswinkel wird hier über die Längs- und Querbewehrungsgehalte, ρ_l und ρ_v, abgeschätzt [9]. Das Schub- zu Biegeverformungsverhältnis folgt damit abhängig von der Axialdehnung im Schwerpunkt des Querschnittes ε_l als:

$$\frac{\Delta_s}{\Delta_{fl}} = 0.75\alpha \frac{\varepsilon_l}{\phi \sqrt[4]{\dfrac{\rho_v + (E_s/E_c)\rho_v\rho_l}{\rho_l + (E_s/E_c)\rho_v\rho_l}}} \frac{1}{L_s} \tag{6}$$

Zur Berücksichtigung der Beobachtung, dass Bauteile mit geringem Schubwiderstand grössere Schubverformungen aufweisen, wird der Korrekturfaktor α auf Basis des Schub-Zugwiderstandes V_n gemäss [10] sowie des Stegdruckwiederstandes V_{wc} gemäss EC2 6.2.3 (3) [11] berücksichtigt:

$$1 \le \alpha = \frac{V}{V_n} + \frac{V}{V_{wc}} \le 2$$

$$V_n = \rho_v\, b\, f_{yv}\,(h - x_c - c)\cot 30^\circ + \left(3 - \frac{L_s}{h}\right)(0.5 + 20\rho_l)\,0.05\sqrt{f_c}\,0.8hb + P\frac{h - x_c}{2L_s} \tag{7}$$

$$V_{wc} = 1.0\, b\, z\, 0.6 \frac{f_c}{\cot\theta + \tan\theta}$$

Der innere Hebelarm z und die Höhe der Druckzone x_c können aus der Momenten-Krümmungsanalyse bestimmt werden. Bei Längsbewehrungsgehalten $\rho_l > 2.5$% wird der Term $(0.5+20\rho_l)$ zu 1.0 gesetzt. Der Term $(3-L_s/h)$ berücksichtigt nur einen Übergang zwischen den Schubschlankheiten 1.5 bis 2.0, d.h. $1 \leq (3-L_s/h) \leq 1.5$. Der Anteil der Axiallast P wird nur im Fall einer Druckkraft berücksichtigt und ist andernfalls gleich null.

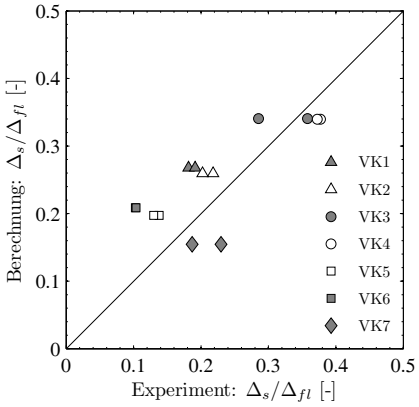

Abb. 4: *Berechnete und experimentell bestimmte Schub- zu Biegeverformungs-verhältnisse bei Maximallast (Versuche [1], [3]).*

Mit diesem Ansatz zur Bestimmung des Schub- zu Biegeverformungsverhältnisses Δ_s/Δ_{fl} werden für die sieben hier betrachteten Versuchskörper [1], [3] die in Abb. 4 dargestellten Ergebnisse für das Verhältnis bei Maximallast erzielt.

Gesamtverformung

Die Gesamtverformung setzt sich aus den Biege- und Schubverformungen zusammen. Bis zum Fliessbeginn der Längsbewehrung werden die Schubdeformationen jedoch als vernachlässigbar betrachtet und lediglich die Biegedeformationen berücksichtigt. Daher kann bei Fliessbeginn ($\phi = \phi'_y$) die Gesamtdeformation wie folgt abgeschätzt werden:

$$\Delta = \Delta'_{y,fl} = \phi'_y \frac{L_s^2}{3} \qquad F'_y = \frac{M_y}{L_s} \tag{8}$$

Im inelastischen Bereich, das heisst für Krümmungen $\phi > \phi'_y$, wird die Gesamtverformung wie folgt berechnet:

$$\Delta = \Delta_{fl} + \Delta_s = \Delta_{fl}\left(1 + \frac{\Delta_s}{\Delta_{fl}}\right) \qquad F = \frac{M}{L_s} \tag{9}$$

Die Biegeverformungen sowie das Biege- zu Schubverformungsverhältnis in dieser Gleichung werden gemäss Gl. (1) und (5) – (7) bis zu der Krümmung, bei welcher die Dehnungslimits gemäss Gl. (2) – (3) erreicht werden, bestimmt. Für die beiden zuvor exemplarisch betrachteten Versuchskörper ergeben sich damit die in Abb. 5 dargestellten Last-Verformungskurven.

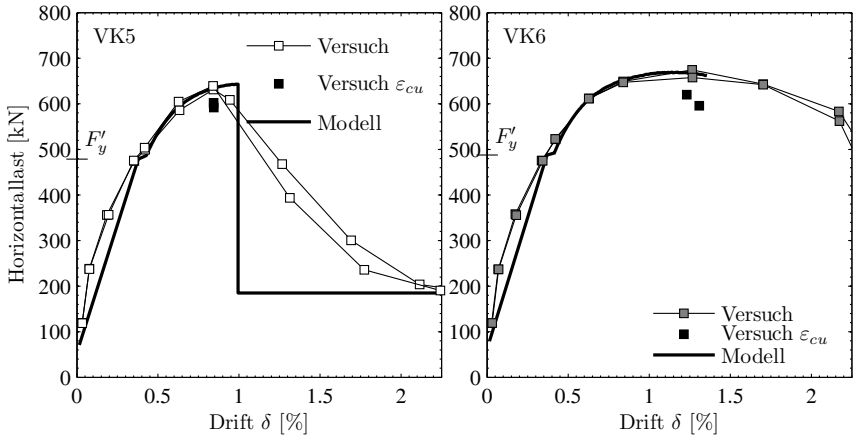

Abb. 5: *Berechnete und experimentell bestimmte Gesamtverformungen je eines Versuchskörpers mit (VK5) und ohne (VK6) Stoss.*

Kinematisches Modell

Einführung

Das kinematische Modell basiert auf der sich bei ausgeprägter Schubrissbildung einstellenden Kinematik. Dies bedeutet, es kann weder für eindeutig biegebestimmte Bauteile angewendet werden noch für solche mit Bewehrungsstoss am Fuss. Das Modell wurde basierend auf einem ähnlichen Modell für Balken mit grosser Querschnittshöhe [12] entwickelt. In dem Modell für Balken wurde das Verformungsfeld mit nur zwei Parametern beschrieben. Für wandartige Stützen wurde ein dritter Parameter hinzugefügt, daher der Name „3 Parameter Kinematic Theory (3PKT)“. Eine genaue Einführung in diese Theorie ist im Rahmen dieser Zusammenfassung nicht möglich. Der Leser wird dazu auf die Publikation [13] verwiesen, in welcher die Theorie präsentiert wurde, sowie auf Kapitel 5 des folgenden Berichtes, welches eine Validierung der Theorie enthält.

Im Folgenden werden die Grundlagen der Theorie kurz dargestellt und die vorhergesagten Last-Verformungskurven einiger Stützen mit den experimentellen Daten verglichen. Mit Hilfe dieser Theorie können die Verformungen bis zur Degradation des Schubmechanismus und somit bis zum Verlust sowohl der Querkraft- als auch der Axiallasttragfähigkeit vorhergesagt werden. Damit ist eine bessere Ausnutzung der tatsächlichen Verformungskapazität eines Bauteils nach Erreichen der Maximallast möglich.

Grundlagen der Modellierung

In Abb. 6 werden die im Modell angenommene Kinematik sowie die berücksichtigten Tragmechanismen dargestellt. Der linke Teil des Bildes zeigt die angenommene Verformung der Stütze. Unter dem Schubriss wird ein radial gerissener Bereich angenommen, oberhalb ein Starrkörper. Am Fuss der Stütze direkt über dem Schubriss wird ein Bereich angenommen, in dem sich die Schädigung des Starrkörpers konzentriert. Das gesamte Verformungsfeld wird durch die drei eingezeichneten Parameter $\varepsilon_{s,avg}$, Δ_c und Δ_{cv} dargestellt. Der erste Parameter $\varepsilon_{s,avg}$ bezeichnet die mittlere Dehnung der Längsbewehrung, welche die Verlängerung auf der Zugseite der Stütze sowie die Rotation des Starrkörpers beeinflusst. Die beiden übrigen Parameter Δ_c und Δ_{cv} bezeichnen die Translation und die vertikale Verschiebung des Starrkörpers, die durch Verformung des geschädigten Bereiches am Fuss des Starrkörpers verursacht werden.

Der zweite Teil von Abb. 6 zeigt die in der Theorie berücksichtigten Tragmechanismen. Alle Kräfte werden im Modell als Federn dargestellt, deren Gesetze sich aus den Materialeigenschaften ergeben. Die Dehnungen der Federn wiederum resultieren aus den mit den drei genannten Parametern bestimmten Verformungen.

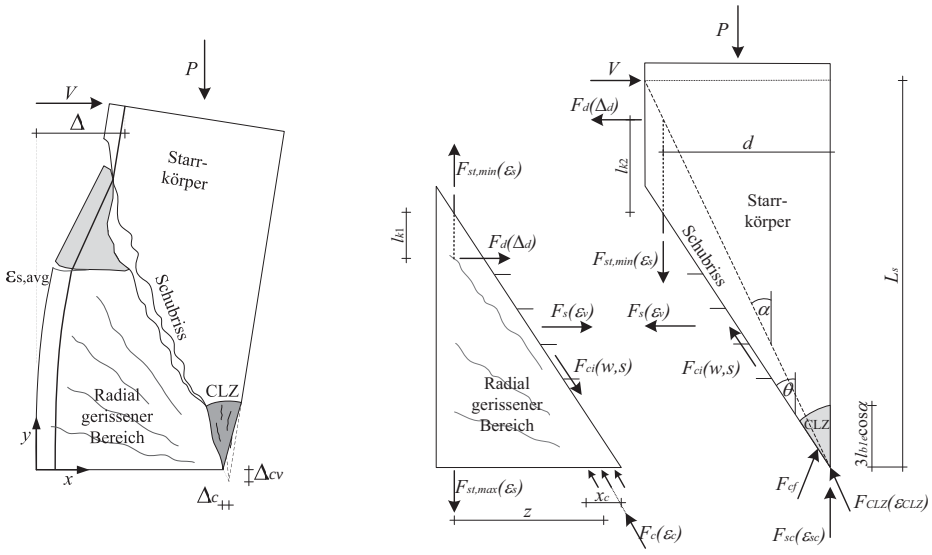

Abb. 6: *Grundlagen der kinematischen Theorie.*

Die Längs- und Querbewehrung werden als jeweils eine Feder dargestellt die im Schwerpunkt der jeweiligen Bewehrung angreifen und deren Resultierende F_{st} bzw. F_s sich durch die vom Verformungsfeld abhängigen Dehnungen ε_s und ε_v ergeben. Zur Berücksichtigung der Dübelwirkung wird angenommen, dass die Längsbewehrung am Rissufer zweier benachbartes Schubrisse eingespannt ist. Die Dübelkraft F_d folgt dann aus dem Momentenprofil über die Länge l_k, welches von der Relativverschiebung zwischen den beiden Einspannpunkten Δ_d abhängt. Entlang des Schubrisses wirkt ausserdem die Resultierende der Rissverzahnung F_{ci}, die von der Rissöffnung w und dem Schlupf s entlang des Risses abhängt.

Im stärker geschädigten Bereich am Fuss des Starrkörpers greifen mehrere Kräfte an. Zum einen ist dies die aus der Stauchung dieser Zone ε_{CLZ} resultierende Betondruckkraft F_{CLZ}, deren Wirkungsrichtung von der Translation sowie der Verkürzung dieser Zone (Δ_c und Δ_{cv}) abhängt. Je nach Schlankheit der Stütze und aufgebrachter Axiallast entsteht zwischen der Spitze des Starrkörpers und dem radial gerissenen Bereich eine hohe Kontaktkraft. Durch eine Abwärtsbewegung des Starrkörpers resultiert daraus eine Reibungskraft und damit die Kraftresultierende F_{cf}. Ausserdem greift in diesem Bereich der Stütze die aus der Stauchung der Längsbewehrung ε_{sc} resultierende Druckkraft F_{sc} an.

Im radial gerissenen Bereich unterhalb des massgebenden Schubrisses ensteht eine Betondruckkraft am Fuss der Stütze F_c. Neben dieser Kraft wirken die bereits erwähnten über den Riss übertragenen Kraftkomponenten auf den Bereich unterhalb des Schubrisses ein.

Durch Gleichgewichts- und Kompatibilitätsbetrachtungen können für jede Kopfverschiebung Δ das Verformungsfeld und die Kraftkomponenten, aus welchen sich die Gesamtquerkraft V ergibt, berechnet werden. Nach dieser Theorie wird Versagen dadurch eingeleitet, dass die Zone am Fuss des Starrkörpers zu stark geschädigt ist und die resultierende Kraft F_{CLZ} abfällt. Dies geht einher mit einer hohen Stauchung dieser Zone, die zu einem Abwärtsgleiten des Starrkörpers entlang des Schubrisses führt. Diese Abwärtsbewegung resultiert in einer höheren Rissverzahnungskraft F_{ci}, die den Verlust der Kraft F_{CLZ} zunächst ausgleicht. Bei weiterem Abwärtsgleiten sowie grösserer Rissöffnung degradiert jedoch auch dieser Mechanismus, was zu einem Verlust der Querkraft- und Axiallastkapazität der Stütze führt.

Darstellung der Ergebnisse

In Abb. 7 werden die mit der kinematischen Theorie erzielten Ergebnisse für zwei der im Rahmen dieses Forschungsprojektes getesteten Versuchskörper dargestellt. Der

Vergleich mit den experimentellen Daten zeigt, dass neben der Querkrafttragfähigkeit auch der stärker degradierende Teil der Last-Verformungskurve gut erfasst wird. Ausserdem wird in den Graphen der Beitrag der einzelnen Querkraftkomponenten dargestellt. Dies veranschaulicht den bereits geschilderten Versagensmechanismus: Nachdem die Querkraftkomponente V_{CLZ} abfällt, wird zuerst ein Ansteigen der Rissverzahnungskomponente V_{ci} beobachtet, bevor auch diese, und damit die gesamte Kapazität der Stütze, degradiert.

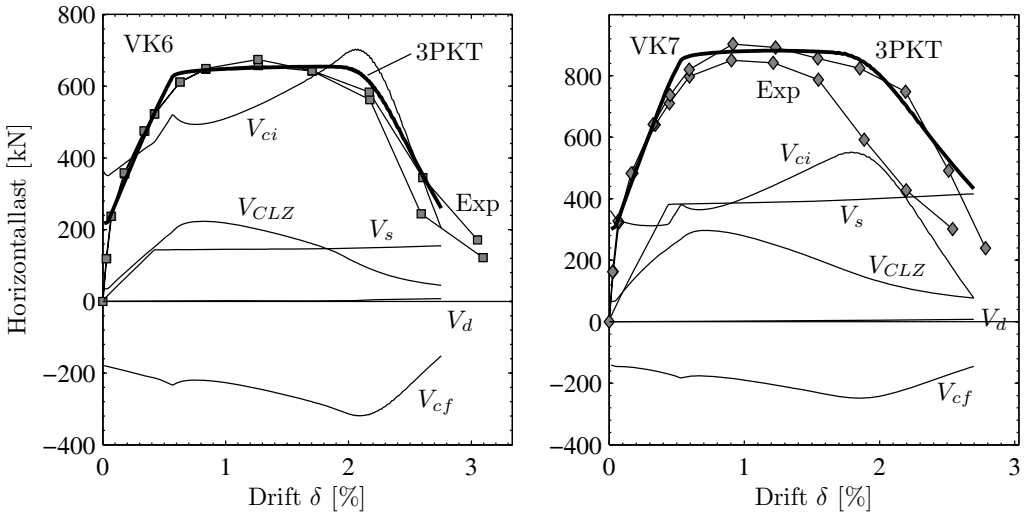

Abb. 7: *Darstellung der mit der kinematischen Theorie erzielten Ergebnisse für zwei Versuchskörper.*

Einfluss ausgewählter Parameter auf die Verformungskapazität

In diesem Abschnitt wird der Einfluss zweier Parameter, die auch Gegenstand der experimentellen Untersuchungen waren, auf das Verformungsvermögen mit Hilfe der 3PKT dargestellt. Zum einen wird der Einfluss der Querbewehrung und zum anderen der Einfluss der Schlankheit untersucht. Die Querbewehrung wurde in den Versuchen VK3 (Querbewehrungsgehalt 0.08%) und VK7 (Querbewehrungsgehalt 0.22%) variiert. Erwartungsgemäss stieg die Verformungskapazität mit zunehmendem Querbewehrungsgehalt an, während die Kraftkapazität unbeeinflusst blieb, siehe Abb. 8. Letzteres kann damit begründet werden, dass auch bei geringem Querbewehrungsgehalt kein vorzeitiges Schubversagen auftrat, sondern die volle Kapazität erreicht wurde.

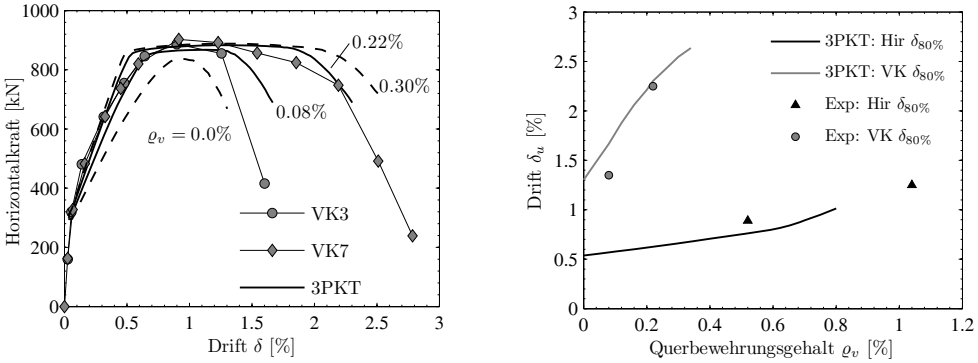

Abb. 8: *Einfluss des Querbewehrungsgehaltes auf das Verhalten der Versuchskörper.*

Ein Vergleich mit weiteren Versuchen [14] zeigte allerdings, dass die Ausprägung des Einflusses stark von der Konfiguration der Versuche abhängt. Während bei den schlankeren Versuchen VK3 & VK7 (L_s/h=2.2) ein starker Anstieg der zu 80% Querkraftkapazität korrespondierenden Verformungskapazität zu beobachten war und auch berechnet wurde, ist der günstige Einfluss der Querbewehrung bei den kürzeren

Versuchen [14] (Hirosawa (1975) in Abb. 8 mit „Hir“ gekennzeichnet, L_s/h=1.0) deutlich weniger ausgeprägt.

Eine Änderung der Schlankheit beeinflusst sowohl den Querkraftwiderstand als auch das Verformungsvermögen. Mit zunehmender Schlankheit nimmt der Querkraftwiderstand ab während das Verformungsvermögen ansteigt, siehe Abb. 9. Die Berechnungen, die mit Hilfe der 3PKT für die Versuchskörper VK3 & VK6 mit gemittelten Materialwerten und variabler Schlankheit durchgeführt wurden, zeigen zudem einen deutlichen Anstieg des Verformungsvermögens zwischen den Schlankheiten 1.5 und 2.0. Der Vergleich der Last-Verformungskurven in Abb. 9 zeigt, dass für die betrachteten Versuchskörper bei Schlankheiten kleiner als ca. 1.5 ein eher sprödes Verhalten vorherrscht, während höhere Schlankheiten mit einem duktileren Verhalten und der Ausbildung eines Fliessplateaus einher gehen.

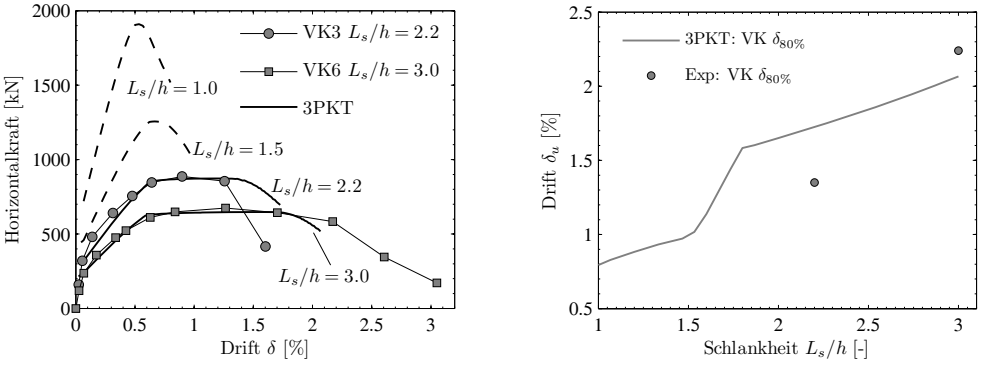

Abb. 9: *Einfluss der Schlankheit auf das Verhalten der Versuchskörper.*

Für eine detailliertere Diskussion des Einflusses verschiedener Parameter sowie einen Vergleich mit Abschätzungen der Driftkapazität gemäss anderer, existierender Formulierungen wird der Leser auf Abschnitt 5.5 des folgenden Berichtes verwiesen.

Schlussfolgerungen

Wie in den vorhergehenden Abschnitten dargestellt, kann mit Hilfe des plastischen Gelenk Modells eine Vorhersage der Last-Verformungskurve bis kurz nach Erreichen der Maximallast getroffen werden. Die Vorgehensweise zur Bestimmung der Last-Verformungskurve einer rechteckigen, wandartigen Stütze ist in diesen Abschnitten zusammengefasst. Zur Abschätzung der Verformungskapazität wird prinzipiell dieses Modell empfohlen, da es eine eher konservative Abschätzung der tatsächlichen Kapazität liefert und zudem einfach und schnell anwendbar ist. Falls es jedoch im Rahmen der verformensbasierten Überprüfung einer Brückenstütze für sinnvoll erachtet wird, den post-peak Bereich der Antwort stärker zu berücksichtigen, z.B. wenn die mit dem plastischen Gelenk Modell berechnete Kapazität knapp unter dem erwarteten Verformungsbedarf liegt, kann das kinematische Modell angewendet werden. Hierbei ist jedoch zu beachten, dass zum einen die Implementierung aufwendiger ist und zum anderen der abfallende Teil der Last-Verformungskurve mit einer Degradation des Mechanismus, der auch die Axiallastkapazität sicherstellt, einhergeht. Es muss daher im Einzelfall überlegt werden, wie weit die mit diesem Modell vorhergesagte Verformungskapazität ausgenutzt werden soll.

Berechnungsbeispiel

Einleitung

In diesem Abschnitt wird ein Berechnungsbeispiel zur Anwendung des plastischen Gelenk Modells für eine Brückenstütze mit (VK5) und ohne (VK6) Bewehrungsstoss gegeben. Die Vorgehensweise wird Schritt für Schritt dargestellt und die Unterschiede zwischen dem Vorgehen bei Stützen mit und ohne Bewehrungsstoss werden verdeutlicht. Bei den im Beispiel verwendeten Stützen handelt es sich um die gleichen, die auch im Bericht selbst näher untersucht werden.

Stützendaten

Der Querschnitt der Stützen, für welche die Beispielrechnung durchgeführt wird, sowie alle notwendigen Eingangsdaten sind in Abb. 1 dargestellt. Es handelt sich hierbei um zwei rechteckige Stützen mit gleichmässig im Querschnitt verteilter Bewehrung. VK6 hat eine durchgängige Längsbewehrung, während die Längsbewehrung von VK5 direkt über dem Fundament auf einer Länge von 60cm, entsprechend 43 Stabdurchmessern, gestossen ist. Bis auf den Bewehrungsstoss unterscheiden sich die beiden Stützen nur durch eine leichte Streuung der Materialwerte. Für die Beispielrechnung werden die Materialwerte von VK5 verwendet.

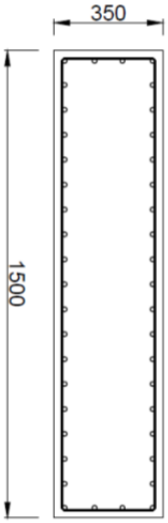

Abmessungen Stütze
b / h / L_s = 0.35m / 1.50m / 4.50m

Bewehrung
Längsbewehrung: ρ_l = 1.23%
42 Stäbe d_{bl} = 14mm, Abstand s_l = 80mm
Querbewehrung: ρ_v = 0.08%
zweischnittige Bügel d_{bv} = 6mm, Bügelabstand s = 200mm
Betondeckung: c_{nom} = 25mm

Material
Beton: f_c = 35.2MPa
Längsbewehrung: f_y = 520MPa, f_u/f_y = 1.17
ε_{su} = 11%
Querbewehrung: f_y = 528MPa, f_u/f_y = 1.29
ε_{su} = 7.1%

Abb. 1: *Abmessungen und Materialeigenschaften der Brückenstützen.*

Momenten-Krümmungsbeziehung

Zuerst wird die Momenten-Krümmungsanalyse des Querschnittes durchgeführt. Dies kann zum Beispiel mittels eines Programmes wie Response2000 [94] geschehen. Die im Beispiel verwendete Analyse wurde mit einem in Matlab [57] programmierten Code durchgeführt. Für den Beton wurde die Spannungs-Dehnungsbeziehung für umschnürten Beton gemäss Mander et al. [5] verwendet. Im betrachteten Fall sind zwar nur Bügel mit 90° Haken und keine zusätzlich umschnürten Randbereiche vorhanden, aber mit diesem Materialmodell wurde auch nach Erreichen der Betondruckfestigkeit eine realistische Momentenkapazität abgeschätzt. In Bezug auf die Steigerung der Druckfestigkeit ist der durch die vorhandenen Bügel hervorgerufene Effekt allerdings gering, wie Abb. 2 zeigt. Die dort dargestellte Kurve des nicht umschnürten Betons wurde nur für den Überdeckungsbeton verwendet. Bei diesem wurde angenommen, dass er abplatzt, sobald eine Dehnung von 4‰ erreicht ist. Aus diesem Grund fällt die Spannung in der dargestellten Kurve bei einer Dehnung von 4‰ direkt auf null ab. Für den Stahl wurde eine bilineare Spannungs-Dehnungsbeziehung verwendet und Zugversteifung („tension stiffening“) wurde nicht berücksichtigt.

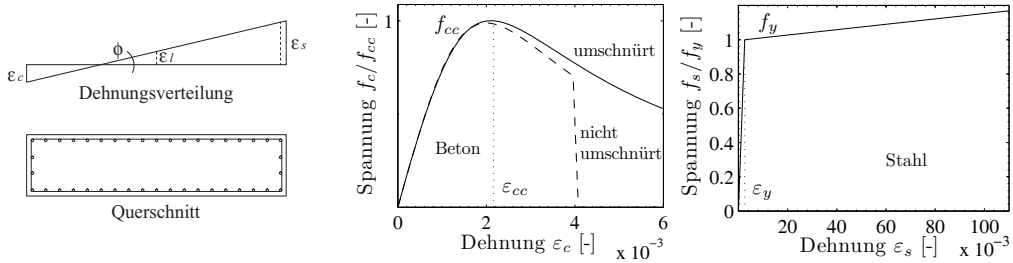

Abb. 2: *Bei der Querschnittsanalyse angenommene Dehnungsverteilung und verwendete Materialgesetze.*

Dehnungslimits

Durchgängige Längsbewehrung

Die Momenten-Krümmungsbeziehung wird verwendet bis zu der Krümmung, bei welcher das Dehnungslimit, durch welches das Versagen definiert ist, erstmals erreicht wird. Zur Berechnung des Dehnungslimits für Beton $\varepsilon_{cu,cyc}$ und Stahl $\varepsilon_{su,cyc}$ werden bei einer Stütze mit durchgängiger Längsbewehrung die folgenden Gleichungen verwendet [6]:

$$\varepsilon_{cu,cyc} = 0.0035 + \left(\frac{1}{x_{c,con}}\right)^{3/2} + 0.4\frac{k_{con}\rho_v f_{yv}}{f_{cc}}$$
$$k_{con} = \left(1 - \frac{s}{2b_{con}}\right)\left(1 - \frac{s}{2h_{con}}\right)\left(1 - \frac{\sum s_{l,c}^2 / 6}{b_{con}h_{con}}\right) \qquad (10)$$
$$\varepsilon_{su,cyc} = 0.375\varepsilon_{su}$$

In den Gleichungen bezeichnen $x_{c,con}$ die Tiefe der umschnürten Druckzone, h_{con} und b_{con} die Dimensionen des umschnürten Querschnittes, ρ_v den Querbewehrungsgrad, f_{yv} die Fliessgrenze der Querbewehrung, f_{cc} die Druckfestigkeit des umschnürten Betons, s den Abstand der Querbewehrung und $s_{l,c}$ den Abstand der Längsbewehrungsstäbe, die zum Beispiel durch Haken gegen Ausknicken gesichert sind. Die Dimensionen des umschnürten Querschnittes und die Tiefe der Druckzone werden im Folgenden bis zur Mitte der Bügel berechnet. Die Stababstände werden ebenfalls jeweils von Mittelpunkt zu Mittelpunkt der Stäbe angesetzt.

Als Tiefe der umschnürten Druckzone wird hier die minimale Tiefe der Druckzone, die bei der Querschnittsanalyse ermittelt wurde, abzüglich der Betonüberdeckung bis zum Mittelpunkt der Bügel angesetzt. Die vier Längsbewehrungsstäbe in den Ecken des Querschnittes wurden aufgrund der Verbügelung als gehalten angesehen, und daher bei der Ermittlung von k_{con} berücksichtigt (s_{l1}). Beim Bau der Stützen wurden ausserdem zur Stabilisierung des Bewehrungskorbes zwei Reihen Haken eingefügt, mit denen die Längsbewehrung gehalten wurde. Diese wurde ebenfalls als Ausknickbewehrung in Rechnung gestellt (s_{l2}). In Gleichung (2) sollte prinzipiell die umschnürte Betonfestigkeit verwendet werden. Da jedoch bei den hier betrachteten Stützen der Einfluss der Umschnürung auf die Betonfestigkeit sehr gering ist, wird hier vereinfachend die Betonfestigkeit f_c angesetzt.

Für den betrachteten Querschnitt werden damit die folgenden Dehnungslimite berechnet:

Berechnung

h_{con} = 1500mm – 2·25mm – 6mm = 1444mm

b_{con} = 350mm – 2·25mm – 6mm = 294mm

s = 200mm

s_{l1} = 350mm – 2·25mm – 2·6mm – 14mm = 284mm

s_{l2} = (1500mm – 2·25mm – 2·6mm – 14mm)/3 = 478mm

$\rightarrow k_{con}$ =0.24

x_{ccon} = 320mm – 28mm = 222mm

$$\rightarrow \varepsilon_{cu} = 0.0035 + \left(\frac{1}{320}\right)^{\frac{3}{2}} + 0.4\frac{0.24 \cdot 0.0008 \cdot 528}{35.2} = 0.0049$$

$$\rightarrow \varepsilon_{su} = 0.375 \cdot 0.11 = 0.041$$

Übergreifungsstoss der Längsbewehrung am Stützenfuss

Bei Stützen, bei welchen die Längsbewehrung am Stützenfuss gestossen ist, wird als Dehnungslimit die kleinste der mit Gleichungen (2) und (3) ermittelten Dehnungen angesetzt.

$$\varepsilon_{cc} = \varepsilon_c \left(1 + 5\left(\frac{f_{cc}}{f_c} - 1\right)\right)$$

$$f_{cc} = f_c \left(1.254 + 2.254\sqrt{1 + \frac{7.94 f_l'(k_{con}, \rho_v)}{f_c}} - 2\frac{f_l'(k_{con}, \rho_v)}{f_c}\right) \qquad (3)$$

$$f_l' = k_{con}\rho_v f_{yv}$$

In dieser Gleichung wird k_{con} nach Gl. (2) mit einem Bügelabstand s, der dem Abstand zwischen dem Fundament und dem untersten Bügel entspricht, bestimmt. Ausserdem werden zur Ermittlung der Effektivität der Umschnürung (ebenfalls Faktor k_{con}) alle Längsbewehrungsstäbe angerechnet, da diese durch das Fundament in Querrichtung gehalten sind. Der Längsbewehrungsabstand der gegen Knicken gesicherten Stäbe $s_{l,c}$ entspricht somit dem Längsbewehrungsabstand s_l. In Längs- (x) bzw. Querrichtung (y) der Bügel wird die Spannung $f'_{lx/y}=k_{con}\rho_{vx/y}f_{yv}$ angesetzt. Das Dehnungslimit nach Gleichung (3) wird für einen quadratischen Bereich am Rand des Stützenquerschnittes ermittelt, das heisst mit $h = b$, siehe auch Abb. 3. Der Abstand der Längsbewehrung an den langen Seiten der Stütze beträgt s_l = 80mm; an der Stirnseite wird als Abstand ein Drittel des Abstands der beiden in den Ecken des Bügels gehaltenen Längsbewehrungsstäbe angesetzt.

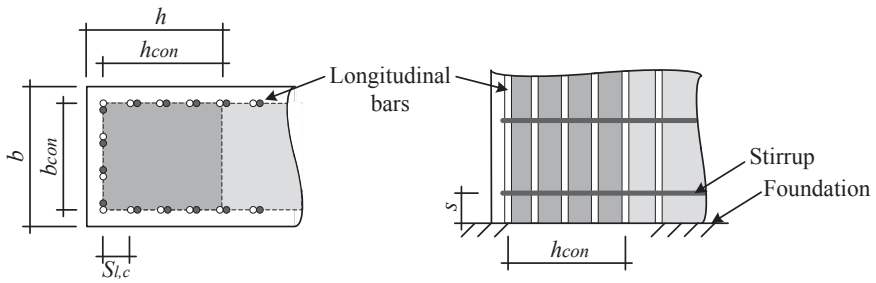

Abb. 3: *Berücksichtigter Randbereich zur Bestimmung des Dehnungslimits bei Stützen mit Längsbewehrungsstoss.*

Berechnung

h_{con} = 350mm – 28mm = 322mm

b_{con} = 350mm – 2·28mm = 294mm

s = 75mm

s_{l1} = (350mm – 2·25mm – 2·6mm -14mm)/3 = 98

s_{l2} = 80mm

$$\rightarrow k_{con} = 0.70$$

$$f'_{ll} = 0.7 \cdot (2 \cdot 28.3\text{mm}^2 / (294\text{mm} \cdot 75\text{mm})) \cdot 528\text{MPa} = 0.95\text{MPa} \qquad (2\ d_{bv} = 6\text{mm})$$

$$f'_{lq} = 0.7 \cdot (28.3\text{mm}^2 / (322\text{mm} \cdot 75\text{mm})) \cdot 528\text{MPa} = 0.44\text{MPa} \qquad (1\ d_{bv} = 6\text{mm})$$

$$f'_l = (0.44 + 0.95)\text{MPa} / 2 = 0.69\text{MPa}$$

$$f_{cc} = 35.2\left(-1.254 + 2.254\sqrt{1 + \tfrac{7.94 \cdot 0.69}{35.2}} - 2 \cdot \tfrac{0.69}{35.2}\right) = 39.8\text{MPa}$$

$$\rightarrow \varepsilon_{cc} = \varepsilon_{cu,St} = 0.002\,(1 + 5(39.8 / 35.2 - 1)) = 0.0033$$

Abb. 4 zeigt die auf Basis der genannten Materialmodelle und Berechnungsannahmen ermittelte Momenten-Krümmungsbeziehung des Querschnittes und die Krümmungen, bei denen die berechneten Dehnungslimits erreicht sind.

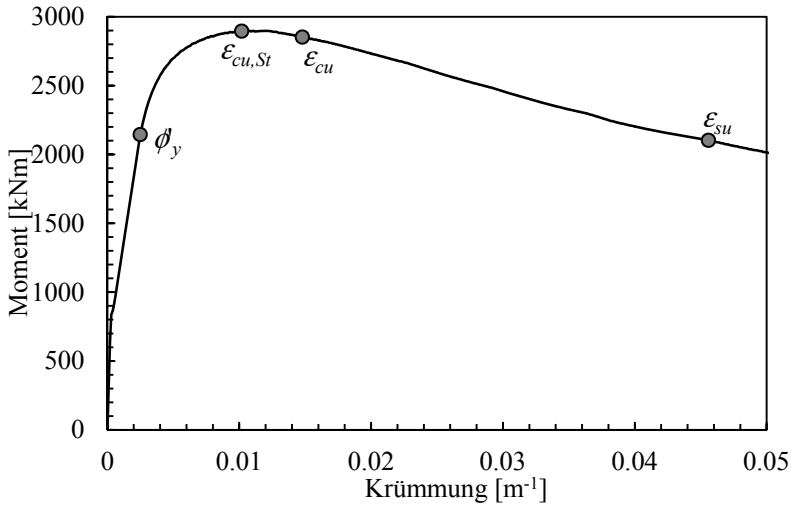

Abb. 4: *Momenten-Krümmungsbeziehung des betrachteten Querschnittes. Die Krümmungen, bei denen die Dehnungslimits für Stützen mit Stoss $\varepsilon_{cu,St}$, Beton ε_{cu} und Bewehrung ε_{su} erreicht sind, sind markiert.*

Länge des plastischen Gelenkes

Die Länge des plastischen Gelenkes wird mit der von [4] vorgeschlagenen Gleichung berechnet:

$$L_p = \left(0.2h + 0.05L_s\right)\left(1 - 1.5\frac{P}{A_g f_c}\right) \leq 0.8h \qquad (1)$$

Bei den hier betrachteten Stützen wurde während der Versuche eine Vertikallast von P = 1300kN aufgebracht. Zusammen mit dem Gewicht der Stütze und des Aufbaus ergibt sich eine Vertikallast von circa P = 1365kN.

Berechnung

$$L_p = (0.2 \cdot 1.5 + 0.05 \cdot 4.5)\text{m}\left(1 - 1.5\left(\frac{1.365}{1.5 \cdot 0.35 \cdot 35.2}\right)\right) = 0.47\text{m}$$

$$\leq 0.8 \cdot 1.5\text{m} = 1.2\text{m}$$

Berechnung der Biegeverformung

Die Biegeverformung wird mit der Momenten-Krümmungsbeziehung und der Länge des plastischen Gelenkes wie folgt berechnet:

$$\Delta'_{y,fl} = \phi'_y \frac{L_s^2}{3} \qquad F'_y = \frac{M_y}{L_s}$$
$$\Delta_{fl} = \Delta'_{y,fl} \frac{M}{M_y} + \left(\phi - \phi'_y \frac{M}{M_y} \right) L_p L_s \qquad F = \frac{M}{L_s} \tag{5}$$

In den Gleichungen bezeichnet ϕ'_y die Krümmung bei welcher erstmaliges Fliessen auftritt. Erstmaliges Fliessen wird durch das Erreichen der Fliessdehnung der Bewehrung in der Zugzone oder das Erreichen einer Betondehnung von $\varepsilon_c = 0.002$ in der Druckzone des Querschnittes definiert. Im betrachteten Fall wird die Fliessdehnung der Bewehrung zuerst erreicht. Die Fliesskrümmung ist zur Veranschaulichung ebenfalls in Abb. 4 eingetragen. Die Biegeverformung wird mittels Gleichung (5) bis zum Erreichen der zuvor bestimmten Dehnungslimits berechnet, siehe Abb. 5.

Bei einer Stütze mit Bewehrungsstoss wird angenommen, dass der Widerstand bei Erreichen des Dehnungslimits auf den Widerstand abfällt, der durch die maximal mögliche Exzentrizität der Normalkraft definiert ist. Dieser wird wie folgt berechnet:

$$V = \frac{P}{L_s} \frac{h_c - a}{2} \quad \text{mit} \quad a = \frac{P}{0.85 f_c b_c} \tag{4}$$

Berechnung

a = 1.365MN / (0.85·35.2MPa·0.284m) = 0.16m

V = (1365kN / 4.5m)·((1.5m – 2·0.033m) – 0.16m) / 2 = 193kN

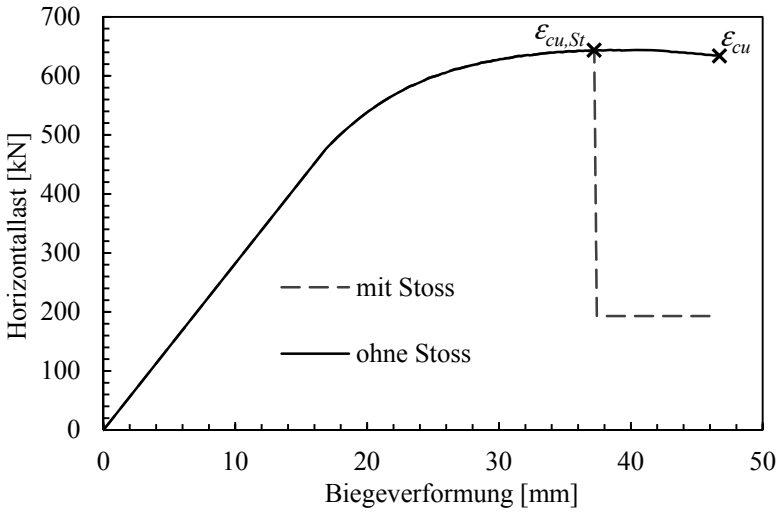

Abb. 5: *Biegeverformung einer Stütze ohne und mit Bewehrungsstoss am Fuss.*

Schubverformungen

Die Schubverformungen werden über ihr Verhältnis zu den Biegeverformungen in der Modellierung berücksichtigt. Dieses Verhältnis wird mit einem modifizierten Ansatz nach [8] abhängig von der Axialdehnung im Schwerpunkt des Querschnittes ε_l und den Längs- und Querbewehrungsgehalten, ρ_l und ρ_v, abgeschätzt:

$$\frac{\Delta_s}{\Delta_{fl}} = 0.75\alpha \frac{\varepsilon_l}{\phi \sqrt[4]{\frac{\rho_v + (E_s/E_c)\rho_v\rho_l}{\rho_l + (E_s/E_c)\rho_v\rho_l}}} \frac{1}{L_s} \tag{6}$$

Die vierte Wurzel im Nenner dieser Gleichung entspricht dem Tangens des in der Berechnung verwendeten Risswinkels θ. Zur Berücksichtigung der Beobachtung, dass Bauteile mit geringem Schubwiderstand grössere Schubverformungen aufweisen, wird wie in [28] vorgeschlagen, der Korrekturfaktor α auf Basis des Schub-Zugwiderstandes V_n nach [10] sowie des Stegdruckwiederstandes V_{wc} gemäss EC2 6.2.3 (3) [11] berücksichtigt:

$$1 \le \alpha = \frac{V}{V_n} + \frac{V}{V_{wc}} \le 2$$

$$V_n = \rho_v\, b\, f_{yv}\,(h - x_c - c)\cot 30^\circ + \left(3 - \frac{L_s}{h}\right)(0.5 + 20\rho_l)\,0.05\sqrt{f_c}\,0.8hb + P\frac{h - x_c}{2L_s} \tag{7}$$

$$V_{wc} = 1.0\, b\, z\, 0.6 \frac{f_c}{\cot\theta + \tan\theta}$$

Bei Längsbewehrungsgehalten $\rho_l > 2.5\%$ wird der Term $(0.5 + 20\rho_l)$ zu 1.0 gesetzt. Der Term $(3 - L_s/h)$ berücksichtigt nur einen Übergang zwischen den Schubschlankheiten 1.5 bis 2.0, d.h. $1 \le (3 - L_s/h) \le 1.5$. Im Berechnungsbeispiel ist $L_s/h=3$ und somit der einzusetzende Wert gleich 1.0. Der Anteil der Axiallast P wird nur im Fall einer Druckkraft berücksichtigt und ist andernfalls gleich null. Für den inneren Hebelarm z und die Höhe der Druckzone x_c werden hier die zum maximalen Moment gehörigen Werte aus der Querschnittsanalyse verwendet. Zur Ermittlung des Korrekturfaktors α wird hier, sofern in Gleichung (8) nicht anders spezifiziert, der gleiche Risswinkel wie in Gleichung (7) angesetzt. Falls die Berechnung zum Beispiel mit Excel durchgeführt wird, kann der Korrekturfaktor abhängig von der jeweiligen Horizontalkraft V berechnet werden. Dies wurde im hier dargestellten Berechnungsbeispiel getan. In der folgenden Berechnung ist der Faktor exemplarisch für den Maximalwert $V_{max} = M_{max}/L_s$ ermittelt. Die Berechnung des Verhältnisses der Schub und Biegeverformungen wurde mit Excel durchgeführt und ist in Abb. 6 abhängig von der Axialdehnung dargestellt.

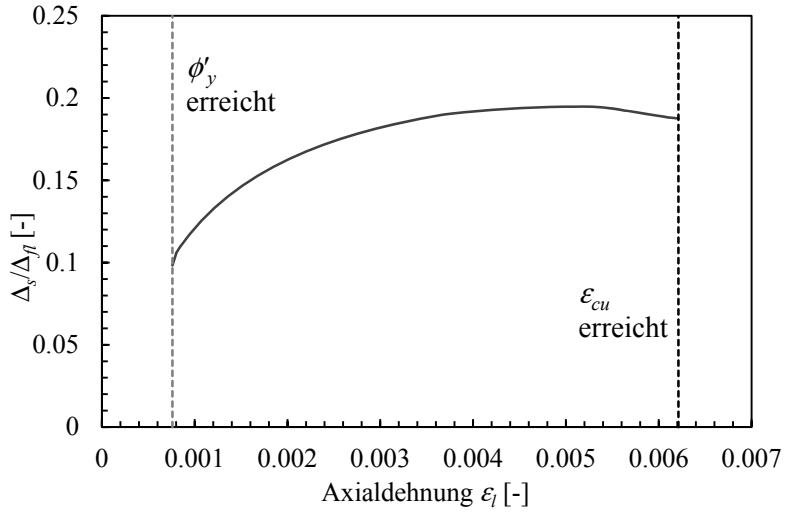

Abb. 6: *Verhältnis der Schub- zu Biegeverformungen.*

Berechnung

$x_c = 0.322\text{mm}$

$h - x_c - c = 1500 - 322 - 25 = 1153\text{mm}$

$z = 0.87\text{m}$ (aus Querschnittsanalyse)

$V_{n,v} = 0.0008 \cdot 0.35\text{m} \cdot 528\text{MPa} \cdot 1.153\text{m} \cdot \cot 30° = 295\text{kN}$

$V_{n,c} = (0.5 + 20 \cdot 0.0123) 0.05 \sqrt{35\text{MPa}} \cdot 0.8 \cdot 1.5\text{m} \cdot 0.35\text{m} = 93\text{kN}$

$V_{n,p} = 1300\text{kN} \frac{(1.5 - 0.322)\text{m}}{2 \cdot 4.5\text{m}} = 170\text{kN}$

$\rightarrow V_n = 295 + 93 + 170 = 558\text{kN}$

$$\tan\theta = \sqrt[4]{\frac{0.0008 + \frac{200}{25} \cdot 0.0123 \cdot 0.0008}{0.0123 + \frac{200}{25} \cdot 0.0123 \cdot 0.0008}} = 0.516$$

$\rightarrow V_{wc} = 0.35\text{m} \cdot 0.87\text{m} \cdot 0.6\ 35\text{MPa} / (1/0.516 + 0.516) = 2.6\text{MN}$

$\rightarrow \alpha = 2900\text{kNm} / 4.5\text{m}\ (1 / 558\text{kN} + 1 / 2600\text{kN}) = 1.4$

Gesamtverformung

Die Gesamtverformung setzt sich aus den Biege- und Schubverformungen zusammen. Bis zum Fliessbeginn der Längsbewehrung werden die Schubdeformationen jedoch als vernachlässigbar betrachtet und lediglich die Biegedeformationen berücksichtigt. Daher kann bei Fliessbeginn ($\phi = \phi'_y$) die Gesamtdeformation wie folgt abgeschätzt werden:

$$\Delta = \Delta'_{y,fl} = \phi'_y \frac{L_s^2}{3} \qquad F'_y = \frac{M_y}{L_s} \tag{8}$$

Im inelastischen Bereich, das heisst für Krümmungen $\phi > \phi'_y$, wird die Gesamtverformung wie folgt berechnet:

$$\Delta = \Delta_{fl} + \Delta_s = \Delta_{fl} \left(1 + \frac{\Delta_s}{\Delta_{fl}} \right) \qquad F = \frac{M}{L_s} \tag{9}$$

Gleichungen (9) und (10) werden mit den zuvor bestimmten Grössen (L_p, $\Delta s/\Delta fl$ etc.) ausgewertet. Die daraus resultierenden Kraft-Verformungsbeziehungen sind in Abb. 7 dargestellt. Der Knick in der Kraft-Verformungsbeziehung wird durch das Vernachlässigen der als klein eingeschätzten Schubverformungen vor Fliessbeginn verursacht.

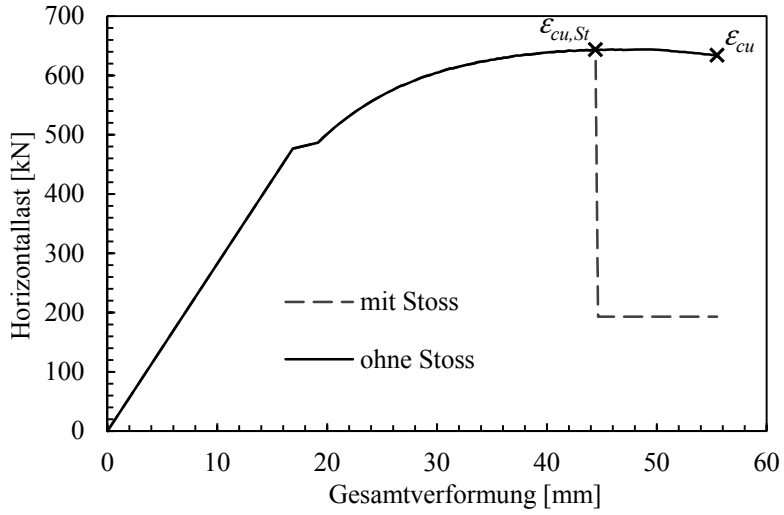

Abb. 7: *Last-Verformungsbeziehung je eines Versuchskörpers mit und ohne Stoss.*

Résumé

Les ponts existants peuvent, selon les normes utilisées pour les dimensionner, avoir été construits sans inclure de dimensionnement sismique. En Suisse, comme dans d'autres pays où la sismicité est faible, les normes parasismiques n'ont été introduites que récemment, puisque le danger a été longtemps sous-estimé. En conséquence, il se peut que les ponts existants aient une faible capacité de déformation, de par leur type structural ou leurs détails de conception. C'est pourquoi un projet en deux parties visant à évaluer les ponts existants a été initié. La première partie de ce projet [1], [2] a été menée à l'ETHZ et visait à estimer la déformabilité requise. Celle-là s'est concentrée sur la modélisation des ponts et l'identification des configurations critiques pour les piles de pont. Dans cette partie trois points critiques ont étaient identifiés et concernent (i) les zones de recouvrement dans la région potentiellement plastique au-dessus des fondations, (ii) les faibles taux d'armature transversales et (iii) l'absence d'un confinement par frettage. La vérification de ces ponts se fait notamment par des méthodes basées sur la déformation, en comparant les déformations entraînées par un séisme et la capacité de déformation [1], [2].

La deuxième partie de ce projet de recherche, exposée dans le présent rapport, concerne l'estimation de la capacité de déformation de piles rectangulaires ayant un élancement d'environ 1 à 3. Puisque l'évaluation de la déformabilité doit être appliquée par des ingénieurs à un grand nombre de ponts, les modèles d'estimation de la capacité de déformation doivent être relativement simples à mettre en œuvre tout en donnant des résultats acceptables et pas trop conservateurs. Le présent travail a pour but de contribuer au développement de tels modèles. Les études sur les piles avec les manques constructifs susmentionnés qui ont été menées à l'ETHZ dans le cadre des deux parties du projet de recherche [1], [3] ont fourni les données expérimentales de base pour la vérification et la validation des modèles. Deux approches ont été choisies pour une étude approfondie sur la base des critères mentionnés : la modélisation avec des rotules plastiques et l'utilisation d'un modèle cinématique pour les murs critiques soumis à un effort tranchant.

La première partie de ce rapport concerne la modélisation avec des rotules plastiques. D'abord un aperçu des équations est donné qui définissent l'état de rupture et servent à estimer la longueur des rotules plastiques, à trouver la déformation en flexion et en cisaillement ainsi qu'à calculer l'allongement limite. Un procédé permettant de déterminer la relation force-déplacement des piles est ensuite développé sur la base des données expérimentales. Cela permet de prendre en compte l'influence des zones de recouvrement et des déformations en cisaillement sur le comportement.

La deuxième partie de ce rapport traite de la dégradation du comportement au cisaillement ainsi qu'à l'élaboration d'un modèle cinématique pour des piles rectangulaires sensibles au cisaillement. Ce modèle se base sur la cinématique induite par la formation de fissures de cisaillement et a été développé par ailleurs [13]. Ce rapport valide son application aux piles rectangulaires. En outre, l'influence de quelques caractéristiques, comme le taux d'armature ou l'élancement, est mise en évidence, en particulier en ce qui concerne la capacité de déformation.

La comparaison des prédictions avec les résultats expérimentaux a montré que la modélisation par des rotules plastiques, malgré sa simplicité, donne de bons résultats pour les murs considérés dans cette étude dont le comportement n'est que partiellement déterminé par la flexion. Ce modèle donne une estimation plutôt conservatrice de la capacité de déformation, qui correspond globalement à la déformation sous la charge maximale. Pour considérer également la branche descendante de la réponse correspondant à une structure dégradée, il faudrait faire appel au modèle cinématique qui permet de tenir compte des ruptures dues à l'effort tranchant ainsi qu'aux efforts axiaux.

Structure du Rapport

Les paragraphes qui suivent résument les points principaux de ce rapport. La modélisation avec des rotules plastiques est présentée en premier. Pour cela, les principes de base et les grandeurs et formules nécessaires à cette modélisation sont brièvement exposés. Par la suite, une introduction aux bases des modèles cinématiques pour le calcul du comportement piles de pont sensibles au cisaillement est proposée. Ce résumé détaillé est présenté en allemand et en français. Le rapport de recherche proprement dit, en anglais, contient des explications détaillées et les bases des modèles présentés.

Modélisation avec des rotules plastiques

Introduction

Cette partie présente les points nécessaires à la modélisation par des rotules plastiques de piles rectangulaires à section allongée en forme de murs. Dans ceux-ci, la zone plastique au pied de la pile est représentée par une rotule plastique, au niveau de laquelle une courbure plastique constante est supposée. Ceci est une représentation simplifiée de la variation approximativement linéaire de la courbure plastique, souvent observée expérimentalement, figure 1. Selon cette représentation, ϕ_p est la courbure plastique, ϕ'_y la courbure lors de la première plastification de l'armature, ϕ_b la courbure au pied de la pile et ϕ_{sp} la courbure résultant de la propagation de l'allongement dans les fondations. En intégrant le profil de courbure, cette approche avec des rotules plastiques permet de déterminer les déformations en flexion. Les déformations en cisaillement peuvent également être considérées, puisqu'elles sont proportionnelles aux déformations de flexion dans le domaine inélastique.

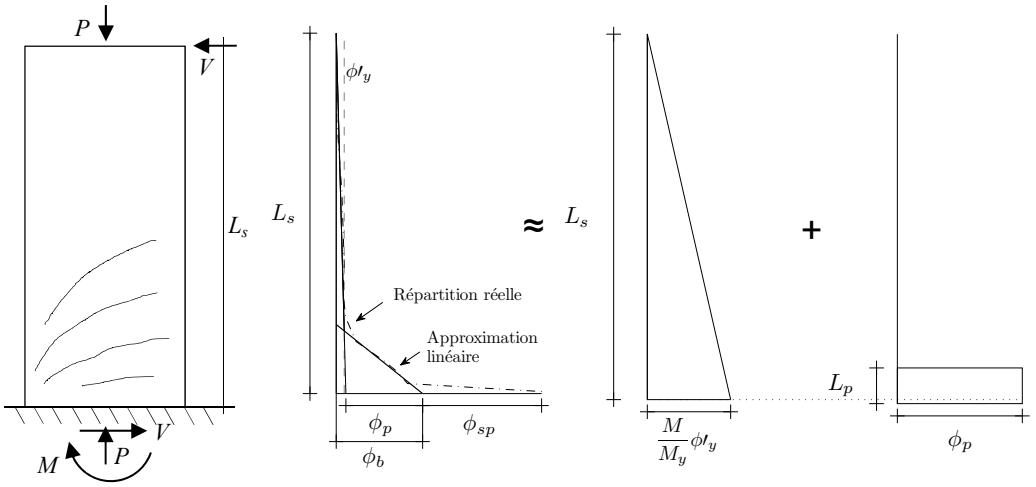

Figure 1: *Pile rectangulaire en forme de mur sous charge, profil de courbure effectif et approximation par le modèle de la rotule plastique.*

Dans ce qui suit, la détermination de la longueur de la rotule plastique basée sur les résultats expérimentaux est d'abord présentée. Ensuite des recommandations pour l'analyse de la relation moment-courbure et de la limite d'allongement sont données. Ces limites servent pour l'estimation des capacités de courbure. Cela mène à la détermination des déformations en flexion et en cisaillement, dont la somme donne la déformation totale. Finalement, des indications sont données pour la prise en compte d'un recouvrement de l'armature longitudinale au pied de la pile.

Choix de la longueur de la rotule plastique

La rotule plastique est une variable de modélisation qui décrit dans ce modèle la zone inélastique d'un élément de construction. Sur la base des essais effectués dans le cadre des deux parties de cette recherche [1], [3], diverses équations pour la détermination de

la longueur des rotules plastiques dans les murs ont été évaluées. La meilleure concordance avec les données expérimentales a été obtenue avec l'expression suivante [4] :

$$L_p = \left(0.2h + 0.05L_s\right)\left(1 - 1.5\frac{P}{A_g f_c}\right) \leq 0.8h \qquad (1)$$

Cette équation tient compte de la hauteur de la section h, de la portée du cisaillement L_s, et de l'effet de la charge axiale P qui diminue la longueur de la rotule. La charge axiale est considérée comme charge relative, c'est-à-dire qu'elle est divisée par le produit de la surface de la section A_g avec la résistance du béton en compression f_c. En revanche, la contribution de la deformabilité des barres longitudinales dans la fondation n'est pas incluse (« strain penetration »). La comparaison avec les données expérimentales dans la zone inélastique a montré que ce terme est en général faible et que la déformation totale des piles peut être estimée sans en tenir compte.

Relation entre moment et courbure et allongement limite

La relation moment-courbure a été obtenue au moyen d'une analyse par section avec l'hypothèse que toutes sections planes restent planes. La Fig. 2 résume les paramètres principaux de l'analyse par section. En plus du profil d'allongement admis pour l'analyse par section et de la relation moment-courbure pour un des corps d'essai considérés, la figure montre les lois constitutives des matériaux pour le béton et l'acier. Pour le béton, la relation contrainte-déformation pour du béton confiné selon [5] est utilisée. Pour l'acier, une relation bilinéaire entre contrainte et allongement est utilisée ; elle ne tient pas compte du raidissement dû à la tension (« tension stiffening »).

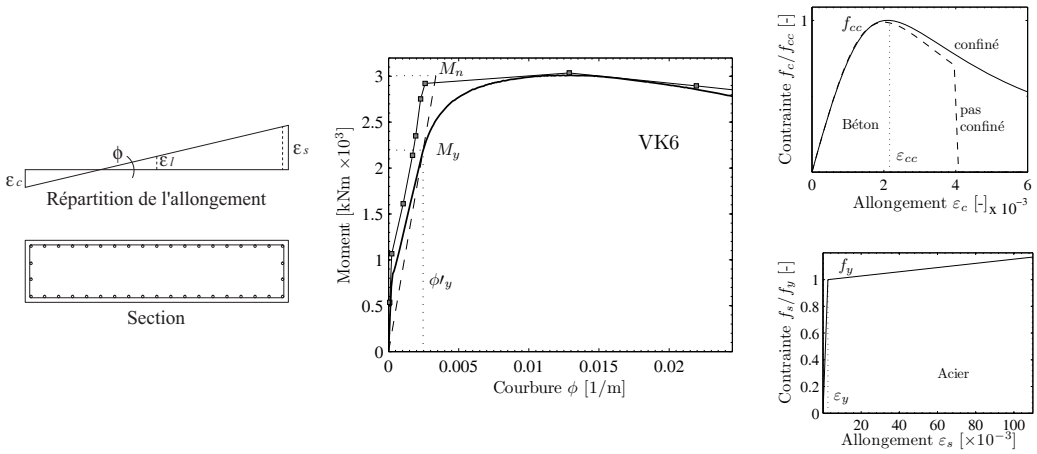

a) Section et profil d'allongement. *b) Relation moment-courbure.* *c) Lois constitutives.*

Figure 2: *Paramètres de l'analyse par section.*

La capacité de déformation d'un élément de construction est définie en général par le point où la limite d'allongement est atteinte au niveau de la rotule plastique. On suppose qu'en cas de dépassement de cet allongement les dommages dans la zone plastique sont suffisants pour entraîner une chute de la résistance donnée, cela définie un état de ruine. Une perte de 20% de la résistance à l'effort tranchant est souvent définie comme une rupture. Les allongements limites ci-dessous pour le béton $\varepsilon_{cu,cyc}$ et l'acier $\varepsilon_{su,cyc}$ [6] ont été développés pour cette chute de résistance :

$$\varepsilon_{cu,cyc} = 0.0035 + \left(\frac{1}{x_{c,con}}\right)^{3/2} + 0.4\frac{k_{con}\rho_v f_{yv}}{f_{cc}}$$
$$k_{con} = \left(1 - \frac{s}{2b_{con}}\right)\left(1 - \frac{s}{2h_{con}}\right)\left(1 - \frac{\sum s_{l,c}^2/6}{b_{con}h_{con}}\right) \quad (2)$$
$$\varepsilon_{su,cyc} = 0.375\varepsilon_{su}$$

Dans ces équations, $x_{c,con}$ désigne la profondeur de la zone frettée soumise à la compression, h_{con} et b_{con} les dimensions de la section confinée, ρ_v le taux d'armature transversal, f_{yv} la limite d'écoulement de l'armature transversale, f_{cc} la résistance à la compression du béton confiné, s l'espacement de l'armature transversale et $s_{l,c}$ l'espacement des barres d'armature longitudinale, dont le flambage est empêché par des crochets ou autres. La limite d'allongement de l'acier n'a pas dû être vérifiée expérimentalement puisque une rupture de l'armature longitudinale n'était pas déterminante dans les essais. Les extrémités des piles de ponts considérées n'étaient pas confinées. Les essais ont montré que des fondations qui restent élastiques entraînent un certain frettage du pied du mur qui devrait être considéré pour l'évaluation de la capacité de déformation du béton. Les dimensions de la section confinée sont ici admises comme égales à celles du noyau défini par la position de l'armature longitudinale de la pile. La déformation correspondant à la déformation atteinte juste après que le matériau ne cède sous une charge maximale est définie comme capacité de déformation pour les piles de section allongée considérés ici, en utilisant l'allongement limite susmentionné. La prise en compte de la capacité de déformation après le pic de la charge horizontale n'est pas possible avec le modèle de la rotule plastique. Cela est dû notamment au fait que l'hypothèse de sections planes admise dans le modèle des rotules plastiques est de moins en moins valable lorsque les dommages subis par l'élément de construction augmentent et aussi au fait qu'une partie des chutes de résistance sont à rapporter à une dégradation du mécanisme de cisaillement, ce qui n'est pas couvert par ce modèle. Si un calcul plus précis de la capacité de déformation après le pic de la charge horizontale est nécessaire, c'est le modèle cinématique décrit plus loin qui devrait être employé.

Prise en compte des zones de recouvrement

Un recouvrement de l'armature longitudinale au pied de la pile, là où se forme la rotule plastique, peut entraîner une chute rapide de la résistance à l'effort tranchant en cas de défaillance du recouvrement. Si le recouvrement n'est pas confiné et qu'il est assez long pour transmettre un effort de traction correspondant à la résistance à la traction de l'acier, sa rupture peut être introduite comme un endommagement du béton en compression. Si le béton n'est pas confiné, le transfert de l'effort entre les barres de recouvrement est assuré uniquement par le béton. Sa résistance à la traction et en conséquence sa capacité à transmettre l'effort sont réduites par l'apparition de fissures de compression dans le matériau. Sous charges cycliques, l'apparition de fissures de fendage est favorisée par l'alternance de charges de compression et de charges de traction, ce qui peut entraîner une perte de la résistance du recouvrement.

L'allongement limite pour une rupture du béton en compression peut être estimé par l'équation donnée dans [5] pour du béton confiné :

$$\varepsilon_{cc} = \varepsilon_c\left(1 + 5\left(\frac{f_{cc}}{f_c} - 1\right)\right)$$
$$f_{cc} = f_c\left(1.254 + 2.254\sqrt{1 + \frac{7.94 f_l'(k_{con},\rho_v)}{f_c}} - 2\frac{f_l'(k_{con},\rho_v)}{f_c}\right) \quad (3)$$

k_{con} est déterminé d'après l'Éq. (2) avec un espacement des étriers s correspondant à la distance entre la fondation et l'étrier le plus bas. Cela signifie que la fondation est

considérée comme un étrier. En outre, toutes les barres de l'armature longitudinale sont prises en compte dans le calcul du confinement (facteur k_{con} également), puisque celles-ci sont tenues transversalement par la fondation. L'écartement des barres renforcées contre les pliures $s_{l,c}$ correspond ainsi à l'écart de l'armature s_l. Une contrainte $f'_{lx/y}=k_{con}\rho_{vx/y}f_{yv}$ est admise dans la direction longitudinale (x), respectivement transversale (y) de l'étrier, qui confine le béton. Le taux d'armature transversale et le nombre de barres considéré dans l'armature longitudinale sont ici déterminés pour une zone carrée en bordure de la section considérée, ceci est dû au fait qu'aucune zone périphérique confinée n'était pas présente pour les piles étudiés. L'allongement limite le plus faible d'après les Éq. (2)-(3) est déterminant pour estimer la capacité de déformation lors de défaillances du recouvrement.

Une fois le cisaillement associé à cette limite atteint, une chute immédiate de la résistance à l'effort tranchant jusqu'au niveau d'une capacité résiduelle déterminée par le décalage de la charge longitudinale est admise. Cette capacité est déterminée par l'équation suivante :

$$V = \frac{P}{L_s}\frac{h_c - a}{2} \quad \text{mit} \quad a = \frac{P}{0.85 f_c b_c} \tag{4}$$

où h_c et b_c désignent les dimensions du volume délimitées par la position de l'armature longitudinale, c'est-à-dire les dimensions de la section de la pile sans le recouvrement de béton.

Déformations en flexion

Les déformations en flexion peuvent être déterminées avec la démarche dite affinée décrite par [7]. Cette démarche permet de déterminer l'ensemble de la courbe de charge-déformation contrairement à l'approximation bilinéaire communément utilisée. Suivant cette démarche, une interpolation linéaire entre l'origine et la déformation en flexion lors de la première plastification $\Delta'_{y,fl}$ (courbure correspondante ϕ'_y) est effectuée (voir aussi figure 2b). La courbure ϕ'_y est définie comme la courbure pour laquelle la barre d'armature la plus excentrée plastifie pour la première fois (allongement correspondant $\varepsilon_s=f_y/E_s$), ou lorsque la déformation spécifique du béton correspondant à la contrainte de compression maximale (typiquement $\varepsilon_c=0.002$) est atteinte pour la première fois dans le bord le plus excentré de la section. La déformation en flexion Δ_{fl} est ensuite calculée en fonction de la courbure déterminée par l'analyse par section.

$$\begin{aligned} \Delta'_{y,fl} &= \phi'_y \frac{L_s^2}{3} & F'_y &= \frac{M_y}{L_s} \\ \Delta_{fl} &= \Delta'_{y,fl}\frac{M}{M_y} + \left(\phi - \phi'_y \frac{M}{M_y}\right) L_p L_s & F &= \frac{M}{L_s} \end{aligned} \tag{5}$$

Les déformations en flexion peuvent être déterminées avec ces équations jusqu'au point défini par la courbure maximale f_u, qui dépend de l'allongement limite des Éq. (2)-(3). Cette déformation en flexion correspond à la capacité de déformation définie par le modèle des rotules plastiques, comme cela a déjà été mentionné. Les Éq. (1)-(5) permettent de déterminer les déformations en flexion représentées comme par exemple sur la figure 3 pour une pile à armature longitudinale traversante (VK6) ainsi que pour la même pile mais avec recouvrement de l'armature longitudinale (VK5). Les déformations en flexion mesurées expérimentalement ainsi que les points, où l'allongement limite tel que défini par les Éq. (2)-(3) a été dépassé, sont représentés en guise de comparaison. Les déformations en flexion sont reportées comme allongements moyens $\delta=\Delta_{fl}/L_s$, en pourcent.

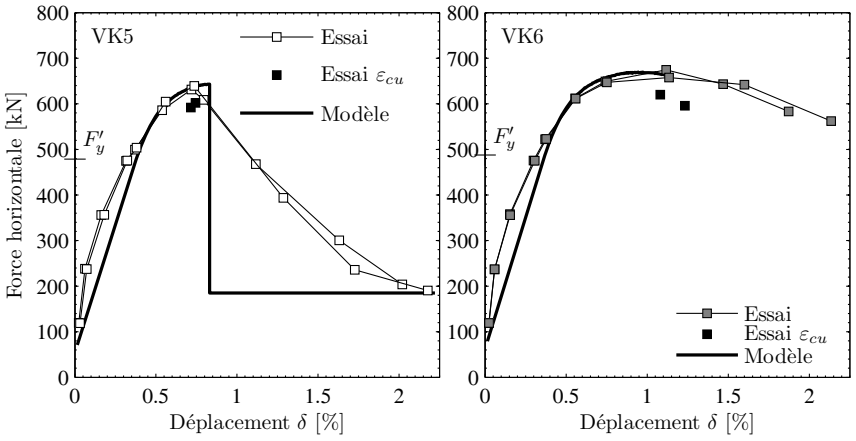

Figure 3: *Déformations en flexion calculées et mesurées pour deux structures testées avec (VK5) et sans (VK6) recouvrement [3].*

Déformations en cisaillement

La modélisation avec des rotules plastiques est d'abord conçue pour prévoir la déformation en flexion d'un élément de construction, comme cela est présenté dans la première section. Les déformations en cisaillement peuvent cependant aussi être considérées par cette modélisation dans la mesure où elles restent, en règle générale, fonction de la déformation en flexion dans le domaine inélastique. Les expériences menées dans le cadre de ce projet ont montré que les déformations en cisaillement restent relativement petites jusqu'à atteindre la charge de plastification F'_y et ne doivent pas nécessairement être prises en compte. Des déformations en cisaillement correspondant jusqu'à 30% de la déformation en flexion ont cependant été déterminées dans le domaine inélastique pour des piles sensibles au cisaillement. Négliger ces déformations entraînerait par conséquent une sous-estimation de la capacité de déformation.

Pour les structures expérimentales considérées ici, une bonne estimation des rapports entre déformation en cisaillement et en flexion a été obtenue avec une démarche modifiée inspirée de [8]. Ces équations donnent la relation entre les déformations en cisaillement et en flexion en utilisant la courbure ϕ et l'allongement longitudinal ε_l au centre de la section. Ces deux valeurs permettent de déterminer les déformations en cisaillement correspondant à des déformations en flexion dans le domaine plastique. Ci-dessous, les déformations en cisaillement dépendent de l'angle de fissuration attendu; plus les fissures sont inclinées, c'est-à-dire plus il se forme de fissures liées au cisaillement, plus les déformations de cisaillement sont importantes. L'angle de fissuration est ici estimé d'après les taux d'armature longitudinale et transversale ρ_l et ρ_v [9]. Le rapport de la déformation en cisaillement sur la déformation en flexion en dépendance de l'allongement longitudinal au centre de la section est donc donné par:

$$\frac{\Delta_s}{\Delta_{fl}} = 0.75\alpha \frac{\varepsilon_l}{\phi \sqrt[4]{\dfrac{\rho_v + (E_s/E_c)\rho_v\rho_l}{\rho_l + (E_s/E_c)\rho_v\rho_l}}} \frac{1}{L_s} \tag{6}$$

Le facteur de correction, basé sur la résistance à la traction en cisaillement V_n donné par [10] ainsi que sur la résistance à la compression de l'âme V_{wc} donné par EC2 6.2.3 (3) [11], est ajouté pour tenir compte de l'observation des éléments de construction de faible résistance au cisaillement subissant des déformations plus importantes :

$$1 \le \alpha = \frac{V}{V_n} + \frac{V}{V_{wc}} \le 2$$

$$V_n = \rho_v\, b\, f_{yv}\left(h - x_c - c\right)\cot 30^\circ + \left(3 - \frac{L_s}{h}\right)\left(0.5 + 20\rho_l\right)0.05\sqrt{f_c}\,0.8hb + P\frac{h - x_c}{2L_s} \qquad (7)$$

$$V_{wc} = 1.0\, b\, z\, 0.6\,\frac{f_c}{\cot\theta + \tan\theta}$$

Le bras de levier interne z et la hauteur de la zone de compression x_c peuvent être déterminés par l'analyse de section. Pour des taux d'armature longitudinale ρ_l > 2.5%, le terme $(0.5+20\rho_l)$ est approché à 1.0. Le terme $(3\text{-}L_s/h)$ ne considère qu'une transition entre des ratios de cisaillement de 1.5 à 2.0, c'est-à-dire $1 < (3\text{-}L_s/h) < 1.5$. La part de charge longitudinale n'est considérée que dans le cas d'une force de compression et est définie nulle sinon.

Cette démarche de calcul des rapports entre déformation en flexion et en cisaillement Δ_s/Δ_{fl} a permis de déterminer les résultats représentés sur la figure 4 pour les sept structures expérimentales considérées ici [1], [3] évaluées à la charge maximale.

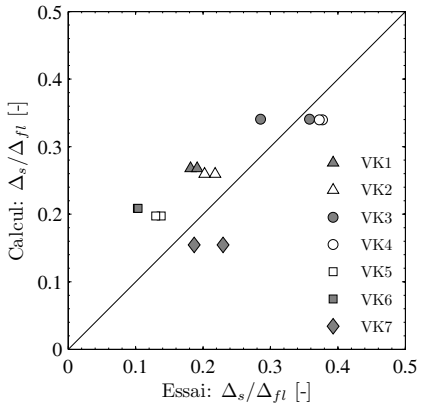

Figure 4: *Rapports calculés et expérimentaux entre déformations en flexion et déformations en cisaillement évaluées à la charge maximale (expériences [1], [3]).*

La capacité de déformation résultante

La déformation résultante se compose de la déformation en flexion et la déformation en cisaillement. Les déformations en cisaillement sont considérées comme négligeables jusqu'au début du flambage de l'armature longitudinale et les déformations en flexion sont alors les seules prises en compte. La déformation résultante peut donc être estimée comme suit à la limite élastique ($\phi = \phi'_y$) :

$$\Delta = \Delta'_{y,fl} = \phi'_y \frac{L_s^2}{3} \qquad F'_y = \frac{M_y}{L_s} \qquad (8)$$

Dans le domaine inélastique, c'est-à-dire pour des courbures ($\phi > \phi'_y$) la déformation résultante est calculée comme suit :

$$\Delta = \Delta_{fl} + \Delta_s = \Delta_{fl}\left(1 + \frac{\Delta_s}{\Delta_{fl}}\right) \qquad F = \frac{M}{L_s} \qquad (9)$$

Les déformations en flexion ainsi que les rapports entre déformation en flexion et en cisaillement dans cette équation sont déterminées avec les Éq. (1) et (5)-(7) pour des courbures inférieures à celle où l'allongement limite selon les Éq. (2)-(3) est atteint. Pour les deux structures expérimentales considérées ci-dessus, la figure 5 représente les courbes de charge-déformation obtenues.

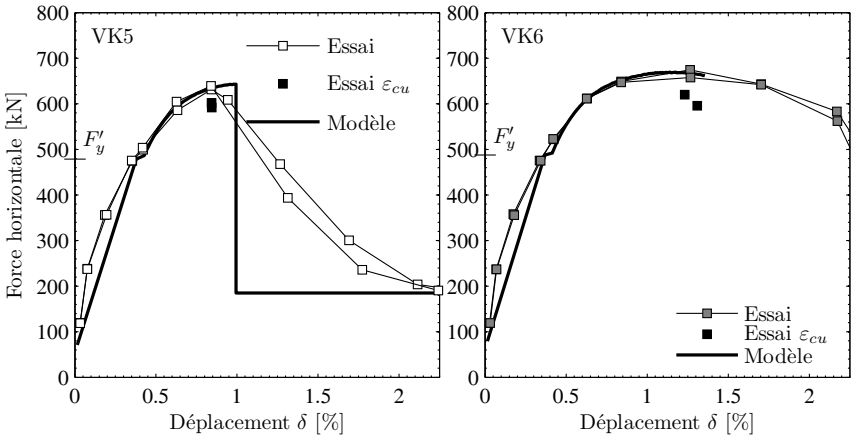

Figure 5: *Déformations résultantes calculées et expérimentales pour une structure expérimentale avec (VK5) et sans (VK6) recouvrement.*

Modèle cinématique

Introduction

Le modèle cinématique se base sur la cinématique induite par la formation de nombreuses fissures de cisaillement. Cela signifie qu'il ne peut être appliqué à des éléments de construction clairement définis par leur résistance en flexion ou définis par un recouvrement à la base. Le modèle a été développé en se basant sur un modèle semblable pour des poutres avec une grande hauteur de section [12]. Le modèle poutre n'utilise que deux paramètres pour décrire le champ de déformation. Pour des piles à section allongée, un troisième paramètre est introduit, d'où le nom « 3 Parameter Kinematic Theory (3PKT) ». Une introduction détaillée à cette théorie n'est pas possible dans le cadre de ce résumé. Le lecteur est prié de s'en référer à la publication [13], où la théorie a été présentée, ainsi qu'au chapitre 5 du rapport qui suit, qui contient une validation de la théorie.

Dans la suite de ce résumé, les fondements de la théorie sont brièvement expliqués et les prédictions obtenues pour les courbes de charge-déformation de quelques piles sont comparées aux données expérimentales. Avec cette théorie, les déformations peuvent être prédites jusqu'au point de dégradation du mécanisme de cisaillement, et donc jusqu'à la perte de la résistance aux forces transversales et longitudinales. Une meilleure estimation des capacités de déformation réelles d'un élément de construction avant d'atteindre la charge maximale est alors possible.

Fondements de la modélisation

La figure 6 donne la cinématique admise dans ce modèle ainsi que les mécanismes de charge considérés. Le schéma de gauche montre la déformation supposée de la pile. Il est supposé qu'une zone radialement fissurée se forme au-dessous de la fissure de cisaillement, la zone du dessus restant d'un bloc. Au pied de la pile, juste au-dessus de la fissure de cisaillement, il est également supposé la formation d'une zone où se concentrent les dommages du bloc supérieur. Le champ de déformation total est représenté par les trois paramètres $\varepsilon_{s,avg}$, Δ_c et Δ_{cv}. Le premier paramètre $\varepsilon_{s,avg}$ désigne l'allongement moyen de l'armature longitudinale, qui influence l'allongement du côté de la pile soumis à la traction ainsi que la rotation du bloc supérieur. Les deux paramètres restants Δ_c et Δ_{cv} désignent respectivement la translation et le déplacement vertical du bloc supérieur causés par la déformation de la zone endommagée au pied du bloc.

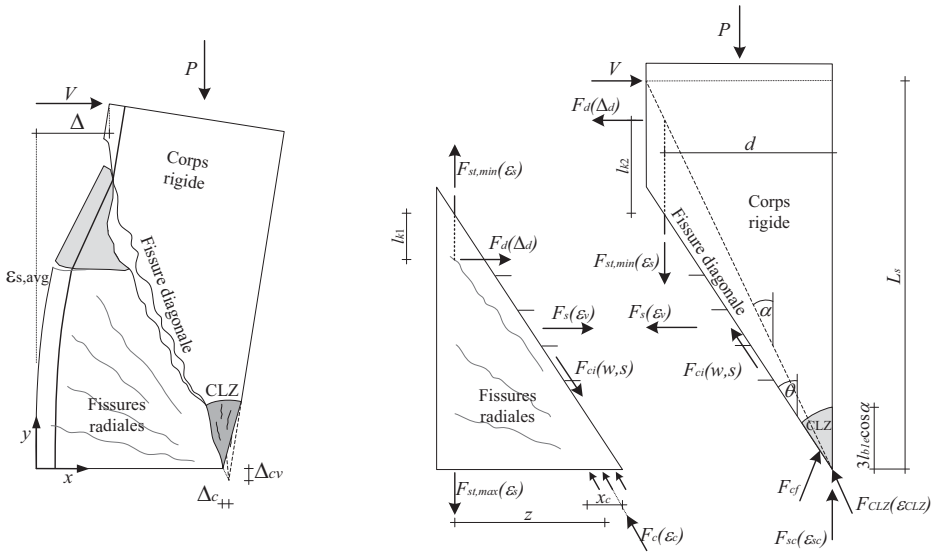

Figure 6: *Fondements de la théorie cinématique.*

La deuxième moitié de la figure 6 montre les mécanismes de charge considérés dans la théorie. Dans ce modèle, toutes les forces sont représentées comme des ressorts dont les lois caractéristiques découlent des propriétés des matériaux. Inversement, les allongements des ressorts découlent des déformations déterminées par les trois paramètres susmentionnés.

Les armatures longitudinale et transversale sont représentées chacune comme un ressort fixé au centre de gravité de l'armature correspondante et dont les forces F_{st} et respectivement F_s résultantes découlent des allongements ε_s et ε_v dépendants du champ de déformation. L'influence des goujons est considérée, en supposant que l'armature longitudinale est sous tension au niveau des bords de deux fissures de cisaillement voisines. La force F_d exercée par les goujons découle alors du profil des moments étant donnée la longueur l_k, qui dépend du déplacement relatif entre les deux bords voisins de la fissure Δ_d. Enfin, la force résultante F_{ci} de l'engrainement le long des fissures, dépend de la largeur w et de la dislocation s de celles-ci.

En ce qui concerne la zone fortement endommagée (CLZ=Critical Loading Zone) au pied du bloc supérieur, plusieurs forces s'y appliquent. Premièrement, il y a l'effort de compression du béton F_{CLZ} résultant de la déformation ε_{CLZ} de cette zone, dont la direction dépend de la translation ainsi que du raccourcissement de la zone (Δ_c et Δ_{cv}). Puis, selon l'élancement de la pile et la charge longitudinale appliquée, une force de contact peut apparaître entre la pointe du bloc supérieur et la zone inférieure. Une force de friction, et donc une résultante F_{cf} découlent d'un glissement vers le bas du bloc supérieur. Une force de compression F_{sc} résultant de la déformation ε_{sc} de l'armature longitudinale s'applique aussi à cet endroit de la pile.

Dans la zone radialement fissurée au-dessous de la fissure de cisaillement principale apparait un effort de compression du béton F_c au pied de la pile. Les composantes des forces déjà mentionnées s'y appliquent aussi et sont transmises au niveau de la fissure critique.

Le champ de déformation et les composantes des forces peuvent être calculés pour chaque distance de dislocation de l'extrémité en utilisant les conditions d'équilibre et de compatibilité. La résultante transversale V des forces peut être alors déduite. D'après cette théorie, des défaillances apparaissent lorsque la zone au pied de la pile est trop endommagée, entraînant une chute de la force résultante F_{CLZ}. Ceci va de pair avec une déformation importante de cette zone, qui conduit à un glissement du bloc supérieur le long de la fissure de cisaillement. Ce glissement entraîne une intense force F_{ci} due à l'imbrication des fissures qui compense finalement la force F_{CLZ}. Pour des glissements encore plus importants et pour des fissures plus larges, ce mécanisme de compensation

est perturbé. Cela conduit à une perte de résistance aux forces transversales et charges longitudinales de la pile.

Présentation des résultats

La figure 7 représente les résultats obtenus avec le modèle cinématique pour deux structures testées dans le cadre de ce projet de recherche. La comparaison avec les données expérimentales montre non seulement que la résistance aux forces transversales est bien couverte–mais aussi que la partie de la courbe de charge-déformation correspondant à une structure est fortement dégradée. La contribution des différentes composantes transversales des forces est également visible sur ces graphes. Ceci illustre le mécanisme de défaillance décrit plus haut : lorsque la composante transversale de la force V_{CLZ} diminue, une augmentation de la composante due à l'imbrication des fissures est observée dans un premier temps avant une chute de charge. Cela se traduit donc par une perte de résistance dans la pile.

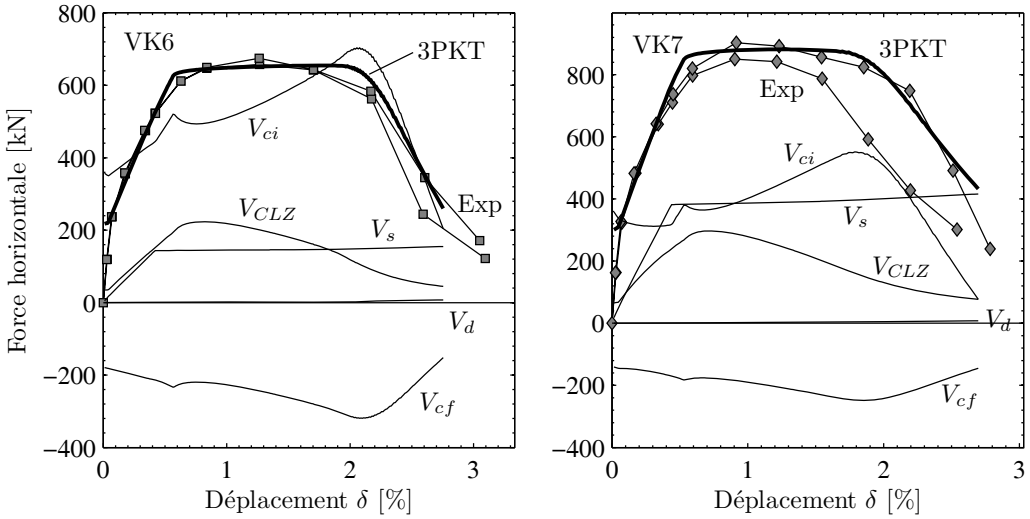

Figure 7: *Représentation des résultats obtenus avec la théorie cinématique pour deux structures testées.*

Influence des paramètres choisis sur la capacité de déformation

Cette partie utilise la 3PKT pour décrire l'influence de deux paramètres, qui ont également fait l'objet de recherches expérimentales, sur les capacités de déformation. D'un côté, l'influence de l'armature transversale est étudiée, de l'autre, l'influence de l'élancement. Les armatures transversales VK3 (taux d'armature 0.08%) et VK7 (taux d'armature 0.22%) sont étudiées. Conformément aux prévisions, la capacité de déformation augmente avec le taux d'armature transversale, tandis que la résistance aux charges reste inchangée, voir figure 8. Cela permet d'expliquer pourquoi aucune défaillance en cisaillement prématurée n'apparait pour de faibles taux d'armature transversale, alors que la capacité de déformation finale est plus vite atteinte.

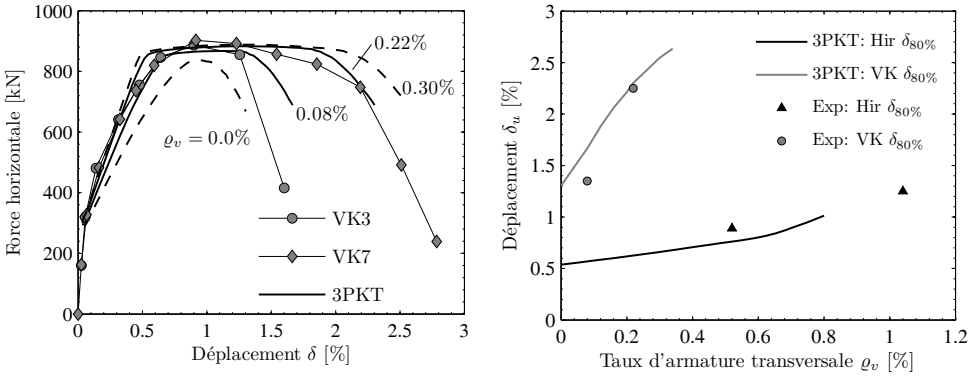

Figure 8: *Influence du taux d'armature transversale sur le comportement des structures testées.*

Une comparaison avec d'autres expériences [14] a toutefois montré que l'importance de cette influence dépend fortement de la configuration de la structure. Alors que pour des structures plus élancées VK3 et VK7 (L_s/h=2.2) une forte augmentation de la capacité de déformation correspondant à une résistance résiduelle de 80% a été observée et calculée, l'influence positive de l'armature transversale pour des structures plus courtes [14] (Hirosawa (1975) dénoté « Hir » en figure 8 ; L_s/h=1.0) est nettement moins importante.

Un changement de l'élancement modifie aussi bien la résistance aux forces transversales que les capacités de déformation. Pour des élancements plus élevés, la résistance aux forces transversales décroit alors que la capacité de déformation augmente, voir figure 9. Les calculs menés avec l'aide de la 3PKT pour les structures testées VK3 et VK6 avec des propriétés moyennes pour les matériaux et un élancement variable montrent de plus une nette augmentation des capacités de déformation avec des élancements de 1.5 et de 2.0. La comparaison, sur la figure 9, des courbes de charge-déformation des structures testées montre que, pour des élancements inférieurs à environ 1,5, un comportement plutôt cassant domine, alors que des élancements plus élevés sont plutôt associés à un comportement ductile et à la formation d'un plateau d'écoulement.

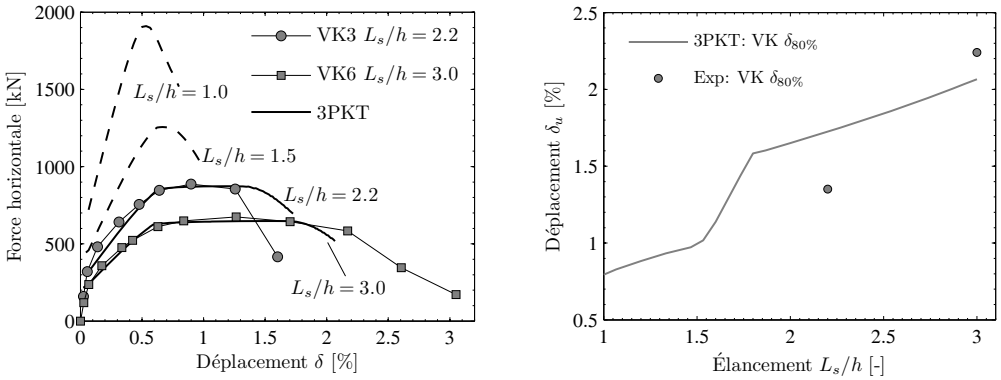

Figure 9: *Influence de l'élancement sur le comportement des structures testées.*

Pour une discussion détaillée de l'influence des différents paramètres et pour une comparaison avec des estimations de la capacité de déformation obtenues par d'autres, le lecteur est renvoyé à la section 5.5 du rapport qui suit.

Conclusions

Comme présenté dans les sections précédentes, le modèle des rotules plastiques permet de prédire des courbes de charge-déformation jusqu'à des charges proches de la charge maximale. La démarche pour obtenir les courbes de charge-déformation de piles rectangulaires de section allongée est résumée dans ces lignes. C'est ce modèle qui est

recommandé pour estimer la capacité de déformation, car il donne une estimation plutôt conservatrice de la capacité réelle et est de plus facile et rapide à appliquer. Le modèle cinématique peut quand même être appliqué si, dans le cadre d'une vérification des capacités de déformation des piles d'un pont, il est considéré comme pertinent de considérer plus attentivement le domaine suivant le pic de charge de la réponse. Par exemple lorsque la capacité de déformation calculée avec le modèle de la rotule plastique est légèrement inférieure à la déformabilité requise prévue. Dans ce cas il faut cependant faire attention au fait que, d'un côté, l'implémentation est ardue et, de l'autre, la partie descendante de la courbe de charge-déformation est associée à une dégradation du mécanisme qui assure aussi la résistance aux charges longitudinales. Il faut donc déterminer au cas par cas à quel point les capacités de déformation prédites avec ce modèle devraient être exploitées.

Exemple de calcul

Introduction

Cette partie présente un exemple de calcul pour l'utilisation de la modélisation par des rotules plastiques, pour des piles de pont avec (VK5) et sans (VK6) recouvrement de l'armature longitudinale. La méthode sera détaillée pas à pas, et les différences entre les piles de pont avec et sans recouvrement seront explicitées. Les piles de pont utilisés en exemple sont les mêmes que ceux qui avaient également été étudiés en détail dans le rapport.

Données des piles de pont

La section des piles, pour lesquelles l'exemple de calcul sera conduit, ainsi que toutes les grandeurs nécessaires, sont présentées dans la figure 1. Il s'agit ici de deux piles rectangulaires avec une armature uniformément répartie dans la section. VK6 a une armature longitudinale continue, alors que celle de VK5, est recouverte directement au-dessus de la fondation, sur une longueur de 60cm, cela équivaut à 43 fois le diamètre d'une barre. Mis à part le recouvrement de l'armature longitudinale, les deux piles ne se différencient que par une légère variation des valeurs du matériau. Pour l'exemple de calcul, celles du matériau de VK5 seront utilisées.

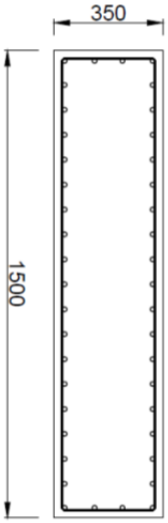

Dimensions de la pile
b / h / L_s = 0.35m / 1.50m / 4.50m

Armature
Longitudinale: ρ_l = 1.23%
42 barres d_{bl} = 14mm, espacement s_l = 80mm
Transversale: ρ_v = 0.08%
Étrier double d_{bv} = 6mm, espacement des étriers s = 200mm
Enrobage: c_{nom} = 25mm

Matériau
Béton: f_c = 35.2MPa
Armature longitudinale: f_y = 520MPa, f_u/f_y = 1.17
ε_{su} = 11%
Armature transversale: f_y = 528MPa, f_u/f_y = 1.29
ε_{su} = 7.1%

Figure 1: *Dimensions et propriétés du matériau des piles de pont.*

Relation Moment-Courbure

Une analyse moment-courbure de la section sera tout d'abord réalisée. Ceci peut par exemple être fait au moyen d'un programme comme Response2000 [94]. L'analyse utilisée dans cet exemple a été effectuée par un code Matlab [57].

La relation contrainte-déformation pour béton confiné selon Mander et al. [5] a été utilisée. Dans le cas considéré, bien que les étriers n'aient que des crochets à 90° et la section n'ait pas des zones confinées, la capacité de reprise du moment estimée avec cette loi de comportement du matériau est réaliste même après avoir atteint la résistance en compression du béton. Comme le montre la figure 2, l'effet causé par les étriers présents sur la résistance en compression est faible. La courbe présentée ici pour le béton non confiné n'a été utilisée que pour le béton d'enrobage. C'est pourquoi il a été admis que celui-ci s'écaille, dès qu'un allongement de 4‰ est atteinte. Pour cette raison la courbe présentant la compression est nulle après avoir atteint un allongement de 4‰. Une relation contrainte-déformation bilinéaire a été utilisée pour l'acier, et le raidissement en traction (« tension-stiffening ») n'a pas été pris en compte.

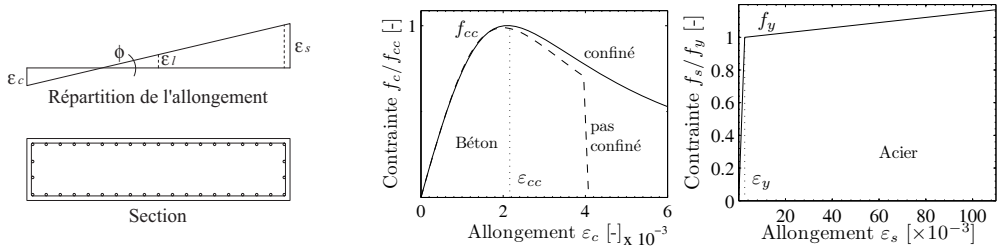

Figure 2: *Paramètres de l'analyse par section.*

Limites de déformation

Armature longitudinale continue

La relation moment-courbure est utilisée jusqu'à la courbure pour laquelle l'allongement limite, qui définit l'état de rupture, est atteinte. Pour le calcul des allongements maximales du béton $\varepsilon_{cu,cyc}$ et de l'acier $\varepsilon_{su,cyc}$, les grandeurs suivantes sont utilisées pour une pile avec armature longitudinale continue [6]:

$$\varepsilon_{cu,cyc} = 0.0035 + \left(\frac{1}{x_{c,con}}\right)^{3/2} + 0.4\frac{k_{con}\rho_v f_{yv}}{f_{cc}}$$
$$k_{con} = \left(1-\frac{s}{2b_{con}}\right)\left(1-\frac{s}{2h_{con}}\right)\left(1-\frac{\sum s_{l,c}^2/6}{b_{con}h_{con}}\right) \quad (10)$$
$$\varepsilon_{su,cyc} = 0.375\varepsilon_{su}$$

Dans les équations, $x_{c,con}$ désigne la hauteur de la zone de béton comprimé confiné, h_{con} et b_{con} sont les dimensions de la section confinée, ρ_v le taux d'armature longitudinal, f_{yv} la limite d'écoulement de l'acier d'armature, f_{cc} la résistance en compression du béton confiné, s l'espacement de l'armature et $s_{l,c}$ l'espacement des barres de recouvrement longitudinales, dont le flambage est par exemple empêché par des crochets. Les dimensions de la section confinée et la profondeur de la zone comprimée seront calculées par la suite jusqu'au milieu des étriers. L'espacement entre deux barres est de même établi du centre d'une barre à l'autre.

La hauteur de la zone comprimée considérée est la hauteur minimale établie par l'analyse par section, moins l'enrobage de béton, calculé jusqu'au milieu des étriers. Les quatre barres d'armatures longitudinales situées aux coins de la section sont considérées comme tenues par des étriers, et sont donc prises en compte pour la détermination (s_{l1}) de k_{con}. Lors de la construction des piles, deux rangées de crochets ont par ailleurs été utilisées pour la stabilisation de la cage de recouvrement, au moyen desquels le recouvrement longitudinal est fixé. Ceci a aussi été pris en compte comme armature au flambage dans les calculs (s_{l2}). Dans l'équation (2), la résistance du béton confiné devrait en principe être utilisée. Cependant, comme l'influence du confinement sur la résistance du béton est très faible pour les piles considérées ici, la résistance f_c du béton est utilisée.

Les déformations maximales suivantes sont donc calculées pour la section considérée :

Calcul

h_{con} = 1500mm – 2·25mm – 6mm = 1444mm

b_{con} = 350mm – 2·25mm – 6mm = 294mm

s = 200mm

s_{l1} = 350mm – 2·25mm – 2·6mm – 14mm = 284mm

s_{l2} = (1500mm – 2·25mm – 2·6mm – 14mm)/3 = 478mm

$\rightarrow k_{con}$ =0.24

x_{ccon} = 320mm – 28mm = 222mm

$$\rightarrow \varepsilon_{cu} = 0.0035 + \left(\frac{1}{320}\right)^{\frac{3}{2}} + 0.4\frac{0.24 \cdot 0.0008 \cdot 528}{35.2} = 0.0049$$

$$\rightarrow \varepsilon_{su} = 0.375 \cdot 0.11 = 0.041$$

Recouvrement de l'armature longitudinale au pied de la pile

Pour des piles avec recouvrement d'armature longitudinale, la plus petite des allongements calculés avec les équations (2) et (3) est utilisée comme allongement limite.

$$\varepsilon_{cc} = \varepsilon_c\left(1 + 5\left(\frac{f_{cc}}{f_c} - 1\right)\right)$$
$$f_{cc} = f_c\left(1.254 + 2.254\sqrt{1 + \frac{7.94 f_l'(k_{con}, \rho_v)}{f_c}} - 2\frac{f_l'(k_{con}, \rho_v)}{f_c}\right) \quad (3)$$

$$f_l' = k_{con}\rho_v f_{yv}$$

Dans cette équation, k_{con} est estimée d'après l'équation (2) avec un espacement des étriers s, correspondant à la distance entre la fondation et l'étrier le plus bas. Toutes les barres d'armatures longitudinales sont par ailleurs considérées pour le calcul de l'efficacité du confinement (également facteur k_{con}), car celles-ci sont tenues transversalement par la fondation. L'espacement $s_{l,c}$ entre deux barres d'armatures longitudinales dont le flambage est empêché correspond ainsi à l'espacement s_l de l'armature longitudinale. Dans le sens longitudinal (x), respectivement transversal (y) aux étriers, la contrainte $f'_{lx/y}=k_{con}\rho_{vx/y}f_{yv}$ est appliquée. L'allongement maximal d'après l'équation (3) est établi pour un carré au bord de la section de la pile, c'est à dire avec $h = b$ (cf. figure 3). L'espacement entre les armatures longitudinales sur le long côté de la pile est s_l = 80mm; sur l'autre, l'espacement sera un tiers de celui des deux armatures longitudinales tenues dans les coins de l'étrier.

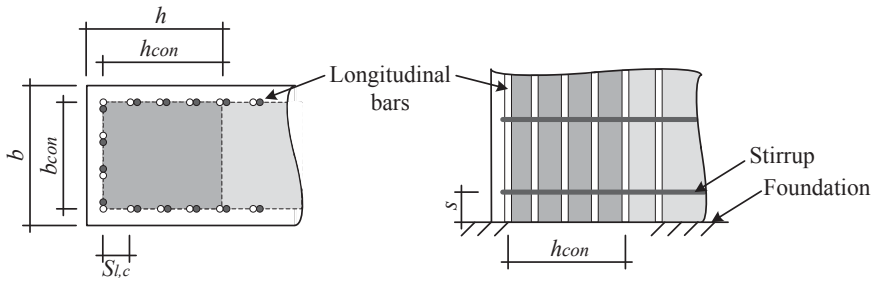

Figure 3: *Marge considérée pour la détermination de la limite d'allongement de piles avec recouvrement d'armature longitudinale.*

Calcul

h_{con} = 350mm – 28mm = 322mm

b_{con} = 350mm – 2·28mm = 294mm

s = 75mm

s_{l1} = (350mm – 2·25mm – 2·6mm -14mm)/3 = 98

s_{l2} = 80mm

$\rightarrow k_{con} = 0.70$

$f'_{ll} = 0.7 \cdot (2 \cdot 28.3\text{mm}^2 / (294\text{mm} \cdot 75\text{mm})) \cdot 528\text{MPa} = 0.95\text{MPa}$ (2 d_{bv} = 6mm)

$f'_{lq} = 0.7 \cdot (28.3\text{mm}^2 / (322\text{mm} \cdot 75\text{mm})) \cdot 528\text{MPa} = 0.44\text{MPa}$ (1 d_{bv} = 6mm)

$f'_l = (0.44 + 0.95)\text{MPa} / 2 = 0.69\text{MPa}$

$$f_{cc} = 35.2\left(-1.254 + 2.254\sqrt{1 + \frac{7.94 \cdot 0.69}{35.2}} - 2 \cdot \frac{0.69}{35.2}\right) = 39.8 \text{ MPa}$$

$\rightarrow \varepsilon_{cc} = \varepsilon_{cu,St} = 0.002\,(1 + 5(39.8 / 35.2 - 1)) = 0.0033$

La figure 4 montre, sur la base du modèle, du matériau et des hypothèses de calcul mentionnées, la relation moment-courbure de la section, ainsi que les courbures auxquelles les limites d'allongement calculées sont atteintes.

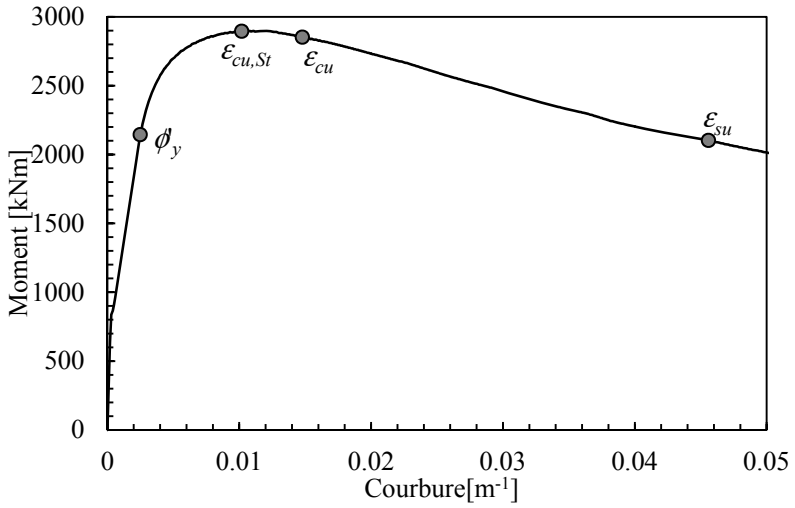

Figure 4: *Relation moment-courbure de la section considérée. Les courbures auxquelles les allongements limites pour les piles avec recouvrement $\varepsilon_{cu,St}$, le béton ε_{cu} et l'armature ε_{su} sont atteintes, sont indiquées.*

Longueur des rotules plastiques

La longueur de la rotule plastique est calculée avec l'équation proposée par [4]:

$$L_p = \left(0.2h + 0.05L_s\right)\left(1 - 1.5\frac{P}{A_g f_c}\right) \leq 0.8h \qquad (1)$$

Aux piles considérées ici, une charge verticale P de 1300kN a été appliquée pendant l'essai. Avec le poids de la pile et de la construction, la charge verticale s'élève environ à P = 1365kN au total.

Calcul

$$L_p = (0.2 \cdot 1.5 + 0.05 \cdot 4.5)\text{m}\left(1 - 1.5\left(\frac{1.365}{1.5 \cdot 0.35 \cdot 35.2}\right)\right) = 0.47\text{m}$$
$$\leq 0.8 \cdot 1.5\text{m} = 1.2\text{m}$$

Calcul de la déformée en flexion

La déformation en flexion est calculée à l'aide de la relation moment-courbure et de la longueur de la rotule plastique comme suit :

$$\Delta'_{y,fl} = \phi'_y \frac{L_s^2}{3} \qquad F'_y = \frac{M_y}{L_s}$$
$$\Delta_{fl} = \Delta'_{y,fl} \frac{M}{M_y} + \left(\phi - \phi'_y \frac{M}{M_y}\right) L_p L_s \qquad F = \frac{M}{L_s} \tag{5}$$

Dans les équations, ϕ_y' correspond à la courbure à laquelle la plastification apparaît pour la première fois. Ce moment est défini lorsque la contrainte dans la zone de traction atteint la limite d'élasticité, ou lorsque la déformation du béton atteint $\varepsilon_c = 0.002$ dans la zone comprimée de la section. Dans le cas considéré, la limite élastique de l'armature est atteinte en premier. La courbure ϕ_y' est également représentée à la figure 4. La déformation en flexion est déterminée par l'équation (5) jusqu'au point où l'allongement limite qui a été calculé avant soit atteinte (cf. figure 5).

Pour une pile avec recouvrement, il est supposé que lorsque la limite élastique est atteinte, la résistance décroit jusqu'à celle définie par l'excentricité maximale de la force normale. Ceci est calculé comme suit :

$$V = \frac{P}{L_s}\frac{h_c - a}{2} \quad \text{mit} \quad a = \frac{P}{0.85 f_c b_c} \tag{4}$$

Calcul

a = 1.365MN / (0.85·35.2MPa·0.284m) = 0.16m

V = (1365kN / 4.5m)·((1.5m – 2·0.033m) – 0.16m) / 2 = 193kN

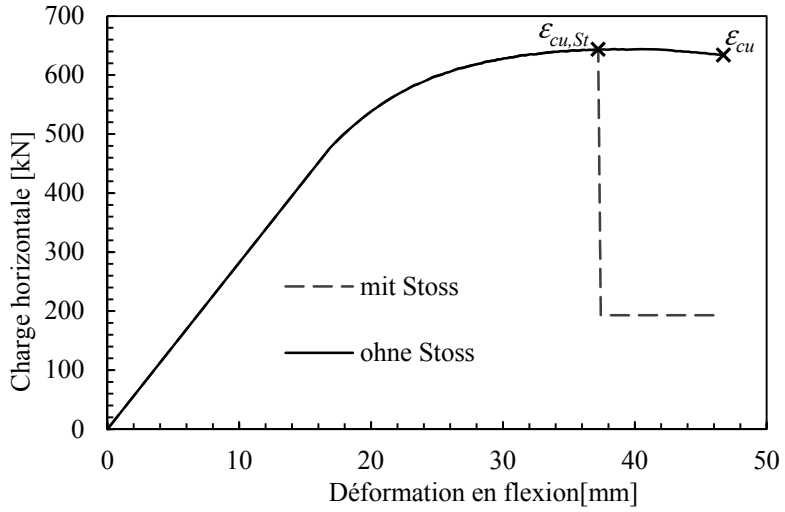

Figure 5: *Déformation en flexion d'une pile avec (mit Stoss) et sans (ohne Stoss) recouvrement au pied*

Déformations en cisaillement

Les déformations dues au cisaillement sont prises en compte dans la modélisation par leur rapport à la déformation en flexion. Celui-ci est estimé par une méthode modifiée selon [8], dépendant de l'allongement axial au centre de gravité de la section ε_l et des taux d'armature longitudinaux et transversaux, ρ_l et ρ_v:

$$\frac{\Delta_s}{\Delta_{fl}} = 0.75\alpha \frac{\varepsilon_l}{\phi \sqrt[4]{\dfrac{\rho_v + (E_s/E_c)\rho_v\rho_l}{\rho_l + (E_s/E_c)\rho_v\rho_l}}} \frac{1}{L_s} \tag{6}$$

La racine quatrième au dénominateur de cette équation correspond à la tangente de l'angle de fissure θ utilisé dans le calcul. Pour tenir compte des observations, selon lesquelles les piles présentant les plus faibles résistances au cisaillement subissent de plus grandes déformations, comme proposé dans [28], le facteur de correction α sera considéré sur la base de la résistance au cisaillement-traction V_n d'après [10] ainsi que de la résistance du champ de compression dans l'âme V_{wc} d'après [11] :

$$1 \le \alpha = \frac{V}{V_n} + \frac{V}{V_{wc}} \le 2$$

$$V_n = \rho_v\, b\, f_{yv} \left(h - x_c - c\right) \cot 30^\circ + \left(3 - \frac{L_s}{h}\right)\left(0.5 + 20\rho_l\right) 0.05\sqrt{f_c}\, 0.8hb + P\frac{h - x_c}{2L_s} \tag{7}$$

$$V_{wc} = 1.0\, b\, z\, 0.6 \frac{f_c}{\cot\theta + \tan\theta}$$

Dans le cas d'un taux d'armature longitudinal $\rho_l > 2.5\%$, le terme $(0.5 + 20\rho_l)$ est fixé à 1.0. Le terme $(3 - L_s/h)$ prend uniquement en compte la transition entre les rapports de cisaillement de 1.5 à 2.0, soit $1 \le (3 - L_s/h) \le 1.5$. Dans l'exemple de calcul, $L_s/h=3$, et la valeur à introduire est donc 1.0. La part de la charge axiale P n'est considérée que dans le cas d'une force de compression, et est nulle sinon. Pour le bras de levier z et la hauteur de la zone comprimée x_c, les valeurs issues de l'analyse de section correspondant au moment maximal sont utilisées ici. Pour la détermination du facteur de correction α, pour autant que rien ne soit précisé dans l'équation (8), le même angle de fissure que dans l'équation (7) est introduit. Dans le cas où le calcul est réalisé à l'aide d'Excel par exemple, le facteur de correction peut être déterminé en fonction de la force horizontale V, comme cela a été fait dans l'exemple de calcul présenté ici. Dans le calcul

suivant, le facteur est par exemple établi pour la valeur maximale $V_{max} = M_{max}/L_s$. Le calcul du rapport des déformations en cisaillement et en flexion a été conduit avec Excel, et est représenté dans la figure 6 en fonction de la déformation axiale.

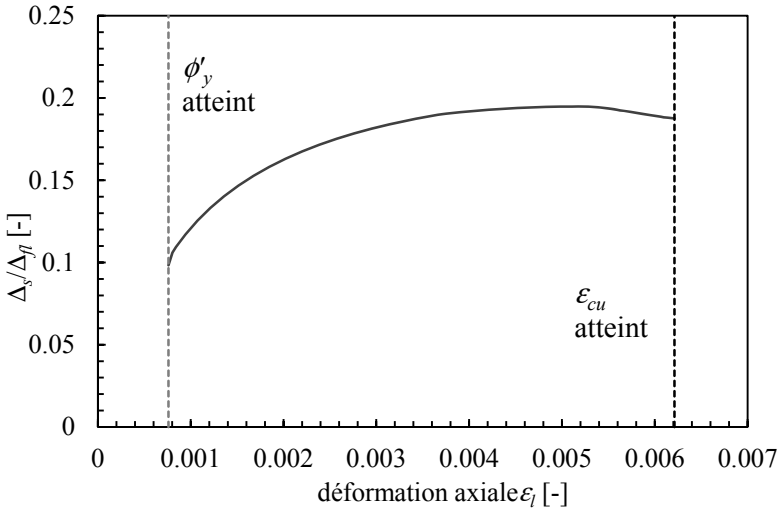

Figure 6: *Rapport des déformations en cisaillement et flexion*

Calcul

$x_c = 0.322\text{mm}$

$h - x_c - c = 1500 - 322 - 25 = 1153\text{mm}$

$z = 0.87\text{m}$ (d'après l'analyse par section)

$$V_{n,v} = 0.0008 \cdot 0.35\text{m} \cdot 528\text{MPa} \cdot 1.153\text{m} \cdot \cot 30° = 295\text{kN}$$

$$V_{n,c} = (0.5 + 20 \cdot 0.0123)0.05\sqrt{35\text{MPa}} \cdot 0.8 \cdot 1.5\text{m} \cdot 0.35\text{m} = 93\text{kN}$$

$$V_{n,p} = 1300\text{kN}\frac{(1.5 - 0.322)\text{m}}{2 \cdot 4.5\text{m}} = 170\text{kN}$$

$$\rightarrow V_n = 295 + 93 + 170 = 558\text{kN}$$

$$\tan\theta = \sqrt[4]{\frac{0.0008 + \frac{200}{25} \cdot 0.0123 \cdot 0.0008}{0.0123 + \frac{200}{25} \cdot 0.0123 \cdot 0.0008}} = 0.516$$

$$\rightarrow V_{wc} = 0.35\text{m} \cdot 0.87\text{m} \cdot 0.6\ 35\text{MPa} / (1/0.516 + 0.516) = 2.6\text{MN}$$

$$\rightarrow \alpha = 2900\text{kNm} / 4.5\text{m}\ (1 / 558\text{kN} + 1 / 2600\text{kN}) = 1.4$$

Déformée totale

La déformation totale est la somme des déformations en flexion et en cisaillement. Les déformations en cisaillement sont considérées comme négligeables jusqu'au début de l'écoulement de l'armature longitudinale, et seule la flexion est alors considérée. Ainsi, la déformée totale au début de l'écoulement ($\phi = \phi'_y$) est estimée comme suit :

$$\Delta = \Delta'_{y,fl} = \phi'_y \frac{L_s^2}{3} \qquad F'_y = \frac{M_y}{L_s} \tag{8}$$

Dans le domaine inélastique, soit pour $\phi > \phi'_y$, la déformée est calculée comme suit :

$$\Delta = \Delta_{fl} + \Delta_s = \Delta_{fl}\left(1 + \frac{\Delta_s}{\Delta_{fl}}\right) \qquad F = \frac{M}{L_s} \tag{9}$$

Les équations (9) et (10) sont évaluées avec les grandeurs déterminées précédemment (L_p, $\Delta s/\Delta fl$ etc.). Les relations force-déformation résultantes sont présentées à la figure 7. Le pli dans la relation force-déformation est dû au fait que la déformation en cisaillement, estimée faible, soit négligée dans la domaine élastique.

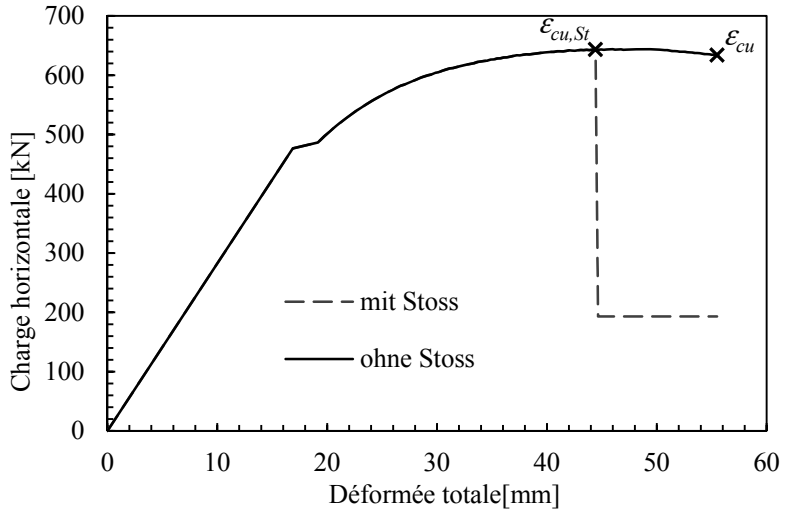

Figure 7: *Relation force-déformation pour une pile avec (mit Stoss) et sans recouvrement de l'armature longitudinale (ohne Stoss)*.

Literaturverzeichnis

[1] M. Bimschas, «Displacement-Based Seismic Assessment of Existing Bridges in regions of Moderate Seismicity,» Swiss Federal Institute of Technology ETH, Zurich, 2010.

[2] A. Dazio und M. Bimschas, «Erdbebensicherheit bestehender Brücken,» *SIA Dokumentation D0234 - Neues aus der Brückenforschung,* pp. 15-36, November 2010.

[3] P. Hannewald, M. Bimschas und A. Dazio, „Quasi-static cyclic tests on RC bridge piers with detailing deficiencies," Swiss Federal Institute of Technology ETH, Zurich, 2013.

[4] A. Bohl und P. Adebar, «Plastic hinge lengths in high-rise concrete shear walls,» *ACI Structural Journal,* Bd. 108, Nr. 2, 2011.

[5] J. B. Mander, M. N. Priestley und R. Park, «Theoretical stress-strain model for confined concrete,» *ASCE Journal of Structural Engineering,* Bd. 114, Nr. 8, pp. 1804-1826, 1988.

[6] D. Biskinis und M. N. Fardis, «Flexure-controlled ultimate deformations of members with continuous or lap-spliced bars,» *Structural Concrete,* Bd. 11, Nr. 2, 2010.

[7] M. Priestley, G. Calvi and M. Kowalsky, Displacement based seismic design of structures, Pavia: IUSS Press, 2007.

[8] K. Beyer, A. Dazio und M. N. Priestley, «Shear deformations of slender RC walls under seismic loading,» *ACI Structural Journal,* Bd. 108, Nr. 2, 2011.

[9] L. G. Hagsten, L. Hestbech und J. Fisker, *Energiprincipper - del 3: Betonkonstruktioner. Teori - Lecture Notes,* Aarhus University, 2011.

[10] M. Kowalsky und M. N. Priestley, «Improved analytical model for shear strength of circular reinforced concrete columns in seismic regions,» *ACI Structural Journal,* Bd. 97, Nr. 3, pp. 388-396, 2000.

[11] E. C. f. Standardization, «Eurocode 2: Design of concrete structures: Part 1-1: General rules and rules for buidlings,» Brussels, 2004.

[12] B. I. Mihaylov, E. C. Bentz und M. P. Collins, «Two parameter kinematic theory for shear behavior of deep beams,» *ACI Structural Journal,* Bd. 110, Nr. 3, pp. 447-456, 2013.

[13] B. I. Mihaylov, P. Hannewald, and K. Beyer, "Three-parameter kinematic theory for shear critical reinforced concrete walls. Part I: Formulation" submitted to ASCE Journal of Structural Engineering

[14] M. Hirosawa, «Past experimental results on reinforced concrete shear walls and analysis on them,» Kenchiku Kenkyu Shiryo, Building Research Institute, Ministry of Construction,, 1975.

1 Introduction

1.1 Background of the project

Switzerland is a region with moderate seismicity where the maximum horizontal peak ground acceleration on rock ground is $a_{gh} = 1.6\text{m/s}^2 = 0.16g$ for a return period of 475 years [15]. With a viscous damping of 5%, this results in elastic peak spectral accelerations of $S_e = 2.5a_{gh} = 0.4g$ for rock and $S_e = 3.5a_{gh} = 0.56g$ for the most unfavorable, alluvial soils. These values are modified in the design depending on the importance of the building and the ductility of the structure. Because of the relatively moderate hazard, the seismic action has long been underestimated and earthquake provisions have found their way into the codes only in recent years. Back in 1970 [16], the maximum peak ground acceleration that was only considered when assigned by local authorities for a certain area, was merely $a_{gh} = 0.05g$. This had to be increased by 40% for buildings in which a large number of people was expected, similar to SIA 261 [15]. In 1989 some measures for construction details, such as ensuring a vertical support in the case of bridge bearing failure, were added to the codes. Furthermore, the peak ground accelerations were raised to the values that still apply today, even though the resulting elastic design spectral accelerations went up to only $0.35g$.

Hence, structures that were constructed before 1989 were designed for a significantly lower seismic input than that assumed today and do not meet seismic requirements with regard to the detailing. According to a technical documentation issued by the Federal roads office (FEDRO) [17], only 10% of existing Swiss bridges were constructed after 1989, while half of the bridges were constructed between 1970 and 1989 and the rest before. This means that only 10% of the then existing 3350 road bridges were constructed according to modern design codes. The remaining 90% of the bridges, and hence about 3000 existing bridges, were not designed to withstand seismic loading and need to be assessed. For this assessment, a two step procedure targeted towards the most widespread type of girder-bridges was suggested by [17]: In a first step, bridges are checked for typical deficiencies which render the structure prone to damage under seismic loading. Bridges that are identified as potentially vulnerable undergo an in-depth assessment in the second step. Besides deciding on whether measures such as providing lateral supports for the superstructure to prevent its unseating are necessary, the performance of a structure itself must be assessed. If this assessment is necessary, it may be done according to either a force-based or a displacement-based approach [17]. In recent years, there is a strong tendency towards displacement-based approaches, as these often prove to be the more economical, especially for the assessment of existing structures. While the force-based approach may almost inevitably lead to the conclusion that costly retrofitting measures are necessary to increase the resistance of a structure, the displacement-based approach may lead to the conclusion that the deformation capacity of a structure is actually sufficient. This might be the case particularly in countries like Switzerland, where the displacement demands are only moderate.

The research project which provides the framework for the study presented here stems out of the need to establish a displacement-based approach for the assessment of existing Swiss bridges. In the first part of this project a survey of the Swiss bridge stock was conducted to identify critical bridge layouts [1]. To this end, the database of the FEDRO, containing all Swiss bridge structures, was evaluated and combined with the results of

the first step assessment by [17], which were then available for three cantons. Out of the bridges for which the latter results were available, almost 40% were multi-span girder-bridges followed by a large percentage of frame bridges which were deemed uncritical [17]. Hence, it was decided to focus the research on multi-span girder-bridges [1]. Within this bridge type, it was found that primarily relatively short and squat piers may prove critical, because they have a low displacement capacity and are prone to shear failure [1, 18, 19].

Based on a sample set of three different existing bridges that feature this type of piers, a test series was initiated to gain experimental evidence on the cyclic behavior of these piers [1]. The test units resembled the existing wall-type bridge piers with rectangular cross section that were considered to be the most critical type of bridge piers and featured the following, commonly found detailing deficiencies: i) The equally distributed longitudinal reinforcement was not confined near the boundaries, which means that neither was the concrete confined nor the reinforcing bars themselves restrained against buckling; ii) the transverse reinforcement ratio was very low and the stirrups did not have hooks that were anchored in the concrete core; iii) the longitudinal reinforcement of one of the test units had a lap splice at the base of the pier in the potential plastic hinge zone. Within the second part of this project, the test campaign was continued to enlarge the available database [3]. The results from this test series serve as experimental data for the evaluation and validation of models for the displacement capacity of these piers, which are required for a reliable displacement-based assessment.

1.2 Problem statement

As outlined in the previous section, a large number of existing bridges has been constructed before earthquake provisions were included in the design codes. A previously identified potentially critical structural component of these bridges are relatively short wall-type piers with detailing deficiencies [1]. Their design and construction does usually not comply with modern capacity design requirements. While their force-capacity may thus be found to be insufficient, their displacement-capacity is largely unknown. Existing models to evaluate the displacement-capacity of structural members have often been developed for columns and validated with the corresponding data. Using these models to predict the displacement-capacity of the mentioned wall-type piers is hence linked to considerable uncertainty, as little suitable experimental data exists to validate the applicability of these models to wall-type piers.

However, to perform a displacement-based assessment of existing bridges, reliable models to predict the force-deformation relationships are necessary. Hence, first, additional experimental data is required to complement the existing data and, second, existing models need to be evaluated and new models need to be developed that allow estimating the force-deformation relationship. An experimental test campaign containing seven large scale pier tests of the investigated type has already been carried out in the framework of the research project [1, 3]. Based on the results of these tests, models that account for the typical detailing deficiencies need to be developed.

1.3 Objectives of this study

The objective of this study is to develop easily applicable engineering type models which can be used for the displacement-based assessment of existing wall-type bridge piers. They need to take into account common detailing deficiencies such as low transverse reinforcement ratios and a lack of confining reinforcement. In light of the large bridge stock that needs to be assessed, the models need to be fairly easy to apply but must yield sufficiently reliable results. Therefore, two types of models are evaluated: the plastic-hinge modeling approach and an approach based on the kinematics of shear critical piers.

The first approach is chosen because it is easily applicable and is known to yield good results in predicting the behavior of flexure dominated members. In this study, the applicability of this modeling approach to shear critical members is evaluated and modifications of the approach to better capture the response are examined and developed. Due to the mentioned deficiencies and the geometry of the piers, the focus within this modeling approach lies on two aspects: Incorporating the shear deformations, which constitute a significant part of the total deformation, into the modeling approach as well as accounting for the influence of lap-splices in the plastic hinge region on the behavior of the pier.

The second approach is chosen because it represents a mechanical modeling approach that is capable of predicting the force and displacement capacity of a pier. As it is a newly developed approach, it is validated against a database of wall-type piers in this study. Furthermore, the influence of several pier characteristics on the displacement-capacity is studied with this approach.

1.4 Outline of the report

Chapter 2 provides a review of existing plastic hinge modeling approaches and all necessary quantities. It starts with introducing the basic mechanical concept behind the modeling in Section 2.1. Section 2.2 then introduces the key quantity that is needed for this type of modeling, i.e. the plastic hinge length. Several suggestions that are either developed for walls or modified for the application to wall-type structures are introduced and discussed. Section 2.3 deals with the rotation due to anchorage slip, which is either taken into account by adding a strain penetration length to the plastic hinge length or by adding an additional rotation component to the deformation. The then following Section 2.4, summarizes strain and curvature limits for the plastic hinge region from the literature that are used for estimating the displacement capacity of the piers. Section 2.5 treats the prediction of the flexural response. Section 2.6 introduces some approaches to incorporate the shear deformations into the plastic hinge modeling approach. Section 2.7 treats the behavior of lap splices under seismic loading and gives example of models to predict the strength and failure strain limits of lap splices.

Chapter 3 contains the application of the previously introduced plastic hinge models and a validation and discussion of results based on the test data provided in [1, 3]. First, the plastic hinge length predictions are compared to experimentally derived measures for the plastic hinge length. Differences in determining the plastic hinge length are discussed and a suitable approach for the investigated piers is identified based on the experimetal data. Section 3.4 compares anchorage slip predictions with the experimental data in the elastic and inelastic range. In Section 3.5 the computation of the moment curvature response is discussed and in Section 3.6 the flexural response of the piers is determined based on the

results of the preceding sections of this chapter and discussed based on the comparison with the experimental data. Section 3.7 contains an in-depth discussion of shear deformations. Besides the models introduced in Chapter 2, the experimental data is evaluated in detail and different approaches to model shear deformations are evaluated. Section 3.8 discusses the incorporation of the lap splice behavior into the modeling and identifies possible limit states for the onset of splice degradation. Finally, in Section 3.9 the determination of the complete force-deformation relationship, taking into account the findings of the preceding sections, is discussed. The chapter closes with conclusions on the plastic hinge modeling approach for the modeling of piers with detailing deficiencies in Section 3.10.

Chapter 4 provides both review and evaluation of existing models to predict the shear strength degradation. Section 4.2 introduces various kinds of models which were primarily developed to capture the shear strength degradation of columns. First, shear capacity models which are based on truss or strut-and-tie approaches and include a partially empirically determined shear strength degradation depending on ductility are introduced. Second, empirically determined drift capacity models, which aim at directly predicting the deformation capacity of a member, are briefly discussed. In the following sections, a truss model with plastic limits for the compression zone, a shear-flexure interaction model and an approach to predict the shear degradation based on the degradation of the load transfer mechanisms across the shear crack are presented. In Section 4.3, the performance of these models when applied to wall-type piers is evaluated and discussed.

Chapter 5 contains the validation of a three parameter kinematic approach to predict the load-displacement response and the degradation of shear critical piers, which has been developed by [13]. The chapter begins with an explanation of the mechanical and kinematic assumptions underlying the approach. Section 5.3 then presents the experimental database used for the validation of the approach in Section 5.4. Section 5.5 discusses the influence of some main characteristics, namely the transverse reinforcement ratio, the aspect ratio, the axial load ratio and the longitudinal reinforcement ratio, on the force-deformation response, especially with regards to their influence on the drift capacity. Section 5.6 provides an in-depth discussion of one of the main parameters of this model: the so-called critical loading zone which represents the area damaged in compression and is a modeling quantity comparable to the plastic hinge length. Finally, Section 5.7 contains the conclusions of this chapter.

The final Chapter 6 provides a summary of the report as well as the key conclusions drawn from this study. Furthermore, topics for which further research is deemed necessary are outlined in the last section.

2 Review of plastic hinge models

2.1 Introduction

Plastic hinge modeling builds on the idea that the global force-deformation response of a structural component can be computed from the local moment-curvature (M-ϕ) relationship determined for the section at which the maximum moment occurs. Furthermore, inelastic curvatures are assumed to concentrate in a limited region along which they are linearly distributed. In plastic hinge models, this region is substituted with an equivalent plastic hinge with constant curvature. Outside the plastic hinge, deformations are taken to be elastic. Figure 2.1 shows the assumptions and simplifications that were just described.

With the procedure briefly outlined above, only flexural deformations can be estimated, which is not sufficient especially for the wall type structures investigated herein. Shear deformations may constitute a significant part of the total deformations of these members. Therefore, models have been developed which relate shear to flexural deformations. They can be used in conjunction with the plastic hinge models to account for shear deformations. The total deformation is then obtained as the sum of flexural and shear deformations.

The reason for choosing such a lumped plasticity method over direct integration of the curvature profile of a member obtained from section analysis is that, according to [7], the latter was not suitable to obtain deformation estimates because neither shear deformations nor tension shift and strain penetration effects can be accounted for. Furthermore, the deflection could only be determined up to maximum load and not beyond peak, when the tangent stiffness might be negative. The assumption of a plastic hinge length L_p with constant curvature captures the tension shift as well as strain penetration effects and partially compensates for shear deformations, according to [7].

In the following sections, procedures outlined by several researchers to determine all necessary quantities for plastic hinge analysis, i.e. the plastic hinge length, the flexural re-

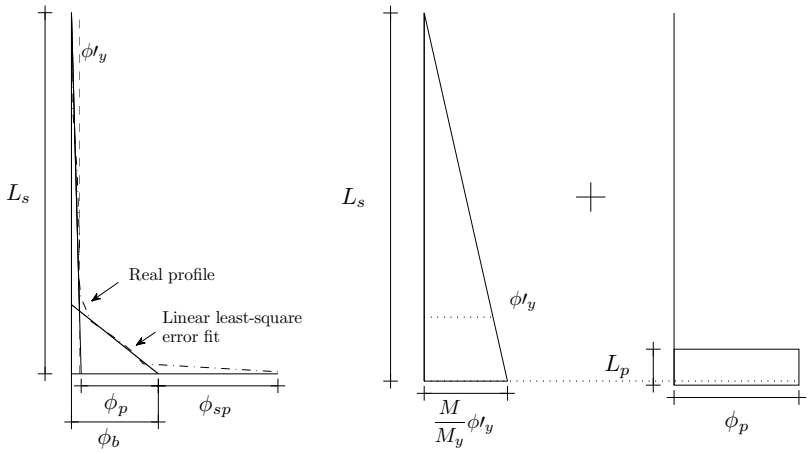

Figure 2.1: *Linear approximations of the true curvature profile (left) and assumptions for the plastic hinge model (right). In the displayed case, the strain penetration length L_{sp} is assumed to be part of the plastic hinge length L_p.*

sponse and the shear response, are briefly introduced. Section 2.2 presents several plastic hinge length equations that were either directly developed for walls or modified to be applicable to wall-type structures. Section 2.2.1 introduces some of the parameters which are typically regarded to influence the length of the plastic hinge of wall-type structures. Section 2.3 deals with anchorage slip, which is either accounted for in the modeling by increasing the plastic hinge length or by introducing a fixed end rotation component. In this section, some approaches to directly determine the slip are introduced and the results of these are compared with those obtained with an increased plastic hinge length. Strain and curvature limits which are used to predict the deformation capacity are introduced in Section 2.4. Section 2.5 then presents approaches to determine the flexural response of a member by using the quantities introduced in the preceding sections. Section 2.6 presents models with which shear deformations can be accounted for within plastic hinge modeling. Finally, stress and strain limits which can be employed to account for the influence of spliced reinforcement in the plastic hinge region are discussed in Section 2.7. In Chapter 3, these modeling approaches are applied to seven test units tested in the framework of this project [1, 3] and the results are compared to their experimental data.

2.2 Plastic hinge length

2.2.1 Parameters influencing the plastic hinge length

Most of the plastic hinge lengths proposed by researchers have originally been developed for and calibrated against beams or columns, but some explicit suggestions or adaptions have been made for wall type structures, such as the suggestion in [7] to increase the tension shift component for walls. Besides the tension shift, the effects primarily accounted for are:

- Spread of plasticity due to moment gradient M_u/M_y
- Spread of plasticity due to strain hardening f_u/f_y
- Pullout of longitudinal reinforcement of the anchorage (or strain penetration effect)
- Aspect ratio
- Axial load
- Type of loading: monotonic or cyclic

It seems that researchers do often not explicitly distinguish between the spread of plasticity due to M_u/M_y and f_u/f_y. Though both effects are certainly also related, the first one can also occur if the steel does not exhibit any strain hardening, because moment capacity will increase from first yield to the ultimate inelastic capacity. For that reason, the two parameters are mentioned separately here. In the following, a brief summary of different plastic hinge length equations for wall-type structures is given, for more exhaustive overviews on plastic hinge lengths in general the reader is referred elsewhere, e.g. [20].

2.2.2 Plastic hinge length according to Priestley et al.

Over the years, several modifications of the plastic hinge length have been suggested by Priestley, Paulay, Park and their co-workers. However, here only the proposition from the

latest book [7] is included, since it is expected to reflect the latest development of the equation. The plastic hinge length of beams and columns is:

$$L_p = kL_s + L_{sp} \geq 2L_{sp} \tag{2.1}$$

where L_s is the length from the critical section to the point of contraflexure in the member, *k* a factor accounting for strain hardening according to Equation (2.4) and L_{sp} the strain penetration length according to Equation (2.3). For a cantilever, L_s is equal to the column height *H*. A lower limit of $L_p = 2L_{sp}$ for the plastic hinge length is suggested, to account for the reinforcement slip out of the structural member as well as the footing.

As tension shift has a larger effect on wall structures than on beams, an additional term of $0.2h$ is recommended for comparison with experimental data. For design, this value is conservatively reduced to $0.1h$. Hence, the total plastic hinge length for a wall-type structure is:

$$L_p = kL_s + 0.2h + L_{sp} \tag{2.2}$$

The strain penetration length is calculated according to the following equation:

$$L_{sp} = 0.022 f_y \cdot d_{bl} \quad \text{SI units} \tag{2.3}$$

where f_y is the yield strength of longitudinal reinforcement in MPa and d_{bl} is the bar diameter of the longitudinal reinforcement in mm. If US customary units are used, the factor 0.022 changes to 0.15.

It is stated that the strain penetration length is related to anchorage slip, which here refers to the pullout of the reinforcement from the foundation, as well as the spread of concrete compressive strains into the foundation. The derivation of the factor 0.022 is not included in [7], but in [21], $6d_{bl}$ were suggested for grade 40 reinforcement and $9d_{bl}$ for grade 60 reinforcement. Those values were determined from large scale tests and result in the recommended factor 0.022 if divided by the respective steel strength. Including a constant strain penetration length implicitly implies that the development length of the anchorage is constant and increasing slip is related to increasing steel strain only.

To also account for the spread of plasticity due to strain hardening of the reinforcement, the following factor *k* is introduced:

$$k = 0.2 \left(\frac{f_u}{f_y} - 1 \right) \leq 0.08 \tag{2.4}$$

Note that here the spread due to strain hardening is directly addressed via the steel properties and not via any moment relation. An explanation on the derivation of the equation and hence the derivation of the factor 0.2 is not presented in [7]. The plastic hinge length expression introduced in this section is mainly targeted towards determining the ultimate displacement of a structure. However, as the authors also introduced a “refined” approach to predict the entire load-displacement response, which is “suitable for prediction of experimental response”, and provide no restrictions for the use of L_p according to Equation (2.2), it can be assumed that L_p may be used for prediction of the entire response as well.

2.2.3 Plastic hinge length according to Fardis et al.

Based on a large test database a plastic hinge length accounting for the loading type (monotonic or cyclic) was presented by [22]. To obtain an estimate for L_p, with which the deformation capacity could be determined, the authors evaluated 875 tests for which an ultimate drift θ_u, defined as the point of at least 20% drop of the lateral load, was reported. From the test data it was concluded that L_p should, in addition to the loading type, be a function of the shear span as well as the reinforcement yield strength and bar diameter. The equations proposed for L_p yield the best fit values for the experimentally determined θ_u. The plastic hinge length was derived based on analytical estimates for the curvatures ϕ_u and ϕ'_y. For the derivation of the curvature expressions an elastic-perfectly plastic steel model and a parabolic-linear concrete model were used.

The plastic hinge length L_p was assumed to be a linear function of L_s and $d_{bl}f_y$. With this assumption, the experimental data for cyclic loading was evaluated and the equation for L_p that matched the data best was found to be:

$$L_{p,cyc} = 0.12L_s + 0.014k_p d_{bl} f_y \tag{2.5}$$

where k_p is a factor accounting for whether bar pullout is possible ($k_p = 1$) or not ($k_p = 0$). The former applies if a plastic hinge develops right above the foundation of a member, which causes pullout of the reinforcement out of the foundation, whereas the latter applies if the plastic hinge develops at midlength of a beam, for instance. For monotonic loading, the plastic hinge length was found to be 1.5 times longer than for cyclic loading: $L_{p,mon} = 1.5L_{p,cyc}$.

According to [4] this equation did not yield good results if only the slender (i.e. $L_s/h > 2.5$) wall-type structures of the above mentioned database were considered: For those walls, the ratio of predicted to observed plastic hinge length varied between 0.25 and 5. However, in [23] this equation is still included as recommended plastic hinge length for bridge piers, this time with the factors 0.1 and 0.015.

In [6] two different equations are presented, one for cyclic loading and good seismic detailing (Equation (2.6b)) and one for monotonic loading regardless of detailing (Equation (2.6a)). The reinforcement bar slippage is no longer included in the plastic hinge length, but as additional rotation component. Models also adopted in Annex A.3.2.2 (8) of [24] were employed for the concrete strength together with a maximum strain relation which takes the confined depth into account. Eventually, the plastic hinge length was again taken to be the length for which the best datafit in conjunction with Equation (2.36), which yields an ultimate drift estimate and is thus included in Section 2.5, was achieved:

$$L_{p,mon} = h\left(1.1 + 0.04\min\left(9, \frac{L_s}{h}\right)\right) \tag{2.6a}$$

$$L_{p,cyc} = 0.2h\left(1 + \frac{1}{3}\min\left(9, \frac{L_s}{h}\right)\right) \tag{2.6b}$$

Note that no distinction was made between beams and walls, since the results apparently fit both data sets. The equation does differentiate, however, between monotonic and cyclic loading. One should keep in mind that this plastic hinge length has been developed to match the ultimate rotation best and not the entire flexural response.

2.2.4 Plastic hinge length in Eurocode

In Annex A of Eurocode 8 (EC8) Part 3 [24] for the assessment and retrofitting of buildings two slightly different plastic hinge lengths are recommended for use. The choice between the two lengths depends on the choice of the models with which ultimate steel and concrete strains are computed. If the more complex strain limits according to A.3.2.2 (8) are used, the plastic hinge length is recommended to be:

$$L_p = \frac{L_s}{30} + 0.2h + 0.11\frac{d_{bl} f_y}{\sqrt{f_c}} \tag{2.7}$$

For the steel, the proposed limit strain is $\varepsilon_{s,u} = 0.06$ for ductile steel of class C. For concrete, strains have to be evaluated using a confined concrete model similar to Equations (3.3) and (2.26). The confined concrete strength and ultimate strain are then:

$$f_{cc} = f_c \left(1 + 3.7 \left(\frac{k_{con}\varrho_v f_{yv}}{f_c}\right)^{0.86}\right) \tag{2.8a}$$

$$\varepsilon_{cu} = 0.004 + 0.5\frac{k_{con}\varrho_v f_{yv}}{f_{cc}} \tag{2.8b}$$

where k_{con} is obtained from Equation (2.29). The strain penetration component of L_p corresponds to the component suggested in Equation (2.5) if the concrete strength is $f_c = 62\,\text{MPa}$ and to the one proposed in Equation (2.3) if $f_c = 25\,\text{MPa}$. With this plastic hinge length and the curvatures corresponding to the defined limit strains, the ultimate deflection and not the entire response of a member can be determined.

2.2.5 Numerically determined plastic hinge lengths

A study in which a plastic hinge length was developed explicitly for walls is presented in [4]. Based on experiments conducted by one of the authors, a VecTor2 [25] model was set up and used to conduct a parametric study with the objective to investigate the influence of shear on L_p. The latter was taken as half the length over which plasticity spreads. The spread of plasticity was obtained from the distribution of inelastic steel strains predicted in the analysis. Furthermore, it was investigated whether the comparatively low normal force ratios of walls and their geometry and reinforcement distribution, which is different from columns, influence L_p. All walls in the study were modeled as cantilever with the same concrete and steel constitutive relationships. The steel was modeled with a yield plateau and linear strain hardening setting in at $10‰$. The ratio of ultimate to yield stress was $f_u/f_y = 625/400 = 1.625$. It was found that cyclic loading did not have much influence on the distribution of vertical strains compared to monotonic loading, but resulted in a slight increase in horizontal and shear strains. Furthermore, the authors observed that the spread of plasticity was not directly proportional to the wall length.

Shear was found to have a significant influence on the spread of plasticity, especially in squat walls after the onset of diagonal cracking. Contrarily to what [26] observed for columns, an axial load was found to reduce the plastic hinge length of walls. This was explained with the observation that the ratio M_u/M_y decreases when the normal force increases.

Even though shear was found to have a significant influence, the authors eventually concluded that if shear span and wall length are included in the formulation for the plastic hinge length, the shear stress does not need to be explicitly accounted for. The proposed equation is hence merely a function of wall length *h*, shear span L_s and normal force *P*. The plastic hinge length was taken as half the length over which plasticity spreads, L_{pr}, since the authors observed that the inelastic curvature varies linearly over this length. That means, unlike for instance [6], the authors did not adjust the plastic hinge length to fit the overall displacement best, but used the actual plasticity spread from the numerical model. Comments on the agreement of the top displacement, which is predicted with this plastic hinge length, with experimental or numerical results are not provided in [4]. The authors interpret the resulting L_p as a lower bound estimate for the plastic hinge length of an isolated cantilever wall:

$$L_p = (0.2h + 0.05L_s)\left(1 - 1.5\frac{P}{A_g f_c}\right) \leq 0.8h \tag{2.9}$$

Another numerical study to investigate the plastic hinge length of structural walls has been conducted by [27] using the software ANSYS. Structural walls that were several stories high were analyzed with a hybrid FE model: the two bottom stories were modeled with solid continuum elements and the upper stories with Timoshenko-beam elements. The wall was modeled with horizontal flanges at the height of the floors in the two bottom stories to account for the influence of floor-slabs on the shear flow in the wall. Material properties were again kept constant throughout the study with a concrete strength of $f_c = 25$ MPa and a steel yield strength of $f_y = 420$ MPa. The steel was modeled bilinear with a hardening modulus of $E_{sh} = 1500$ MPa which would result in a ratio $f_u/f_y = 1.35$ if a strain of $\varepsilon_{su} = 0.10$ is assumed. The objective of this numerical study was to investigate the influence of the wall length h, shear span L_s, axial load ratio n, longitudinal reinforcement ratio of the boundary element $\varrho_{l,b}$ and transverse reinforcement ratio ϱ_v on the spread of plasticity and the length of the plastic hinge. The latter was not assumed to correspond to half the length over which plasticity spreads L_{pr}, but was calculated from the numerically determined curvatures and top displacement by rearranging Equation (2.34). No distinction between top displacements due to flexure and shear was made. Finally, the plastic hinge length was derived by means of a regression analysis taking into account the varied parameters:

$$L_p = 0.27h\left(1 - \frac{P}{A_g f_c}\right)\left(1 - \frac{f_{yv}\varrho_v}{f_c}\right)\left(\frac{L_s}{h}\right)^{0.45} \tag{2.10}$$

In the analysis, the wall and the foundation were modeled with smeared reinforcement. The latter was modeled to capture a potential strain penetration effect. However, no detailed information is provided on how this is done with the smeared reinforcement approach and on whether or how possible influences such as bond strength and bar diameters were considered. As yielding did not proceed into the foundation, strain penetration was concluded to be negligible and hence not included in L_p. Furthermore it was observed that the plastic hinge length corresponded to about 43% of L_{pr} rather than 50%, as usually assumed. The provided curvature profiles do not indicate a perfectly linear shape and the value of 43% can hence stem from a slight concentration of curvatures towards the base.

2.2.6 Experimentally determined plastic hinge length

Techniques to evaluate the plastic hinge length using experimental data are presented in [20] and [28]. The plastic flexural deformations $\Delta_{p,fl}$, which are needed to backcalculate L_p, can be computed from the total deformations Δ if the flexural deformations at first yield $\Delta'_{y,fl}$ as well as the shear deformations Δ_{sh} are known:

$$\Delta_{p,fl} = \Delta - \Delta_{sh} - \Delta'_{y,fl}\frac{M}{M'_y} \tag{2.11}$$

All the deformation values are experimentally determined. The flexural deformation at first yield is the experimentally determined flexural deformation corresponding to the analytically determined first yield force (e.g. the first yield force according to moment-curvature analysis). With $\Delta_{p,fl}$, the plastic hinge length L_p can be computed as:

$$\phi_p L_s L_p = \Delta_{p,fl} \rightarrow L_p = \frac{\Delta_{p,fl}}{\phi_p L_s} = \frac{L'_p}{2} + L_{sp} \tag{2.12}$$

where L'_p is the length over which plasticity spreads and ϕ_p the plastic flexural curvature at the base of the wall:

$$\phi_p = \phi_b - \phi'_y\frac{M}{M'_y} \tag{2.13}$$

To obtain the base curvature ϕ_b a least squares approximation of the curvature profile, using at least three inelastic curvature values, is recommended. For a cantilever pier, developing the inelastic curvatures right above the base, this means that at least the first three measurements taken above the basecrack should be used. If the inelastic curvatures spread further up, more measurements may of course be used. The intersection between the linear least-squares approximation of the inelastic curvatures and the horizontal axis is assumed to be the base curvature. The difference between this value and the one measured at the base is usually ascribed to strain penetration effects. Figure 2.1 visualizes the assumptions on which the calculation of the plastic hinge length is based. One of the assumptions is that inelastic curvatures follow an approximately linear trend. Often, this is not exactly the case for experimentally derived curvature profiles. Compressive strain concentrations due to a fan-like crack pattern and variations in crack locations render them slightly irregular [20]. Plastic hinge lengths determined according to Equation (2.12) contain a strain penetration component L_{sp}, because the latter is also included in the top displacement used for the computation of L_p. Based on the assumption that L_{sp} is independent of the curvature and that the rotation due to strain penetration can be calculated by multiplying L_{sp} with the base curvature ϕ_b, the strain penetration length can be calculated as follows:

$$L_{sp} = L_b\left(\frac{\phi_{measured}}{\phi_b} - 1\right) \tag{2.14}$$

where L_b is the actual base length of the measurement devices covering the base crack and $\phi_{measured}$ the curvature determined with the readings of those devices in conjunction with L_b.

2.2.7 Summary of plastic hinge lengths

Table 2.1 summarizes the different plastic hinge length equations which were introduced in Sections 2.2.2 to 2.2.5. It also lists the components that are included in the equations, to give an overview over which characteristics that influence the plastic hinge length were taken into account by different researchers. Differences in the equations do not only exist with regard to the effects that are assumed to influence the net plastic hinge length along the member L_p', but also with regard to whether strain penetration is included as extra component L_{sp} in the plastic hinge length. Furthermore, the assumed location of the center of rotation – at the center or at the bottom of the hinge – influences the length. Or in other words, if the same plastic hinge length with different centers of rotation is used, different top displacements are predicted. Hence, all plastic hinge lengths derived from top displacements are influenced by the assumed center of rotation.

Table 2.1: *Summary of plastic hinge length equations.*

	Includes influence of						
Equation for plastic hinge length	L_s	h	$\frac{f_u}{f_y}$	$\frac{P}{A_g f_c}$	SP	LT	CR
Eq. (2.2): $0.2\left(\frac{f_u}{f_y}-1\right)L_s+0.2h+L_{sp}$	✗	✗	✗		✗		b
Eq. (2.6b): $0.2h(1+\frac{1}{3}\min\left(9,\frac{L_s}{h}\right))$	✗	✗				✗	m
Eq. (2.7): $\frac{L_s}{30}+0.2h+0.11\frac{d_{bl}f_y}{\sqrt{f_c}}$	✗	✗			✗		m
Eq. (2.9): $(0.2h+0.05L_s)\left(1-1.5\frac{P}{A_g f_c}\right)$	✗	✗		✗			-
Eq. (2.10): $0.27h(1-\frac{P}{A_g f_c})\left(1-\frac{f_{yh}\varrho_v}{f_c}\right)\left(\frac{L_s}{h}\right)^{0.45}$	✗	✗		✗			m

Table 2.1 summarizes also which influences are considered in the plastic hinge length formulation. If strain penetration is included in the hinge length, column “SP” is checked and if the loading type, i.e. cyclic or monotonic loading, is considered, column “LT” is checked. The last column indicates, where the center of rotation is assumed in the equation for the flexural response that is recommended in combination with the respective plastic hinge length. Two locations are possible, either at the base (b) of the plastic hinge and hence the base of the pier or at midheight (m) of the plastic hinge. If no recommendation for the location of the center of rotation is made, the last column is dashed. Another short summary with comparison to the experimental data is given in Table 3.2.

2.3 Rotation due to anchorage slip

2.3.1 Anchorage slip

As indicated previously, the deformation due to anchorage slip or strain penetration can be included by increasing the plastic hinge length, see for instance Equations (2.1) and (2.7). Another possibility is to include the component when the flexural response is computed, see for instance Section 2.5.1. For the latter, different methods exist to calculate the slip of the anchored bars with which the rotation is determined. To compare the results of the methods and the influence of some parameters, three common approaches to calculate the slip are briefly examined: 1) Integration of bond-slip relations along the development length

of a bar, 2) use of simplified, constant bond stress distributions and integration of the reinforcement strains along the development length and 3) use of stress-slip relations obtained from pull-out tests with long embedment length. The first method requires some computational effort, because it is an iterative procedure requiring a rather fine mesh. Furthermore, bond-slip relations are generally determined from tests on bars whose strains are low, but for determining the total slip, the bond conditions of reinforcement bars that are yielding, need to be known [29]. To overcome this deficit and include the effect of inelastic strains in the bond slip relations, modification factors have been proposed by several researchers. The second method requires less computational effort than the first by assuming a stepped bond stress distribution with constant values for both elastic and inelastic steel strains. With this assumption, the development length l_d can easily be calculated. The slip is then calculated by integration of the linear strain profile along l_d. This approach is appealing because of its simplicity. Furthermore, since the results have sometimes been calibrated against tests with long embedment length satisfactory agreement is expected despite the simplified bond stress distribution. Method 3) uses slip-strain relations which have been determined from pullout tests on specimen with long embedment length, which closely reflect the real conditions in a pier footing. Due to the mentioned computational efforts and shortcomings of approach 1), only models following approaches 2) and 3) are included in this section.

Researchers have proposed different bond strength values τ_b for approach 2), which are typically related to the concrete strength. Cyclic loading effects are generally not considered which means this approach serves to calculate the envelope of the expected slip under cyclic loading. For steel strains below yield, bond stresses of e.g. $\tau_{b1} = \sqrt{f_c}$ [30, 31] or $\tau_{b1} = 0.6 f_c^{2/3}$ [32] have been proposed and for inelastic strains bond stresses of $\tau_{b2} = 0.5\tau_{b1}$ [30, 32]. These bond stresses are then used to calculate the development length. The development length l_d, which corresponds to the elastic range of the reinforcement bar, and l'_d, which corresponds to the length along which yield strain is exceeded, can be derived from:

$$f_s A_{sb} = \tau_b \pi d_{bl} l_d \tag{2.15a}$$

$$\rightarrow l_d = \frac{f_y d_{bl}}{4\tau_{b1}} \tag{2.15b}$$

$$\rightarrow l'_d = \frac{(f_s - f_y) d_{bl}}{4\tau_{b2}} \tag{2.15c}$$

where d_{bl} and A_{sb} are the diameter and the cross section of a reinforcement bar, respectively, f_s is the considered steel stress and f_y the yield strength of the steel. With the development length, the slip δ_s can be calculated:

$$\delta_s = \frac{\varepsilon_s l_d}{2} \qquad \text{for} \quad \varepsilon_s \leq \varepsilon_y \tag{2.16a}$$

$$\delta_s = \frac{\varepsilon_y l_d}{2} + \frac{(\varepsilon_s + \varepsilon_y) l'_d}{2} \qquad \text{for} \quad \varepsilon_s > \varepsilon_y \tag{2.16b}$$

In [29] pullout tests on deformed bars with an anchorage length long enough to prevent end slip as well as varying concrete strength and bar diameter have been reported. Bar diameters were not smaller than 19.5 mm and the rib orientation was almost perpendicular to the bar axis. An unbonded region was provided at the loaded end and the bars were

pulled against the casting direction. The aim of the tests was to develop a bar strain-slip relationship which can be used for seismic analysis in both the elastic and inelastic range. Relations developed from tests with long embedment length seem appealing to determine the anchorage slip, because the slip and corresponding steel strain conditions reflect the real conditions of an anchored reinforcement bar. It was found that the non-dimensional slip $\delta_{s,n}$

$$\delta_{s,n} = \frac{\delta_s}{d_{bl}} \left(\frac{f_c}{20} \right)^{2/3} \tag{2.17}$$

could be expressed uniquely as a function of the steel strain ε_s according to the following equations:

$$\delta_{s,n} = \varepsilon_s (2 + 3500\varepsilon_s) \qquad \text{for} \quad \varepsilon_s \leq \varepsilon_y \tag{2.18a}$$

$$\delta_{s,n} = \delta_{s,n,y} + 0.047\,(f_u - f_y)\,(\varepsilon_s - \varepsilon_{sh}) \qquad \text{for} \quad \varepsilon_s > \varepsilon_y \tag{2.18b}$$

These strain-slip relations are presented as envelope for cyclic loading and are therefore well suited for monotonic analysis of piers subjected to cyclic loading.

Based on the tests of [29], amongst others, monotonic and cyclic stress-slip relationships have been proposed in [33]. For the slip at yield $\delta_{s,y}$, the following equation is presented for monotonic loading:

$$\delta_{s,y} = 2.54 \left(\frac{d_{bl} f_y}{8437\sqrt{f_c}} (2\alpha + 1) \right)^{1/\alpha} + 0.34 \tag{2.19}$$

where α is a parameter stemming from the assumed bond-slip relation which is here $\alpha = 0.4$. Two different models have been proposed for the stress-slip relation between $\delta_{s,y}$ and the ultimate slip $\delta_{s,u}$: a cyclic and a monotonic one. The cyclic model partially depends on the loading history and is thus not suitable for monotonic analysis. The monotonic relationship is as follows:

$$f_s = \frac{\frac{\overline{\delta_s}}{\mu - \overline{\delta_s}} (f_u - f_y)}{\left[\left(\frac{1}{\mu m} \right)^{R_e} + \left(\frac{\overline{\delta_s}}{\mu - \overline{\delta_s}} \right)^{R_e} \right]^{1/R_e}} + f_y \tag{2.20a}$$

$$\overline{\delta_s} = \frac{\delta_s - \delta_{s,y}}{\delta_{s,y}} \tag{2.20b}$$

$$\mu = \frac{\delta_{s,u} - \delta_{s,y}}{\delta_{s,y}} \tag{2.20c}$$

with $R_e = 1.01$ to create a gradient close to zero in the vicinity of the ultimate bar strength. That means the stress-slip relationship is not bilinear but curved after the yield stress has been exceeded and asymptotically approaching the ultimate stress value. For some quantities, namely transition factor *m* and the ultimate slip $\delta_{s,u}$, a range of possible values was proposed by [33]. In the following computations, intermediate values were chosen to evaluate Equation (2.20). Thus, the stiffness transition factor *m* was assumed to be $m = 0.4$ (recommended $0.3 - 0.5$) and the ultimate slip $\delta_{s,u} = 35\delta_{s,y}$ (recommended $30 - 40\delta_{s,y}$).

Hence, in contrast to slip at yield $\delta_{s,y}$ according to Equation (2.19), which has been obtained by linear regression analysis of experimental data, only a range of possible ultimate slip values $\delta_{s,u}$ is proposed, due to a lack of sufficient test data. Recommendations on how to choose $\delta_{s,u}$ and *m* are not provided which renders evaluation of the applicability of the model rather difficult.

As mentioned previously, there is no direct calculation of slip values or the rotation due to slip if the strain penetration effect is included in the plastic hinge length. According to [7] the strain penetration length is assumed to capture not only the effect of the pullout of steel in tension, but also the spread of the concrete compressive strains into the footing. However, to compare the results obtained with the different approaches, slip values are derived from the rotation θ_{sp} according to Equation (2.25) by means of the following equation:

$$\delta_s = \theta_{sp}(d - x_c) \tag{2.21}$$

where *d* is the distance of the outer reinforcement bar to the opposite edge of the section and x_c the compression zone depth which is determined from moment-curvature analysis corresponding to θ_{sp}.

In Figure 2.2 the slip values predicted with the equations presented in this section are plotted against the maximum strain in the reinforcement bar. A bilinear stress-strain relationship with a strain hardening ratio of $f_u/f_y = 1.17$ and bar diameter $d_{bl} = 14\,\text{mm}$ has been used for the steel. Differences in the estimated slip are significant, especially after the onset of yielding. When the slip is predicted according to Equation (2.21) [7] the steel properties are, except for the yielding stress, not explicitly taken into account. Hence, the slip is predicted to increase in proportion to the curvature regardless of the strain hardening characteristics. Even for an elastic-perfectly plastic steel the slip is predicted to increase proportionally to the curvature, which does not appear physical. All other predictions are either based on integration of steel strains along the development length [32, 30, 31] or steel strain-slip relationships at the loaded end of the bar [29, 33] and exhibit significant differences between pre-yield and post-yield range. Only two values are contained in the graph displaying the estimated slip values according to [6], one for yielding and one for the ultimate slip, which were determined based on the strain limits proposed by the same authors, provided in Section 2.4. All the models mentioned in this paragraph have been developed to capture the envelope of the cyclic response, except for the one by [32], who does not explicitly mention this loading case.

2.3.2 Rotation due to anchorage slip

The rotation due to anchorage slip θ_{sp} can be calculated from the slip and the depth of the cross section under tension $d - x_c$, following the procedure also used by e.g. [30]. The distance between the outer reinforcement bars and the outer compression fiber is used as effective section depth *d*. The compression zone depth x_c is obtained from moment-curvature analysis which also yields the reinforcement strains necessary for the slip calculation. With these values the rotation can be calculated:

$$\theta_{sp} = \frac{\delta_s}{d - x_c} \tag{2.22}$$

If the strain penetration effect is included in the choice of the plastic hinge length L_p, the flexural top displacement $\Delta_{f,top}$ of a member with shear-span length L_s in the inelastic range follows as [7]:

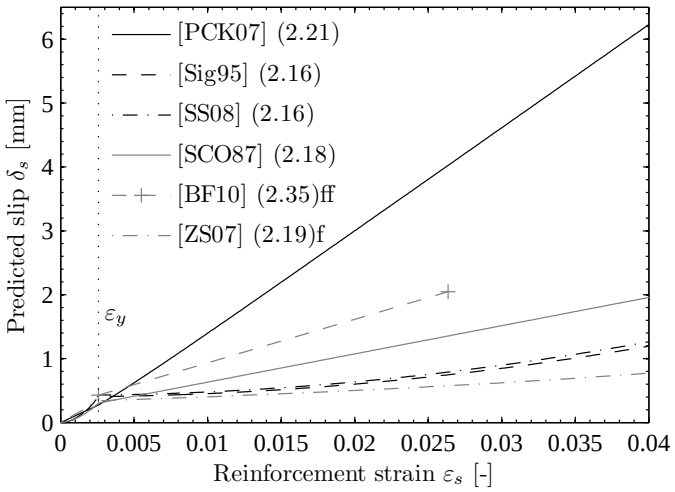

Figure 2.2: *Slip predictions according to equations presented in this section against reinforcement strain for reinforcement bars with $d_{bl} = 14\,mm$ and $f_u/f_y = 1.17$.*

$$\Delta_{f,top} = \phi'_y \frac{M}{M_y} \frac{(L_s + L_{sp})^2}{3} + \left(\phi - \phi'_y \frac{M}{M_y}\right)(L'_p + L_{sp})L_s \tag{2.23}$$

where ϕ'_y is the first yield curvature, *M* the current moment, M_y the first yield moment and L'_p the part of the plastic hinge length along the member. Within plastic hinge modeling, it is commonly assumed that the inelastic curvature profile is linear and L'_p corresponds to half the length over which plasticity spreads. If only the top displacement due to strain penetration is of interest, L'_p is not considered in the second part of the equation. In the first term of the equation, the separation of the components is not as simple because of the quadratic relation. The rotation corresponding to a certain top displacement is obtained by dividing $\Delta_{f,top}$ by the shear-span length L_s. To remove the dependency of the rotation due to strain penetration on L_s, the following assumption is made:

$$\frac{(L_s + L_{sp})^2}{L_s} = L_s + 2L_{sp} + \underbrace{\frac{L_{sp}^2}{L_s}}_{\approx 0} \approx L_s + 2L_{sp} \tag{2.24}$$

Equation (2.23) is then divided by L_s, the components due to L_s and L'_p are neglected and the simplifying assumption according to Equation (2.24) is introduced. This yields the rotation due to strain penetration θ_{sp}, which has already been used in Equation (2.21):

$$\theta_{sp} = \phi \frac{2}{3} L_{sp} \qquad \text{for} \quad \phi \leq \phi'_y \tag{2.25a}$$

$$\theta_{sp} = \phi L_{sp} - \frac{1}{3}\phi'_y \frac{M}{M_y} L_{sp} \qquad \text{for} \quad \phi > \phi'_y \tag{2.25b}$$

2.4 Strain and curvature limits

To define the ultimate limit state, a so called “damage-control compression strain” as well as “damage-control tension strain limit” are recommended by [7]. Following the assumptions made for the ultimate compression strain and corresponding stress in the confined concrete model by [5] the ultimate compression state is assumed to be reached when the confining reinforcement fractures. Hence, the formulation for the ultimate compressive strain was derived by equating the strain energy absorbed by the concrete post-peak to the strain energy absorbed by the confinement. This yields the following expression for the ultimate compression strain $\varepsilon_{c,dc}$:

$$\varepsilon_{c,dc} = 0.004 + \frac{C_2 \varrho_v f_{yv} \varepsilon_{su}}{C_1 f_{cc}} = 0.004 + 1.4 \frac{\varrho_v f_{yv} \varepsilon_{su}}{f_{cc}} \tag{2.26}$$

where the coefficients C_1, C_2 depend on the shapes of the stress-strain relationships of concrete and steel and f_{cc} is the confined concrete strain according to Equation (3.3) [5]. The average ratio C_2/C_1 is considered to be 1.4. The ultimate strain of the unconfined concrete is assumed to be $\varepsilon_{c,u} = 0.004$. Because this relation is based on pure axial compression and does not consider confinement provided by an adjacent member, such as a foundation, [7] state it underestimates the actual ultimate strain at combined flexure and axial force by about 23 - 37%. A criterion for buckling of the longitudinal bars is not included in the limit, but the authors include a recommendation for the maximum spacing of the stirrups to prevent buckling before $\varepsilon_{c,u}$ is reached.

With regard to the steel strain limit, the authors advise to use a lower limit for structures subjected to cyclic loading than for those subjected to monotonic loading: Under cyclic loading, the ultimate tensile strain capacity is affected by previously experienced compression strains in reversed cycles. Due to previously experienced plastic tensile strains, the reinforcement is also prone to buckling under compressive loading and hence to low cycle fatigue. Furthermore, reinforcement bar slip and tension shift are stated to contribute to a strain capacity under cyclic loading that is lower than the strain determined with monotonic testing ε_{su}. Hence, [7] suggest to limit the strain capacity under cyclic loading to 60% of the monotonic value:

$$\varepsilon_{su,cyc} = 0.6 \varepsilon_{su} \tag{2.27}$$

In [6], experimentally determined strains of an extensive database at ultimate displacement were examined and employed to derive strain limits for cyclic loading. Ultimate displacement was defined as corresponding to a drop of the lateral load of at least 20%. For the ultimate concrete compression strain $\varepsilon_{cu,cyc}$, the authors propose a formulation that accounts for the size of the area of the confined concrete under compression and the effectiveness of the confining reinforcement:

$$\varepsilon_{cu,cyc} = 0.0035 + \left(\frac{1}{x_{c,con}} \right)^{3/2} + 0.4 \frac{k_{con} \varrho_v f_{yv}}{f_{cc}} \tag{2.28}$$

where $x_{c,con}$ is the depth of the neutral axis in the confined core in mm. Factor k_{con} accounts for the effectiveness of the confinement according to [34]:

$$k_{con} = \left(1 - \frac{s}{2b_{con}}\right)\left(1 - \frac{s}{2h_{con}}\right)\left(1 - \frac{\sum s_{l,c}^2/6}{b_{con}h_{con}}\right) \tag{2.29}$$

where s is the stirrup spacing and h_{con}, b_{con} are the dimensions of the confined core, all measured to the centerline of the stirrups, and $s_{l,c}$ the distance between those longitudinal bars that are confined by stirrup corners or cross ties.

For the ultimate tensile steel strain, [6] suggest the following value:

$$\varepsilon_{su,cyc} = \frac{3}{8}\varepsilon_{su} = 0.375\varepsilon_{su} \tag{2.30}$$

Instead of defining limit strains with which an ultimate curvature is defined, [35] directly presented curvature limits. Based on a numerical study, ultimate curvature, drift, and rotation values were derived. The ultimate state here refers to the point at which one of the following occurs: Either the shear capacity has slowly degraded to 85% of the peak load or experienced a sudden drop, or the steel strains exceed 10% on the tension side or buckling and spalling strain on the compression side. The objective of the study by [35] was to investigate the influence of certain parameters on the deformation capacity, namely that of aspect ratio L_s/h, axial load ratio $P/(A_g f_c)$, wall length h, detailing of boundary elements, transverse reinforcement ratio ϱ_v and shear stress *v*. All resulting limit responses have been derived from a finite element model, in which the two bottom stories were modeled with solid continuum elements. The curvatures were computed from the strains in the elements along the edge of the wall. The ultimate curvature was obtained by extrapolating the linear approximation of the curvature profile of the two bottom stories to the base. Afterward, a regression analysis was performed on all curvatures obtained for the various investigated parameters. This yielded the following formulation for the ultimate curvature:

$$\phi_u = \frac{1}{h}0.8k_l k_{cs}\varepsilon_{su}\left(1 - 2.4\frac{P}{A_g f_c}\right)\left(1 - 1.5\frac{f_{sv}\varrho_v}{f_c}\right)\left(\frac{L_s}{h}\right)^{0.29} \tag{2.31}$$

where the correction factors k_l and k_{sc} take into account the loading conditions and the shape of the cross section and are 0.75 and 1.0 for cyclic loading and rectangular cross sections, respectively.

Besides the above mentioned strain limits, which provide an estimate for the damage of the material, strain limits based on stability considerations have been developed as well. Under cyclic loading the edges of a wall may be subjected to large tensile strains and hence feature cracks in which the reinforcement yields. Due to irregularities in the structure and – in the event of an earthquake – out of plane response, the compression force under reversed loading might not be introduced centrically and hence cause out-of-plane buckling [36]. To prevent this buckling, equations to compute the minimum wall thickness have been developed. They are based on the expected tensile strain in the plastic hinge and the assumption that the compression force acts with the largest possible eccentricity [36, 37]. If the wall thickness is given, these equations can be rearranged to yield the maximum allowable tensile strain. However, this stability problem occurs mainly if the wall thickness is small in relation to the height over which plastic tensile strains occur, which is not the case for the wall-type piers considered herein.

2.5 Flexural response

2.5.1 Bilinear approaches

Using the results from the moment-curvature analysis and the mentioned strain limits, one can predict the overall flexural force-deformation response of a structural member. A very simple approach to do so is the bilinear approach presented in [7]. With this approach, the response is described by two characteristic points only. The first point is the so-called nominal yield point, which is a fictitious point inserted after the point at which the yield strains of the materials are first reached. The second point corresponds to the ultimate displacement value. To compute these values, the following equations are used:

$$F = \frac{M}{L_s} \tag{2.32a}$$

$$\Delta_y = \phi_y \left(L_s + L_{sp}\right)^2 / 3 \tag{2.32b}$$

$$\Delta_u = \Delta_y + \Delta_p = \Delta_y + \phi_p L_p L_s = \Delta_y + \left(\phi_u - \phi_y\right) L_p L_s \tag{2.32c}$$

where ϕ_y is the nominal yield curvature according to Equation (2.33) and ϕ_p is the plastic curvature. Using L_s as lever arm to calculate the deformation is strictly speaking only correct if the center of plastic rotation is at the member end. This holds if the plastic hinge length is twice the strain penetration length $L_p = 2L_{sp}$. However, it is deemed an acceptable approximation even if $L_p > 2L_{sp}$. Nevertheless, [7] note that predictions could in this case be improved by using the distance between the point of contraflexure and the center of the plastic hinge.

The nominal yield curvature is not obtained from section analysis, but computed as first yield curvature times the ratio of nominal to first yield moment. The nominal yield moment, on the contrary, is obtained from moment-curvature analysis. It corresponds to the lowest curvature at which either $\varepsilon_s = 0.015$ steel strain or $\varepsilon_c = 0.004$ concrete strain are reached. These strains are defined as serviceability limit strains, as they are assumed to correspond to residual crack widths of approximately 1 mm and the onset of spalling of concrete, respectively.

$$\phi_y = \frac{M_N}{M_y} \phi'_y \tag{2.33}$$

A frequently found variation of the above equations assumes that there is no influence of strain penetration at yield and the center of rotation is in the center of the plastic hinge. With these modifications, the flexural displacement is calculated as:

$$\Delta_u = \Delta_y + \Delta_p = \frac{\phi_y L_s^2}{3} + \left(\phi_u - \phi_y\right) L_p (L_s - 0.5 L_p) \tag{2.34}$$

Several similar suggestions to calculate the drift at yield and ultimate have been made by Fardis and his co-workers in [22, 23, 31, 6] and [38]. In general, the equations proposed therein have been slightly changed over the years by fitting them to a more extensive experimental database. Different recommendations were made for varying cross sections and loading conditions, i.e. monotonic or cyclic loading. Originally, all equations were presented in a form that yields the rotation, but to be consistent with the previously presented

equations they are multiplied with the shear span herein. As mentioned, the formulations depend on the cross section shape. For brevity, only the ones recommended for wall-type or hollow rectangular bridge piers [31] are noted here. They include, contrary to the previous equations, a shear component and a factor accounting for a potential deformation increase due to inclined shear cracking. Based on the database used in [31] criteria for the application of the equations have been set. They include boundaries for the normal force ratio $n = P/(A_g f_c)$, aspect ratio and transverse reinforcement ratio. Those criteria are assumed to ensure that flexural yielding of the test units occurs before shear failure or yielding of the transverse reinforcement and are met by the tests reported in [1, 3].

At first yield of either concrete or steel, the displacement is assumed to be composed of flexural Δ_{fl} and shear displacement Δ_s as well as displacement due to anchorage slip Δ_{sp}:

$$\begin{aligned} \Delta'_y &= \Delta_{fl} + \Delta_s + \Delta_{sp} \\ \Delta'_y &= \phi'_y \frac{L_s + k_v z}{3} L_s + 0.0013 L_s + k_{sl} L_s \frac{\phi'_y d_{bl} f_y}{8\sqrt{f_c}} \end{aligned} \tag{2.35}$$

In [31] it is recommended to multiply the theoretical yield curvature ϕ'_y by 1.02 as this was the median of the predicted to experimentally determined moment M_{pred}/M_{Exp}. However, the moments were calculated assuming bilinear constitutive laws for concrete and steel. If shear cracking occurs before flexural yielding, the factor k_v is set to 1 to account for an increased top displacement due to tension shift. Shear cracking is assumed to occur before flexural yielding if $V_{cr} < M_y/L_s$, where V_{cr} is the shear resistance of a member without transverse reinforcement according to Equation (2.55b) from [11].

The second component in Equation (2.35) represents the shear deformation and is a purely empirical component obtained from data fitting. In [22], where this term was presented in a slightly different form, the authors state that the component corresponds to the difference between the measured total top displacement and the calculated flexural top displacement. This difference was determined for members where bar pullout was physically impossible, for instance because the plastic hinge was at the center of a simply supported beam.

The third component is the rotation caused by pulling the reinforcement bars out of the foundation. When pullout is not possible, $k_{sl} = 0$, otherwise $k_{sl} = 1$. Since a constant bond stress of $\tau_b = \sqrt{f_c}$ is assumed in the elastic range, the third component can be derived from Equations (2.15c), (2.16b) and (2.22).

The authors also recommend using the rotation $\theta_y = \Delta'_y/L_s$ instead of ϕ'_y to calculate the effective flexural stiffness at yield, $EI_{eff} = M_y L_s/(3\theta_y)$, whereas in [23] a more complex equation is presented for EI_{eff}.

The ultimate displacement is calculated according to the following formulation [6]:

$$\Delta_u = \Delta'_y + k_{sl} \Delta\theta_{u,slip} L_s + \left(\phi_u - \phi'_y\right) L_p \left(1 - \frac{L_p}{2L_s}\right) L_s \tag{2.36}$$

The rotation due to bar slip that has to be added to the yield rotation is estimated as:

$$\Delta\theta_{u,slip,mon} = \frac{\phi'_y + \phi_u}{2} 16 d_{bl} \tag{2.37a}$$

$$\Delta\theta_{u,slip,cyc} = \frac{\phi'_y + \phi_u}{2} 10 d_{bl} \tag{2.37b}$$

These formulations were determined from data fitting. It is noteworthy that neither shear nor additional deformations due to inclined cracking, which have been explicitly included in Equation (2.35), are included in Equation (2.36). This means that these deformation components are either, contrarily to what one might expect, not assumed to increase after yield or they are accounted for in the choice of the plastic hinge length. The authors themselves state that they were not satisfied with the scatter of the results obtained with this equation together with the plastic hinge length according to Equation (2.6). Therefore, they developed alternative empirical models. Those empirical formulations are the basis of the equations included in [24], which are presented in Section 2.5.3. However, the agreement of predictions and experiments does not differ significantly according to the table provided in [6]. The median predictions are generally good, but the scatter is considerable in all cases with coefficients of variation between 30% and 50%.

2.5.2 Refined approach according to Priestley et al.

A “refined” approach for the prediction of the entire load deformation relationship is proposed by [7]. According to the authors, this might be used for comparison with experimental results. In this approach, the strain penetration is only considered after flexural cracking Δ_{cr} and the deformation Δ after first yield Δ'_y is calculated from the difference in current and first yield curvature. Between cracking and first yield displacement, the deformation is simply interpolated linearly.

$$\Delta_{cr} = \phi_{cr} L_s^2/3 \qquad \phi = \phi_{cr} \tag{2.38a}$$

$$\Delta'_y = \phi'_y \left(L_s + L_{sp}\right)^2/3 \qquad \phi = \phi'_y \tag{2.38b}$$

$$\Delta = \Delta'_y \frac{M}{M_y} + \left(\phi - \phi'_y \frac{M}{M_y}\right) L_p L_s \qquad \phi > \phi'_y \tag{2.38c}$$

2.5.3 Drift according to Eurocode

Annex A of [24] includes several equations to calculate yield and ultimate deformations of structural components for seismic assessment. The yield deformation of rectangular, barbelled or T-shaped walls can be estimated according to the following equation:

$$\theta'_y = \phi'_y \frac{L_s + k_v z}{3} + 0.002\left(1 - 0.135\frac{L_s}{h}\right) + \frac{\varepsilon_y d_{bl} f_y}{(d-d')6\sqrt{f_c}} \tag{2.39}$$

where $d - d'$ is the distance between tension and compression reinforcement. To compute the ultimate drift the following equation is proposed:

$$\theta_u = k_d \frac{1}{\gamma_{el}} \frac{1}{1.6} 0.016 \cdot 0.3^n \left(\frac{\max(0.01;\omega')}{\max(0.01;\omega)} f_c\right)^{0.225} \left(\frac{L_s}{h}\right)^{0.35} 25^{k_{con}\varrho_v \frac{f_{yv}}{f_c}} 1.25^{100\varrho_d} \tag{2.40}$$

where $\omega' = \varrho_{comp} f_y/f_c$, $\omega = \varrho_{tens} f_y/f_c$ are the mechanical reinforcement ratios of the longitudinal reinforcement in compression and tension, $n = P/(A_g f_c)$ is the normal force

ratio, k_{con} is a factor accounting for the effectiveness of the confinement according to Equation (2.29) and ϱ_v, ϱ_d are the ratios of the transverse and diagonal reinforcement. γ_{el} is a safety factor set to 1.5 for "primary" and 1.0 for "secondary seismic elements" and factor $1/1.6$ is recommended to compute the drift of walls. Thus, for any other type of structure, drift values that are more than 60% larger are predicted with this equation. If no detailing for earthquake resistance is provided, factor k_d is $k_d = 0.825$ and otherwise $k_d = 1$. The formulation is based on work that was presented over several years in e.g. [22] and [6], where it was given in a slightly different form. In the latter, factor 0.016 was replaced by a longer formulation taking into account the steel type, loading and slip. The ultimate state from which the formulation was derived was defined to correspond to a 20% drop in the shear force capacity. Some noteworthy trends that are included in the formulation are an increased drift with i) decreasing normal force, ii) increasing compressive to tensile reinforcement ratio and iii) increasing slenderness. This equation is used to predict the "limit state of near collapse" according to Section 2.1 in [24]. It was statistically derived from a large database and can therefore also be compared to the drift capacity models presented in Section 4.2.2.

As an alternative to Equation (2.40), an equation to calculate the ultimate drift based on a plastic hinge approach is included in [24]. Together with the plastic hinge length according to Equation (2.7), the ultimate rotation may be calculated as:

$$\theta_u = \frac{1}{\gamma_{el}} \left(\theta'_y + (\phi_u - \phi'_y) L_p \left(1 - \frac{0.5 L_p}{L_s} \right) \right) \tag{2.41}$$

2.6 Shear response

2.6.1 Shear deformations based on axial strains

So far, only the flexural response of a RC structural member has been treated. But, especially for wall-type structures, shear deformations constitute a significant part of the total deformation and need to be considered. Based on the observation that the shear to flexural deformation ratio of flexure-dominated walls is roughly constant, a model to account for shear deformations in conjunction with plastic hinge modeling was presented in [8]. The constant ratio was observed for walls whose shear mechanism was not significantly degrading, such as capacity designed walls. Furthermore, the simplifying assumption that significant shear deformations only occur in the plastic hinge, where a constant curvature is assumed, was made. If, additionally, the strain state in this region is regarded as homogeneous, the shear strain γ can be expressed using relations from Mohr's circle:

$$\gamma = \frac{\varepsilon_l}{\tan\theta} + \varepsilon_v \tan\theta - \frac{2\varepsilon_2}{\sin(2\theta)} \tag{2.42}$$

where ε_l is the longitudinal strain along the centroidal axis of the wall, ε_v the transversal strain, θ the crack angle and ε_2 the principal compressive strain which is assumed to be the strain along the compression strut. It was concluded that the transversal and compressive strains were small in the examined cases and that the shear strains could hence be expressed as a function of the axial strains only. As γ is assumed constant along the length of the plastic hinge L_p and approximately zero outside it, the shear deformation can be estimated as:

$$\Delta_s \approx \gamma L_p = \frac{\varepsilon_l}{\tan\overline{\theta}} L_p \tag{2.43}$$

where $\overline{\theta}$ is an average angle of the crack pattern in the plastic region. If both elastic and inelastic flexural deformations are computed with a plastic hinge mechanism

$$\Delta_{fl} = \phi L_p L_s \tag{2.44}$$

the shear to flexural deformation ratio can be expressed as:

$$\frac{\Delta_s}{\Delta_{fl}} = 1.5 \frac{\varepsilon_l}{\phi \tan\theta} \frac{1}{L_s} \tag{2.45}$$

In this case, θ is the crack angle at the top of the fan-like crack pattern, where cracks start to be rather parallel and 1.5 is an empirically determined correction factor.

2.6.2 Shear deformations based on crack inclination

Based on the same observation of a constant ratio between shear and flexural deformations in the inelastic deformation range, an equation to include the shear deformations in the plastic hinge models is also suggested in [28]. The idea behind the model is that shear deformation stems from deformation in shear cracks. The elongation of the longitudinal reinforcement due to flexure causes a rotation at the crack and thus causes horizontal deformations, which is defined as shear deformation. Shear deformation is assumed to occur between the lowest crack, with an estimated crack angle of 60°, and the highest crack whose tip reaches the base, with an angle θ_{max}. Based on the examined test data, it was concluded that 35% of the flexural displacement stem from the deformation in between these two cracks and contribute to the shear deformations. Hence, the shear deformation was related to 35% of the flexural deformation, which is the reason why a factor of 0.35 is included in Equation (2.46). Because of the dependence on the crack angle, the Δ_s/Δ_{fl} relationship is partially geometrical, which is also evident in the included inverse aspect ratio h/L_s. Since it was found that this approach underestimated the shear deformation if little transverse reinforcement was provided or the web was thin, a correction factor α was introduced. With this, deformations are increased if the ratio of shear demand to diagonal tension capacity V/V_n or shear demand to web crushing capacity V/V_{wc} is high. V_n is assumed to be the total capacity according to the “revised UCSD model”, see Equation (4.1). Based on the considerations mentioned in this paragraph, the shear to flexural deformation ratio follows as:

$$\frac{\Delta_s}{\Delta_{fl}} = \alpha 0.35 \left(1.6 - 0.2\theta_{max}\right) \frac{h}{L_s} \tag{2.46a}$$

$$1 \leq \alpha = \left(\frac{V}{V_n} + \frac{V}{V_{wc}}\right) \leq 2 \tag{2.46b}$$

Shear deformations are assumed to occur in the region over which plasticity spreads L_{pr}. To predict this length L_{pr}, an equation derived from moment equilibrium along the crack was proposed, which can be rearranged to yield the crack angle:

$$\cot\theta_{max} = \frac{L_{pr}}{z} = \frac{1}{z}\sqrt{\frac{2(T-T_{yav})z}{(A_v f_{yv})/(s)+(f_{ct}b2d_{cr})/(1.4z)}} \tag{2.47a}$$

$$T_{yav} = 0.5\left(T'_y + T_y\right) \tag{2.47b}$$

where T is the tensile force resultant, T'_y is the tensile force resultant at first yield of the extreme steel fiber, T_y is the tensile force resultant when either a tensile steel strain of $\varepsilon_s = 0.015$ or a compression strain of $\varepsilon_c = 0.004$ first occur and d_{cr} is the lever arm between the tensile and compressive force resultant.

2.6.3 Shear deformations based on stiffness

[7] present an approach in which shear deformations are calculated for three different stages of the response: prior to shear cracking, prior to attainment of the nominal flexural strength and in the inelastic range. Before shear cracking, while the structural member is assumed to be elastic, it is suggested to estimate the shear deformations using the elastic shear stiffness together with the relation of cracked to uncracked flexural stiffness. Shear cracking is estimated using the concrete component of the “revised UCSD model” with $k_\mu = 0.29$, see Equation (4.1). The effective shear stiffness $K_{sh,eff}$ is computed as follows:

$$K_{sh,eff} = \frac{GA_{sh}}{L_s}\frac{EI_{eff}}{EI_g} \tag{2.48}$$

where $A_{sh} = 0.87A_g$ is the shear area and $G = 0.43E$ the shear modulus. The relation between the effective and uncracked flexural stiffness, EI_{eff} and EI_g, respectively, can be obtained from moment-curvature analysis. Using this stiffness, the shear displacement at shear cracking is:

$$\Delta_{sh,1} = \frac{V_c}{K_{sh,eff}} \tag{2.49}$$

Once the nominal flexural strength is reached, a unitary shear stiffness $K_{sh,cracked}$, based on a strut-and-tie model with a 45° compression strut is defined. This shear stiffness equates to:

$$K_{sh,cracked} = \frac{0.25\varrho_v}{0.25+(E_s/E_c)\varrho_v}E_s bd \tag{2.50}$$

where ϱ_v is the transverse reinforcement ratio, E_s and E_c are the modulus of elasticity of steel and concrete, respectively, and *b* and *d* the width and effective depth of the section. Using this stiffness, the shear deformation corresponding to the attainment of nominal flexural strength is:

$$\Delta_{sh,N} = \Delta_{sh,1} + \frac{(V_N - V_c)}{K_{sh,cracked}} L_s \tag{2.51}$$

Afterward, in the plastic deformation range, assuming a constant ratio of shear to flexural deformations $\Delta_{sh,N}/\Delta_{fl,N}$ is suggested.

2.6.4 Shear crack angles

To determine the crack angle θ that is needed to evaluate Equation (2.42), [8] recommend an equation given in [39]:

$$\theta = \arctan\left(\frac{z}{V}\left(f_{ct}b + \frac{A_{sv}f_{yv}}{s}\right)\right) < 90° \tag{2.52}$$

where *z* is the internal lever arm, *V* the shear force, f_{ct} the concrete tension strength and A_{sv}, f_{yv} and *s* are the transverse reinforcement area, yield strength and spacing. Originally, the equation was presented as shear strength equation for beams and θ denotes the angle between the longitudinal axis of the structural component and the crack.

Another possibility to calculate the crack angle for shear panels has been suggested in [40], based on a number of MCFT calculations:

$$\theta = (29° + 7000\varepsilon_l)\left(0.88 + \frac{s_{xe}}{2500}\right) \leq 75° \tag{2.53a}$$

$$s_{xe} = \frac{35 s_l}{a_g + 16} \tag{2.53b}$$

where ε_l is the unitless strain along the member axis at shear failure, s_l the horizontal distance between the longitudinal reinforcement bars and a_g the maximum aggregate size. The equation contains components accounting for the influence of the longitudinal strain (first term) as well as for a size effect (second term) and was developed for cases in which ε_l was below yield strain. Equally to Equation (2.52) this equation estimates the angle between longitudinal member axis and crack.

For fully cracked concrete membranes, subjected to plane stress conditions, the crack angle may also be derived based on the elastic energy [9]. Both concrete and steel are considered to be linear elastic in this case and Poisson's effect is neglected. It is furthermore assumed that the concrete is subjected only to compression stress and the tensile strength of the concrete is zero. The crack angle corresponds in this case to the angle of the principal compression stress, i.e. they are perpendicular to the principal tensile stress. The crack angle can then be derived from equilibrium equations and the minimization of elastic energy. If the membrane is subjected to stresses in the direction of both axes and shear, the crack angle will depend on the applied stresses. If the membrane is subjected to only shear, the equation for the crack angle relative to the *x*-axis simplifies to [9]:

$$\tan\theta = \sqrt[4]{\frac{\varrho_y + k_E \varrho_x \varrho_y}{\varrho_x + k_E \varrho_x \varrho_y}} \tag{2.54}$$

where k_E is the ratio of the modulus of elasticity of steel and concrete $k_E = E_S/E_c$ and ϱ_x and ϱ_y are the geometrical reinforcement contents in *x* and *y* direction, respectively. The crack angles obtained with this relatively simple equation correspond well to the maximum crack angles predicted with the software Membrane-2000 [41], which is based on the MCFT. For this study, equations to predict a representative crack angle of a cantilever wall subjected to lateral load are necessary and using an equation that is valid for a membrane subjected to pure shear might seem approximate. However, within the wall the stress state varies along the height of the wall as well as along the width of the section and it is thus difficult to define a membrane with a representative stress state. As this would furthermore complicate the determination of the crack angle significantly, only the equation for pure shear, i.e. Equation (2.54), is considered here.

2.6.5 Shear cracking

As indicated in previous sections, shear deformations are sometimes estimated to increase once shear cracking occurs, see for instance Equations (2.35) and Section 2.6.3. For the former, it is suggested to assume shear cracking initiates once the shear resistance of a member without shear reinforcement according to [11] is exceeded. With the recommended standard values this yields:

$$V_c = \left[k \left(1 + \sqrt{\frac{0.2}{d}} \right) f_c^{1/3} + 0.15 \frac{P}{A_g} \right] bd \tag{2.55a}$$

$$k = \frac{180}{\gamma_c} \left(100 \varrho_l \right)^{1/3} \geq 35 \sqrt{1 + \sqrt{\frac{0.2}{d}}} f_c^{1/6} \tag{2.55b}$$

where *b* and *d* are the section width and the effective flexural depth in m and γ_c is a safety factor for concrete which is assumed to be one for comparison with experimental data. The upper bound for the size effect factor is $\sqrt{0.2/d} \leq 2.0$. Since a crack angle of 45° is assumed for the formulation one may conclude that V_c corresponds to the force at which the first cracks steeper than 45° are expected to form. Based on results of MCFT analyses [42] performed regression analysis and proposed a formulation depending on the vertical load *P* and the shear stiffness of the uncracked structure *GA*. With units MN and m, it follows as:

$$V_{cr} = \left(\frac{P}{8757} + \frac{1}{6351} \right) \frac{GA}{L_s} \tag{2.56}$$

2.7 Influence of lap-splices

2.7.1 Behavior of lap-splices under cyclic loading

Several experimental studies have been conducted to investigate the behavior of lap-splices under cyclic inelastic loading. An overview of selected studies including their main findings is presented in [43]. In the following, a few studies and findings which provide insights into the behavior of splices in general and are of interest for this project are summarized.

The influence of load history, transverse and longitudinal reinforcement as well as lap-splice length was investigated in uniaxial monotonic and reversed cyclic tests by [44]. A test setup with square columns with concrete blocks at both ends, through which the loading was applied, was used in this study. The cyclic load history comprised six fully reversed cycles between $1.0f_y$ and $1.25f_y$ in tension and approximately $0.31 - 0.42f_c$ in compression before the test unit was loaded to failure in tension. Transverse reinforcement was found to have more influence on the deformation capacity than on the strength of the relatively long splices ($44 - 60d_{bl}$) tested in this study. All splices were sufficiently strong to transfer the yield load, but the splices with less transverse reinforcement failed at a smaller displacement and under lower ultimate load than those with larger transverse reinforcement ratios. Several other researchers also found that the behavior of lap-splices subjected to reversed inelastic cyclic loading is significantly improved in terms of attained ductility or number of cycles prior to failure, if sufficient transverse reinforcement is provided (e.g. [45, 46, 47]). However, in another experimental study on beams with lap splices, the effectiveness of the transverse reinforcement was found to depend also on the relative rib area of the longitudinal bars and the strength of the aggregate used in the concrete [48]. Inconsistent observations have been made regarding the optimum distribution of the confining reinforcement: concentrated at the ends of the splice or evenly distributed [43]. With regards to the length, some researchers argue that a mere increase of lap-splice length is no useful measure to improve the earthquake resistance of splices, due to an “unzipping” effect of the splitting failure [49]. Others, on the contrary, include the length of the splice as factor for the strain criteria, based on experimental data [6].

Comparison between the monotonically and cyclically loaded tests [44] showed that the load history applied in this study, with six fully reversed cycles, did not have a significant effect on strength or deformation capacity of the test units. However, load histories with more cycles proved more detrimental than static or repeated loading in terms of sustained deformation ductility elsewhere [46, 47]. In the latter studies it was also found that the number of sustained cycles is very sensitive to the peak load applied in the cycles.

2.7.2 Modeling approach

A lap-splice at the base of a pier may result in a reduced flexural strength of the section if the splice length is insufficient. However, even if the length is sufficient to transfer the load under monotonic loading, the strength may still be reduced in the inelastic deformation range under cyclic loading. Initially, the concrete surrounding a splice transfers the load from one reinforcement bar to another. If the splice is not well confined it will thus loose its load bearing capacity once the splitting cracks forming around the bars (compare Fig. 2.3b) are too wide to transfer stresses. If, on the contrary, sufficient confinement is provided, some force may still be transferred when the concrete is cracked.

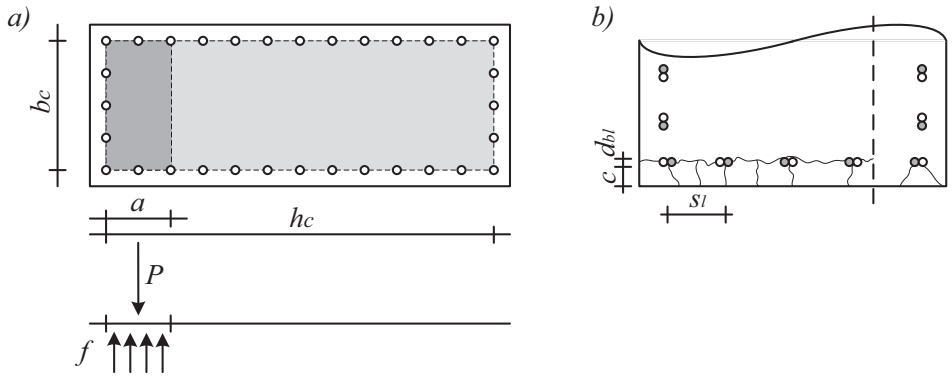

Figure 2.3: *Residual moment of a section according to [50] to the left and lap-splices with splitting cracks to the right.*

The influence of lap-splices on the behavior of a pier can be modeled by reducing the flexural strength of a section once the strain that triggers degradation of the lap-splice has been reached, as suggested in [50]. The procedure presented therein consists of three steps. First, the load bearing capacity of the splice is checked based on the tensile strength of the concrete or the confining reinforcement of the splice. Second, if the flexural strength of the section is not reduced due to a weak splice, it is assumed to degrade under cyclic loading once the compression strain causing microcracking of the concrete has been reached. It is argued that, when these cracks develop, the tension strength of the concrete and thus the capacity of the splice is reduced. In a third step, the residual moment capacity M_r is calculated from the maximum eccentricity of the normal force within the core concrete, see Fig. 2.3a. The normal force is assumed to result in a stress block with width b_c and length $a = P/(0.85 f_c b_c)$. With this assumption, the residual moment follows to be:

$$M_r = P\frac{h_c - a}{2} \tag{2.57}$$

Based on experimental results of circular and rectangular bridge piers, the authors suggested to assume that the residual capacity is reached at curvature ductility $\mu_\phi \approx 8$ or at $\mu_\phi = 8$ plus the curvature ductility at which degradation starts: $\mu_\phi = \mu_{\phi,deg} + 8$, respectively. In the following sections, some possible definitions of limit strengths and strains are summarized. The aim is to provide a concise overview over different modeling approaches rather than a complete survey of existing models. Therefore, the overview focuses on recent developments and models for cyclic loading. Generally, the strength limits may for instance be used in a section analysis to limit the tensile strength of the reinforcement to the tensile strength of the lap-splice. The strain limits may equally be used in the section analysis to limit the maximum tension or compression strain, whichever applies. Hence, the moment or curvature capacity of a section may be limited due to the lap-splice.

2.7.3 Strength of lap-splices

The transfer of forces in a lap-splice is often described with two mechanisms: The bond mechanism transferring the force from one bar to the surrounding concrete and a truss mechanism transferring the load from one reinforcement bar to another through concrete and confining reinforcement. The concrete may in this case act as both strut (compression

strength) and tie (tensile strength) while the transverse reinforcement provides a tie. The bond and truss mechanism interact in a real structure, but models assume that one or the other controls the strength of the lap-splice. The strength of the lap-splice is therefore either expressed in terms of the bond strength between reinforcement and concrete or in terms of the tensile strength of concrete. In the first case, the force capacity of a lap-splice is assumed equal to that of an embedded bar with the same length. In the second case, the maximum tensile force of a splice is assumed to be the force which is necessary to form a splitting crack around the splice.

In [50] the resistance of the splice is estimated with the second approach. The maximum possible force of a reinforcement bar T_b is thus expressed in terms of the concrete tensile strength f_{ct} as follows:

$$T_b = A_b f_s = f_{ct} p l_s \tag{2.58a}$$

$$p = 0.5 s_l + 2\,(d_{bl} + c) \leq 2\sqrt{2}\,(c + d_{bl}) \tag{2.58b}$$

where l_s is the length of the lap-splice, s_l the spacing of the longitudinal bars measured between the center lines, d_{bl} the diameter of the longitudinal reinforcement bars and *c* the clear concrete cover of the longitudinal bars, see Figure 2.3b. The limit in the second equation accounts for the possibility that two cracks with a 45° angle could form at a splice instead of the cracks in between the splices and perpendicular to the surface, as indicated in Figure 2.3b. Furthermore, [50] advised that the lap-splice should have sufficient confinement in case the tensile strength of the concrete is lower than expected. To calculate the required confinement, a coefficient of friction of 1.4 is recommended for the force transferred on the surface of the splitting crack and a limit strain of $\varepsilon = 0.0015$ for the stirrups to restrain crack opening. As the confinement is only active when the concrete is cracked, the authors suggest to not sum up the resistance provided by the two mechanisms.

A similar approach to determine the strength of a splice has been suggested by [51]. Also here, the strength is expressed in dependence of the concrete tensile strength. However, the model was not derived purely theoretically but validated against an experimental database containing 203 beams with unconfined splices and 278 beams with confined ones. Splice length varied between $\sim 10\,d_{bl}$ and $58\,d_{bl}$ with bar diameters between 9.5 mm and 57 mm. There are two main differences between this model and the preceding one: Splitting cracks are assumed to either form only in between the spliced bars over the width of the beam (“side splitting”) or only perpendicular to the beam surface (“face splitting”). The bond stress is assumed to vary along the splice and the radial tensile stresses around the bars are assumed to decrease with increasing distance to the bar. To account for this variation of stresses, the forces are computed based on effective crack areas instead of total crack areas. Based on the available experimental data, the following geometrical relations for the effective concrete cover *c* and splice length l_s were derived:

$$c_{b,\mathit{eff}} = c_b \frac{0.77}{\sqrt{c_b/d_{bl}}} \leq c_b \tag{2.59a}$$

$$c_{so,\mathit{eff}} = c_{so} \frac{0.77}{\sqrt{c_{so}/d_{bl}}} \leq c_{so} \tag{2.59b}$$

$$c_{si,\mathit{eff}} = c_{si} \frac{0.77}{\sqrt{c_{si}/d_{bl}}} \leq c_{si} \tag{2.59c}$$

$$l_{s,\mathit{eff}} = l_s \frac{53.48}{\sqrt{l_s/d_{bl}}\sqrt[4]{f_c}} \leq l_s \tag{2.59d}$$

where c_b is the clear cover between the longitudinal reinforcement and the bottom face (corresponding to *c* in Fig. 2.3b), $c_{si} = s_l - 2d_{bl}$ the clear distance between longitudinal reinforcement bars and c_{so} the clear cover between a longitudinal reinforcement bar and the side face. With the effective crack areas, the splitting forces F_{sp} can be calculated:

$$F_{\mathit{sp,side}} = l_{s,\mathit{eff}} \left[2c_{so,\mathit{eff}} + (n_{bl} - 1)2c_{si,\mathit{eff}}\right] f_{ct} \tag{2.60a}$$

$$F_{\mathit{sp,face}} = l_{s,\mathit{eff}} \left[2c_{b,\mathit{eff}}(0.1\frac{c_{so}}{c_b} + 0.9) + 2c_{b,\mathit{eff}}(n_{bl} - 1)\left(0.1\frac{c_{si}}{c_b} + 0.9\right)\right] f_{ct} \tag{2.60b}$$

$$\text{with } \left(0.1\frac{c_s}{c_b} + 0.9\right) \geq 1.0$$

where n_{bl} is the number of lap-splices at the considered face of the member. The correction factor $0.1(c_s/c_b) + 0.9$ accounts for the observation that the crack inclination and thus the crack surface increased with an increasing concrete cover at the side. If transverse reinforcement is present in the splice area, an increase of the splice resistance due to the provided confinement is considered:

$$F_{\mathit{st,side}} = \sum A_{vb} f_{sv} = n_{st} n_{st,l} A_{vb} f_{sv} \tag{2.61a}$$

$$F_{\mathit{st,face}} = \sum A_{vb} f_{sv} = n_{st} n_{bl} A_{vb} f_{sv} \tag{2.61b}$$

where n_{st} is the number of stirrups crossing the splitting cracks, $n_{st,l}$ the number of stirrup legs, f_{sv} the stress in the stirrups and A_{vb} the cross sectional area of one transverse reinforcement bar. From the test data, the angle of the resultant, which is composed of the force along the longitudinal reinforcement bar and the splitting and transverse reinforcement forces perpendicular to it, was found to be $\beta = 20°$. With this angle, the maximum bar stress can be evaluated:

$$f_s = \frac{F_{sp} + F_{st}}{n_{bl} A_{sb} \tan\beta} \tag{2.62}$$

Note that in this model the resistance due to the tensile strength of concrete and due to confinement are summed up.

A formulation based on the bond strength is proposed by [31] to estimate the yield moment of a section with spliced reinforcement. Instead of using the yield strength of the reinforcement as limit, it is suggested to use the minimum value of yield and bond strength.

To estimate the bond strength a formulation now included in the fib model code [52] is recommended:

$$f_s = 54 \left(\frac{f_c}{25}\right)^{0.25} \left(\frac{25}{d_{bl}}\right)^{0.2} \left(\frac{l_s}{d_{bl}}\right)^{0.55} \left[\left(\frac{c_{min}}{d_{bl}}\right)^{0.33} \left(\frac{c_{max}}{c_{min}}\right)^{0.1} + k_m K_{tr}\right] \begin{cases} \leq \dfrac{k_b\sqrt{f_c}4l_s}{d_{bl}} \\ \leq f_y \end{cases} \tag{2.63}$$

where $c_{min} = \min(c_b, c_{so}, c_{si})$ and $c_{max} = \max(c_{so}, c_{si})$ are the minimum and maximum value of the concrete covers and distance between longitudinal bars, respectively: Confinement conditions are considered with factors k_m and K_{tr}. The former takes into account the effectiveness of the confinement and is 12 if a hook of at least 90° or comparable is provided. The latter is $K_{tr} = n_{st}A_{vb}/(nd_{bl}s) \leq 0.05$ where n_{st} is the number of stirrup legs crossing a splitting surface at one section, n_{bl} is the number of considered splices along a splitting crack, *s* is the stirrup spacing and A_{vb} is the cross sectional area of a stirrup. Factor k_b considers bond conditions and is 2.5 or 1.25 for good and poor bond conditions, respectively.

Another simplified expression has been proposed in [31] and adopted in EC8 Part 3 [24]:

$$f_s = \min \begin{cases} f_y \\ \dfrac{l_s}{l_{s,min}} f_y = \dfrac{\sqrt{f_c} l_s}{0.3 d_{bl} f_y} f_y \end{cases} \tag{2.64}$$

[31] recommend to use this equation only when properties of a member are within the range of those included in the database for derivation of the equation. Otherwise Equation (2.63) should be applied. With regard to the lap-splice, the piers investigated here (see Table 3.1) meet all criteria, the only difference is that the columns in the database were more slender with a minimum aspect ratio of 2.75. In EC8 Part 3 the use is only restricted to splices with deformed, straight bars.

2.7.4 Strain limits

As mentioned previously, the strength of a section with spliced bars might degrade once certain strains are exceeded in either tension or compression. Hence, the strain limit which defines the ultimate curvature of a section with a lap-splice should correspond to the strain at which splice failure initiates. [50] assumed this strain to be the concrete compression strain corresponding to peak stress, $\varepsilon_c = 0.002$, because at this strain microcracking of the concrete initiates. [50] suggest this strain limit regardless of any confinement.

A database of experiments with spliced reinforcement, mainly on columns and beams, was evaluated by [31, 6] to derive relations for yield and ultimate deformations. The latter was defined as corresponding to a 20% drop of lateral force. It is noteworthy that [6] observed in their database that members with long splice lengths had larger ultimate rotations than members with continuous reinforcement. Hence, they recommend to consider both bars of the splices in compression for the section analysis, which results in a higher flexural stiffness of the section and thus in larger curvature estimates and therefore partially evens out this underestimation. Furthermore, limiting stress and strain in the reinforcement according to the length of the splice was recommended. In combination with the plastic hinge length and deformation estimate according to Equations (2.6) and (2.36), respectively, the steel

strain at ultimate limit state should be limited to a fraction of the limit strain for continuous bars under cyclic loading $\varepsilon_{su,cyc}$ (Equation (2.30)):

$$\varepsilon_{su,s} = \left(1.2\frac{l_s}{l_{su,min}} - 0.2\right)\varepsilon_{su,cyc} \geq \frac{l_s}{l_{su,min}}\varepsilon_y \tag{2.65a}$$

$$l_{su,min} = \frac{d_{bl} f_y}{\left(1.05 + 14.5\left(1 - 0.5\frac{s}{h_{con}}\right)\left(1 - 0.5\frac{s}{b_{con}}\right)\frac{n_{res}}{n_{bl}}\frac{\varrho_v f_{yv}}{f_c}\right)\sqrt{f_c}} \tag{2.65b}$$

where n_{res}/n_{bl} is the ratio of the number of restrained splices n_{res}, which are placed in a stirrup corner or held by a cross tie, to the total number of splices n_{bl}, *s* is the center-line spacing of the stirrups and h_{con}, b_{con} are the dimensions of the confined core defined by the center of the stirrups. The minimum splice length increases with increasing transverse reinforcement spacing, decreasing transverse reinforcement content and decreasing bond strength, expressed in terms of $\sqrt{f_c}$. The transverse reinforcement ratio is inserted dimensionless and not as percent value. This expression for the length of splices has also been included in EC 8, Part 3 [24]. There it is suggested to double the reinforcement in compression in Equation (2.40) and multiply the resulting ultimate drift with $l_s/l_{su,min}$, if the latter is smaller than 1.0. [6] did not derive a concrete strain limit explicitly for members with lap-splices, hence it can be assumed that the limit according to Equation (2.28) was still valid based on the experimental results included in their database.

3 Application of plastic hinge models

3.1 Introduction

In the following sections, the plastic hinge models presented in Sections 2.2 through 2.7 are applied to test units VK1 - VK7 [1, 3]. As stated previously, modeling the behavior of a structural member using a plastic hinge approach is based on the observation that inelastic curvatures spread approximately linearly over a certain height and can therefore be substituted with a constant inelastic curvature over half that height. With this approach, the local curvature is linked with the global deformation, i.e. the top displacement, in a simple manner. While the assumption of a linear curvature profile roughly holds for the test units with continuous reinforcement, this is not the case if the reinforcement is spliced at the bottom. The application of the plastic hinge models to determine the force-deformation response of those test units rests therefore solely on the notion that even though local measures (e.g. curvatures) are considerably affected by the splice, global measures (e.g. top displacement) are similar before the splice fails.

In Section 3.3, the plastic hinge length is determined from the experiments according to the procedure outlined in Section 2.2.6 and compared to the predicted plastic hinge lengths according to Sections 2.2.2 through 2.2.5. Furthermore, the influence of some underlying assumptions on the experimentally determined plastic hinge length and differences between experiments and predictions are discussed. The influence of strain penetration on the experimental results is examined in Section 3.4. In Section 3.5 the material models and assumptions underlying the moment-curvature analysis are presented and the analytical relation is compared with measurements. In Section 3.6 the predicted and measured flexural responses are compared and evaluated; in Section 3.7 the same is done for the shear deformations. Section 3.8 briefly discusses the predicted and measured influence of lap splices on the flexural response. Finally, in Section 3.9, the predicted and measured total deformations are compared and evaluated.

3.2 Experimental data

To ease the understanding of the following sections, the seven tests that were conducted within the framework of the research project that this study was a part of are briefly introduced in this section. Some important characteristics, i.e. dimensions, longitudinal and transverse reinforcement ratios ϱ_l and ϱ_v, concrete strength f_c and lap splice characteristics, of the test units are listed in Table 3.1. In the graphs in the following sections, the data of each of these tests is always plotted with its specific marker to ease comparisons between the graphs.

Figure 3.1 shows the failure modes of the test units. Two test units (VK1 & VK3) failed in tensile shear combined with a severe damage of the compression zone at the tip of the shear crack. Test unit VK6, which was a variation of test unit VK3 with higher slenderness, failed in a flexural shear mode with significant shear cracking and a loss of the concrete in the compression zone. VK7, which had the largest transverse reinforcement ratio, failed

Table 3.1: *Characteristics of test units VK1 - VK7.*

Reference	Test unit	L_s/h [m]	Reinforcement	Lap splice	f_c [MPa]
[1]	VK1	3.3/1.5 = 2.2	ϱ_l = 0.82%, ϱ_v = 0.08%	no splice	39.0
	VK2	3.3/1.5 = 2.2	ϱ_l = 0.82%, ϱ_v = 0.08%	$43d_{bl}$	35.0
	VK3	3.3/1.5 = 2.2	ϱ_l = 1.23%, ϱ_v = 0.08%	no splice	34.0
[3]	VK4	3.3/1.5 = 2.2	ϱ_l = 1.23%, ϱ_v = 0.08%	$43d_{bl}$	34.6
	VK5	4.5/1.5 = 3.0	ϱ_l = 1.23%, ϱ_v = 0.08%	$43d_{bl}$	35.2
	VK6	4.5/1.5 = 3.0	ϱ_l = 1.23%, ϱ_v = 0.08%	no splice	44.4
	VK7	3.3/1.5 = 2.2	ϱ_l = 1.23%, ϱ_v = 0.22%	no splice	30.0

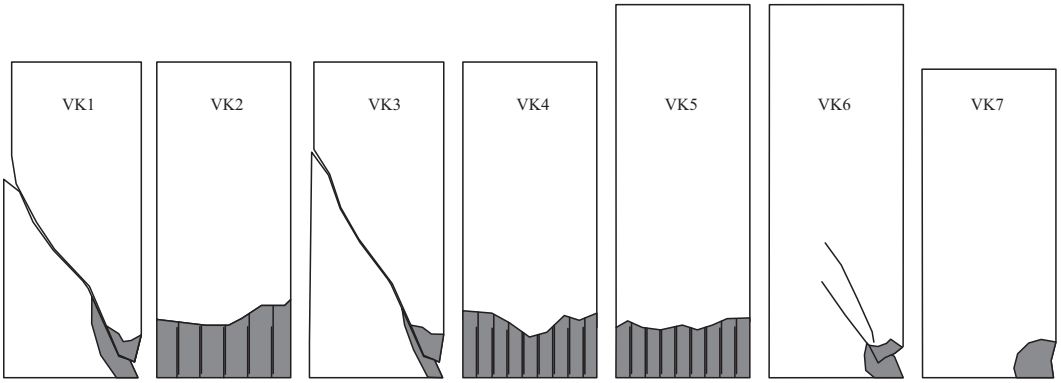

Figure 3.1: *Sketches of the seven test units [1, 3] which are used for model validation in this chapter after failure.*

due to crushing of the concrete in compression. All test units with spliced reinforcement exhibited a splice failure with spalling of the concrete surrounding the splice.

Figure 3.2a shows a photo of the test setup. The test units were rigidly connected to the strong floor by means of post-tensioned bars and rigid horizontal supports and the horizontal force and deformation at the top was applied with a servo-hydraulic actuator. Figure 3.2b shows a scheme of the instrumentation whose readings are used in this chapter. Each test unit was instrumented with a rectangular grid of either optical or Demec measurements on the surface. Furthermore, chains of LVDTs were provided along the sides of the wall over almost the entire height. The horizontal deformation Δ_{Top} was measured with LVDTs as well. For further information on the test setup, the testing procedure as well as a comprehensive summary of the test results, the reader is referred to the reports [1, 3].

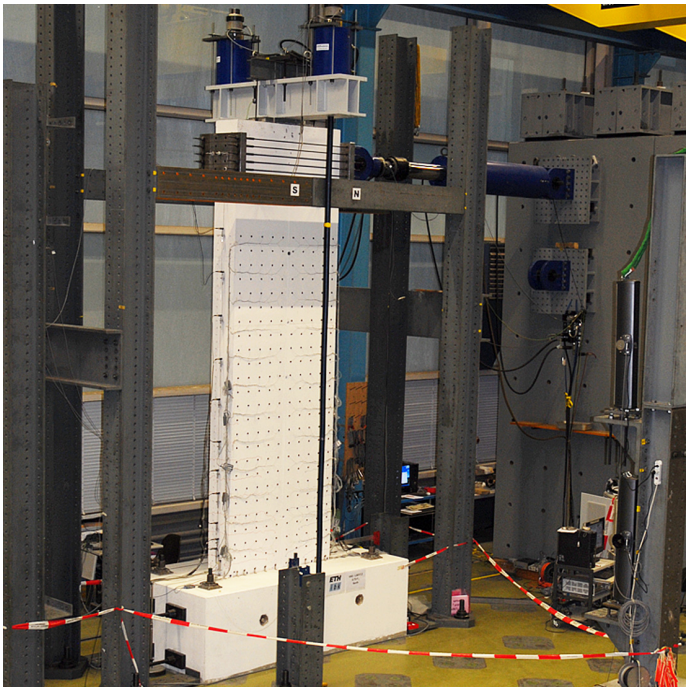

(a) Test setup

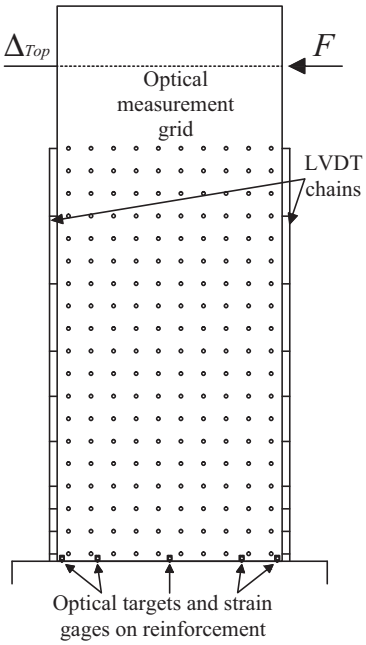

(b) Instrumentation

Figure 3.2: *Photo of the test setup and drawing of the instrumentation which is used in this chapter.*

3.3 Plastic hinge length

3.3.1 Experimental plastic hinge length

The experimental plastic hinge length L_p has been determined according to the procedure outlined in Section 2.2.6. To obtain the plastic base curvature ϕ_p, curvature profiles along the height of the test units have been calculated from the measurements of the LVDTs along the narrow faces of the piers, see Figure 3.3. In these graphs one can see that the profiles determined from positive and negative loading directions are not absolutely equal, partially due to a not exactly symmetric crack pattern. Furthermore, significant differences between test units with spliced (Fig. 3.3a) and continuous (Fig. 3.3b) reinforcement are visible. While the latter has a roughly linear curvature profile near the base once the crack pattern is fully developed, the former has not. Curvatures clearly concentrate below (at 0 mm height) and above the splice (at approximately 600 mm height), before the splice is damaged at LS μ_Δ= 3.0. At later load steps the curvature concentrates in a few cracks at the bottom. Thus, only test units with continuous reinforcement are considered for the experimental determination of the plastic hinge length in the following.

Following the suggestion in [20], the curvatures at positive and negative loading direction at first cycles were averaged and then approximated with a linear least-square error fit. The first four curvature measurements above the base crack were used for the linear fit in each case, because inelastic curvatures were commonly observed up to this value, see Figure 3.4. In these graphs one can also see that while averaging the curvatures may remove some of the effects of asymmetry, the effect of inclined cracking is still visible and a clear

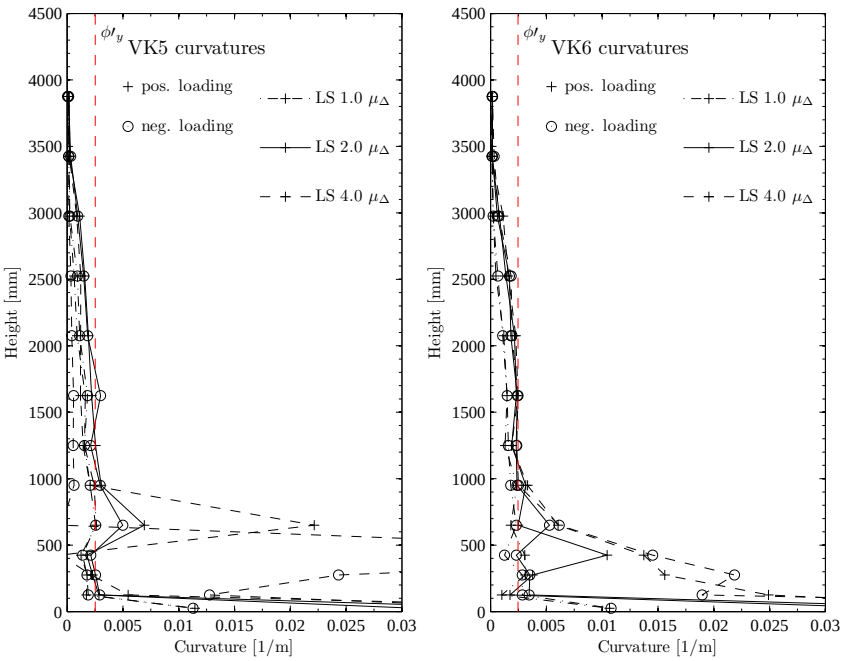

(a) Spliced reinforcement **(b)** Continuous reinforcement

Figure 3.3: *Curvature profiles of two test units calculated from LVDT measurements.*

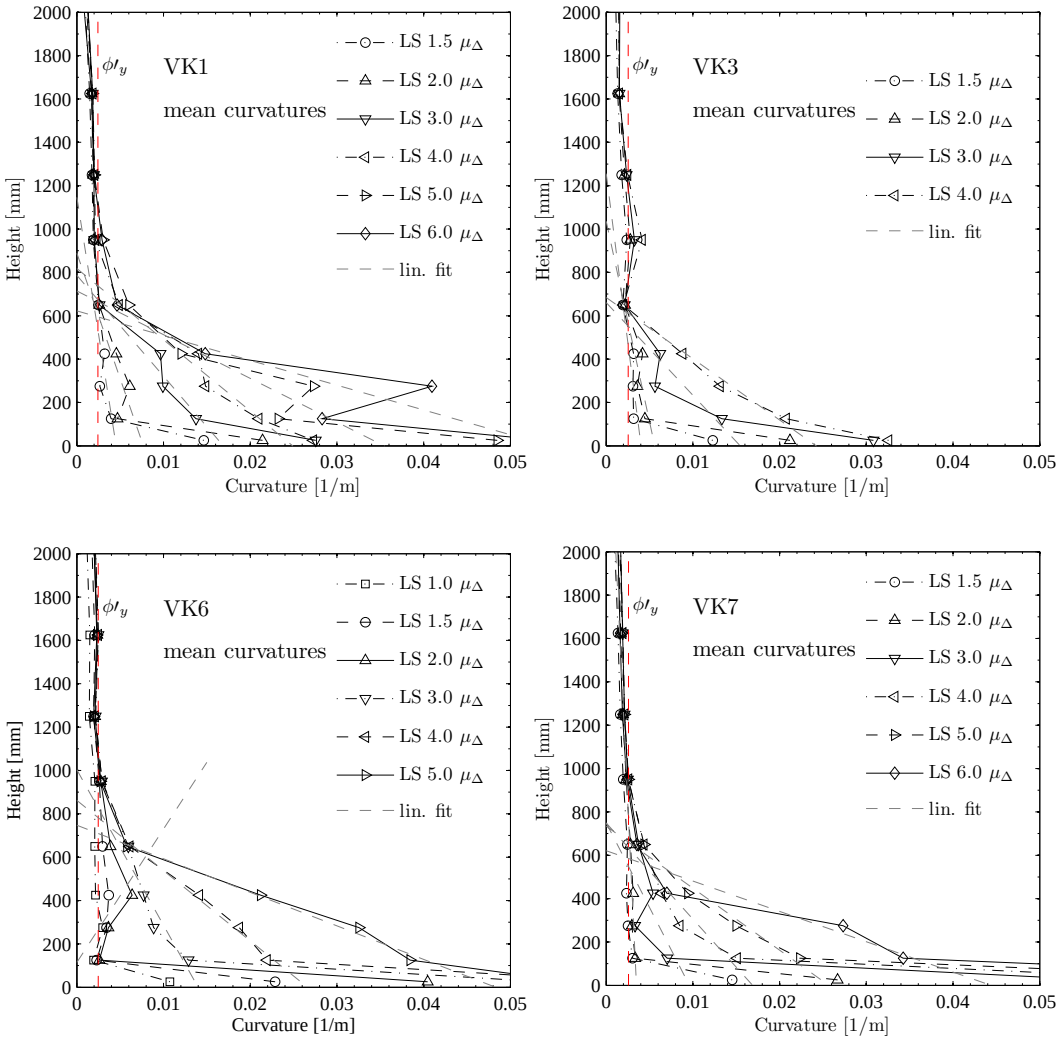

Figure 3.4: *Mean curvature profiles of test units with continuous reinforcement.*

linear trend was not always perceptible, especially before load steps $\mu_\Delta \sim 1.5 - 2.0$ were reached.

If the plastic hinge length corresponded to half the height over which inelastic curvatures develop, it could be determined from the intersections between the linear approximations and the first yield curvature. If the first yield curvature which is obtained from moment-curvature analysis is used in combination with this technique, lengths from approximately $L'_p = 230\,\text{mm}$ to $L'_p = 413\,\text{mm}$ are obtained, see Figure 3.5. These lengths do not include strain penetration effects and are plotted against the base curvature obtained by extrapolation of the linear fit of the inelastic curvature profile. As Figure 3.4 shows, extrapolated base curvatures that are smaller than $0.01\,\text{m}^{-1}$ mostly stem from curvature profiles for which the linear fit does not approximate the curvature very well, i.e. the crack pattern in these cases is not yet fully developed. These results should hence be taken with caution.

To employ the procedure suggested by [20] for the determination of the experimental plastic hinge length, the experimental plastic flexural deformation $\Delta_{p,fl}$ needs to be determined.

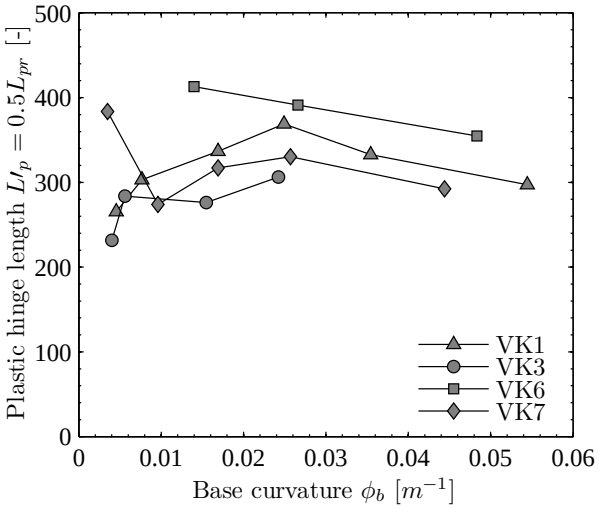

Figure 3.5: *Plastic hinge length that corresponds to half the spread of plasticity, which is determined from the linear approximation of the inelastic curvature and the intersection with the analytical first yield curvature.*

It was here not determined according to Equation (2.11), i.e. by subtracting the elastic flexural deformation as well as the shear deformation from the top displacement, but from the flexural displacements at each load step and at first yield, both computed by double integration of the experimentally determined curvature profiles:

$$\Delta_{p,fl} = \Delta_{fl} - \Delta'_{y,fl}\frac{M}{M'_y} \tag{3.1}$$

In this equation, the ratio of the moment to the first yield moment M/M'_y is a theoretical value whereas the displacements are determined from the experimental data. Subtracting the elastic curvature at the base of the pier $\phi'_{y,a}M/M'_y$ from the total base curvature ϕ_b yields an estimate of the experimental plastic base curvature ϕ_p according to Equation (2.13). In this equation $\phi'_{y,a}$ is an analytical value obtained from section analysis, see Section 3.5, and the total base curvature corresponds to the extrapolation of the linear curvature approximation to the base. With the so obtained plastic base curvature ϕ_p and the previously computed plastic flexural displacement $\Delta_{p,fl}$, the plastic hinge length L_p corresponding to these deformation was calculated according to Equation (2.12). Table 3.2, row one ($L_p(\Delta'_{y,exp})$), and Figure 3.6 summarize the results. In Figure 3.6b the plastic flexural drift $\Delta_{p,fl}/L_s$ was plotted against the plastic base curvature ϕ_p, to check if the trend is in fact linear, which it should be if L_p was a constant. Both graphs indicate a decreasing plastic hinge length with increasing deformation and exhibit some scatter in the predictions. The observation that plastic hinge lengths decrease with increasing ductility, if they are determined as outlined in this section, has also been made for other structural walls [53, 54]. However, Figure 3.6b also suggests that reasonable average deformations should be predicted when a constant length is used.

One needs to keep in mind that the plastic hinge lengths determined according to Equation (2.12) contain a strain penetration component, which can be calculated from the extrapolated and measured base curvatures, ϕ_b and $\phi_{measured}$, according to Equation (2.14). This equation is based on the assumption that L_{sp} is constant in the inelastic deformation range and rotation due to strain penetration is directly related to L_{sp} through the plastic

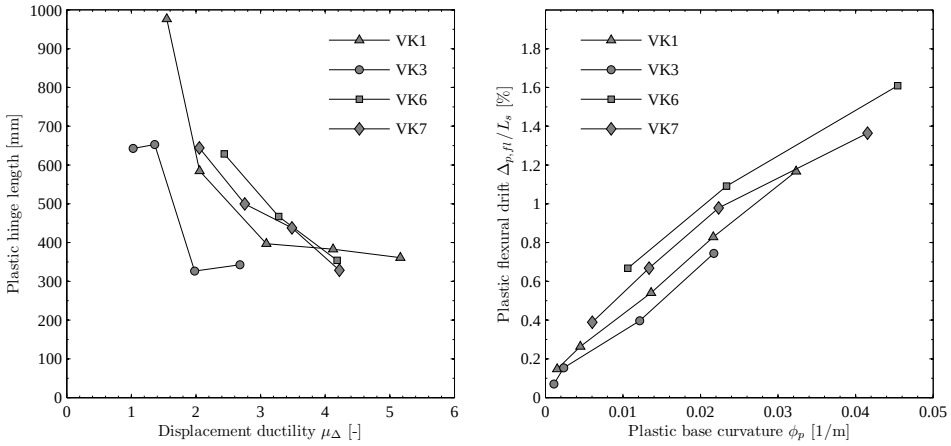

(a) L_p against displacement ductility

(b) Plastic flexural drift against plastic base curvature

Figure 3.6: *Experimentally determined plastic hinge lengths L_p (a) and plastic flexural drift (b).*

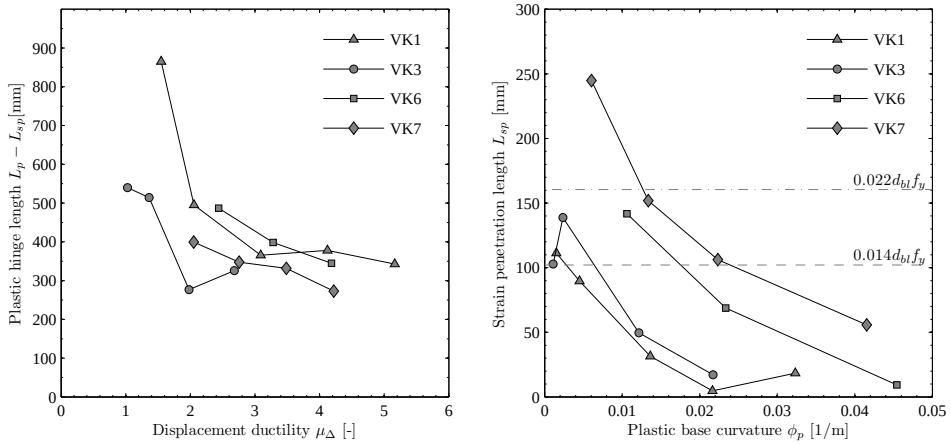

Figure 3.7: *Experimentally determined plastic hinge length without strain penetration component to the left and experimentally determined strain penetration length to the right.*

base curvature ϕ_p. In Figure 3.7a the plastic hinge length from which this strain penetration length has been subtracted is presented. Even though the factor between the upper and lower bound, framing most of the values, remains approximately two, the absolute difference slightly decreased. The graph containing the strain penetration lengths L_{sp} against plastic curvature ϕ_p in Figure 3.7b suggests that also for L_{sp}, if the rotation due to strain penetration is related to ϕ_p, decreasing lengths L_{sp} are necessary instead of constant ones. Predictions of L_{sp} according to Equations (2.5), i.e. with factor 0.014, and (2.3), i.e. with factor 0.022, have been included for comparison. The other approaches do not all include a strain penetration component in the plastic hinge length, but add a deformation component due to anchorage pullout to the top deformation instead.

3.3.2 Variations in experimentally determined plastic hinge lengths

a Previous assumptions and observed trends

As mentioned before, the trend of decreasing plastic hinge length with increasing ductility has been observed for structural walls before, but for circular bridge columns, the inverse trend has also be observed [55]. To find out why opposite trends were obtained, the assumptions underlying the determination of L_p were investigated, as shown in the following sections. In the previous section, the center of rotation was assumed to be at the base of the pier. Furthermore, the first yield flexural displacement as well as the total flexural displacement were calculated by integrating the curvature profiles obtained from the LVDT readings. To obtain the first yield flexural displacement, the LVDT readings taken when the theoretical first yield force according to moment-curvature analysis was reached were integrated. This means that all deformation values were measured ones and contained the influence of anchorage pullout. Anchorage pullout was not measured directly in the inelastic range in any test and could hence not simply be corrected for. When the plastic hinge length was determined, the averaged curvature profile from positive and negative loading direction was used for the linear fit and the extrapolation of the base curvature ϕ_b and the average flexural deformation of both excursions was taken as corresponding displacement. Theoretical values from the moment curvature analysis were used for both the first yield curvature and moment.

b Experimental and analytical first yield displacement

While the detailed experimental values are necessary references to evaluate the accuracy of a theoretical prediction or assumption, one also needs to bear in mind that in a prediction several assumptions are combined to obtain a result. Hence, an estimate that provides the best global results in combination with other assumptions is not necessarily the most accurate estimate of the actual local deformations. In the plastic hinge analysis, a hinge length estimate is combined with an analytically determined first yield displacement with the aim to obtain a good estimate of the total flexural deformation. Therefore, a possible influence of exchanging the experimental flexural deformation at the theoretical first yield load for the analytical first yield displacement ($\Delta'_{y,a} = \phi'_{y,a} L_s^2/3$) should be considered. Figure 3.7 shows the plastic hinge length that corresponds best to the actual flexural displacements when the procedure in Section 2.2.6 is followed, whereas Figure 3.8a shows the plastic hinge lengths that correspond best to the total flexural deformation if only analytical input values ($\phi'_{y,a}, \Delta'_{y,a}$) are used. The latter follow a more constant trend over the ductility range. At low ductility levels, the flexural deformations are small and an overestimation of the first yield displacement has a larger relative influence on the predicted plastic flexural displacements and thus the plastic hinge lengths derived from these.

A change in the trend of experimentally obtained plastic hinge lengths has not only been observed for VK1 to VK7, but also for the mostly capacity designed walls with slenderness $L_s/h = 2.26 - 2.28$ tested by Dazio [56], refer to Figure 3.8b. As mentioned above, decreasing plastic hinge lengths with increasing ductility are predicted for these walls as well when only experimental displacements are used (compare Fig. 15e in [53]). Using analytical first yield displacements instead even leads to a reversed trend for some walls. Especially for WSH5, which had a relatively high axial load ratio of $n = 0.13$ in combination with a low longitudinal reinforcement ratio of $\rho = 0.39$, the first yield displacement is grossly overestimated, which leads to short plastic hinge lengths. The first yield curvature was cal-

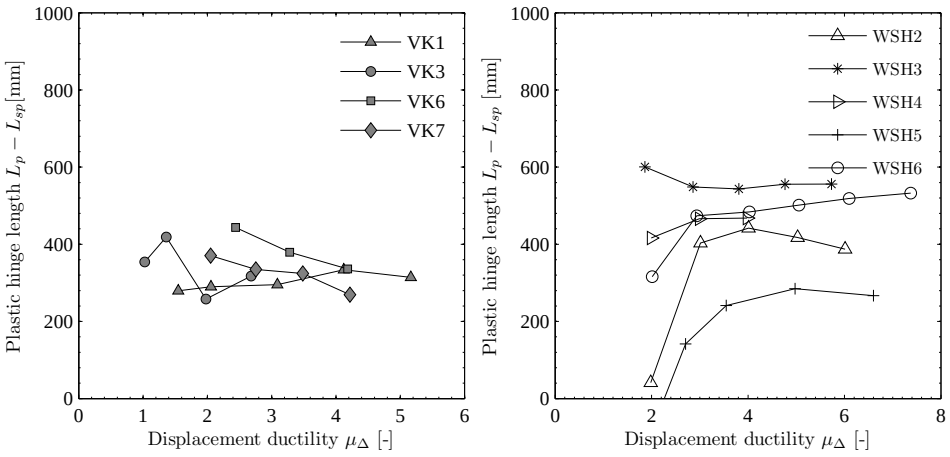

(a) Tests by [1, 3] **(b)** Tests by [56]

Figure 3.8: *Influence of using theoretical first yield displacement on experimentally determined plastic hinge lengths from which the strain penetration component according to Eq.* (2.14) *has been subtracted.*

culated according to Section 3.5 and the ductilities were calculated using the nominal yield displacements reported in [53].

As already indicated, the change in the trend is mainly due to the fact that the experimental first yield displacement is overestimated with the analytical expression, which has a larger relative influence at low ductility levels. For test units VK1 to VK7, the predicted displacements are 5-36% larger than the measured ones. One possible reason for this is the neglect of tension stiffening in the moment-curvature analysis, which results in an overestimation of the predicted first yield curvature. Another reason is the observed nonlinear curvature profile along the height of the test unit. Figure 3.9 shows averaged curvature profiles (VK3: curvature at LS F'_y South, as no data was available for F'_y North) at the load step at which the theoretical yield force was reached that were normalized with the corresponding analytical curvature $\phi'_{y,a}$. For comparison, the curvature profile that results from the moment-curvature analysis (M-ϕ) is included as well. As the dashed line in the figure indicates, the curvature along the height is overestimated with the assumption that it is decreasing linearly. The real curvature profile has a more concave shape, that means especially the curvatures in the central to upper part of the structure are smaller than assumed. Comparison with the analysis shows that this corresponds well to the results of the moment-curvature analysis, according to which the pier is at this stage still uncracked in the upper part. The photos taken of the test units also show that the piers are only partially cracked when the first yield load is reached. The linear curvature profile on the contrary would results if the pier had a uniform bending stiffness over the height, i.e. was either fully cracked or completely uncracked.

c Incorporation of strain penetration

As mentioned previously, slip of the reinforcement bar right above the foundation was not measured in the inelastic deformation range. Hence, no direct correction for the deformation component due to anchorage slip could be made. However, by linear extrapolation of the experimentally determined curvature profiles to the base of the pier one obtains an estimate of the base curvature without strain penetration influence. One possibility to correct

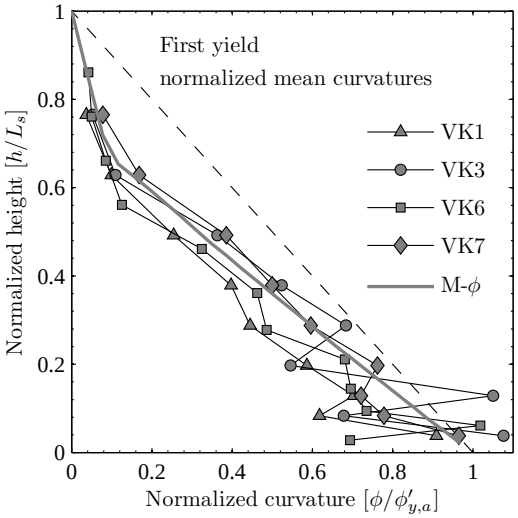

Figure 3.9: *Experimental and analytical curvature profiles normalized by the theoretical first yield curvature and L_s.*

for the influence of strain penetration is then to use this extrapolated curvature ϕ_b instead of the measured curvature $\phi_{measured}$ when integrating the curvature profile. By doing so, the top displacement $\Delta = \Delta_{fl,y} + \Delta_{fl,p}$ is obtained, whereas, so far, the top displacement $\Delta = \Delta_{fl,y} + \Delta_{fl,p} + \Delta_{sp}$ was computed and the strain penetration length subtracted from the plastic hinge length.

Figure 3.10a shows the plastic hinge lengths that result if the curvature profile which contains the extrapolated base curvature instead of the measured base curvature is integrated. Comparison with Figure 3.8a reveals that, again, changing the calculation procedure, has a pronounced influence at low ductility levels. Besides the correction for strain penetration, all calculations were performed as in the previous section. The differences between the results in this and the previous section can be explained by looking at the equations with which each quantity was determined and the formulation that results for L'_p if all equations are combined in one. In the previous approach, L_p was calculated from the top displacement $\Delta_{fl}+\Delta_{sp}$ and $L_{sp} = L_b(\phi_{measured}/\phi_b-1)$ was subtracted afterwards to obtain $L'_p = L_p-L_{sp}$. According to Equation (2.14), L_b is the actual base length of the measurement device. This means the final equation results as $L'_p = L_p - L_b\frac{\phi_{sp}}{\phi_b}$, where $\phi_{sp} = \phi_{measured} - \phi_b$.

If, on the contrary, the measured curvature at the base $\phi_{measured}$ is replaced with the extrapolated curvature ϕ_b before the integration of the curvature profile and the top displacement Δ_{fl} is determined, L'_p changes. In this case, the plastic hinge length finally follows to be $L'_p = L_p - L_b\frac{\phi_{sp}}{\phi_b-\phi'_y}(1-\frac{L_b}{2L_s})$. The term $(1-\frac{L_b}{2L_s})$ is approximately one and does hence not explain the difference between the obtained plastic hinge lengths. But comparison between the this equation and that of the previous section shows that while in this case the term $L_b\frac{\phi_{sp}}{\phi_b-\phi'_y}$ is subtracted from L_p, the term $L_b\frac{\phi_{sp}}{\phi_b}$ is subtracted from L_p in the previous case. Especially at small ductility levels, when ϕ_b might not be much larger than ϕ'_y (compare Figure 3.4), this changes results significantly. Hence, even though the strain penetration effect is corrected for based on the same curvature ϕ_b in both cases, the term that is subtracted from the plastic hinge length L_p varies.

d Location of the center of rotation in the plastic hinge

Another assumption with a potential influence on the experimental plastic hinge length estimate is the location of the center of rotation. As mentioned, this far the center of rotation was assumed to be at the base of the structures, which complies to Equations (2.32) and (2.38) for the flexural response. However, one can also assume that the center of rotation is located at the center of the plastic hinge. This assumption conforms to the solution obtained by integration of the idealized curvature profile shown in Figure 2.1, which is also employed in Equation (2.41). With this assumption, the plastic flexural displacement and the corresponding plastic hinge length $L'_p = L_p - L_{sp}$ are computed as follows:

$$\Delta_{p,fl} = \phi_p L'_p \left(L_s - \frac{L'_p}{2} \right) \tag{3.2a}$$

$$\rightarrow L'_p = L_s - \sqrt{L_s^2 - \frac{2\Delta_{p,fl}}{\phi_p}} \tag{3.2b}$$

Strictly speaking, this is only valid if the plastic hinge length and hence also the plastic flexural top displacement do not contain a component due to strain penetration. To obtain a flexural top displacement that reflects only the deformation in the pier itself, the measured base curvature has been substituted for the linearly extrapolated base curvature prior to the integration. This replacement of curvatures has already been done in the previous section. The analytical first yield flexural displacement and the experimental total flexural displacement have been used again. Figure 3.10b shows that, compared to Figure 3.10a, shifting the center of rotation to midheight of the plastic hinge leads to a further reduction of the plastic hinge lengths by about 5%. The reduction can easily be explained by examining the plastic top displacement and Equation (2.12). The plastic displacement is either calculated by multiplying the curvature with L_s or $L_s - 0.5L_p$, hence the ratio between the top displacements obtained with the different locations of the center of rotation is $(L_s - 0.5L_p)/L_s$. With a plastic hinge length of $L_p = 400$ mm ratios of $\sim 95\%$ and thus 5% difference between the top displacements are obtained for the four examined test units with continuous reinforcement. Therefore, if the top displacement is given and the plastic hinge length is derived from it, the difference in the obtained plastic hinge length must also be approximately 5%.

3.3.3 Summary and comparison of plastic hinge lengths

The equations presented in Section 2.2, have been used to predict the plastic hinge lengths of test units VK1-VK7. The material properties that are necessary for the determination of the plastic hinge length are provided in [1, 3] and repeated in Table 3.1. For the steel, yielding stresses of $f_y = 521$ MPa were used in all cases and ultimate steel stresses of $f_u = 630$ MPa (VK1-VK3) and $f_u = 609$ MPa (VK4-VK7), respectively. The bar diameter was always $d_{bl} = 14$ mm.

Table 3.2 summarizes the results for all test units. It shows the mean values and standard deviation of the plastic hinge lengths that were back-calculated from the peak flexural displacements of cycles with displacement ductilities $\mu_\Delta \geq 1.0$ according to the procedures in the preceding paragraphs. The equations that were used for the predictions are repeated below the table for convenience. Furthermore, it is indicated whether a component accounting for strain penetration is included in L_p or whether the value represents a net plastic hinge length without this component L'_p and where the center of rotation is assumed

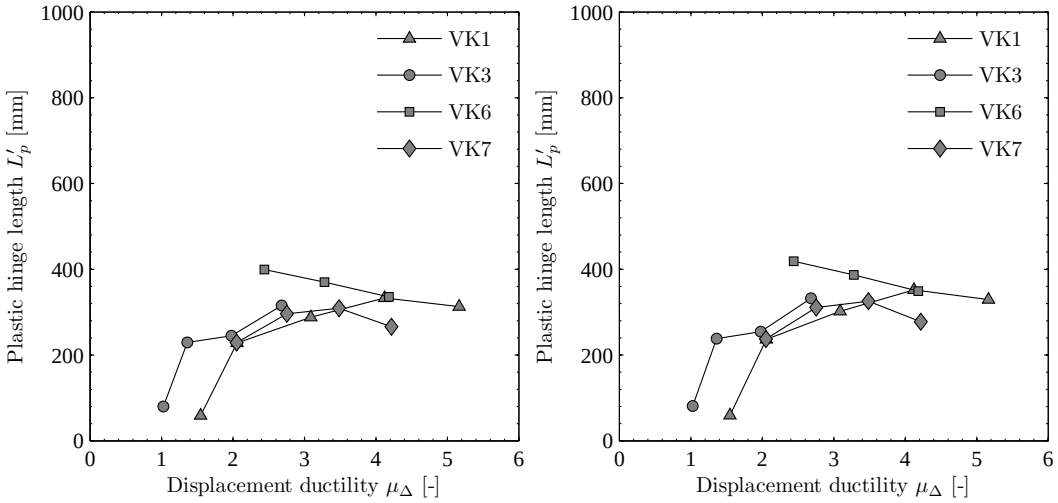

(a) Experimental plastic hinge lengths determined from curvature profiles corrected for strain penetration.

(b) Experimental plastic hinge lengths according to Eq. (3.2) with center of rotation at center of hinge.

Figure 3.10: *Influence of the method for the correction of strain penetration and of the assumed location of the center of rotation.*

to be located (at midheight of the plastic hinge or at its base). When the experimental first yield displacement $\Delta'_{y,exp}$ is exchanged for the analytical $\Delta'_{y,a}$, the strain penetration component is not affected, hence the plastic hinge length $L_p(\Delta'_{y,a})$ can be obtained by adding L_{sp} (row 2 of Table 3.2) to $L'_p(\Delta'_{y,a})$ (row 4 of Table 3.2). For comparison with the plastic hinge lengths calculated from the top displacement, the plastic hinge lengths determined from the spread of plasticity, shown in Figure 3.5, are included in row 6 of Table 3.2.

3.3.4 Discussion of plastic hinge lengths

Two main conclusions can be drawn from the experimental results shown in the previous section: The experimentally determined plastic hinge length is very sensitive to some of the assumptions made for backcalculating the length and it does not necessarily appear to be constant but rather dependent on ductility.

Regarding the sensitivity to certain assumptions, Section 3.3.2 has shown that especially the determination of the first yield displacement and the approach to correct for the influence of strain penetration influence the results. In the original approach, the first yield displacement was taken as the mean flexural displacement in positive and negative loading direction corresponding to the analytical first yield force. However, in plastic hinge modeling one obviously has to add the predicted plastic flexural deformation to an analytical estimate of the first yield displacement. Hence, the plastic hinge length was also backcalculated from plastic flexural deformations that were determined based on an analytical first yield deformation. This method yielded, in contrast to the original method, a more constant estimate of the plastic hinge length. This was mainly due to an overestimation of the first yield displacement which influences in particular the plastic hinge length at low displacement ductilities. Besides the first yield displacement, the method that was chosen to correct for the influence of strain penetration significantly influenced the results. As the rotation due to anchorage slip, which essentially corresponds to the rotation due to strain penetration, was

Table 3.2: *Summary of experimentally determined and predicted plastic hinge lengths L_p, strain penetration lengths L_{sp} and net plastic hinge lengths $L'_p = L_p - L_{sp}$. All lengths are given in mm as mean value with standard deviation.*

Test unit	VK1	VK2	VK3	VK4	VK5	VK6	VK7
Experimental							
L_p ($\Delta'_{y,exp}$)	540±260		491±181			483±138	478±132
L_{sp}	51±47		77±54			73±66	140±80
L'_p ($\Delta'_{y,exp}$)	489±218		414±132			410±72	338±52
L'_p ($\Delta'_{y,a}$)	303±22		337±67			386±54	325±42
L'_p ($\Delta'_{y,a}$,ϕ^*)	286±41		263±46			368±32	266±37
$L'_{p,mh}$ ($\Delta'_{y,a}$,ϕ^*)	300±45		275±50			385±35	278±40
$L'_p = 0.5L_{pr}$	317±36		275±31			386±29	319±42
Predicted							
Eq. (2.2) $= L_p$	599	599	599	572	612	612	572
Eq. (2.9) $= L'_p$	419	414	412	412	467	479	405
Eq. (2.6b) $= L'_{p,mh}$	520	520	520	520	600	600	520
Eq. (2.7) $= L_{p,mh}$	538	546	548	546	585	570	556
Eq. (2.10)$= L'_{p,mh}$	535	530	529	530	610	621	509

$\Delta'_{y,a}$ and $\Delta'_{y,exp}$ indicate whether the analytical or experimental first yield displacement has been used.

ϕ^* indicates that the measured base curvature has been replaced with the extrapolated base curvature prior to integrating the curvature profile and thus determining Δ_{fl}.

Index *mh* indicates that the center of rotation was assumed at the center of the hinge, whereas in all other cases it was assumed at the base of the hinge.

Eq. (2.2) [7] $L_p = kL_s + 0.2h + L_{sp}$

Eq. (2.9) [4] $L_p = (0.2h + 0.05L_s)\left(1 - 1.5\frac{P}{A_g f_c}\right) \leq 0.8h$

Eq. (2.6b) [6] $L_p = 0.2h\left(1 + \frac{1}{3}\min\left(9, \frac{L_s}{h}\right)\right)$

Eq. (2.7) [24] $L_p = \frac{L_s}{30} + 0.2h + 0.11\frac{d_{bl} f_y}{\sqrt{f_c}}$

Eq. (2.10) [27] $L_p = 0.27h\left(1 - \frac{P}{A_g f_c}\right)\left(1 - \frac{f_{yv}\varrho_v}{f_c}\right)\left(\frac{L_s}{h}\right)^{0.45}$

not measured directly during the experiments, the strain penetration had to be corrected for in an approximate manner. As outlined in Section c this does again influence primarily the plastic hinge lengths that are obtained for low ductility levels.

Due to the approximate correction for the strain penetration effect and because all predictions must be based on an analytical first yield displacement, it seems reasonable to use mainly $L_p(\Delta'_{y,a})$ and $L_{p,mh}(\Delta'_{y,a})$ for comparison with the predicted plastic hinge lengths. Regarding the estimate of the first yield displacement, one might of course argue that the prediction of Δ'_y needs to be improved instead of correcting for an overestimation of the displacement with an underestimation of the plastic hinge length at low ductilities. However, one needs to keep in mind that the two main causes for the error in the first yield displacement seem to be the nonlinear curvature profile and possibly the neglect of tension stiffening in the moment-curvature analysis. However, the curvature profiles of the different

test units are not uniform, as evident in Figure 3.9, and tension stiffening can only be incorporated in the moment-curvature analysis with certain approximations. Hence, accounting for these effects would complicate the determination of the first yield displacement, but not improve it significantly. For this reason, the experimental plastic hinge lengths that are based on the analytical estimate of the first yield displacement are used for comparison here. As Table 3.2 shows, the predictions generally overestimate the plastic hinge lengths. The prediction according to Equation (2.9) yields the estimate that is closest to the experimental ones. In the following sections, the plastic hinge lengths will be further evaluated based on the predictions of the displacements that are obtained with them.

3.4 Strain penetration influence

3.4.1 Experimentally determined strain penetration influence

As the first part of the examined test series showed that this issue needed to be investigated [1], the anchorage slip was directly measured with an optical system and targets that were glued to some reinforcement bars right above the foundation in the second part of the series (i.e. VK6 and VK7, [3]). To measure the strain of the same bars, these bars were also instrumented with strain gages. Figure 3.11a shows the experimental data for load steps that were reached prior to the attainment of the first yield load. For comparison, the predictions according to the approaches introduced in Section 2.3 are included in the graph as well. As evident from Figure 3.11a, the experimental data follows a clear trend and from extrapolation of the slip to the yield strain a slip value between those according to [31] and [33] would result. These two predictions are made only for the yield strain and were linearly connected to zero in the plot.

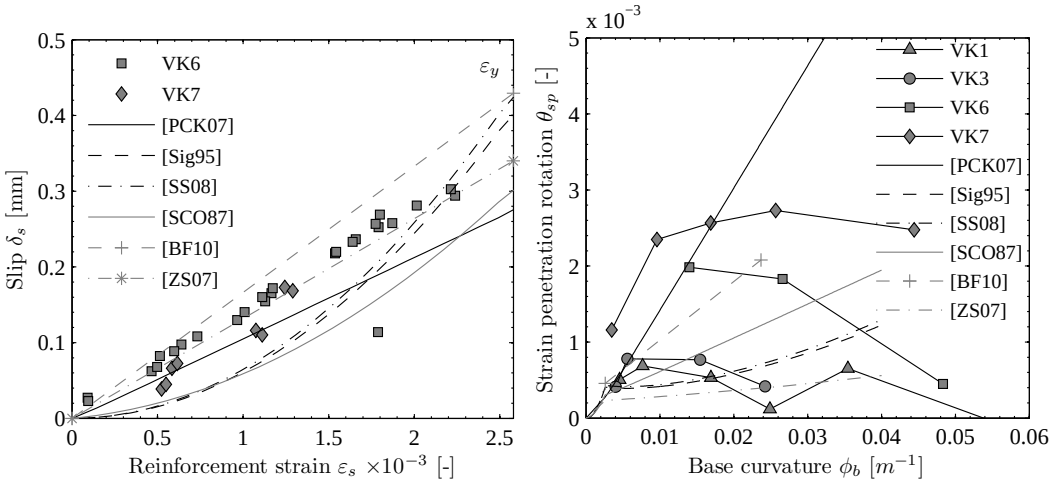

(a) Measured and predicted anchorage slip

(b) Experimentally determined and predicted rotation due to strain penetration

Figure 3.11: *Anchorage slip against strain measured during the experiment compared to predictions (a) and experimentally determined rotation due to strain penetration against extrapolated base curvature compared to predictions (b).*

With a slip of $\delta_s = 0.35$ mm at yield and the neutral axis location according to the respective moment-curvature analysis a rotation due to strain penetration θ_{sp} of $0.33 \cdot 10^{-3}$ and $0.35 \cdot 10^{-3}$ is predicted for VK6 and VK7, respectively. With this rotation top displacements of $\Delta_{sp} = 1.5$ mm (VK6) and $\Delta_{sp} = 1.2$ mm (VK7), corresponding to around 10% of the flexural deformation at first yield, are obtained.

When the load steps in the inelastic range were reached, the measurement targets had usually fallen off because the concrete started spalling and the strain gages were no longer working either [3]. Hence, the slip corresponding to the strain could no longer be experimentally determined. Therefore, another way of investigating the strain penetration effects and visualizing the data had to be chosen. Figure 3.11b shows the rotation due to strain penetration θ_{sp} against the extrapolated base curvature ϕ_b. The experimental base curvature was determined by linear extrapolation of the curvature profile as shown in Figure 3.4. The rotation due to strain penetration corresponds to the difference between the measured rotation and the rotation resulting from this extrapolated base curvature. Predicted rotations were obtained from the slip estimates determined with the various equations and the neutral axis location, strains and curvatures from the moment-curvature analysis of VK7. If the strain penetration length was constant, a linear prediction of the rotation due to strain penetration with gradient $L_{sp} = \theta_{sp}/\phi_b$ would result. This is the case for the prediction according to [7], whereas the remaining predictions as well as the experimental data in Figure 3.11b do not indicate such a linear relationship.

3.4.2 Discussion of strain penetration estimates

With regard to the estimate of the reinforcement slip in the elastic range, Figure 3.11a shows that the differences in the examined approaches are relatively small and all equations yield satisfying estimates. The best prediction of the slip is here obtained with Equation (2.19) [33], which exactly matches the strain-slip relationship that was obtained from the experimental data.

Concerning the slip and the corresponding rotation in the inelastic range, Figure 3.11b shows that it is difficult to draw conclusions from the available experimental data. As already obvious in Figure 3.7, assuming a constant strain penetration length seems to overestimate the strain penetration effect in the inelastic range. However, which approach is most suitable to determine the actual effect is hard to tell as the experimental data does not show a clear trend. This might be due to the way the experimental base curvature is determined. Linear extrapolation can be difficult, depending on how well the crack pattern is developed (see load step μ_Δ=2.0 of VK6 in Figure 3.4, for instance), and it is also questionable to which extend the linear approximation is usable. As evident in Figure 3.4 it is certainly a reasonable assumption, but Figure 3.9 indicates that the curvature profile is in fact slightly curved. This curved shape is also visible at load steps in the inelastic range. Even though this appears to be a minor variation in the curvature profile, the extrapolated base curvature and the results obtained with it could be notably affected due to the high gradient of the inelastic curvatures.

3.5 Moment curvature analysis

The results of moment-curvature (M-ϕ) analyses made with varying material models and softwares were compared with the experimentally obtained M-ϕ relationship. For the latter, the readings from the LVDTs just above the basecrack, measuring the elongation between 50-200 mm height, were used. Eventually, fiber based calculations made with MATLAB [57] were employed for all further calculations. The concrete was modeled according to the confined concrete model proposed by [5], see Figure 3.12b:

$$f_{cc} = f_c \left(-1.254 + 2.254 \sqrt{1 + \frac{7.94 f_l'}{f_c}} - 2 \frac{f_l'}{f_c} \right) \tag{3.3a}$$

$$\varepsilon_{cc} = \varepsilon_c \left(1 + 5 \left(\frac{f_{cc}}{f_c} - 1 \right) \right) \tag{3.3b}$$

where f_{cc} and ε_{cc} are the confined concrete strength and strain corresponding to peak stress, respectively. f_l' is the lateral confining pressure exerted by the stirrups and is calculated as $f_{l,x}' = k_{con} \varrho_x f_{yv}$ and $f_{l,y}' = k_{con} \varrho_y f_{yv}$ in each direction with the confinement effectiveness factor k_{con} according to Equation (2.29). This constitutive relationship for the concrete was chosen over the modified Popovics model [58, 59], because it provided better post-peak responses than the latter, with which the moment capacity degraded too fast. All concrete inside the centerline of the stirrups was assumed to be confined. For the unconfined cover concrete a spalling strain of $\varepsilon_c = 0.004$ was assumed. Since a linear degradation of stress between twice the strain at peak stress (here $\varepsilon_{c0} = 0.002$) and the spalling strain is recommended, the stress was assumed to drop to $f_c = 0$ at $\varepsilon_c = 0.004$, see Figure 3.12b. No tension stiffening is considered, because as stated by [31], the tension stiffening effect is degrading due to the deterioration of bond under cyclic loading and can therefore generally be neglected in cyclic analysis. The tensile strength of concrete was considered in the analysis in order to capture the first kink in the M-ϕ response that was also observed in the experiments.

A bilinear steel constitutive law with strain-hardening was chosen over the measured stress-strain relationship for the determination of the plastic hinge lengths as well as for the moment-curvature analysis because of the cyclic loading. Depending on the loading history, the envelope under cyclic loading might be very different from that under monotonic loading. Test data indicates that when steel is subjected to large load reversals the yield plateau disappears due to the Bauschinger effect and the ultimate stress might increase due to isotropic strain hardening. To account for these effects, [60] introduced a strain and stress shift in their cyclic steel model. Similar observations were made in [61, 62]. Even though the exact steel strain-history during the tests remains unknown, it is deemed reasonable to assume that the yield plateau disappears because the steel strains are expected to alternate between tensile and at least small compressive strains. A stress shift is not included since this is strongly dependent on the load history and reported to be small [60, 62]. One can note, however, that due to the rather small f_u/f_y ratio, the choice of the steel constitutive relationship has merely a moderate influence on the results.

All material properties not explicitly mentioned herein were taken from [1, 3]. A normal force of $P = 1350$ kN was considered in the M-ϕ analysis of all test units with aspect ratios of $L_s/h = 2.2$ and $P = 1365$ kN in the analysis of those with $L_s/h = 3.0$. The material models as well as the predicted and experimentally determined moment-curvature relationships are shown in Figure 3.12. The experimental moment-curvature relationships were obtained by

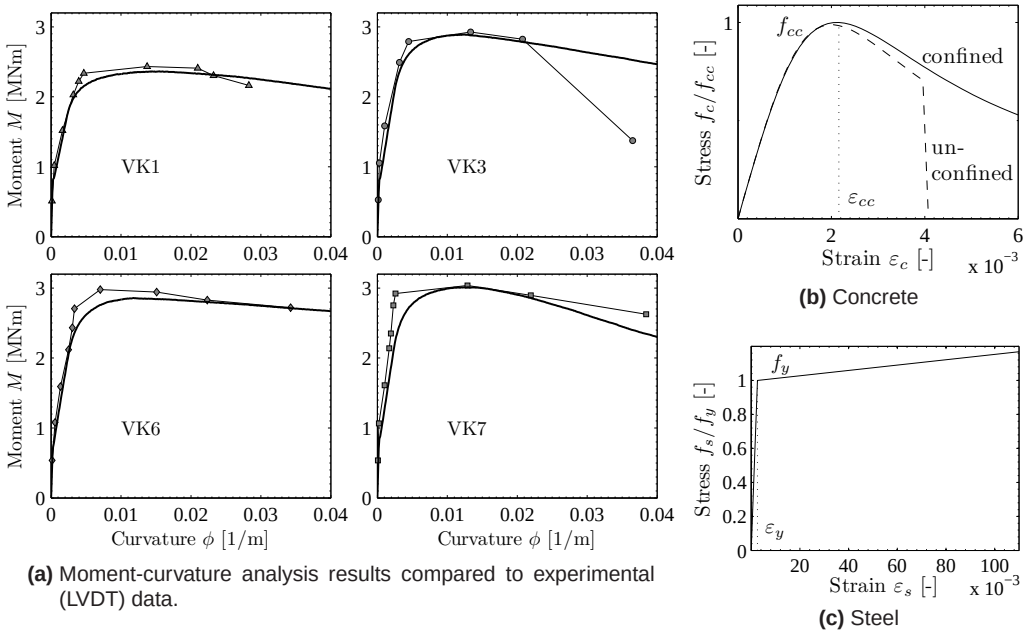

(a) Moment-curvature analysis results compared to experimental (LVDT) data.

(b) Concrete

(c) Steel

Figure 3.12: *Experimental and analytical moment-curvature relationships and constitutive relationships used for the analysis.*

averaging the readings of the LVDTs located 50-200 mm above the base in positive and negative loading direction. Only the data of the test units with continuous reinforcement is included here, as the experimental data of the test units with splice is influenced by the splice and hence not apt for comparison with the analysis.

As evident in the figure, the moment-curvature response is captured well with the predictions. The post peak response is predicted well until a strong degradation sets in for VK1 and VK3. This degradation was due to the onset of shear degradation in the experiment and thus due to a mechanism that cannot be captured with section analysis. The maximum moment of VK6 is slightly underestimated but the post-peak response is captured well, whereas the post-peak moment capacity of VK7 is slightly underestimated. Before the cracks developed in the instrumented section of the test unit, the stiffness is obviously underestimated by the analysis. However, despite these small deviations, one can conclude that the analyses predict the responses well and should thus provide a good basis for the plastic hinge modeling approach.

3.6 Flexural response

3.6.1 Summary of approaches

The flexural deformation of test units VK1-VK7 was modeled according to the approaches introduced in Chapter 2 using the plastic hinge length predictions provided in the bottom part of Table 3.2. Table 3.3 gives an overview over the employed approaches for determining the flexural displacement and the plastic hinge length used in relation with each of them. Note that Equations (2.39) and (2.35) are included here without the components that account for shear deformations, as only the flexural deformations are of interest at the mo-

Table 3.3: *Overview over approaches to determine the flexural displacement and related plastic hinge lengths. The last column shows the legend entry that is used for the corresponding approach in the following figures.*

Reference	Equations for flexural deformation and plastic hinge length.	Legend
[24]	Eq. (2.39): $\Delta'_y = \frac{\phi'_y (L_s + k_v z) L_s}{3} + \frac{\varepsilon_y d_{bl} f_y L_s}{(d-d') 6\sqrt{f_c}}$ Eq. (2.41): $\Delta_u = \left(\theta'_y + (\phi_u - \phi'_y) L_p \left(1 - \frac{L_p}{2L_s}\right)\right) L_s$ Eq. (2.7): $L_p = \frac{L_s}{30} + 0.2h + 0.11 \frac{d_{bl} f_y}{\sqrt{f_c}}$	EC8-3
[31] [6]	Eq. (2.35): $\Delta'_y = \phi'_y \frac{L_s + k_v z}{3} L_s + L_s \frac{\phi'_y d_{bl} f_y}{8\sqrt{f_c}}$ Eq. (2.36): $\Delta_u = \Delta'_y + \Delta_{u,slip} + \left(\phi_u - \phi'_y\right) L_p \left(1 - \frac{L_p}{2L_s}\right) L_s$ Eq. (2.6b): $L_p = 0.2h \left(1 + \frac{1}{3} \min\left(9, \frac{L_s}{h}\right)\right)$	[BF10]
[7]	Eq. (2.38): $\Delta'_y = \phi'_y \left(L_s + L_{sp}\right)^2 / 3$ $\Delta = \Delta'_y \frac{M}{M_y} + \left(\phi - \phi'_y \frac{M}{M_y}\right) L_p L_s$ Eq. (2.2): $L_p = 0.2(f_u/f_y - 1) L_s + 0.2h + L_{sp}$	[PCK07]
[7] [4]	Eq. (2.38): $\Delta'_y = \phi'_y L_s^2 / 3$ $\Delta = \Delta'_y \frac{M}{M_y} + \left(\phi - \phi'_y \frac{M}{M_y}\right) L_p L_s$ Eq. (2.9): $L_p = (0.2h + 0.05 L_s) \left(1 - 1.5 \frac{P}{A_g f_c}\right) \leq 0.8h$	[BA11]
[24]	Eq. (2.40): $\Delta_u = \frac{8.25}{1000} 0.3^n f_c^{0.225} \left(\frac{L_s}{h}\right)^{0.35} 25^{\frac{k_{con} \varrho_v f_{yv}}{f_c}} L_s$	EC8-3 Eq. (2.40)

ment. The component which accounts for an increase of deformation due to shear cracking was considered nevertheless, as it was interpreted as a tension shift component and not as shear deformation component. An approach using the plastic hinge length for capacity designed walls according to [27] is not included, but it should yield similar estimates as that labeled [BF10] as the plastic hinge lengths are similar (see Table 3.2). The last equation (EC8-3 Equation (2.40)) does not utilize the plastic hinge length and is repeated here without the terms that are not relevant for the investigated piers for ease of reading. That means the terms that equal one, i.e. the ratio of the mechanical reinforcement contents ω'/ω and the term accounting for diagonal reinforcement, are omitted here.

3.6.2 Limit strains and curvatures

The ultimate curvature can either be calculated according to Equation (2.31) or it can be defined by the strain limits according to Equations (2.26) to (2.30). Table 3.4 provides on overview over these strain limits and Table 3.5 summarizes the curvature limits that result from these strain limits as well as the directly calculated curvature limits.

To check whether the predictions agree well with the experiments on a global and a local level, the predicted and measured deformations corresponding to certain force and strain levels were compared. First, the predicted flexural deformation at first yield force was compared to the experimentally determined flexural deformation at first yield force. Figure 3.13a shows flexural drifts that were predicted at first yield force against the experimental drifts. In case of the first yield values, the mean flexural first yield displacement, determined from

Table 3.4: *Steel and concrete strain limits suggested for the use in plastic hinge analysis. Only one value is given if the strains vary only slightly due to different f_c.*

Test unit		VK1-VK3	VK4-VK6	VK7
Eq. (2.26)	$\varepsilon_{cu} = 0.004 + 1.4\frac{\varrho_v f_{yv} \varepsilon_{su}}{f_{cc}}$	$\sim 5.3‰$	$\sim 5.1‰$	$7.8‰$
Eq. (2.27)	$\varepsilon_{su} = 0.6\varepsilon_{su}$	$75.6‰$	$66.0‰$	$66.0‰$
Eq. (2.28)	$\varepsilon_{cu} = 0.0035 + \left(\frac{1}{x_{c,con}}\right)^{\frac{3}{2}} + \frac{0.4 k_{con} \varrho_v f_{yv}}{f_{cc}}$	$4.8‰$	$\sim 4.7‰$	$8.6‰$
Eq. (2.30)	$\varepsilon_{su} = \frac{3}{8}\varepsilon_{su} = 0.375\varepsilon_{su}$	$47.3‰$	$41.3‰$	$41.3‰$

Table 3.5: *Curvature limits suggested by [35] compared to the curvatures corresponding to the strain limits in Table 3.4.*

Test unit	VK1	VK2	VK3	VK4	VK5	VK6	VK7
Curvature m^{-1}	$\times 10^{-3}$	$\times 10^{-3}$	$\times 10^{-3}$	$\times 10^{-3}$	$\times 10^{-3}$	$\times 10^{-3}$	$\times 10^{-3}$
Eq. (2.31)	52.8	51.7	51.3	45.0	49.4	51.7	41.8
Eq. (2.26) & (2.27)	21.0	19.2	16.0	15.6	15.3	17.6	22.1
Eq. (2.28) & (2.30)	19.3	17.7	14.6	14.8	14.5	16.3	24.4

the first cycle in positive and negative loading direction, was used as experimental value. As the first yield displacement is defined by the corresponding lateral force, the displacements of all test units can be used for comparison. The shapes of the markers in Figure 3.13 correspond to the respective test unit and the colors indicate which approach for determining the flexural displacement has been used. The approaches to calculate the flexural deformations have been named as shown in Table 3.3.

Second, the flexural drift corresponding to the ultimate concrete strain ε_{cu} according to Equation (2.28) was compared. Only the experimental flexural displacement in positive loading direction was used for comparison. The strain was compared to the strain obtained from the second LVDT above the base, i.e. the one at 50-200 mm height. Only the positive loading direction was chosen because compressive strains in positive and negative loading direction showed considerable differences during the same cycle. As the positive loading corresponds to the first loading direction, the strain measured in this direction was deemed an appropriate comparison, because it might be slightly less influenced by previously applied tensile strains. Only test units with continuous reinforcement are included in the latter plot because the strains measured at the bottom of the pier are affected by the spliced reinforcement.

The strain limit that is predicted for VK7 ($8.6‰$) is considerably higher than the strain limits of the other test units. Furthermore, the concrete to which the LVDTs are attached is already considerably damaged at this point. Thus, a concrete strain limit $\varepsilon_c = 0.004$ was chosen for comparison in the plot. The limit strains of all other test units are within the range that was well measurable by the LVDTs and hence included in the plots. As the prediction of the displacement according to Equation (2.36) [BF10] can only be made corresponding to the higher limit strain, it is not included for VK7. The drift capacity according to EC8-3 Equation (2.40) [24] is not included in Figure 3.13 as it could only be used for the ultimate drift but is not directly linked to a strain limit.

Comparison between the experimental and analytical first yield drift shows that this drift is generally slightly overestimated. This can be explained with an overestimation of the cur-

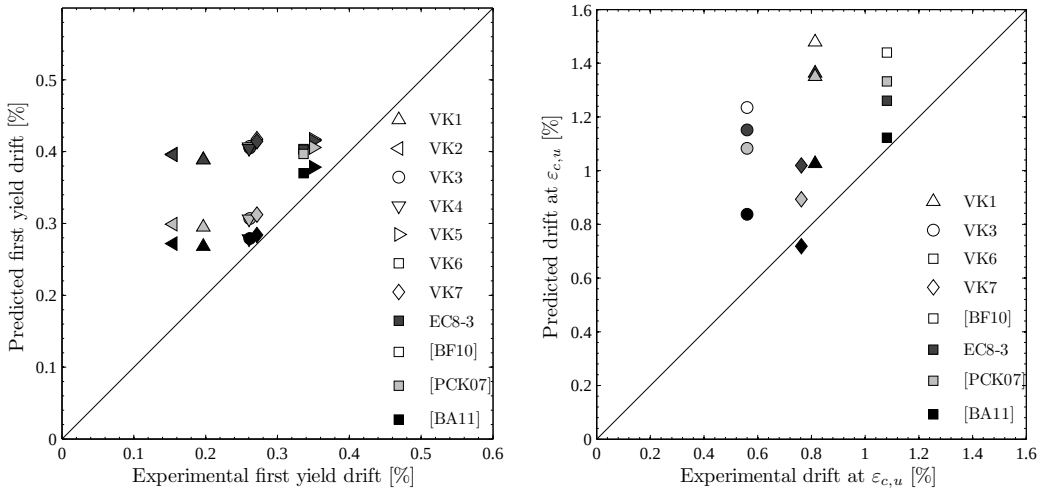

(a) Flexural drift at first yield force F'_y. **(b)** Flexural drift at ultimate concrete strain ε_{cu}.

Figure 3.13: *Comparison of predicted and measured flexural drifts. The shape of the symbols corresponds to the test unit and its color to the applied model.*

vature at the first yield moment, see Figure 3.12, as well as with the concave instead of linear curvature profile at first yield, see Figure 3.9. Nevertheless, the drift is predicted well, except for VK1 & VK2, if the approaches named [7] and [4] are used. Considering strain penetration at this stage leads to a slightly larger overestimation of the drift than not considering it, even though the experimental data is not corrected for this effect. Approaches [BF10] and "EC8-3", which include an influence due to shear cracking, significantly overestimate the flexural drift of all test units with $L_s/h = 2.2$ at first yield, for which shear cracking is predicted. However, also the flexural drift of VK5 and VK6, which does not include this component as shear cracking is expected only for forces that are higher than F'_y, is larger than measured. As the equations of both approaches differ only very little in the term accounting for the reinforcement slip, the predictions obtained with these two approaches are almost equal.

Similar observations are made for the drift at $\varepsilon_{c,u}$ with relatively large overestimation of drift according to [6] ([BF10]) and [24] (EC8-3). With the approach according to [7], the drift prediction of VK6 and VK7 is satisfactory, whereas a larger overestimation of drift is obtained for VK1 and VK3. The best estimate on average is obtained with the approach labeled [4]. As the same moment curvature analysis is used for all predictions, this good correspondence of results indicates that the plastic hinge estimate according to [4] yields the best results in combination with the refined approach to determine the flexural deformations according to [7]. Concerning the limits themselves one can furthermore note that the strain limits result in comparable curvature limits, whereas the limit curvatures according to [35] are about three times as high, see Table 3.5. This is most likely due to the fact that these curvatures were determined from a numerical model of walls with confined boundaries. This type of walls is expected to sustain much higher curvatures than piers with detailing deficiencies that are considered here. Besides, this curvature limit is dependent only on the steel strain, whereas in the other cases as well as in the experiments themselves, the limit strain and thus the failure of concrete was governing.

3.6.3 Force-flexural deformation response

In Figure 3.14, the predictions of the flexural deformations of two test units are compared with the experimental data. One is the prediction of the force-displacement relationship of VK1, which is the test unit with the lower longitudinal reinforcement ratio and continuous reinforcement. Yield and "ultimate" deformation were overestimated with all approaches for this test unit, see Figure 3.13. However, in Figure 3.14 one can see that especially with the comparatively short plastic hinge length according to [4] and no consideration of strain penetration, the estimate of the force-deformation relationship is satisfactory. In the two continuous predictions using the refined approach according to Equation (2.38), the displacements corresponding to the limit curvatures summarized in Table 3.5 are marked with dots. These graphs show that the strain limits correspond to a point in the response that is attained right after peak load and hence provide a conservative displacement limit. The curvature limit for capacity designed walls, on the other hand, results in displacement capacities that are significantly larger than the measured ones. With the approach [BF10] the deformation capacity is overestimated as well. For more clarity in the plot, the prediction named "EC8-3" has not been plotted, but as Figure 3.13 shows, it yields approximately the same deformation as [PCK07] in this case. The drift capacity for the "near collapse" state according to EC8-3 is included in this plot ("EC8-3 Eq. 2.40"), but overestimates the drift capacity. It should be noted though, according to [24], the predicted ultimate drift value needs to be divided by 1.5 for "primary seismic elements". However, this is not necessary for "secondary" elements and was thus interpreted as safety factor. Therefore, this factor was disregarded for the predictions displayed in Figure 3.14.

Test unit VK7 is shown because both the first yield displacement and the displacement at which $\varepsilon_c = 0.004$ concrete strain was reached were predicted well. In Figure 3.14 one can notice a difference between the force-displacement relation measured in positive and negative loading direction, which is due to a better confinement of the compression zone in positive loading direction. In negative direction, the confinement was weakened because the locks of all the stirrups were placed at the side of the pier which was the compression zone in that loading direction. While the force in positive loading direction is underestimated, displacement predictions are partially satisfactory. The force-displacement prediction that is be obtained with the prediction labeled "EC8-3" in Table 3.3 is not included for clarity, but Figure 3.13 shows that this approach predicts a larger deformation capacity than [PCK07]. The drift capacity according to [24] "EC8-3 Eq. 2.40" does again yield unconservative predictions of the deformation capacity if the "safety factor" of 1.5 is neglected.

3.6.4 Discussion of flexural deformation results

Generally, Figure 3.13 shows that all approaches tend to overestimate the flexural deformation corresponding to a certain concrete strain at the base of the pier at least slightly. With regard to the first yield displacement, especially the approaches that consider an increase in deformation due to inclined cracking, i.e. Equation (2.35) [31] and Equation (2.39) (EC8-3 [24]), overestimate the deformation significantly. Very good agreement is obtained with the other approaches except for the two test units with the lowest longitudinal reinforcement ratio. For these test units, the first yield displacements was overestimated by 36% to 93%.

Regarding the displacements at which the concrete strain according to Equation (2.28) was reached, there are considerable differences in the approaches as well. Also for this ultimate limit state, Equation (2.36) [6] predicts the largest displacement. The prediction with the plastic hinge length according to Equation (2.9) [4] agrees best with the measured

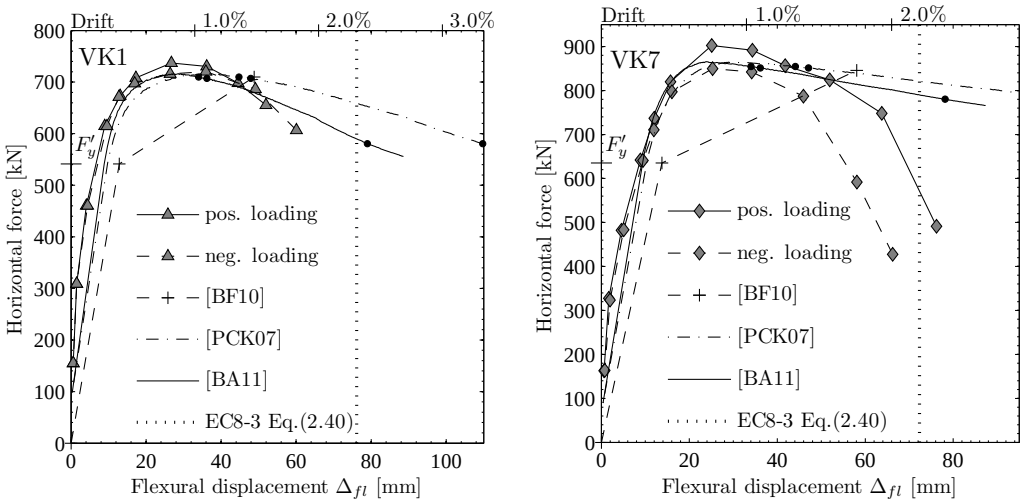

Figure 3.14: *Prediction of load - flexural deformation relationships and measured values.*

displacements on average. This plastic hinge length is the shortest one among all the predictions and contains no strain penetration influence. Besides, it considers a decreasing effect due to the applied axial load.

Figure 3.14 shows that even though the drift corresponding to a certain strain might be overestimated (compare Figure 3.13), the overall shape of the response is still captured relatively well with the refined predictions. The only prediction with a larger deviation is that according to [31] because of the previously mentioned consideration for inclined cracking (term $\phi'_y k_{vz} L_s/3$ in Equation (2.35)). Figure 3.14 also indicates the displacements at which, according to the predictions, the limit curvatures listed in Table 3.5 are reached. As mentioned before, the limit curvature according to Equation (2.31) results in a large overestimation of the deformation capacity regardless of the plastic hinge length. This is due to the fact that this curvature limit was derived for capacity designed walls and depends only on the steel strain. The other two curvature limits, on the contrary, are defined by the concrete limit strain, which was always reached first, according to the analyses. This is in line with the experiments, where degradation of the shear capacity was always triggered by damage of the concrete in compression. One can note, though, that the displacement capacities predicted with these strain limits are rather conservative and correspond to a state that is reached shortly after the peak load. The displacement capacity that corresponds to the onset of the stronger degradation could not be captured with any of the existing limits. However, this degradation is also related to a changing mechanism for all test units that eventually failed in shear which cannot be captured with the plastic hinge modeling approach. Based on the remaining test unit VK7 that failed in flexural compression, no improved limit strain could be established. A model which is capable of predicting the onset of shear degradation will be discussed in Chapter 5.

3.7 Shear response

3.7.1 Introductory remarks

In this section, the shear deformation is investigated in more detail. First, the experimental data is presented and compared to the predictions according to the models reviewed in Section 2.6. Based on the evaluation of this comparison, modifications of the existing models are examined. In particular the prediction of the crack angle and the inclusion of a correction factor accounting for the shear resistance are investigated to this end. Finally, based on a different evaluation of the experimental data, an alternative approach to relate the shear deformation to the axial elongation is developed.

3.7.2 Experimental data

To compare the predictions with the experimental data, flexural and shear deformations were calculated from the Demec or optical measurement data of each test unit (see Figure 3.2b for a drawing of the measurement grid). The deformation components at the top of element *i* were calculated from the outer columns of the measurement grid according to Equation (3.4) and Figure 3.15, with $b = 1350$ mm and $h = 150$ mm. The overall measurement grid was 9×150 mm = 1350 mm wide in each case and between 2550 and 3600 mm high, depending on the height of the pier. No correction for curvature was made as it is assumed that the curvatures are constant over the height of 150 mm, for which the shear deformations are calculated.

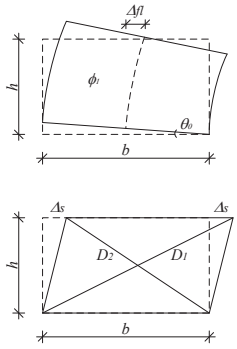

$$\Delta_{fl,i} = \Delta_{fl,i-1} + \theta_{i-1} h + \frac{\phi_i h^2}{2} \tag{3.4a}$$

$$\Delta_{s,i} = \Delta_{s,i-1} + \frac{D_{1,i}^2 - D_{2,i}^2}{4b} \tag{3.4b}$$

Figure 3.15: *Calculation of shear and flexural deformation for an element defined by four measurement nodes.*

In Figure 3.16 the ratio of shear to flexural deformations of test units VK1-VK7, calculated according to the procedure outlined above, is plotted against the imposed displacement ductility. The shear deformations include the sliding deformation and the flexural deformations include the deformation due to strain penetration. In the figure, the average ratios of shear to flexural displacements from the first cycles in positive and negative loading direction are displayed. The figure shows that the ratios are approximately constant for the more slender test units VK5 & VK6 as well as for VK7, which had the highest transverse reinforcement ratio, from $\mu_\Delta \approx 1.2$ on. These test units were the most flexure-controlled out if this test series and the observation of approximately constant Δ_s/Δ_{fl} is in line with the observations made by other researchers (e.g. [54, 56]). The ratios of the more shear critical test units deviate from this constant trend. While VK3 appears to have reached a

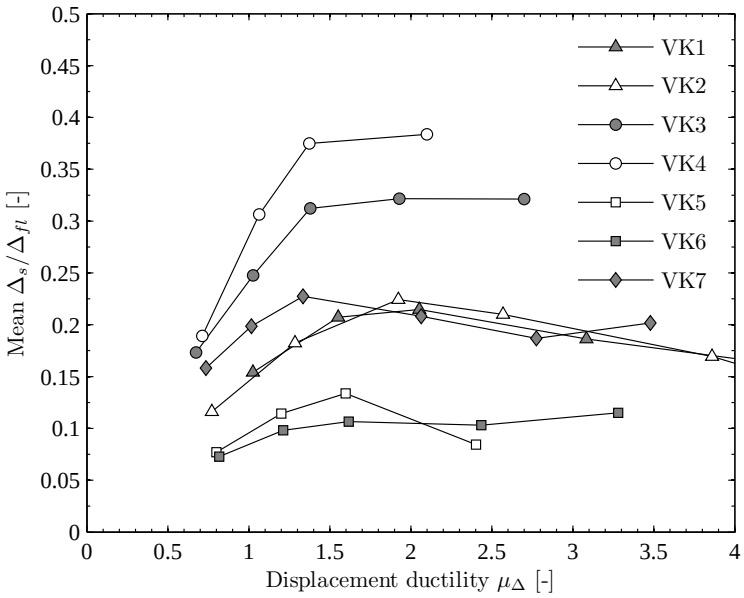

Figure 3.16: *Experimentally determined average shear to flexural deformation ratios as computed from optical measurements at positive and negative first loading cycles against displacement ductility.*

constant value at the relatively high ratio of $\Delta_s/\Delta_{fl} >\sim 0.30$ at $\mu_\Delta \approx 1.4$, the ratio of VK1 decreases after the peak ratio has been reached at $\mu_\Delta \approx 2.0$.

The Δ_s/Δ_{fl} ratio of the test units considered here are not necessarily constant, which appears to be contrary to what has been observed for flexure controlled walls. However, one has to keep in mind that these flexure controlled walls have a much more pronounced plateau and reach higher ductility, whereas the degradation sets in for the walls investigated here soon after the attainment of the maximum load. One can also note that, the more flexure-controlled a wall is, the more it has a constant ratio: the Δ_s/Δ_{fl} ratio of the slender test units VK5 and VK6 is approximately constant while there is a strong increase in shear deformation up to $\mu_\Delta \approx 1.4$ for the shear critical test units VK3 and VK4.

One important aspect to keep in mind when evaluating the data is the method with which the shear deformations are determined. As outlined above, the Δ_s/Δ_{fl} ratios are computed from the nodal displacements of a rectangular grid of measurement targets. Computing the deformation components this way is considered accurate due to the relatively fine measurement grid. The accuracy of the deformation components is confirmed by a good agreement between the sum of the deformation components and the measured total top displacement. The average ratio of this sum of deformation components to the total top displacement is 0.987 with a standard deviation of 3.8% in the inelastic range.

However, for comparison with the data according to the measurements taken along the rectangular grid, the shear deformation can also be determined from the readings of the LVDT chains along the sides in an indirect manner. Only the flexural deformation can directly be determined by double integration of the curvatures computed with the LVDTs. The shear deformation can then be computed as the difference between the flexural deformation and the top displacement. Hence, it may be regarded as shear deformation including an error component due to inaccuracies in the measurements and approximations underlying the calculations, for instance. However, this error component should be negligibly small.

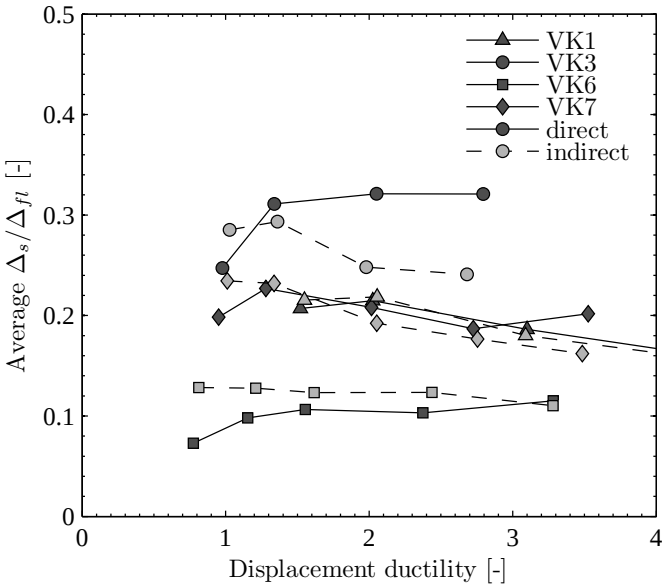

Figure 3.17: *Experimentally determined average shear to flexural deformation ratios: directly and indirectly determined.*

Figure 3.17 shows the average Δ_s/Δ_{fl} ratios obtained with both the direct and the indirect method in the inelastic range. For clarity, only the ratios of the test units with continuous reinforcement are shown here. As the indirect ratios were calculated from the average flexural displacement, the average shown here is slightly different to the one shown previously. Here, Δ_s/Δ_{fl} is computed from average displacements in positive and negative loading direction, whereas previously Δ_s/Δ_{fl} was computed for both loading directions and then averaged. However, the differences are minimal and the data presented in this figure is only used to illustrate the differences in the results. As evident in Figure 3.17 there are some differences in the directly and indirectly determined Δ_s/Δ_{fl} ratios of VK3 and VK6, which stem from differences in the flexural deformation. However, while the differences in the ratios seem significant ($\sim 20-30\%$), the differences in the absolute shear deformation values are rather small ($\sim 1-2\,$mm). This comparison of data thus illustrates that even small differences in the measurements can, depending on the type of evaluated data that is displayed, cause some variation in the results. This should be kept in mind when the data is interpreted. In the following, the directly determined shear deformation is used due to the previously mentioned quality of the data as evident in the good agreement between the sum of components and the top displacement.

3.7.3 Summary of approaches

Three existing approaches to include the shear deformation in plastic hinge modeling have been presented in Sections 2.6.1 to 2.6.3. One of them utilizes the crack angle and centroidal axial strain in the plastic hinge to estimate the shear distortion and, based on that, the shear deformation [8]. In the second approach, shear deformations are related to flexural deformations based on the kinematics at a shear crack [28]. The third approach estimates the deformation based on the shear stiffness of a cracked structure, which is estimated using a truss model [7]. Table 3.6 summarizes the mentioned approaches and the predicted shear to flexural deformation ratios for each test unit at peak load compared to the exper-

Table 3.6: *Summary of models to estimate shear to flexural deformation ratios* Δ_s/Δ_{fl}.

Test unit	VK1	VK2	VK3	VK4	VK5	VK6	VK7
Mean $(\Delta_s/\Delta_{fl})_{exp}$	0.19	0.21	0.32	0.37	0.13	0.10	0.21
[8] Eq. (2.45)	0.23	0.24	0.23	0.21	0.13	0.16	0.23
[28] Eq. (2.46)	0.15	0.17	0.22	0.20	0.10	0.11	0.15
[7] Eq. (2.51)	0.89	0.94	1.32	1.34	0.36	0.24	0.58
Eq. (2.45)	$1.5\frac{\varepsilon_l}{\phi \tan\theta}\frac{1}{L_s}$						
Eq. (2.46)	$\left(\frac{V}{V_n}+\frac{V}{V_{wc}}\right)0.35\,(1.6-0.2\theta_{max})\,\frac{h}{L_s}$						
Eq. (2.51)	$\left(\Delta_{sh,1}+\frac{(V_N-V_c)}{K_{sh,cracked}}\right)/(\phi_y\frac{(L_s+L_{sp})^2}{3})$						

imental values. The experimental ratios are the mean ratios at peak load in positive and negative loading direction. For the test units with continuous reinforcement this means the ratio at load step μ_Δ=3.0 was used. For the test units with splices load step μ_Δ=2.0 was used instead. At this load step, measurements were still available for both loading directions, while the lap-splice had always started degrading at the negative loading to μ_Δ=3.0. All predictions in Table 3.6 that utilize the crack angle were evaluated based on the measured crack angle. With Equation (2.51) very large shear to flexural deformation ratios were predicted, as evident in Table 3.6. The large ratios stem from the large differences between the nominal yield force and shear cracking force V_c. This difference leads to the prediction of a large shear deformation at nominal yield and hence a high ratio of shear to flexural deformations. Due to the considerable overestimation of the shear deformations this prediction is not examined further. The remaining two models and the predictions obtained with them are discussed in the following sections.

If a crack angle is necessary to evaluate the model, it was determined from pictures of the test units taken when the crack pattern was fully developed. The crack angles in the upper part of the piers was used, according to the suggestion made by [8]. Since it is necessary for the assessment of bridge piers to estimate the crack angle beforehand, angles calculated from Equations (2.52), (2.53) and (2.47) are listed in Table 3.7 for comparison. The measured values represent the angles of the parallel crack pattern at the top of the test units, which also corresponds to the predictions according to (2.52) and (2.53). The prediction according to (2.47) yields the angle of the steepest crack reaching to the base, which also corresponds to the angle of the parallel crack pattern. Equation (2.53) was initially evaluated for the axial strain corresponding to the maximum moment according to moment curvature analysis and thus the largest possible axial strain at the base. This strain is out of the range for which the equation was developed, however. Besides, it might not be considered to be the optimum choice for the strain with which a crack angle forming higher up the pier is to be estimated. However, the question is which height might represent a good location. As the model according to [8] was developed based on the observation that the shear deformation primarily stems from the plastic region, which corresponds to roughly $2L_p$, the crack angle is also evaluated for the strain at 1 m $\approx 2L_p$ height. Forces, lever arms and centroidal strains obtained from moment-curvature analysis were used to calculate the crack angles. All angles were calculated using the strains and forces obtained from the moment-curvature analysis corresponding to the predicted maximum moment at the base of the pier. The measured angles were similarly determined from photos that were taken after the peak load, which is close to the nominal yield load, had been reached. Only the concrete compression force and the steel tension force were considered to compute the internal

Table 3.7: *Measured and calculated crack angles at or after peak force level.*

Test unit	VK1	VK2	VK3	VK4	VK5	VK6	VK7
Measured	45°	42°	40°	43°	48°	45°	39°
[28] (2.47)	22°	23°	19°	19°	20°	19°	30°
[39] (2.52)	60°	60°	54°	50°	60°	61°	52°
[40] (2.53) ε_{max}	79°	72°	61°	60°	60°	66°	57°
[40] (2.53) $\varepsilon(\sim 2L_p)$	32°	31°	31°	31°	31°	31°	31°
[9] (2.54)	30°	30°	27°	27°	27°	27°	34°
[28] (2.47)	$\arccos\left(\frac{1}{z}\sqrt{\frac{2(T-T_{yav})z}{(A_v f_{yv})/(s)+(f_{ct}b2d_{cr})/(1.4z)}}\right)$						
[39] (2.52)	$\arctan\left(\frac{z}{V}\left(f_{ct}b+\frac{A_{sv}f_{yv}}{s}\right)\right) < 90°$						
[40] (2.53)	$(29° + 7000\varepsilon_l)\left(0.88+\frac{s_{xe}}{2500}\right) \leq 75°$						
[9] (2.54)	$\arctan\sqrt[4]{\frac{\varrho_v+k_E\varrho_l\varrho_v}{\varrho_l+k_E\varrho_l\varrho_v}}$						

lever arm, because the other forces were considered to be negligibly small. To compute the crack angle according to (2.54), only the reinforcement contents and the ratio of the elastic moduli are necessary. The ratio of the latter has been set to $E_s/E_c = 200\text{GPa}/25\text{GPa}$ in all cases.

3.7.4 Evaluation of shear deformation models

a Shear deformation based on axial strain

To estimate the Δ_s/Δ_{fl} ratios of the test units according to [8], the measured crack angles and the strains from the moment-curvature analysis were used. Instead of keeping a constant ratio of ε_l/ϕ for the entire ductility range, as originally suggested, the ratio was always obtained from the curvature and axial strains from the M-ϕ analysis. The Δ_s/Δ_{fl} ratio, that is in then known in relation to the curvature, was related to the displacement ductility according to Equation (2.38) [7]. Figure 3.18a shows the average experimental ratios from positive and negative loading direction against the imposed displacement ductility in positive direction.

For comparison, the ratios estimated according to Equation (2.45) are also included in the plot. Since the model was developed for the deformations in the inelastic range, the ratios are plotted from displacement ductility μ_Δ= 1.0 onwards. For clarity, only the test units with continuous reinforcement have been included in that plot. Figure 3.18b shows the predicted and experimentally determined ratios at the peak load. As mentioned previously, this corresponds to load step μ_Δ= 3.0 for test units with continuous reinforcement and μ_Δ=2.0 for those with spliced reinforcement. This figure does not include the averaged experimental ratios but those from positive and negative loading to give an idea of the difference between the two loading directions.

With predicted instead of measured angles, the ratios shown in Figure 3.19 are obtained. If the angles predicted for the strain at 1 m height are used instead of the measured crack angles, the ratios increase about 66% ($= \tan 45°/\tan 31°$) and are thus larger than measured, see Figure 3.19a. The increase in the ratios is even larger with the crack angles according

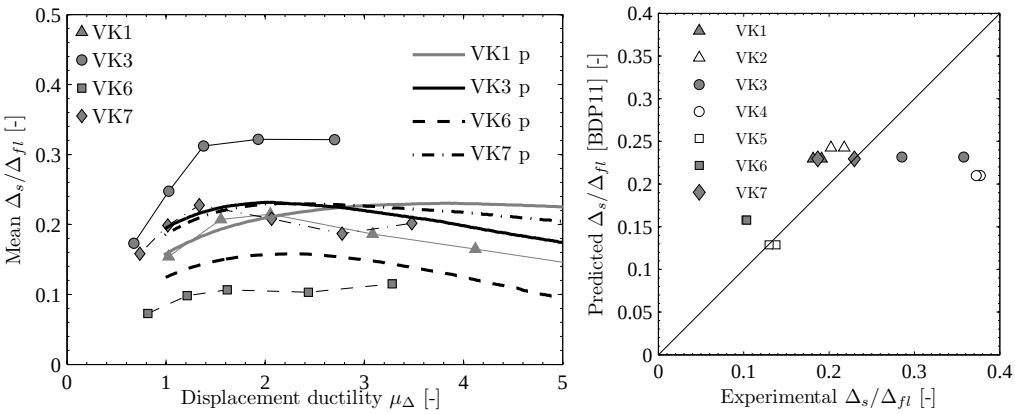

(a) Mean experimental and predicted (p) Δ_s/Δ_{fl} ratios of VK with continuous reinforcement against μ_Δ.

(b) Predicted against experimental Δ_s/Δ_{fl} ratios at peak load.

Figure 3.18: *Shear deformation according to Equation* (2.45) *[8].*

to Equation (2.54). As Table 3.7 shows, these angles are smaller than the measured ones and even smaller than those according to [40]. However, this is the only prediction that yields some differences between the different test units and would thus lead to different shear ratio predictions which corresponds to the experimental data. Comparison with the photos of the test units shows that these angles correspond approximately to the steeper part of the shear crack angles. Hence, they might be useful if the correction factor in Equation (2.45) is modified accordingly.

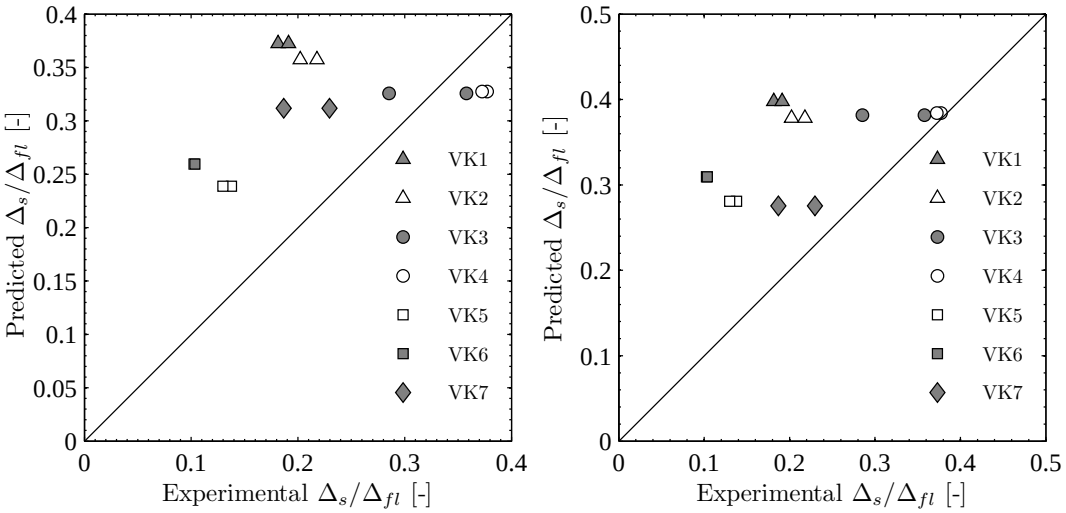

(a) Predicted against experimental Δ_s/Δ_{fl} ratios at peak load - using the angle according to [40] for the prediction.

(b) Predicted against experimental Δ_s/Δ_{fl} ratios at peak load - using the angle according to [9] for the prediction.

Figure 3.19: *Shear deformation according to Equation* (2.45) *[8] using predicted angles.*

b Shear deformation based on crack inclination

Predictions with Equation (2.46) were made using the measured crack angles listed in Table 3.7 and the web crushing strength was taken to be the compression strut capacity $V_{Rd,max}$ according to [11] 6.2.3 (3). To compute $V_{Rd,max}$ the internal lever arm from the moment-curvature analysis at maximum moment has been used. In the plastic range, the diagonal tension capacity V_n was calculated with the factor $k_\mu = 0.05$ according to Equation (4.1). Shear to flexural deformation ratios were computed for all first cycle peak load levels. In Figure 3.20a the predicted Δ_s/Δ_{fl} ratios of the test units with continuous reinforcement are plotted against the mean measured ones in the inelastic range. The ratios at the peak load levels are again compared in positive and negative loading direction. Hence, there are two data points for each test unit in Figure 3.20b.

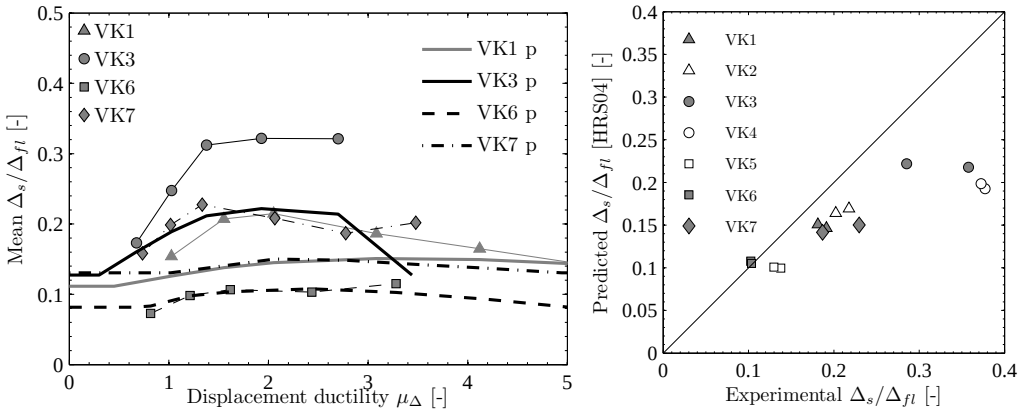

(a) Mean experimental and predicted (p) Δ_s/Δ_{fl} ratios of VK with continuous reinforcement against μ_Δ.

(b) Predicted against experimental Δ_s/Δ_{fl} ratios at peak load step.

Figure 3.20: *Shear deformation according to Equation* (2.46) *[28].*

The shear deformations shown in Figure 3.20 have been computed using measured angles. For comparison, the shear to flexural deformation ratios obtained with the predicted crack angle according to Equation (2.47) are shown in Figure 3.21. As this angle is much steeper than the measured ones, the predicted ratios exceed the experimentally determined ones. To examine whether the basic assumptions of the model apply to the investigated test units, the shear and flexural deformations in between the two cracks where determined from the measurement grid. In Figure 3.21b one can see that the flexural deformations ratios originating from this region vary significantly between the different test units and that only a part and not the total shear deformations stem from this region. Both deformation components were determined from a rectangular grid whose width almost corresponds to the wall length and whose height equals the distance between the two respective cracks. That means the deformations were not determined along the cracks by explicitly taking into account the kinematics suggested by [28].

3.7.5 Discussion of results

Generally, one can note that without correction factor, i.e. 1.5 and $(V/V_{wc} + V/V_n)$, respectively, the predictions according to Equation (2.45) and (2.46) yield relatively constant shear to flexural deformation ratios for all piers at peak load level. Figure 3.18 shows this for Equation (2.45) which utilizes a constant correction factor. The slightly curved shape of

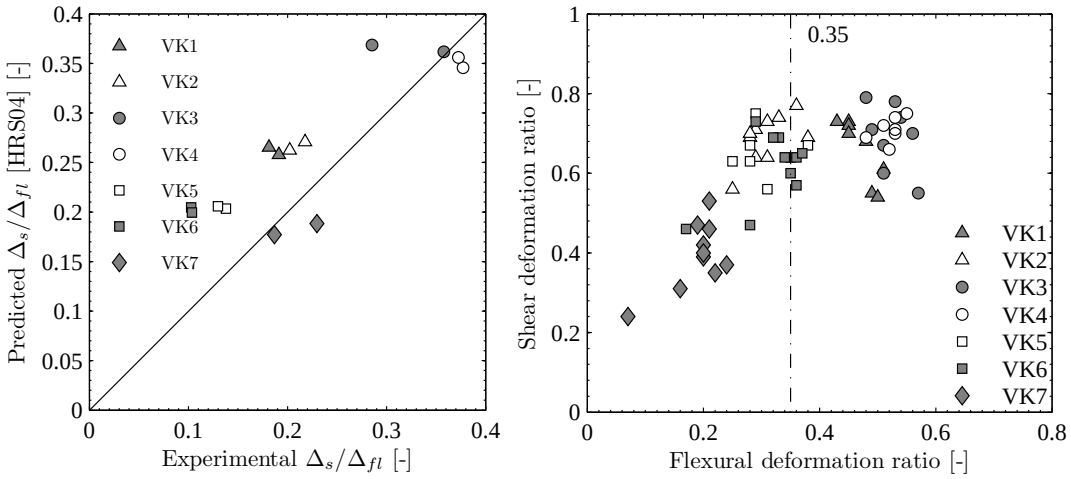

(a) Δ_s/Δ_{fl} ratios with angles from Eq. (2.47)

(b) Fraction of shear and flexural deformation, related to the total of each component, that stems from the area in between bottom-flexure and top-shear crack.

Figure 3.21: *Shear to flexural deformation according to [28].*

the Δ_s/Δ_{fl} predictions is the result of changing ε_l/ϕ ratios according to moment-curvature analysis. As this model considers the ratios to be related to the shear span length L_s, the ones predicted for the shorter piers are generally 36% higher ($L_{s,l}/L_{s,s} = 4.5/3.3 = 1.36$) than those predicted for the longer piers. Further differences in the ratios stem from varying material properties, so that generally the ratios of the shorter piers lie between 21-24%, whereas the ones of the longer piers lie between 13-16%. Without correction factor, the predicted ratios would hence be around 15% and 10% for the piers with aspect ratio 2.2 and 3.0, respectively.

The figures show that the predicted ratios are similar to the measured ones, except for the most shear critical piers VK3 & VK4 and the slender pier VK6. The average ratios of the shear critical test units are underestimated by about 40% (VK3) to almost 80% (VK4). One has to keep in mind, however, that, as evident in Figure 3.18b for VK3, there is also some variation in the experimental ratios. The Δ_s/Δ_{fl} ratio of the test unit with the highest aspect ratio, VK6, is overestimated by about 50%. Hence, based on the experimental data considered here one may say that Equation (2.45) yields good estimates for walls with intermediate aspect ratios ($L_s/h < 3.0$), but does neither capture well the response of shear critical piers such as VK3 nor that of more slender piers such as VK6.

The dependence on the geometry is primarily accounted for by means of the correction factor in the approach according to [28]. Without correction factor α, there are only slight variations in the predicted ratios. Due to the strength dependent correction factor, larger Δ_s/Δ_{fl} ratios are predicted for test units VK3 & VK4, which also had significantly higher shear deformations. As evident in Figure 3.20a, the shape of the Δ_s/Δ_{fl} is well predicted but the ratios are too low. The ratio of the more slender test unit VK6 on the other hand is well predicted both with regard to the magnitude of the ratio and the shape of the curve. Hence it appears that, especially for predicting good ratios for the shorter, more shear critical piers, the correction factor plays an important role.

With regard to the crack angle predictions, one can see that very low angles are predicted with Equation 2.47 and hence application of the original shear model according to [28],

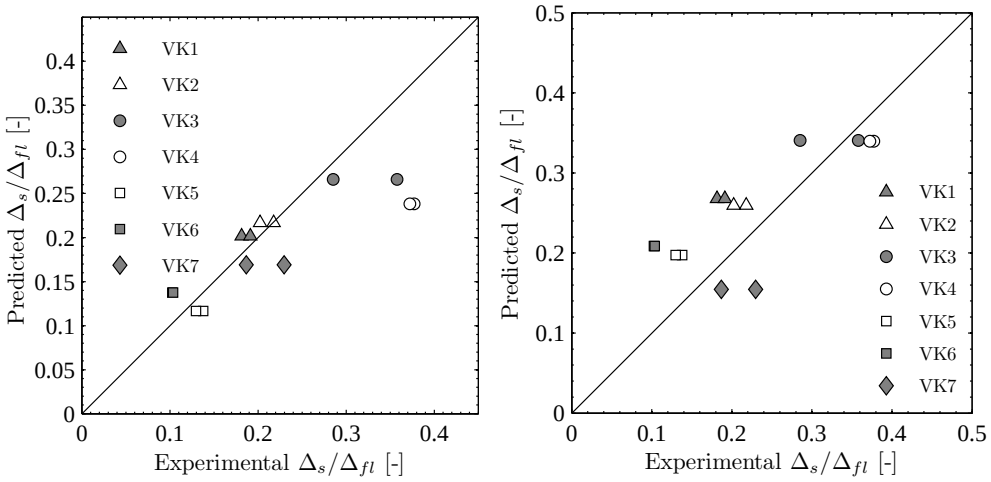

Figure 3.22: *Shear to flexural deformation ratios at peak load level according to model by [8] with correction factor according to [28] using measured crack angles (to the left) and the angle according to Eq. 2.54 with adjusted correction factor to the right.*

including this predicted angle, leads to an overestimation of the shear deformations. Also the crack angle predicted for the strain at 1.0 m height corresponding to the maximum lateral load and the one dependent on the reinforcement content are lower than predicted. On the contrary, the rest of the predicted crack angles that are listed in Table 3.7 are larger than the measured ones. As both of the investigated models to predict Δ_s/Δ_{fl} depend on the crack angle, the crack angle predictions need improvement for application with the models if the dependence on the crack angle is not removed.

3.7.6 Modifications of existing models

To use the models for the prediction of deformation, the dependency on measured quantities, such as the crack angle and the shear resistance, must be replaced by predicted ones. This may then require an adjustment of correction factors. As previously noted, whether the trend was captured well depends partially on the correction factor, as this is an easy way to capture the influence of e.g. increased shear deformation due to low transverse reinforcement ratios. Hence, predictions of the shear to flexural deformation ratios were first made with Equation (2.45) in which the correction factor 1.5 was substituted with α of Equation (2.46). Compared to the predictions presented in Figures 3.18 and 3.20, predictions with the modified equation, Figure 3.22, are slightly better. Furthermore, as previously shown, the crack angle that depends on the reinforcement ratios predicts the differences between the piers better. However, if this was used, the ratios were predicted with a slight offset which necessitated the introduction of a correction factor again. Figure 3.22 shows the shear to flexure deformation ratios predicted with the modified crack angle and correction factor. The shear to flexural deformation ratios in this plot have thus been determined according to the following equation:

$$\frac{\Delta_s}{\Delta_{fl}} = \alpha 0.75 \frac{\varepsilon_l}{\tan\theta\phi}\frac{1}{L_s} = 0.75\alpha \frac{\varepsilon_l}{\sqrt[4]{\frac{\varrho_v + k_E\varrho_v\varrho_l}{\varrho_l + k_E\varrho_v\varrho_l}}\phi}\frac{1}{L_s} \quad \text{with} \quad 1 \leq \alpha = \left(\frac{V}{V_n} + \frac{V}{V_{wc}}\right) \leq 2 \quad (3.5)$$

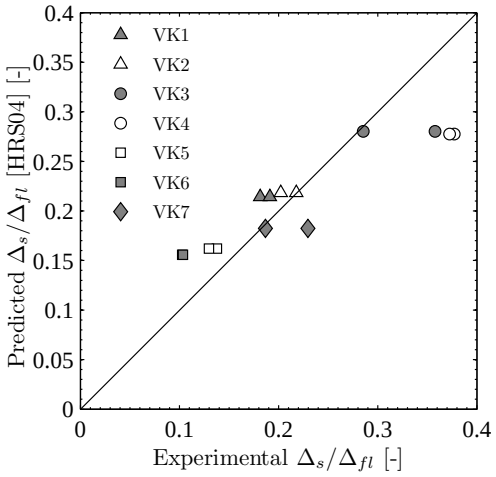

Figure 3.23: *Shear to flexural deformation ratio according to modified prediction by [28].*

Figure 3.22 shows that the Δ_s/Δ_{fl} ratios predicted with this formulation are on average well predicted, but with a certain deviation. Also the shear deformation prediction according to [28] has been modified with the crack angle prediction based on the reinforcement ratio. With this angle, the equation becomes:

$$\frac{\Delta_s}{\Delta_{fl}} = \alpha 0.35 \left(1.6 - 0.2 \arctan \sqrt[4]{\frac{\varrho_v + k_E \varrho_v \varrho_l}{\varrho_l + k_E \varrho_v \varrho_l}}\right) \frac{h}{L_s} \tag{3.6}$$

Figure 3.23 shows the predictions made with this equation and the correction factor evaluated with the peak load according to moment-curvature analysis against the experimentally determined ratios at peak load. As evident in the figure, these simple modifications add to improved predictions of the Δ_s/Δ_{fl} ratios, compared to the initial prediction, shown previously.

As evident in Figures 3.22 and 3.23 none of the modified approaches is clearly superior to the other but both modified equations yield approximately equally good results. Hence, based on the data of the test units considered here, one may conclude that they may be used interchangeably.

3.7.7 New approach based on axial elongation

a Distribution of shear strains

In Figure 3.24 the shear strain distribution of two of the test units is shown. The shear deformations in the plot were calculated from the measurement grid on the surface of the test units as explained in Section 3.7.2. The strain corresponds hence to the shear deformation per row of the measurement grid divided by the height of this row. One can see that there is no clear concentration of shear deformations, but rather a constant or linear distribution along the height. To better compare the deformations of the two presented test units, the vertical axes of both graphs are plotted with the same limit, even though VK7 was shorter. Similar trends as those shown here were observed for the other test units. There was a

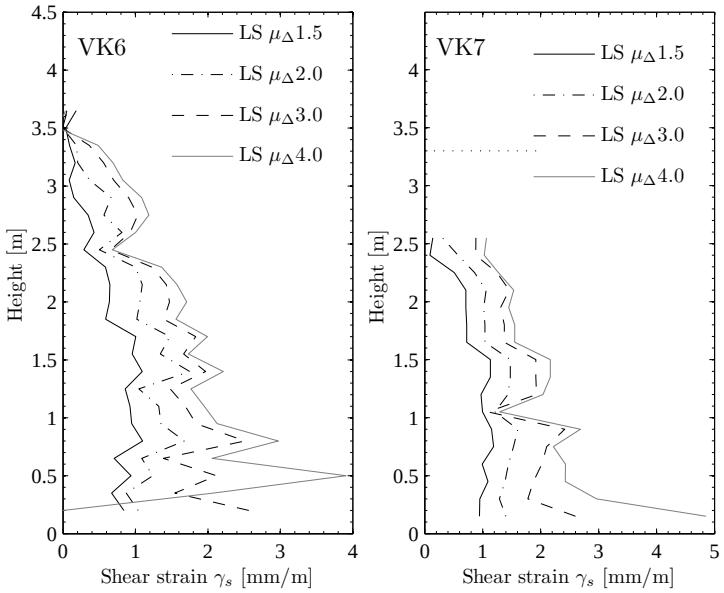

Figure 3.24: *Shear strain distribution as computed from the optical measurement grid along the height of two of the test units.*

slight difference in whether the strain distribution appeared to be more linear and decreasing towards the top of the test unit (VK1, VK6 and VK7, see also Figure 3.24) or almost constant over the entire measurement grid (VK3, see Figure 3.27). In each case, the shear strain was thus distributed over almost the entire cracked height.

b Deformation due to crack opening

To gain a better understanding of what types of deformation exactly are interpreted as shear deformation applying the data evaluation method outlined in Section 3.7.2, the deformation determined for an element *i* located at height L_i in the pier is looked at with regard to its relation to deformations along the cracks. As Figure 3.25 illustrates, there may be cracks running through the entire element and hence crossing it at the top edge, as well as some crossing at the left edge. As a simplification, the cracks are assumed linear in the following. The dashed and dotted lines in the right part of Figure 3.25 then indicate the boundaries for all cracks that cross the element *i* at the left and top edge, respectively.

In reality, there will be several cracks, but to examine the influence of the displacement along the cracks on the deformation components, all cracks crossing one edge will be merged into one crack in the following. Before severe degradation of the entire structure commences, it is assumed that only crack opening due to rotation around the tip and little sliding occurs (compare also Chapter 5). This rotation around the crack tip results in the deformations shown in Figure 3.26. The cracks below element *i*, do only cause rigid body rotation of the entire element and do hence not need to be considered. Pure lateral elongation and constant curvature in an element do similarly not contribute to the shear deformation. If the illustrated mechanism is valid, the shear deformation determined from the experimental data should be a combination of both deformation modes shown in Figure 3.26.

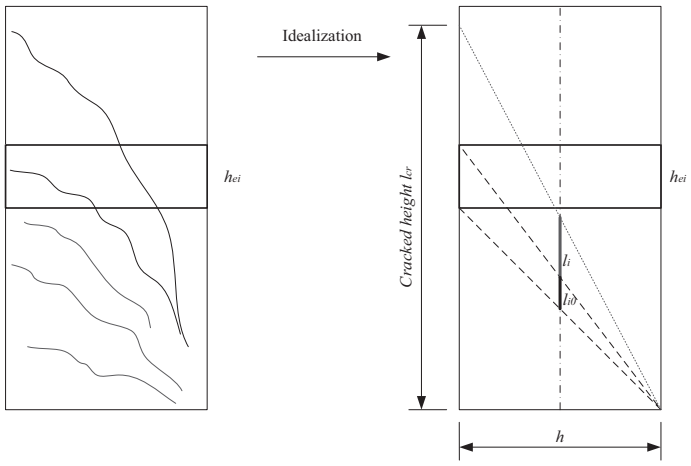

Figure 3.25: *Cracked wall with element i at height L_i and idealization of crack pattern.*

Figure 3.26 shows that the element to the right is subjected to a horizontal elongation and a rotation of the part above the crack. The bottom edge of the element to the left is also elongated, but not the top edge, which is interpreted as shear deformation according to the method chosen here for the evaluation of the deformation components. The directly determined shear deformation was computed from the difference in the elongation of the two diagonals D_1 and D_2, as outlined in Section 3.7.2. This procedure yields the following shear deformation for an element with cracks crossing at the left edge:

$$D_1^2 = (h + \Delta_{x3})^2 + h_{ei}^2 \tag{3.7a}$$

$$D_2^2 = h^2 + h_{ei}^2 \tag{3.7b}$$

$$\Delta_s = \frac{(h + \Delta_{x3})^2 + h_{ei}^2 - (h^2 + h_{ei}^2)}{4h} \tag{3.7c}$$

$$= \frac{1}{2}\Delta_{x3} + \frac{\Delta_{x3}^2}{4h} \tag{3.7d}$$

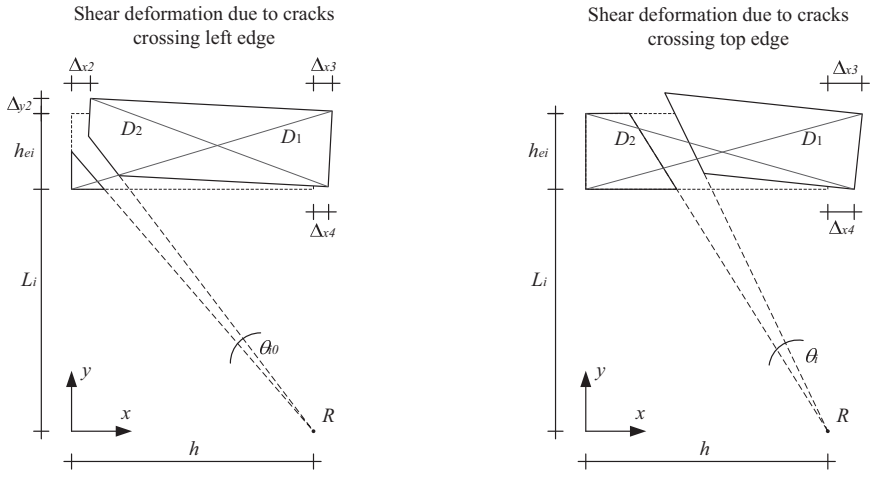

Figure 3.26: *Deformation of element i due to rotation at cracks crossing the element at the left and top edge.*

Diagonal D_2 is not elongated and does hence not need to be expressed in terms of the nodal coordinates and displacements. Doing so would merely add a small error component if linear kinematics are employed. The displacement of the upper right node can be expressed as follows by using linear kinematics:

$$\Delta_{x3} = (L_i + h_{ei})\theta_{i0} \tag{3.8}$$

This displacement can be inserted in Equation (3.7). If the quadratic term is neglected, as its contribution to the displacement is small, the shear displacement is:

$$\Delta_{s,i} = \frac{1}{2}\left(L_i + h_{ei}\right)\theta_{i0} \tag{3.9}$$

Following the same procedure, the shear displacement of the element displayed at the right side of Figure 3.26, with cracks crossing at the top edge, can be derived. The shear deformation due to elongation of the diagonals is:

$$D_1^2 = \left(h + \Delta_{x3}\right)^2 + h_{ei}^2 \tag{3.10a}$$

$$D_2^2 = \left(h + \Delta_{x4}\right)^2 + h_{ei}^2 \tag{3.10b}$$

$$\Delta_s = \frac{\left(h + \Delta_{x3}\right)^2 + h_{ei}^2 - \left[\left(h + \Delta_{x4}\right)^2 + h_{ei}^2\right]}{4h} \tag{3.10c}$$

$$= \frac{1}{2}\left(\Delta_{x3} - \Delta_{x4}\right) + \frac{\Delta_{x3}^2 - \Delta_{x4}^2}{4h} \tag{3.10d}$$

Again, the quadratic terms Δ_x^2 will be neglected in the following, as their contribution to the deformation is small. The nodal displacements, expressed by using linear kinematics, are:

$$\Delta_{x3} = (L_i + h_{ei})\theta_i \tag{3.11a}$$

$$\Delta_{x4} = L_i\theta_i \tag{3.11b}$$

$$\tag{3.11c}$$

These displacements are inserted in Equation (3.10). The shear displacement in function of the rotation θ_i is:

$$\Delta_{s,i} = \frac{h_{ei}\theta_i}{2} \tag{3.12}$$

The sum of the rotations of all cracks crossing the element at the left edge can be expressed as a function of the axial strain $\varepsilon_l(y)$:

$$\theta_{i0} = \frac{\Delta_{li0}}{0.5h} = \frac{1}{0.5h}\int_{l_{i0}} \varepsilon_l(y)\mathrm{d}y = \frac{1}{0.5h}\int_{0.5L_i}^{0.5(L_i+h_{ei})} \varepsilon_l(y)\mathrm{d}y \tag{3.13}$$

The base length for integration of the strains l_{i0} is illustrated in Figure 3.25 and the boundaries for integration can be obtained by looking at Figure 3.25. The sum of the rotation of all cracks crossing the top edge of the element can similarly be expressed as:

$$\theta_i = \frac{1}{0.5h}\int_{l_i} \varepsilon_l(y)\mathrm{d}y = \frac{1}{0.5h}\int_{0.5(L_i+h_{ei})}^{0.5l_{cr}} \varepsilon_l(y)\mathrm{d}y \tag{3.14}$$

The equations presented in this section show, that this approach resembles the previously presented approaches to determine the Δ_s/Δ_{fl} ratio. Similarly to the model according to [20], the shear deformation is here related to the deformation that is expected along the shear cracks. However, here the shear deformation is not calculated in relation to the flexural deformation. Furthermore, the shear deformation is not assumed to depend on the elongation of the outer longitudinal reinforcement, but rather on the centroidal axial elongation, similar to what is done in the approach by [8].

c Check assumed deformation pattern

To check whether the assumptions regarding the shear deformations that were presented in the previous section are valid, the shear deformations according to the two mechanisms have been computed with the measured axial strains and compared to the experimental data. The axial strains were obtained from the readings of the LVDTs along the sides of the wall. Straight, radial cracks have been assumed to determine the rotation of an element. That means, to compute the rotations θ_i and θ_{i0} of an element at height L_i, the strains between $0.5L_i$ and $0.5(L_i + h_{ei})$ as well as $0.5(L_i + h_{ei})$ and the top of the instrumented area were used. The strains above the instrumented area were assumed to be zero for simplicity. Figure 3.27 shows the distribution of shear strains as determined from the experimental data compared to the one obtained with the equations shown in the previous section.

The approach outlined in Section 3.7.7 would eventually yield shear deformations that are related to the axial strain, as the rotations are expressed as functions of the axial strain. Hence, the relation between the shear deformations and the axial elongation of the piers was checked. Figure 3.28 indicates that there is indeed a good relation between the elongation of the test units and their shear deformation. Only the data of the test units with continuous reinforcement was used for this comparison, as the axial elongation of the test units with splices is influenced by the splice. However, as Figure 3.16 indicates, the shear deformations of the test units with lap-splices are almost equal to the ones of the corresponding test unit without lap-splices. Therefore, it should ultimately be possible to determine the shear deformations of piers with lap-splices with the same approach as that used for piers with continuous reinforcement. Furthermore, a prediction of the axial elongation was compared to the measured axial elongation. The prediction was obtained in a manner resembling the refined approach for the flexural deformation according to Equation (2.38). That means the axial strain at first yield, obtained from the moment-curvature analysis, was multiplied by factor M/M'_y and assumed to follow a linear distribution over the height of the pier. The difference between this factored axial strain at first yield and the axial strain corresponding to the current curvature was taken as plastic axial strain, that was assumed constant in the plastic hinge length according to [4]. As Figure 3.28 shows, the agreement between measured and predicted elongation is good.

The comparisons between experimental data and predictions shown in this section indicate that relating the shear deformations to the axial strains, based on the deformation due to

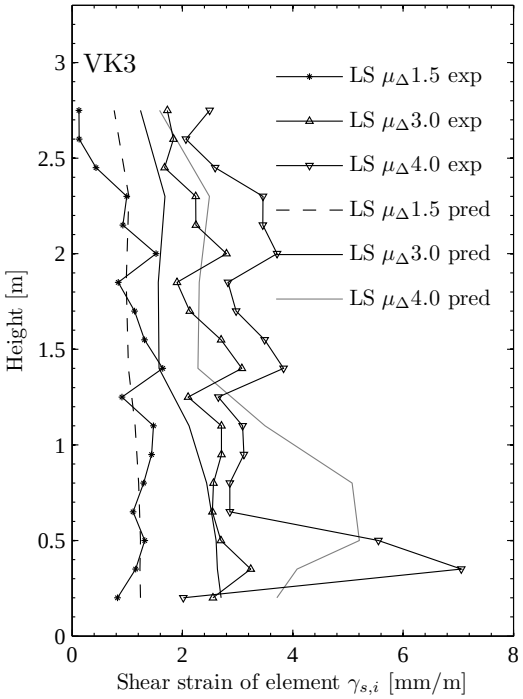

Figure 3.27: *Distribution of shear strains.*

rotation at the cracks, seems possible. Figure 3.27 indicates that this mechanism, while not yet perfected, seems reasonable and Figure 3.28 shows that it is possible to determine the axial elongation of the piers with reasonable accuracy within the scope of plastic hinge modeling.

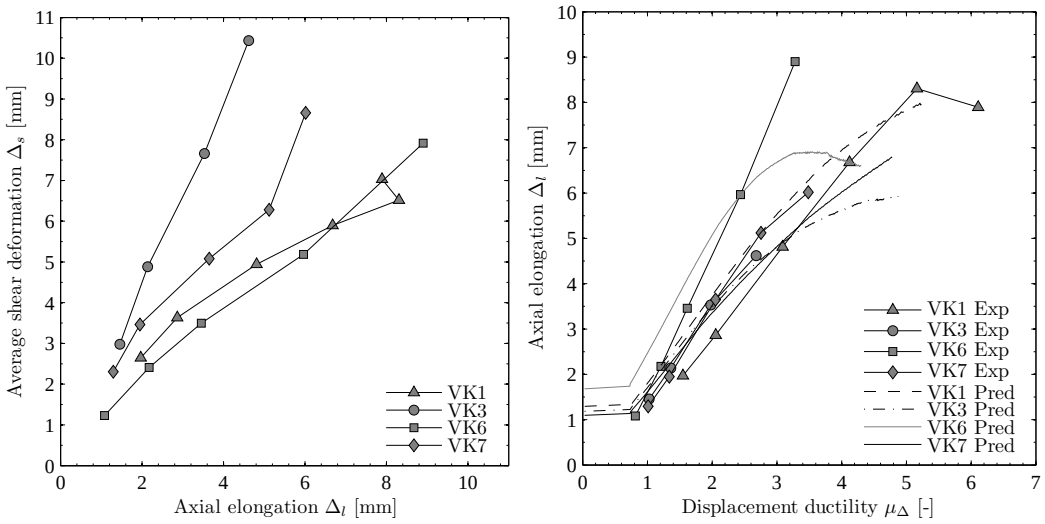

Figure 3.28: *Experimentally determined shear deformation against experimentally determined axial elongation of the test units with continuous reinforcement and comparison of predicted and experimentally determined axial elongation.*

d Analytical solution and comparison to data

To predict the shear deformations based on the principle outlined in the previous section, but independent of the measurement grid, an analytical solution is necessary. The shear deformations stemming from the cracks that cross the elements at the top edge can easily be obtained with the following equation:

$$\Delta_s = \frac{1}{2}\int_{dy}\int_{l_i}\theta_i(y_1)\mathrm{d}y_1\mathrm{d}y = \frac{1}{2}\int_{0}^{l_{cr}}\frac{1}{0.5h}\int_{0.5y}^{0.5l_{cr}}\varepsilon_l(y_1)\mathrm{d}y_1\mathrm{d}y \tag{3.15}$$

The cracked height l_{cr} was here chosen as upper integration limit as shear deformation can occur only within the cracked area according to this approach. The solution to this integral depends on the assumed strain distribution. For the simplest case of a constant axial strain, it evaluates as:

$$\Delta_s = \frac{1}{2}\int_{0}^{l_{cr}}\frac{1}{0.5h}\int_{0.5y}^{0.5l_{cr}}\varepsilon_l\mathrm{d}y_1\mathrm{d}y \tag{3.16a}$$

$$= \frac{1}{2}\frac{1}{0.5h}\int_{0}^{l_{cr}}\varepsilon_l\left(0.5l_{cr}-0.5y\right)\mathrm{d}y \tag{3.16b}$$

$$= \frac{l_{cr}}{2h}\underbrace{\frac{\varepsilon_l l_{cr}}{2}}_{\Delta_l} = \frac{\varepsilon_l l_{cr}^2}{4h} \tag{3.16c}$$

In plastic hinge modeling, the strains are assumed to be linearly distributed above the plastic hinge itself. With the linear distribution of strains $\varepsilon_l(y) = \varepsilon_m(1 - y/(0.5l_{cr}))$, where ε_m is the maximum strain, the integration yields:

$$\Delta_s = \frac{1}{2}\int_{0}^{l_{cr}}\frac{1}{0.5h}\int_{0.5y}^{0.5l_{cr}}\varepsilon_m - \frac{\varepsilon_m}{0.5l_{cr}}\mathrm{d}y_1\mathrm{d}y \tag{3.17a}$$

$$= \frac{\varepsilon_m l_{cr}^2}{12h} = \Delta_l\frac{l_{cr}}{3h} \tag{3.17b}$$

Similarly, the analytical solution for the component due to shear cracks crossing the left edge of an element and a constant axial strain is:

$$\Delta_s = \frac{\varepsilon_l l_{cr}^2}{4h} \tag{3.18}$$

If the strain distribution is linear, the solution is:

$$\Delta_s = \frac{\varepsilon_m l_{cr}^2}{12h} \tag{3.19}$$

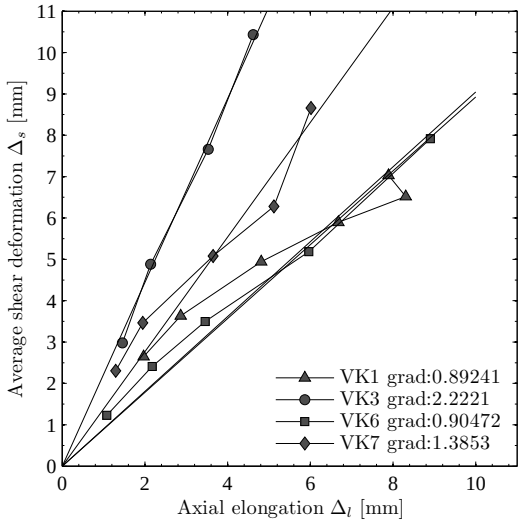

Table 3.8: *Measured shear deformation against axial elongation.*

Table 3.9: *Cracked heights l_{cr} calculated from gradient assuming that ε_l is constant.*

VK1	$l_{cr} = 1.34\,\text{m}$
VK3	$l_{cr} = 3.33\,\text{m}$
VK6	$l_{cr} = 1.36\,\text{m}$
VK7	$l_{cr} = 2.08\,\text{m}$

As Equations (3.16c) to (3.19) show, cracks crossing the left and the top edge each contribute the same amount of shear deformations. This was already indicated by Equations (3.12), (3.9), (3.14) and (3.13). With a constant strain, θ_i decreases linearly over the height, which leads to a linear decrease of the shear deformations predicted for each element. On the contrary, θ_{i0} is constant over the height if the strain is constant. In this case, however, the term with which the rotation is multiplied increases with the height. As the maximum $\Delta_{s,i}$ is the same as that obtained with the other mechanism each of the two mechanisms contributes to half the total deformation.

Hence, if the axial strain ε_l is constant the total shear deformation follows to be:

$$\Delta_s = \frac{\varepsilon_l l_{cr}^2}{2h} = \Delta_l \frac{l_{cr}}{h} \tag{3.20}$$

where Δ_l is the axial elongation of the pier. If the axial strain is linearly distributed between the base and $0.5 l_{cr}$ with maximum value ε_m at the base the shear deformation is:

$$\Delta_s = \frac{\varepsilon_m l_{cr}^2}{6h} = \frac{2}{3}\Delta_l \frac{l_{cr}}{h} \tag{3.21}$$

To render this approach applicable, two quantities still need to be predicted: The height over which cracking extends l_{cr} and the axial strain distribution (linear or constant). To get an estimate of the first, the data shown in Figure 3.28 is used again. As the plot shows, the shear deformation seems to be linearly dependent on the axial elongation. According to Equation (3.20), the term l_{cr}/h equals Δ_s/Δ_l. This means, the gradient of the linear relationship between shear deformation and axial elongation, which equals Δ_s/Δ_l, can be used to calculate l_{cr}, as the height of the test unit *h* is known. Figure 3.8 shows the data that was already shown in Figure 3.28, but this time the linear approximation and the gradient of this linear approximation are included. Table 3.9 shows the heights over which cracking extends l_{cr} that are calculated from the gradients assuming a constant axial strain, i.e. $l_{cr} = \text{grad} \cdot h$.

e Discussion of results

While the experimental data and predictions presented in Section 3.7.7 show that it should be possible to relate the shear deformation to the axial elongation of a test unit based on the rotation at shear cracks, the previous paragraph showed that the simple approach outlined herein needs further improvement. This section should hence not be regarded as presentation of a perfected model, but rather as an idea for a potential approach to estimate the shear deformations. Two issues that still need to be solved are how the height over which cracking extends, and thus the height over which shear deformations are expected to occur, is predicted and how a reasonable axial strain distribution is chosen.

3.8 Influence of lap-splices

3.8.1 Previously introduced stress and strain limits

The influence of a lap-splice at the base of the pier is considered based on the strain and stress levels introduced in Sections 2.7.3 and 2.7.4. The general modeling procedure is as outlined in Section 2.7.2, which means that the same plastic hinge modeling approach as for the piers without splice is used up to the onset of splice degradation. Hence, the difference between a model for a pier with and without splice lies merely in the assumed strain limits. Those strain limits for splices have either been derived for a certain drop of lateral resistance [6] or for the onset of splice degradation [50]. The stress limits can be used as an alternative to strain limits or, as in [31], to check whether the yield moment can be attained at all. Table 3.10 summarizes the stress and Table 3.11 the strain limits for piers VK2, VK4 & VK5.

If the distance between bars is taken into account in the stress criteria, the distance between the outer bars of the cross section is generally used, because these splices are expected to fail first. The concrete tension strength of VK2 was assumed to be $f_{ct} = 0.6\sqrt{35} = 3.5$ MPa and that of VK4 and VK5 was measured as 3.0 MPa and 3.3 MPa, respectively [3]. The stress limits determined by splitting failure are calculated with this concrete tension strength only, i.e. the additional force component of the stirrups in Equation (2.62) was not considered. Equation (2.63) was evaluated with $k_m = 8$ according to [63]. In [52] $k_m = 12$ is suggested for spliced bars placed in a hook of at least 90°, but no recommendations are made for other cases.

3.8.2 Additional strain limit

The confined concrete strain corresponding to peak stress is included in Table 3.11 for comparison with the previously introduced strain limits for concrete. While the strain limit according to Equation (2.28) [6] is intended as limit to determine the deformation corresponding to 20% degradation of lateral load, [50] estimate the strain corresponding to the onset of splice degradation. The argument for the latter limit is that the initiation of microcracking at peak stress weakens the concrete in tension and hence also the capacity of the

Table 3.10: *Maximum allowable stress in spliced bars according to splitting strength and bond stress criteria.*

Test unit	VK2	VK4	VK5
Eq. (2.58)	$\gg f_y$	$\gg f_y$	$\gg f_y$
Eq. (2.62)	$1.3f_y$	$1.1f_y$	$1.2f_y$
Eq. (2.63)	$1.3f_y$	$1.3f_y$	$1.3f_y$
Eq. (2.64)	$1.6f_y$	$1.6f_y$	$1.3f_y$
Eq. (2.58)	$f_s = 0.5s_l + 2\left(d_{bl} + c\right) f_{ct} l_s$		
Eq. (2.62)	$f_s = (l_{s,\mathit{eff}}[2c_{b,\mathit{eff}}k + 2c_{b,\mathit{eff}}(n_{bl} - 1)k]f_{ct})/(n_{bl}A_{sb}\tan\beta)$		
Eq. (2.63)	$f_s = 54\left(\frac{f_c}{25}\right)^{0.25}\left(\frac{25}{d_{bl}}\right)^{0.2}\left(\frac{l_s}{d_{bl}}\right)^{0.55}\left[\left(\frac{c_{min}}{d_{bl}}\right)^{0.33}\left(\frac{c_{max}}{c_{min}}\right)^{0.1} + k_m K_{tr}\right]$		
Eq. (2.64)	$f_s = ((l_s\sqrt{f_c})/(0.3d_{bl}f_y))f_y \leq f_y$		

Table 3.11: *Maximum allowable strains for sections with spliced bars.*

Test unit	VK2	VK4	VK5
[50]	$\varepsilon_{cu,s} = 0.002$	$\varepsilon_{cu,s} = 0.002$	$\varepsilon_{cu,s} = 0.002$
Eq. (3.3)	$\varepsilon_{cu,s} = 0.0031$	$\varepsilon_{cu,s} = 0.0033$	$\varepsilon_{cu,s} = 0.0033$
Eq. (2.28) (Tab.3.4)	$\varepsilon_{cu,s} = 0.0048$	$\varepsilon_{cu,s} = 0.0047$	$\varepsilon_{cu,s} = 0.0047$
Eq. (2.65)	$\varepsilon_{su,s} = 0.021$	$\varepsilon_{su,s} = 0.018$	$\varepsilon_{su,s} = 0.018$
Eq. (3.3)	$\varepsilon_{cc} = \left(1 + 5\left(\frac{f_{cc}}{f_c} - 1\right)\right)\varepsilon_c$		
Eq. (2.65)	$\varepsilon_{su,s} = \left(1.2\frac{l_s}{l_{su,min}} - 0.2\right)\varepsilon_{su}$		

concrete to confine the lap-splices. However, the peak stress f_{cc} and the corresponding strain ε_{cc} at which microcracking begins are larger if the concrete is confined. Therefore, ε_{cc} may also be considered a reasonable limit for the onset of splice degradation. To determine ε_{cc}, Equation (3.3) was employed together with the confinement effectiveness factor according to Equation (2.29), which is repeated here for convenience.

$$k_{con} = \left(1 - \frac{s}{2b_{con}}\right)\left(1 - \frac{s}{2h_{con}}\right)\left(1 - \frac{\sum s_{l,c}^2/6}{b_{con}h_{con}}\right)$$

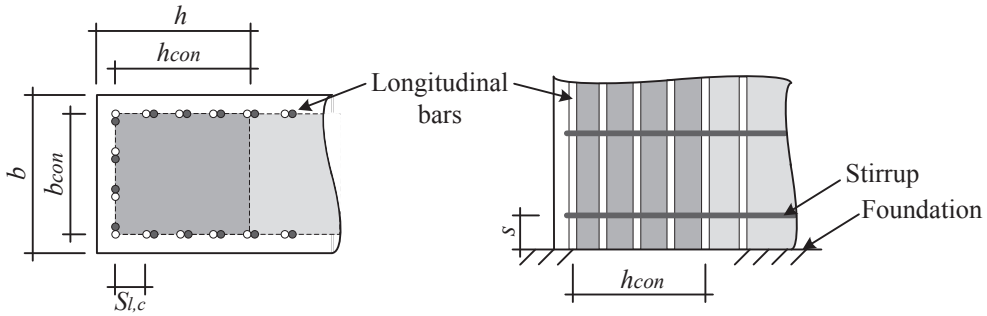

Figure 3.29: *Confined concrete in section with spliced reinforcement.*

As the piers do not have confined boundaries that could have been used to calculate the lateral confining stresses, the reinforcement in the outer square section of $350 \times 350\,\text{mm}$ was used, see Figure 3.29. The section right above the foundation is subjected to the highest bending moment and hence concrete crushing with subsequent splice failure may initiate right above the foundation. Therefore, the confined concrete strength needs to be estimated for this section. To do so, the foundation was treated like a stirrup in the sense that the distance between the foundation and the first stirrup above was assumed as stirrup spacing *s* and used for the calculation of the reinforcement ratio. It was also assumed that all longitudinal bars are restrained against lateral movement by the foundation and can hence be used to evaluate the third term in the above equation for k_{con}. The strain limits obtained with this calculation are included in Table 3.11 together with the previously mentioned limits.

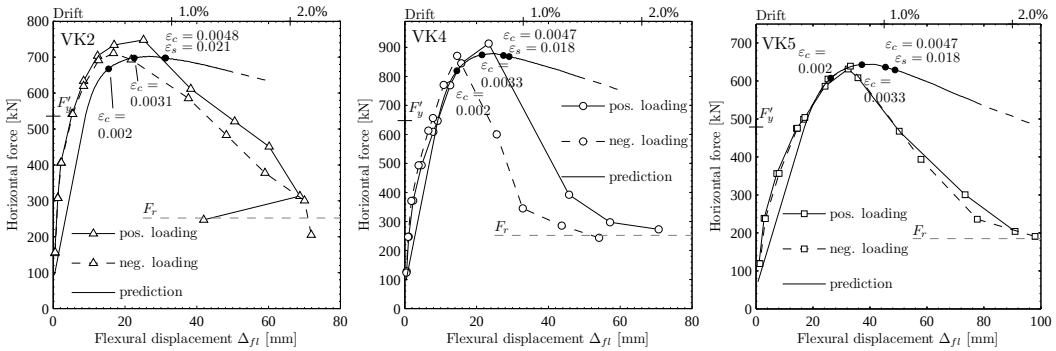

Figure 3.30: *Prediction of force-flexural displacement relations according to Eqs.* (2.38) *and* (2.9) *for test units with lap-splices compared to experimentally determined displacement. The markers indicate at which displacements the strain levels listed in Tab. 3.11 are reached.*

3.8.3 Computation of response

Table 3.11 shows that according to the evaluated splitting and bond stress criteria the lap-splices should be strong enough to sustain yield stress or even ultimate stress, which is $f_u = 1.17 f_y$. The lowest stress limits are predicted with Equation (2.62) which is rather sensitive to the tension strength of the concrete. With a tension strength of about 2.7 MPa, which is only about 10% lower than the concrete tension strength of VK4, splitting cracks are predicted to occur already at yield of the longitudinal reinforcement. The stirrups were neglected in the evaluation of this equation based on the argument given in [50]: They are activated only after the concrete cracks and neglecting them was assumed to yield a better estimate of the stress which causes development of the first cracks. As there is some scatter associated with the tension strength of concrete, one may come to the conclusion that, according to this criterion, the splices might not be strong enough to sustain yield load in reality. However, no experimental data is available to directly compare the stresses or strains that occurred in the tests with the criteria listed in Table 3.10 and 3.11. Even though the strains were measured, all measurement devices at the base of the pier cover also the basecrack which impairs their data.

Despite the above mentioned scatter, it was assumed that the yield stress can be reached. Hence, only the strain limits were set as boundaries for the outer fiber of a section in the moment-curvature analysis. The section analysis was made for a section with single reinforcement, i.e. the splices were not taken into account in any specific way, because the section right at the end of the splice is assumed to be the one that initiates failure as it is weaker. Figure 3.30 shows the predicted flexural top displacement compared to the experimental flexural displacements. The force capacity resulting from the eccentricity of the normal force according to Equation (2.57) is indicated with a gray dashed line. To compute the residual moment, an axial load of $P = 1300$ kN has been used for all test units and core dimensions were assumed corresponding to the center lines of the longitudinal reinforcement.

3.8.4 Discussion of results

With regard to the displacement at which degradation begins, several observations can be made for the examined test units: The strain limit $\varepsilon_c = 0.002$ [50], which intends to

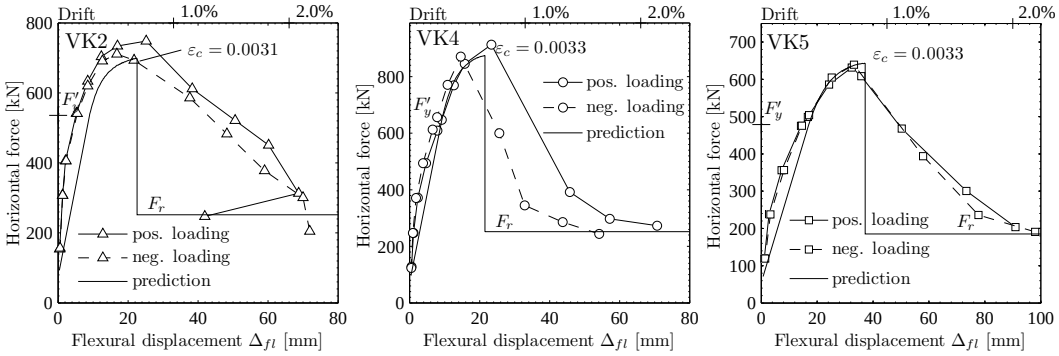

Figure 3.31: *Prediction of force-flexural displacement relations according to Eqs.* (2.38) *and* (2.9) *for test units with lap-splices compared to experimentally determined displacement.*

mark the onset of degradation, appears to be a rather conservative strain limit. This is also confirmed by local measurements above the basecrack, between 50 and 200 mm height, which even partially indicate higher strains before degradation begins. Hence, it seems too conservative to assume that a strain of $\varepsilon_c = 0.002$, reached only at the outer fiber of the section, causes sufficient damage to weaken the splices. On the other hand, the strain limits according to [6] in rows 3 and 4 of Table 3.11 correspond to a displacement that is reached just after the splices start degrading, according to the predictions. This seems logical as they are supposed to capture the point at which the force has dropped by 20%. While this was apparently a reasonable limit for the test units included in the database from which the limit was derived, it does not seem to be a good definition for the limit state of VK2 - VK5. Contrary to what [6] apparently observed in their database, the response of these piers is characterized by a rapid and not a slow degradation once the splice starts to loose strength.

Therefore, it seems reasonable to not assume a slow degradation in between the onset of splice failure and a larger ductility at which the residual capacity is reached, as also suggested by [50], but divide the response in only two parts: before and after degradation onset with an immediate drop of capacity in between. In the initial part of the response, the lap-splices are still intact and able to transfer the full load which means that globally the pier behaves like one with continuous reinforcement. After onset of splice degradation it enters the second part of the response in which the resistance corresponds to that provided by the eccentricity of the axial load. Strain limits similar to that of [50], which correspond to the onset of degradation, are hence necessary to compute the response.

For the three analyzed test units, the displacement at which the confined concrete strain according to Equation (3.3) (see Table 3.11) was reached provided the best estimate for the onset of degradation, see Figure 3.30. With this strain and the residual moment according to Equation (2.57), the responses shown in Figure 3.31 are calculated.

3.9 Force-deformation relationship

3.9.1 Computation of response

In the following, the complete force-deformation relationship including flexural and shear deformations is determined for the investigated piers. The plastic hinge length, strain limits and all other quantities that are necessary to obtain the response are chosen based on the results presented in the preceding sections. To compute the flexural response, Equation (2.38) [7] was used. This equation allows predicting the envelope of the force-deformation response and not merely a bilinear approximation. This equation was evaluated in combination with the plastic hinge length according to Equation (2.9) [4]. Both equations are repeated here for convenience:

$$\Delta_{cr} = \phi_{cr} L_s^2/3$$
$$\Delta'_y = \phi'_y L_s^2/3$$
$$\Delta_{fl} = \Delta'_y \frac{M}{M_y} + \left(\phi - \phi'_y \frac{M}{M_y}\right) L_p L_s$$

with

$$L_p = (0.2h + 0.05L_s)\left(1 - 1.5\frac{P}{A_g f_c}\right) \leq 0.8h$$

With this plastic hinge length, good estimates of the flexural deformation were obtained, as shown in Section 3.6. Strain penetration was not considered, since the flexural deformations were overestimated with the approaches that explicitly account for this effect. The deformation capacity, corresponding to a point that is reached shortly after the peak load before the onset of significant degradation, is defined based on the attainment of the concrete and steel limit strains according to Equations (2.28) and (2.30) [6]:

$$\varepsilon_{cu,cyc} = 0.0035 + \left(\frac{1}{x_{c,con}}\right)^{3/2} + 0.4\frac{k_{con}\varrho_v f_{yv}}{f_{cc}}$$
$$\varepsilon_{su,cyc} = \frac{3}{8}\varepsilon_{su} = 0.375\varepsilon_{su}$$

The confinement effectiveness factor k_{con} is calculated using Equation (2.29). These limits yielded slightly higher estimates of the limit curvature and thus a little less conservative estimates of the deformation capacity than the limits according to Equations (2.26) and (2.27).

As Section 3.7.4 shows, the models that were reviewed for the estimation of the Δ_s/Δ_{fl} ratio yield similar results, if some modifications were made. To illustrate the determination of the complete response, the Δ_s/Δ_{fl} ratio will here be included based on Equation (3.5) (modified approach according to [8]), which directly relates the ratio to the axial strain:

$$\frac{\Delta_s}{\Delta_{fl}} = 0.75\alpha\frac{\varepsilon_l}{\tan\theta\phi}\frac{1}{L_s} = 0.75\alpha\frac{\varepsilon_l}{\sqrt[4]{\frac{\varrho_v + k_E\varrho_l\varrho_v}{\varrho_l + k_E\varrho_l\varrho_v}}\phi}\frac{1}{L_s}$$

The ratio was determined for each curvature based on the corresponding axial strain and moment obtained from the M-ϕ analysis. That means contrary to what was suggested in the original approaches, no constant ratio was assumed in the inelastic range. Shear deformation was only considered after F'_y was exceeded because shear deformations seemed negligible for smaller forces, also in light of the inaccuracies of both the experimental data and the predictions at very small displacement levels. Hence, there is a little kink in the predicted responses as they pass from flexural deformation only to flexural and shear deformation. In the inelastic range, the total deformation $\Delta = \Delta_s + \Delta_{fl}$ is hence evaluated according to the following equation:

$$\Delta = \left(\Delta'_y \frac{M}{M_y} + \left(\phi - \phi'_y \frac{M}{M_y} \right) L_p L_s \right) \left(1 + 0.75\alpha \frac{\varepsilon_l}{\sqrt[4]{\frac{\varrho_v + k_E \varrho_l \varrho_v}{\varrho_l + k_E \varrho_l \varrho_v}} \phi} \frac{1}{L_s} \right)$$

$$1 \leq \alpha = \left(\frac{V}{V_n} + \frac{V}{V_{wc}} \right) \leq 2$$

If the test unit had a lap-splice at the base, the strain limit according to Equation (3.3) [5] was used in combination with Equation (2.29) [34]:

$$\varepsilon_{cc} = \varepsilon_c \left(1 + 5 \left(\frac{f_{cc}}{f_c} - 1 \right) \right)$$

$$f_{cc} = f_c \left(-1.254 + 2.254 \sqrt{1 + \frac{7.94 f'_l(k_{con}, \varrho)}{f_c}} - 2 \frac{f'_l(k_{con}, \varrho)}{f_c} \right)$$

$$k_{con} = \left(1 - \frac{s}{2b_{con}} \right) \left(1 - \frac{s}{2h_{con}} \right) \left(1 - \frac{\sum s^2_{l,c}/6}{b_{con} h_{con}} \right)$$

Figure 3.32 shows the results obtained with the procedure summarized in this section for the investigated seven test units. All responses were determined up to the limit strain. For comparison, the deformation at which this limit strain is reached in the experiments is indicated with a black marker in the plots.

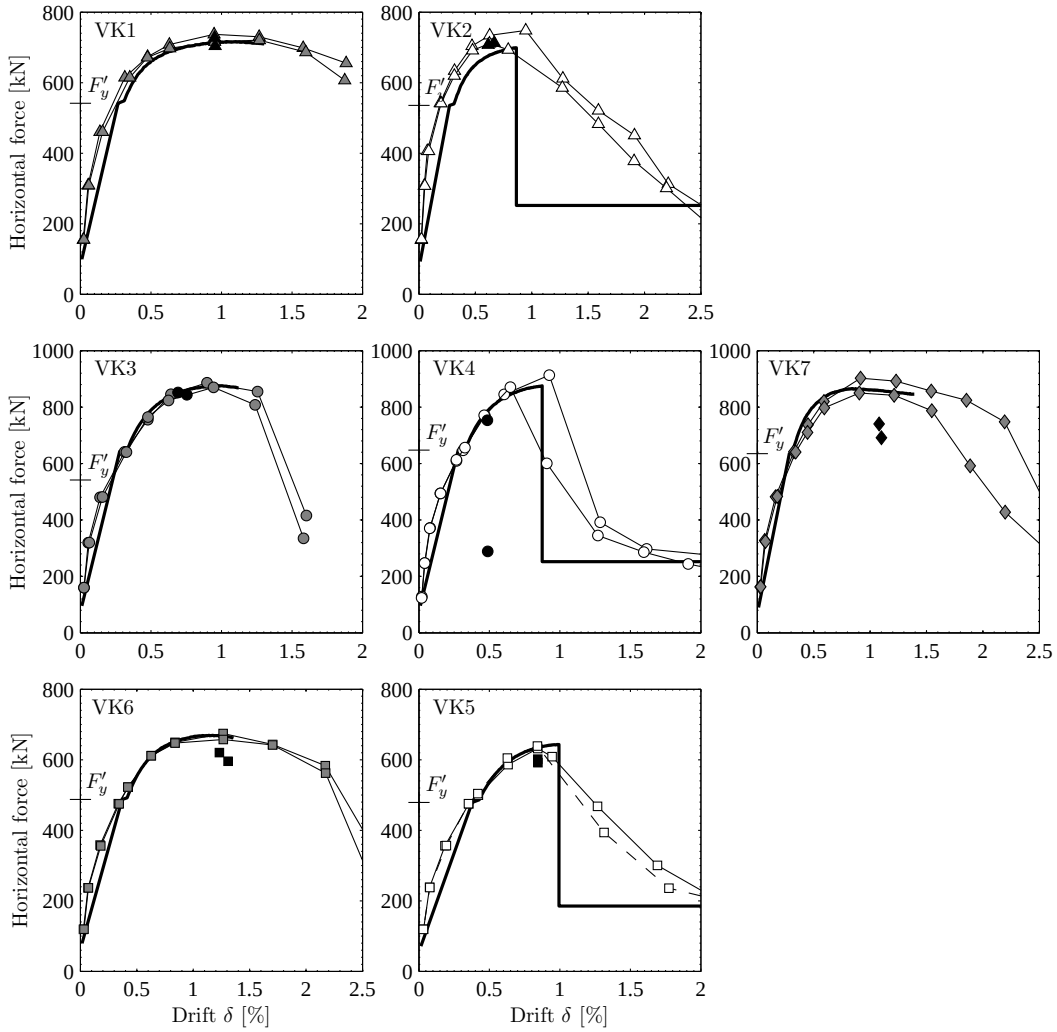

Figure 3.32: *Predicted and measured response.*

3.9.2 Discussion of results

In Figure 3.32 one can see that even though the modeling is based on relatively simple assumptions the response is predicted reasonably well. The deformations at which the predicted limit strains were, according to the LVDT readings, first reached in the experiment in both positive and negative loading are indicated with black markers. Those strains were not necessarily reached at peak load and during first cycles. As a result, the markers may lie well below the envelope of the response. Except for VK6, the displacement that is predicted for the limit strain level is up to 33% larger than the measured one (VK3). As indicated previously, the strain limit for VK7 is rather high and a different strain had thus been considered in Figure 3.13 for comparison with the experimental data. This time, for comparison, the experimental deformation corresponding to this strain limit is included. Generally, as indicated previously, the strain limits yield a rather conservative estimate of the deformation capacity. However, VK3 failed shortly after the predicted deformation capacity in a shear mechanism (see [1]). Since the latter cannot be accounted for within plastic hinge

analysis and limits other than those based on strain are difficult to incorporate, the applied limits hence seem to be a reasonable choice.

For the test units with spliced reinforcement concrete limit strains have been used, as the splice failure was initiated by damage in compression. VK5 was an exception in the tests, as failure of the splice was not initiated by a previous damage of the concrete in compression. Consequently, the deformation capacity is overestimated by using a compressive limit strain. However, according to the estimates for the tensile force capacity of the lap-splice that were evaluated here, the length of the splice should be sufficient to transfer the maximum possible load, see Table 3.10. No further insight into what could have triggered failure of that splice was gained from the experimental data of the large scale tests. Hence, a series on test units that are instrumented in more detail with lap-splices corresponding to those of the large scale tests has been initiated [64].

As evident in Section 3.7, an exact prediction of the shear deformations within the scope of plastic hinge analysis appears difficult. Simplifying assumptions made in some models to estimate the shear to flexural deformation ratios of well detailed piers, such as a concentration of shear deformations in the plastic hinge and a constant ratio over the entire ductility range, do not hold for the investigated piers. However, satisfactory results were obtained through modification of existing models to estimate the shear to flexural deformation ratio. Especially in light of the simplicity of the plastic hinge modeling approach, the quality of the predicted deformations appears to be good.

3.10 Conclusions

Based on comparison with the experimental data, a plastic hinge modeling approach was identified with which very good agreement of the flexural deformation was obtained. The predictions of the flexural deformation were made with the refined approach according to Equation (2.38) [7] in combination with the plastic hinge length according to Equation (2.9), that was explicitly developed for walls by [4]. To define the deformation capacity, the strain limits according to [6] were used as they were larger than the ones according to [7] in the examined cases. Nevertheless, they still yield conservative estimates of the deformation capacity, corresponding to a point shortly after peak shear force. For a less conservative estimate of the deformation capacity, a change in the mechanism needed to be taken into account in most cases, as all test units with continuous reinforcement, except for VK7, eventually failed in shear or a combined flexure-shear mode. This mechanism can, however, not be accounted for within the scope of plastic hinge modeling, and models such as the one presented in Chapter 5 are necessary. Based on the test data of VK7 alone, no additional limit for an ultimate flexural state that marks the onset of a severe degradation of the compression zone could be established.

Regarding the shear deformation, one critical point in the two reviewed models that predict the shear to flexural deformation ratio Δ_s/Δ_{fl} was the dependency on the measured crack angles. If the models were employed with a crack angle estimate accounting for the reinforcement contents and a correction factor accounting for the shear resistance of the pier, satisfactory predictions were obtained with both of them. However, both models do then partially rely on some correction factors, which might not be regarded an optimum solution and is linked to a certain scatter.

Besides the existing approaches that aim at predicting Δ_s/Δ_{fl}, an approach that relates the shear deformation to the axial elongation of the pier was investigated. While the preliminary results appear promising, this approach needs further development to be applicable within

the scope of plastic hinge modeling. However, comparison with the experimental data showed that the mechanism the approach is based on appears reasonable. Furthermore, it was shown that the prediction of the axial elongation of the piers agrees well with the experimentally determined one.

With regard to the influence of lap-splices at the base of the pier it was observed that the global response of these test units is the same as that of corresponding test units with continuous reinforcement until the degradation of the splice sets in. Hence, the influence of the lap-splices on the behavior could easily be accounted for with a strain limit corresponding to the peak strain of confined concrete. Once this limit is exceeded, the shear force resistance decreases quickly. For this reason, the resistance is assumed to drop to its residual value which depends on the maximum eccentricity of the axial load. This limit is applicable for lap-splices without confinement that are long enough to sustain the maximum force in tension. It may be regarded as an upper bound limit for these splices and further research is required to investigate whether e.g. certain loading conditions can cause a splice failure in tension before this limit is reached.

4 Review and application of shear-strength degradation models

4.1 Introduction

This chapter presents a brief overview of various types of shear strength degradation models for RC members. It is beyond the scope of this work to provide a complete summary of existing models. Instead, only some modeling approaches which are commonly used in earthquake engineering will be presented as examples.

Generally, three types of shear behavior and failure modes under seismic loading can be distinguished [65]: A brittle shear failure occurs if the shear capacity is lower than the shear demand imposed on the member by the formation of a flexural hinge. In this case, the member fails at relatively small displacements before its flexural capacity is reached. Shear failure in the inelastic range may occur if the shear capacity is decreasing more rapidly than the shear demand with increasing deformations. If the shear capacity is higher than the shear demand in the entire deformation range the member will eventually fail in flexure. The emphasis in this chapter will be on shear failure in the inelastic range, since it is the type of shear failure observed in the experiments that were conducted in the framework of this project [3, 1].

As mentioned, it is commonly recognized that the shear strength of a RC member is decreasing under cyclic loading for several reasons [66]: (i) The resistance provided by aggregate interlock is decreasing due to increased crack widths and grinding of the crack surfaces under cyclic loading; (ii) the shear resistance of the compression zone is reduced by the formation of flexural cracks; (iii) the resistance due to dowel action is decreasing due to the formation of plastic strains; (iv) the development of plastic strains in the reinforcement weakens the capacity of the compression strut, because the tensile strains perpendicular to the strut increase.

In the following section, ductility-dependent shear strength models will be presented. This type of models includes a, typically empirically determined, ductility-dependent factor with which the shear strength in the inelastic range is reduced. Those models are based on the above mentioned observation that the resistance gradually decreases under cyclic loading with increasing displacement amplitudes and is commonly used in earthquake engineering. In the subsequent section, examples of drift capacity models are presented. These models aim at estimating either the deformation capacity corresponding to the loss of lateral resistance or to the loss of axial load bearing capacity. Drift capacity models are generally derived from an experimental database, for instance by least square datafitting. Section 4.2.3 introduces a model which takes into account the shear capacity of the transverse reinforcement and the compression zone. The latter is based on the plastic limit of concrete using Rankine's failure criterion. Section 4.2.4 shows an approach which treats the section of a column between maximum moment and inflection point as shear panel. Both the interaction between the shear and the flexural mechanism and the deformation components due to both mechanisms are determined that way.

4.2 Shear-strength degradation models

4.2.1 Shear-capacity models dependent on ductility

Several researchers have developed shear capacity models on the basis of strut-and-tie models that comprise also a ductility dependent correction factor, e.g. [67, 68, 10, 69, 70]. Unlike the initial capacity, which is composed of the resistance of different load bearing mechanisms, the degradation is mostly empirically determined. Concerning the degradation, the models basically differ with regards to whether only the concrete or also the transverse reinforcement component is assumed to degrade.

According to the “revised UCSD model” [10], which is a further development of the model presented in [68], only the concrete component degrades. Originally, the model was developed for circular columns and validated with a database containing all of the three above mentioned failure types. However, modifications of the geometrical relations make it also applicable to rectangular columns [7]. The shear capacity V_r is assumed to be the sum of a transverse steel truss component V_s, the concrete shear strength V_c and a component V_p which is accounting for the inclination of the compression strut of the axial load.

$$V_r = V_s + V_c + V_p \tag{4.1a}$$

$$V_s = A_v f_{yv} \frac{h - x_c - c}{s} \cot\theta \tag{4.1b}$$

$$V_c = \alpha\beta k_\mu \sqrt{f_c} 0.8 A_g \tag{4.1c}$$

$$V_p = \max\left(P\frac{h - x_c}{2L_s}, 0\right) \tag{4.1d}$$

where *h* is the total section depth, x_c the compression zone depth, *c* the concrete cover measured to the center of the transverse reinforcement, *s* the transverse reinforcement spacing and θ the crack angle. If the member is under tension, and hence the axial load negative, V_p is set to zero. The factors α, β and k_μ are empirically determined values which are introduced to consider the influence of the aspect ratio L_s/h, longitudinal reinforcement content ϱ_l and ductility demand.

$$1 \leq \alpha = 3 - \frac{L_s}{h} \leq 1.5 \tag{4.2a}$$

$$\beta = 0.5 + 20\varrho_l \leq 1.0 \tag{4.2b}$$

An increasing longitudinal reinforcement content is assumed to have a beneficial effect on the shear force capacity for the following reasons: First, the resistance due to dowel action increases. Second, the compression zone depth and thereby its shear resistance increase and third, the crack width is reduced because of a finer, more evenly distributed crack pattern. To incorporate the ductility dependency in the shear force capacity model two relations for the factor k_μ are proposed for the assessment of members subjected to uniaxial loading. One is dependent on curvature ductility μ_ϕ and the other on displacement ductility μ_Δ:

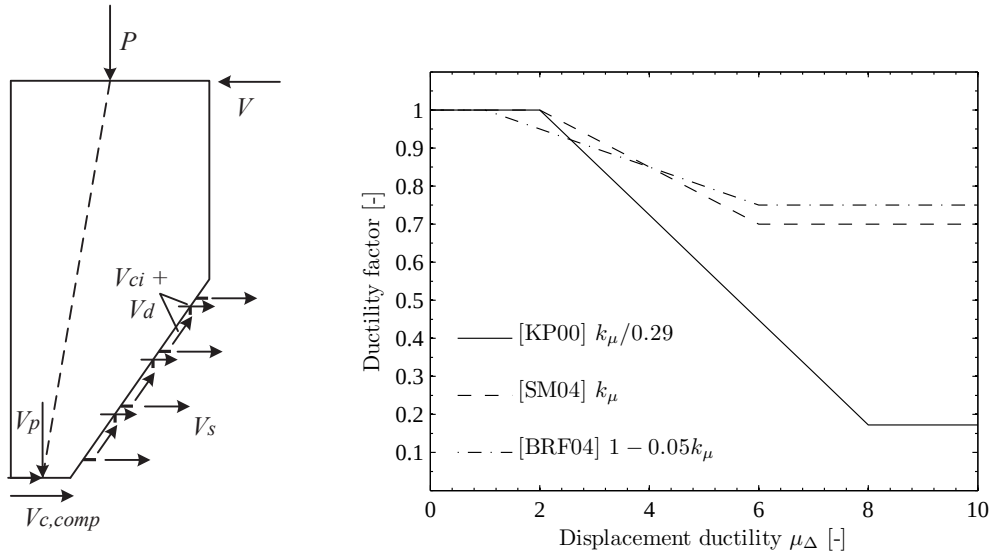

(a) Load bearing mechanisms **(b)** Ductility dependency

Figure 4.1: *Resistance of the compression zone $V_{c,comp}$, aggregate interlock V_{ci} and dowel action V_d, which are illustrated in (a), are commonly implicitly included in V_c. The ductility dependency is illustrated in (b).*

$$k_\mu = \begin{cases} 0.29 & \text{if } \mu_\phi \leq 3 \\ 0.29 - \dfrac{0.24(\mu_\phi - 3)}{12} & \text{if } 3 < \mu_\phi < 15 \\ 0.05 & \text{if } \mu_\phi \geq 15 \end{cases} \quad (4.3) \qquad k_\mu = \begin{cases} 0.29 & \text{if } \mu_\Delta \leq 2 \\ 0.29 - \dfrac{0.24(\mu_\Delta - 2)}{6} & \text{if } 2 < \mu_\Delta < 8 \\ 0.05 & \text{if } \mu_\Delta \geq 8 \end{cases} \quad (4.4)$$

Unlike in the “revised UCSD model”, not only the concrete component but also the transverse reinforcement component is assumed to degrade in the model proposed by [69], see Equation (4.5). Deterioration of both bond and anchorage of stirrups are stated as reasons for this. Just as in the previous model, an increase of shear strength with decreasing aspect ratio as well as a beneficial effect of an axial compression force is included. An increasing strength with increasing longitudinal reinforcement ratio has on the contrary not been observed in the test data used for validation and is thus not incorporated. Diagonal compression failure was assumed to be decisive only for short columns with a high axial load ratio. In all other cases, tensile shear failure was assumed to be the mechanism governing failure. Hence, the concrete component was determined from Mohr’s circle based on the assumption that the maximum capacity is reached when the principal tensile stress equals the tensile strength of concrete.

$$V_r = k_\mu \left(V_s + V_c\right) \quad (4.5a)$$

$$V_s = \frac{A_v f_{yv} d}{s} \quad (4.5b)$$

$$V_c = \left(\frac{0.5\sqrt{f_c}}{L_s/d} \sqrt{1 + \frac{P}{0.5\sqrt{f_c} A_g}} \right) 0.8 A_g \quad (4.5c)$$

Note that the aspect ratio is related to the effective section depth *d* rather than h in this case and that the axial load *P* is included in the concrete component. The ductility dependent degradation factor in this model is:

$$k_\mu = \begin{cases} 1.0 & \text{if} \quad \mu_\Delta < 2 \\ 1.0 - 0.3\dfrac{\mu_\Delta - 2}{4} & \text{if} \quad 2 \leq \mu_\Delta \leq 6 \\ 0.7 & \text{if} \quad \mu_\Delta > 6 \end{cases} \tag{4.6}$$

Another model of this kind was developed based on test data of 239 cyclic tests which exhibited a tensile shear failure after flexural yielding [66]. The database included circular and rectangular columns, beams and six walls. Two models were proposed whose empirical factors were determined by statistical data-fitting, one in which merely the concrete component was assumed to deteriorate, as in [10], and one in which degradation was assumed for concrete and steel truss, similar to [69]. Only the latter is presented herein as it is reported to yield better results. The degradation was incorporated based on the ductility $\mu_\Delta^{pl} = (\theta_{u,exp} - \theta_{y,exp})/\theta_{y,calc}$ with the rotation $\theta_{y,calc}$ according to Equation (4.7), which corresponds to the drift of beams and columns at first yield in [24]. Contrarily to this, experimental ductilities were used in the above mentioned model by [69] and no information is given for the “revised UCSD model”. For an explanation of the components included in Equation (4.7) the reader is referred to Section 2.5.1.

$$\theta_{y,calc} = \phi'_y \frac{L_s + k_v z}{3} + 0.0013\left(1 + 1.5\frac{h}{L_s}\right) + k_{sl}\frac{0.13\phi'_y d_{bl} f_y}{\sqrt{f_c}} \tag{4.7}$$

The steel truss component is calculated based on the transverse reinforcement content ϱ_v, internal lever arm *z* and a crack angle of 45° as follows:

$$V_s = \varrho_v b z f_{yv} \tag{4.8}$$

The total shear capacity is calculated as sum of the steel truss component and the concrete component and includes empirical factors accounting for the influence of the normal force, longitudinal reinforcement content, aspect ratio and displacement ductility:

$$V_r = \frac{h - x_c}{2L_s} k_1 + (1 - 0.05k_\mu)\left[0.16k_2(1 - 0.16k_3)\sqrt{f_c}A_g + V_s\right] \tag{4.9a}$$

$$k_1 = \min(P, 0.55A_g f_c) \tag{4.9b}$$

$$k_\mu = \min(5, \mu_\Delta^{pl}) \tag{4.9c}$$

$$k_2 = \max(0.5, 100\varrho_l) \tag{4.9d}$$

$$k_3 = \min(5, L_s/h) \tag{4.9e}$$

4.2.2 Drift capacity models

When the force - deformation behavior of a structure is computed, the points at which either shear or axial load failure occur are of particular interest. The former is commonly defined as a certain drop of shear resistance and the latter as a loss of both horizontal and axial load bearing capacity. Since the models introduced in Section 4.2.1 are used to compute shear capacity curves, one might conclude they could be employed to determine the point of

shear failure. However, this is typically not recommended by their authors, e.g. [69, 66, 71] because the capacity curves have low gradients and hence a potential intersection with a force-deformation relationship would occur at a low angle. Small variations in the shear capacity relation then result in large variations of the predicted displacement at which shear failure occurs.

Therefore, drift capacity models which aim at directly predicting the drift at which failure occurs have been developed. Different failure criteria, such as Coulomb's failure criterion in conjunction with the mean stress of a section [72], strain limits for curvatures [73] or empirically determined dependence on parameters influencing the drift capacity, such as axial load level $n = P/(A_g f_c)$ and transverse reinforcement content ϱ_v [74, 75, 76], have been established. Examples of the latter type of models are presented in Equation (4.10) [76] and Equation (4.11) [75] which have been derived by nonlinear regression and least-square error fit of experimental data, respectively. Both define drift capacity as the drift corresponding to a 20% drop in lateral load resistance.

$$\left(\frac{\Delta}{L_s}\right) = 0.564 + 8.489k_1 - 7.804k_1^2 \tag{4.10a}$$

$$k_1 = (1 + L_s/h)\left(1 - \sqrt{\frac{P}{A_g f_c}}\right)\sqrt{\frac{\varrho_v f_{yv}}{f_c}} \tag{4.10b}$$

$$\left(\frac{\Delta}{L_s}\right) = \frac{3}{100} + 4\varrho_v - \frac{1}{41.52}\frac{v}{\sqrt{f_c}} - \frac{1}{40}\frac{P}{A_g f_c} \geq \frac{1}{100} \tag{4.11}$$

Besides determining the displacement at shear failure, it is also important to determine the displacement corresponding to the loss of axial load bearing capacity. To predict the latter and also to estimate the gradient of strength degradation after shear failure, a formulation based on the degrading shear friction resistance of the critical diagonal crack is suggested by [74], see Equation (4.12). The friction coefficient is expressed in dependence of the drift ratio which depends on the transverse reinforcement ratio. The drift ratio at failure is the intersection with the x-axis according to Equation (4.12a) and the degrading capacity with Equation (4.12b):

$$\left(\frac{\Delta}{L_s}\right)_{axial} = \frac{4}{100}\frac{1 + \tan^2\theta}{\tan\theta + P\left(\frac{s}{A_v f_{yv} h_{con}\tan\theta}\right)} \tag{4.12a}$$

$$\frac{dV}{d\left(\frac{\Delta}{L_s}\right)} = \frac{-25P}{1 + \tan^2\theta}\left(\frac{A_v f_{yv} h_{con}}{Ps}\tan^2\theta + 1\right)^2 \quad \text{with} \quad \theta = 65° \tag{4.12b}$$

where h_{con} is the depth of the confined core defined by the centerlines of the stirrups.

Due to their empirical nature, the use of the models presented in this section is restricted to RC members with the same characteristics as those they were calibrated against, which renders their possible application range rather narrow. Typically, columns were used for the derivation of the models and shear and axial stresses are thus high in comparison to those of walls, for instance.

4.2.3 Truss model with plastic limits

The shear capacity of columns corresponds to the sum of the transverse steel resistance and the shear resistance of the compression zone, according to the model by [77]. Aggregate interlock and dowel action were considered to be of minor importance. Unlike in the previously mentioned approaches of that type, the degradation of the concrete component is not determined empirically but based on Rankine's failure criterion (see Figure 4.2). The strain distribution in the compression zone is obtained from moment curvature analysis and the stress distribution is determined based on the strain. The allowable shear stress at each point in the compression zone is calculated from Mohr's circle as the capacity left until the principal stress exceeds either compression or tensile strength of the concrete according to Equation (4.13), see also Figure 4.2.

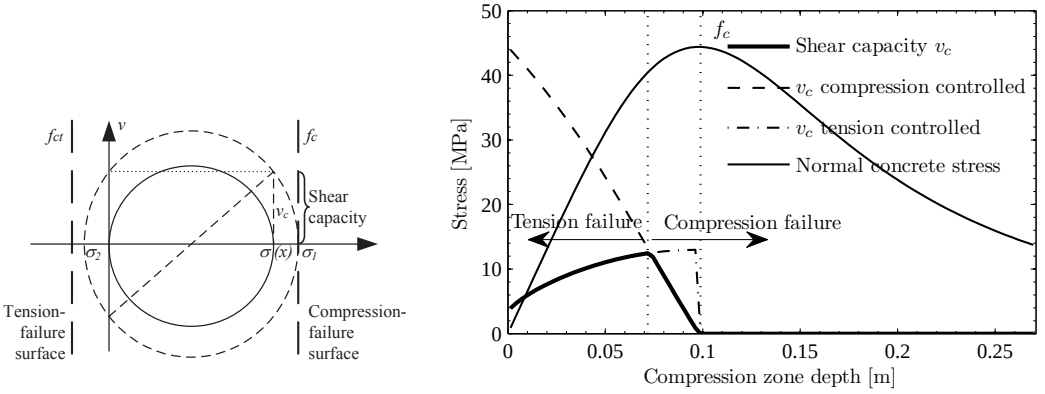

(a) Rankine's failure criterion for concrete.

(b) Shear and axial stress distribution in the compression zone of the section.

Figure 4.2: *Assumptions underlying the model by [77]*

$$V_c = \int_0^{x_c} v_c(x) b dx = \begin{cases} \int_0^{x_c} \sqrt{f_c(f_c - \sigma(x))} & \text{compression failure} \\ \int_0^{x_c} \sqrt{f_{ct}(f_{ct} + \sigma(x))} & \text{tension failure} \end{cases} \tag{4.13}$$

where v_c is the shear stress capacity of concrete, f_c and f_{ct} are the concrete compression and tension strength, respectively, and $\sigma(x)$ is the axial stress. The total shear capacity is the sum of the concrete component V_c and the steel truss component V_s:

$$V_s = \varrho_v b d_{e1} f_{yv} \cot\theta \tag{4.14}$$

where d_{e1} is the effective depth measured between the centerlines of the outer longitudinal reinforcement layers and θ is the crack angle. For the latter, 35° were recommended. Furthermore, strain limits for bar buckling as well as bar rupture were proposed and the deformation was computed using a plastic hinge approach with decreased elastic stiffness to account for slip and shear deformations according to [78]. Note that this model was developed for columns and the authors state that the model still needs verification for structures with different characteristics [77]. All listed criteria are met by test units VK1-VK7 except for the required longitudinal reinforcement ratio, which is higher than that of the examined test units.

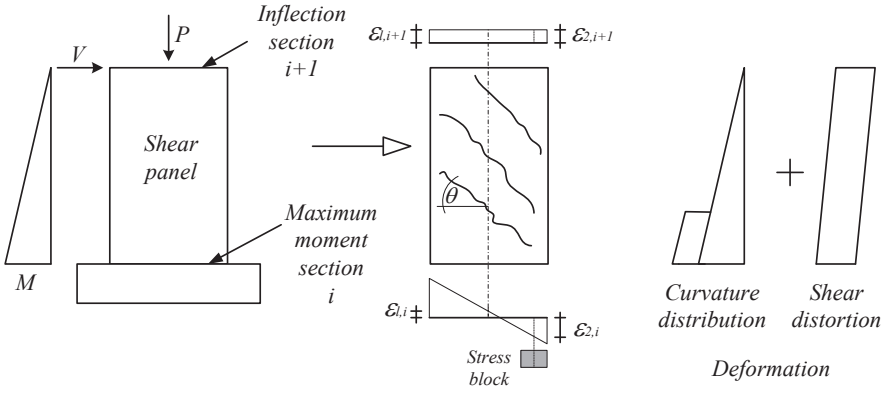

Figure 4.3: *Fundamentals of USFM method (after [83]).*

4.2.4 Shear - flexure interaction model

An approach in which flexural response of a column, obtained from section analysis of a uniaxial fiber element, is combined with the shear response obtained from a biaxial shear panel has been proposed as “axial-shear-flexure interaction” (ASFI) model in [79, 80] and simplified to a “uniaxial-shear-flexure model” (USFM) in [81, 82]. Originally, the approach included a full analysis of the shear panel according to the MCFT. In the more recent publications [81, 82], simplifying assumptions regarding the axial strain and principal compression strain were made with which an iterative calculation of the shear response was eliminated. Both versions of the model are based on two section analyses carried out at the point of inflection and at the point of maximum moment. The element bound by those two sections is regarded as shear panel subjected to the average stresses obtained from the two section analysis. All further calculations in the model are made for this shear panel. Figure 4.3 visualizes some basic assumptions of the USFM method.

Two sources of strength degradation are included in the model: Compression softening of concrete due to transversal strains stemming from the combined action of flexure and shear as well as degradation of the stresses transferred across cracks due to crack opening. The two main assumptions, which enable the simplified calculation without iterations, concern the axial and principal strains. Firstly, it is assumed that the principal compressive strain ε_2 in the shear panel corresponds to the average strain at the center of the compression stress block determined from section analysis. Secondly, the axial strain $\varepsilon_{l,cl}$ is assumed to be the average axial strain at the center line obtained from the two section analysis.

$$\varepsilon_2 = 0.5(\varepsilon_{c,i} + \varepsilon_{c,i+1}) \tag{4.15a}$$

$$\varepsilon_{l,cl} = 0.5(\varepsilon_{l,cl,i} + \varepsilon_{l,cl,i+1}) \tag{4.15b}$$

The axial strain at the center line that are due to shear $\varepsilon_{l,cl,sh}$ could be added to the latter equation but, as stated in [81], this has generally little effect on the final result. Indices *i* and *i+1* denote sections *i* and *i+1* for which section analysis is performed, ε_c is the strain corresponding to the concrete stress block, *l* is the longitudinal axis and *cl* denotes the center line of the member. Relations adapted from the MCFT are then used to calculate

concrete and steel stresses f_{c1}, f_{cy} and f_{sy} as well as the principal tensile strain $\varepsilon_1 = \varepsilon_l + \varepsilon_v - \varepsilon_2$, which is needed to obtain the compression softening factor β.

$$\beta = \frac{1}{0.8 - 0.34\frac{\varepsilon_1}{\varepsilon_{c0}}} \tag{4.16}$$

where ε_{c0} is the concrete strain at peak stress. The stress that can be transferred across a crack and hence the overall shear force is limited by what can be transferred via aggregate interlock and the reinforcement crossing the crack:

$$v_{max} = v_{c,i} + f_{yv}\varrho_v \cot\theta \tag{4.17a}$$

$$v_{c,i} = \frac{0.18\sqrt{f_c}}{0.31 + 24w/(a_g + 16)} \tag{4.17b}$$

where a_g is the maximum aggregate size and ϱ_v and f_{yv} are the transverse reinforcement content and yield strength, respectively. To obtain the overall deformation, the drift due to flexure θ_f, shear θ_s and anchorage slip θ_{slip}, if applicable, are added. The flexural deformation is calculated by means of a plastic hinge model. The shear distortion of the shear panel is equal to the drift due to shear.

$$\theta_{tot} = \theta_f + \theta_s + \theta_{slip} \tag{4.18}$$

with

$$\theta_f = \frac{\Delta}{L_s} = \frac{1}{L_s}\int_0^{L_s} x\phi(x)dx \tag{4.19a}$$

$$\theta_s = \frac{2(\varepsilon_l - \varepsilon_2)}{\tan\theta} \tag{4.19b}$$

where $\phi(x)$ is the curvature distribution along the longitudinal axis. Originally, an approach by Okamura and Maekawa was proposed by the authors to calculate the slip.

To assess the performance of the USFM, the latter was implemented on the basis of a moment-curvature analysis procedure as outlined in [81] for VK1-VK7. Hence, the moment was not calculated using the concrete stress block and the material models were the same as those used in Section 3.5. The secondary shear crack check introduced in [82], which deals with the response of a column subjected to double-curvature at the inflection point, was not included. Instead of including a slip component, the flexural deformation was again calculated according to [7], where the influence of strain penetration is included in the plastic hinge length. The reader is referred to Section 4.3 for an illustration and evaluation of the results obtained with the USFM according to the procedure outlined in this paragraph.

4.3 Application of models to test units

4.3.1 Introduction

To asses their performance, the results obtained with the shear and drift capacity models described in Section 4.2.1 to 4.2.4 were compared to the experimental results. Test units VK6 and VK7 are chosen for the comparison. VK6 did fail in a flexural-shear mode, which means it exhibited severe damage along a diagonal crack accompanied by failure of the compression zone. On the contrary, VK7 failed in flexural compression and the shear cracks did not open significantly during the experiment. Hence, the capacity predicted with all models should exceed the measured resistance of this test unit, whereas the predictions for VK6 should capture the degrading branch of the response. However, one needs to bear in mind that none of the models was specifically developed for wall type structures but rather for columns and beams. Although the models are therefore, strictly speaking, applied outside their original scope, they are examined here as corresponding models for walls are currently lacking.

4.3.2 Ductility dependent models

Figure 4.4 shows the comparison between the predictions according to the models presented in Section 4.2.1 and the experimentally determined force-displacement envelopes in positive and negative loading direction. The predicted shear force capacities for test unit VK7 exceed the measured ones in the entire deformation range, as it was expected. While the model according to [10] predicts a capacity that is significantly higher than the measured resistance, the capacity according to [42] and [66] is only slightly higher than measured. Nevertheless, each of the three models correctly implies that flexural failure occurs eventually. The latter two models consider, besides a degradation of the concrete component, also a degradation of the resistance of the transverse reinforcement. Comparison of the predictions with the experimental data of VK6 visualizes well the above mentioned issue regarding the glancing intersection of the force-displacement response and the shear capacity curve. The predicted gradient of the shear strength degradation of [42, 66] agrees well with the experimental degradation right after attainment of the peak value. However, as evident in Figure 4.4, it would not be possible to define a certain drift as displacement capacity. Even though the initial degradation is captured well by the two mentioned models, the onset of stronger degradation is not predicted by any of the two.

4.3.3 Drift capacity models

As mentioned previously, drift capacity models aim at directly predicting the drift at which failure occurs rather than the degradation of shear mechanisms. Failure is typically defined as a certain drop in lateral resistance, or, as in the axial capacity model [74], as loss of axial load bearing capacity. However, Figure 4.5 shows that the capacities predicted for both test units significantly exceed the measured ones. The main reason for this might be that these empirical drift capacity models are derived from databases containing experimental data of columns and not walls. While the criteria for application are formally met for the drift capacity model by [75], the other two models are actually applied outside their scope. The axial capacity model was originally validated against the columns tested by [84] and [85] which had higher aspect and longitudinal reinforcement ratios as well as lower steel

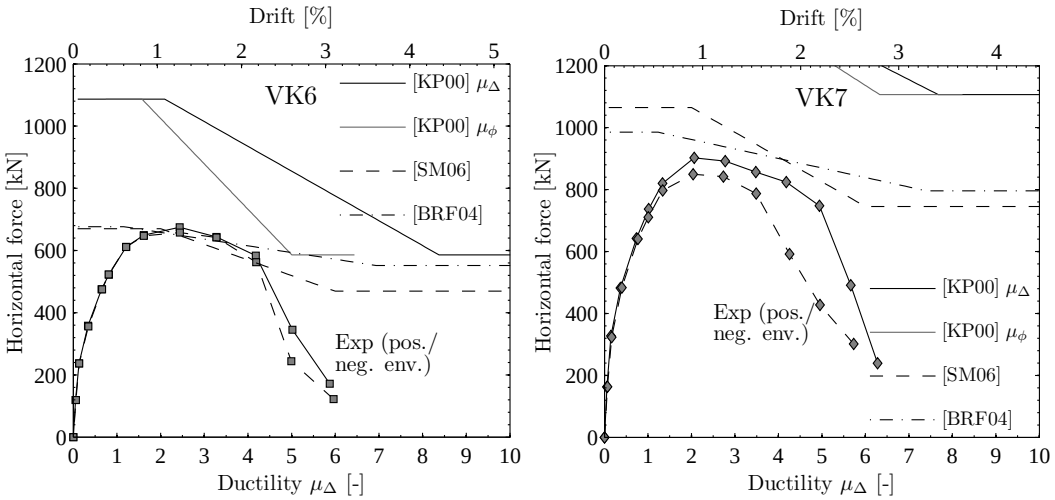

Figure 4.4: *Ductility dependent shear capacity predictions compared to test results.*

strengths of the reinforcement. The columns tested by [76] on the other hand had higher normal force ratios than the test units investigated here. Generally, it is not advisable to apply empirical models to structures which do not comply with the database from which the model was derived. Figure 4.5 confirms that if this is done nevertheless, rather poor predictions of the observed behavior are obtained.

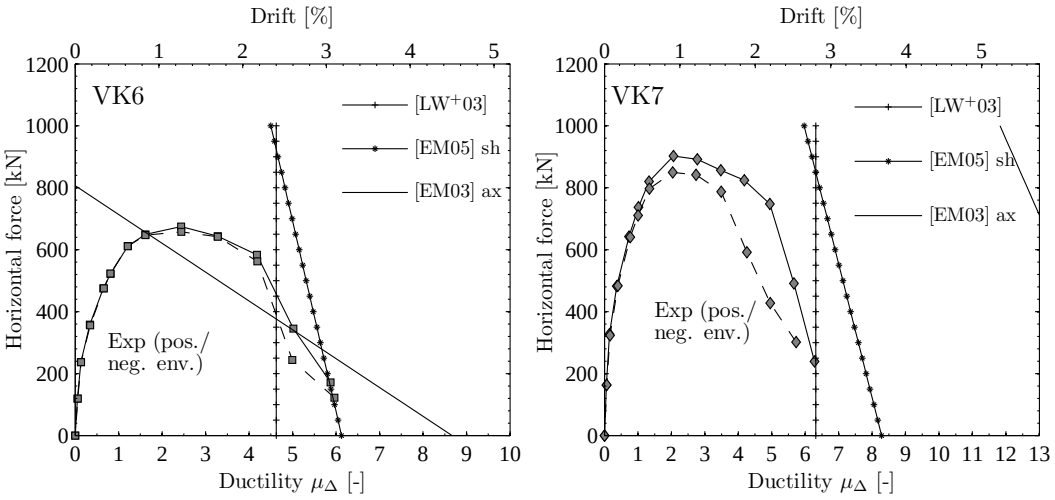

Figure 4.5: *Ductility dependent shear capacity predictions compared to test results.*

4.3.4 Truss and interaction models

The remaining two modeling approaches introduced in Section 4.2 have also been developed for columns, originally. Figure 4.6 shows their application to test units VK6 and VK7. The shear flexure interaction model “USFM” significantly underestimates the shear capacity of both test units. The peak load is not even reached before the capacity starts

degrading. This is mainly due to an overestimation of the compression softening. The simplifying assumption regarding the principal tensile strains leads to an overestimation of the compression softening factor. The axial strain expected at the centroid of a wall section is very high and while the simplification that it corresponds to the principal tensile strain might hold for columns, it seems to be an assumption that is too crude for walls.

The capacity according to the truss model with plastic limits [77] degrades very fast with increasing deformation. This is due to the prediction of a rapid degradation of the concrete component with increasing curvature, so that at relatively low displacement ductility levels, the shear force capacity results almost exclusively from the transverse reinforcement component V_s. As the transverse reinforcement content of VK6 is very low, the model predicts a much earlier onset of degradation than measured. The early degradation and low residual capacity might again be due to simplifications which are feasible for columns but not necessarily for walls. Again, one needs to keep in mind that the model is applied here outside its originally intended scope. The specific assumptions that render the model inapplicable for VK6 might be the those concerning the transfer of shear stresses across the crack. No aggregate interlock or friction forces are considered in this model, which might be a valid assumption for columns but not for walls, where aggregate interlock constitutes an important load transfer mechanism (see Chapter 5).

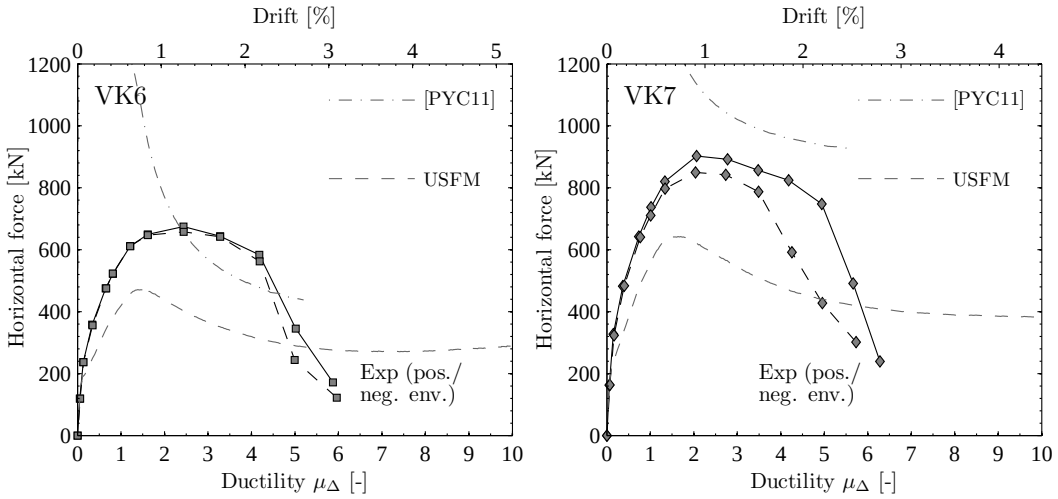

Figure 4.6: *Shear and drift capacity predictions compared to test results.*

4.3.5 Conclusions

As evident from the comparisons of predictions and experiments in the previous sections, the predictions obtained with the drift capacity models for beams and columns do not agree well with the experimental wall data. Especially the models in Sections 4.2.2 through 4.2.4, which have been empirically determined from column and beam data or contain assumptions which are only valid for columns and beams, yield poor estimates of the drift capacity of walls. The assumptions on which these models are based, e.g. the neglect of the aggregate interlock mechanism, simply do not hold for walls. Better estimates are obtained with the ductility dependent shear models, introduced in Section 4.2.1. For VK7 all of them correctly predict a capacity that is higher than the measured resistance and for VK6 two of them [42, 66] predict a degradation that is close to the experimental gradient. However,

Figure 4.4 also shows a large range of capacities predicted with these models which render the predictions unreliable.

Due to the mentioned shortcomings of the existing models for application to wall-type structures the development of new models for walls is necessary. Given the lack of experimental data of wall tests, empirical drift capacity models do not appear to be a good option. Models that specifically take into account the characteristics of walls are necessary to obtain reliable estimates of the drift capacity of walls. One such approach is introduced in Chapter 5.

5 Validation of a kinematic model

5.1 Introduction

The three parameter kinematic theory (3PKT) [13] was developed to describe the load-deformation relationship of structural walls. It predicts not only the pre-peak response of shear critical walls, but it is capable of capturing the post-peak response until failure. Thus, the strength of this model is that it allows predicting both the force and the deformation capacity, while usually a separate approach is required for each.

The theory is based on the simplified kinematics of walls which develop diagonal shear cracks and fail along such a crack eventually. Based on these kinematics, the deformation pattern of the walls is described by means of three independent parameters. Therefore, the 3PKT is a direct extension of the 2PKT, which was previously developed for deep beams [12]. The deformations of deep beams could be completely described with two parameters, namely the elongation of the longitudinal reinforcement and the shear deformation at the tip of the crack. A third parameter, the vertical displacement of the part above the critical crack due to the axial load, was introduced for walls. The force components that contribute to the shear resistance of the wall can be estimated from strains and crack displacements derived from the assumed deformation pattern.

In the following sections, the basics of the 3PKT are explained (Section 5.2) and its performance in predicting the response of potentially shear critical walls is evaluated (Section 5.4). Section 5.3 presents the database used for this evaluation. Furthermore, in Section 5.5 the influence of several characteristics on the response of walls is evaluated using the 3PKT. Section 5.6 discusses the size of the critical loading zone and potential relations with different parameters. Finally, some conclusions are provided in Section 5.7.

5.2 Three parameter kinematic theory - 3PKT

5.2.1 Kinematics assumed in the 3PKT

The three parameter kinematic theory for the behavior of walls was developed by [13] as an extension of a two parameter kinematic theory for deep beams [12]. It is a “kinematic” theory because it is based on an idealized representation of the deformation pattern of walls. The theory was developed for shear critical walls, that means walls which develop diagonal cracks and eventually fail along such a crack. Hence, the 3PKT assumes that such a shear crack develops which separates the upper nearly uncracked part of the wall, which is thus regarded as rigid body, from the radially cracked fan below. Besides the crack and the degradation associated with opening and sliding along the crack, the part just above the crack tip, the so-called “critical loading zone” (CLZ), plays an important role in describing the failure mechanism. In wall tests, it has been observed that failure along a shear crack is accompanied by severe damage of the wall around the crack tip, compare also Figure 5.2 on page 153. The CLZ accounts for this damaged area.

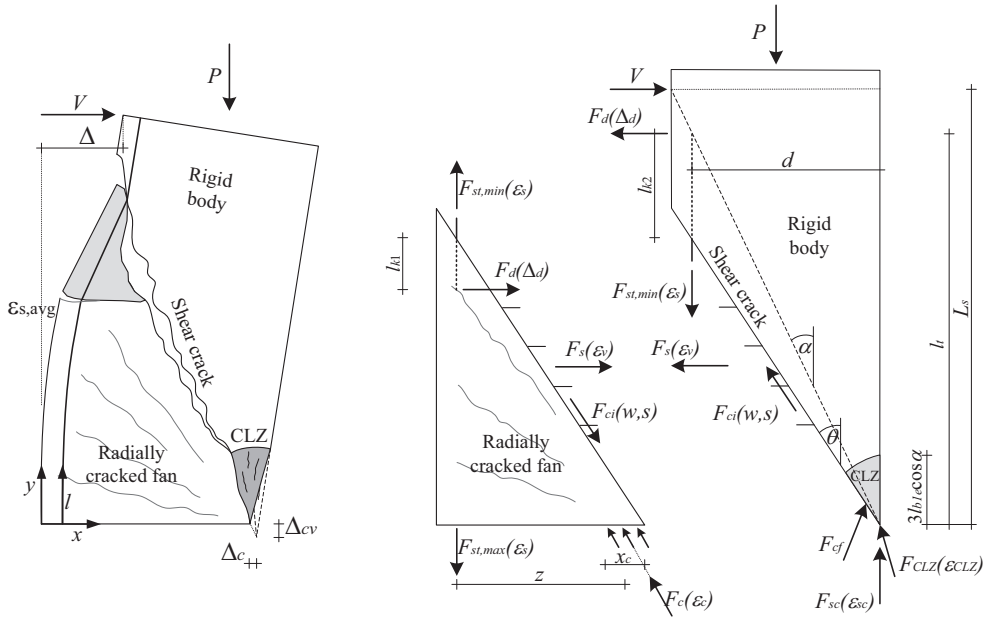

(a) Deformation pattern **(b)** Force components

Figure 5.1: *Deformation pattern with three degrees of freedom and force components as assumed in the 3PKT.*

Figure 5.1a visualizes the kinematics and the resulting deformation pattern assumed in the 3PKT. Basically, the wall is divided in three parts: a radially cracked fan under the shear crack, a rigid body above the shear crack, and the previously mentioned critical loading zone at the bottom tip of the rigid body. The deformation of these parts is described with the three parameters also indicated in Figure 5.1a: The elongation of the longitudinal reinforcement described by the average strain $\varepsilon_{s,avg}$, the horizontal displacement of the CLZ Δ_c and the shortening of the CLZ Δ_{cv}. All points below the crack are assumed to rotate around the crack tip, which means that any deformation is assumed perpendicular to the radial cracks. The magnitude of this rotation is determined by the average strain in the longitudinal reinforcement $\varepsilon_{s,avg}$.

The deformation of the critical loading zone depends on the loading it is subjected to and the resulting angle of the reaction force. If the reaction force of the CLZ, F_{CLZ}, is parallel to the shear crack, the tip of the CLZ is assumed to translate horizontally by Δ_c and the vertical displacement Δ_{cv} is zero. This is always the case for deep beams which are not subjected to axial load, hence parameter Δ_{cv} was not included in the 2PKT [12]. If the wall is, however, subjected to an axial load, the reaction force F_{CLZ} is more vertically inclined. The maximum angle of this force corresponds to the inclination of the center line of the CLZ, i.e. 0.5θ in relation to the vertical axis. In this case, the CLZ is also shortened in compression which yields a vertical deformation component Δ_{cv}.

The rigid body itself is assumed to rotate around the tip of the shear crack and translate according to displacements Δ_{cv} and Δ_c of the CLZ. The latter two cause a downward sliding of the rigid body along the shear crack while the elongation of the longitudinal reinforcement causes the opening of the shear crack.

Taking into account the deformations described in the preceding paragraphs leads to the following expressions for the deformations in the radially cracked fan below the crack:

$$\delta_x(x,y) = \frac{y}{d} \int_0^{\frac{y}{h-x}d} \varepsilon_s(l)\mathrm{d}l \tag{5.1a}$$

$$\delta_y(x,y) = \frac{h-x}{d} \int_0^{\frac{y}{h-x}d} \varepsilon_s(l)\mathrm{d}l \tag{5.1b}$$

where *l* is a variable along the *y*-axis and all dimensions are according to Figure 5.1. Accordingly, the deformation of the rigid body above the crack is described by:

$$\delta_x(x,y) = \left(\frac{\varepsilon_{s,avg} l_t}{d} + \frac{\Delta_{cv}}{d}\right) y + \Delta_c \tag{5.2a}$$

$$\delta_y(x,y) = \frac{\varepsilon_{s,avg} l_t}{d}(h-x) + \frac{\Delta_{cv}}{d}(h-d-x) \tag{5.2b}$$

where l_t is the length over which the longitudinal reinforcement is activated and $\varepsilon_{s,avg}$ is the average tensile strain in the reinforcement $\varepsilon_{s,avg} = (1/l_t)\int_0^{l_t} \varepsilon_s(l)\mathrm{d}l$. To determine the crack angle, the formulation based on a simplified expression of the MCFT [40] is used again (see Equation (2.53)):

$$\theta = 29^\circ + 7000\varepsilon_{axial}(l) \leq \alpha = \arctan\left(\frac{h}{L_s}\right)$$

Due to the generally low spacing of the longitudinal reinforcement, the size effect term of Equation (2.53) is not considered here and the maximum angle is bound by the geometry and the shear span of the wall. Contrary to what has been done in Section 3.7, the equation is here evaluated based on a procedure included in the Canadian standard [86], which utilizes a strut-and-tie approach to determined the shear strength on which the estimate of the angle is based. Hence, the strains used here differ from those used in Section 3.7, where the model proved to not be the best fit estimate for the angle. Furthermore one needs to keep in mind that the approach presented here is less sensitive to variations in the angle. If there is a loading beam at the top of the wall, the clear distance between the base of the pier and the bottom edge of the loading beam is used instead of the entire shear span length. The clear distance is used in these cases because it is assumed that the crack does not cross the loading beam.

5.2.2 Load bearing mechanisms considered in the 3PKT

Figure 5.1b shows the force components that are assumed to contribute to the shear resistance of walls. At the shear crack itself, an aggregate interlock force F_{ci} develops depending on the crack width *w* and the slip *s* along the crack. The opening of the shear cracks also causes a strain ε_v in the transverse reinforcement and thus a force $F_s(\varepsilon_v)$. The latter is located at the centroid of the activated transverse reinforcement crossing the crack as the reinforcement is lumped in one tie in the 3PKT. Also the longitudinal reinforcement distributed in the tension side of the wall, which is assumed to be $0.5hb$, is lumped in one tie at its centroid. Hence, some reinforcement that is possibly in tension in the other half of

the wall is neglected and instead the reinforcement that is considered is assumed to have equal strains and stresses. Besides the longitudinal force the reinforcement also exerts a force due to dowel action F_d as long as it is not yielding at the shear crack. Three separate force components are acting in the CLZ: The reaction force F_{CLZ} originating from compression of the concrete in the CLZ, a vertical force F_{sc} stemming from compression of the reinforcement in the CLZ and a friction force F_{cf} due to contact of the CLZ with the fan underneath the crack. Besides the forces already described, the reaction force F_c, depending on the concrete compression strain ε_c, develops in the compression zone at the base of the radially cracked fan. The following paragraphs summarize the assumptions behind the determination of the force components and the equations with which they are calculated.

The aggregate interlock force F_{ci} along the crack is computed in dependence of crack width and slip utilizing the contact density model by [87] as follows:

$$\begin{aligned} F_{ci} &= 0.18 v_{ci} \frac{bd'}{\sin\theta} \\ v_{ci} &= \int_{-\pi/2}^{\pi/2} \sigma_{con}(w,s) \left(1 - \exp\left(1 - 0.5\frac{a_g}{w}\right)\right) A_{s,u} 0.5 \cos\varphi \sin\varphi \mathrm{d}\varphi \end{aligned} \tag{5.3}$$

where d' is the distance between the outer reinforcement bar and the compression edge of the wall, σ_{con} is the contact stress normal to the contact surface as a function of crack width *w* and slip *s*, a_g is the maximum aggregate size and $A_{s,u} = 4/\pi$ is the entire surface area per unit crack plane. The exponential expression in brackets denotes the ratio of the surface area which is in contact and $0.5\cos\varphi$ is the contact density function which represents the statistical distribution of inclinations φ, which describe the profile of the undulated crack surface. To determine the contact density function, [87] measured the shapes of rugged crack surfaces and found that the above equation is a good representation of the surface profile. The stress is always assumed perpendicular to the surface. To obtain the shear stress, the horizontal components of σ_{con} are integrated for all inclinations occurring along the crack surface based on the contact density function and the surface area per unit crack plane.

Close to the top of the shear crack, a wedge shaped concrete piece is assumed to break out directly under the crack. Dowel action is modeled based on the assumption that the reinforcement tie is clamped at the top and the bottom of this wedge. The relative displacement between the two edges Δ_d, which can be calculated from the three parameters of the 3PKT, causes a clamping moment at both ends. Based on a linear moment profile over the distance $l_k = l_{k1} + l_{k2}$ (see also Figure 5.1b) between the two clamped ends the resulting dowel action force F_d can be calculated:

$$F_d = n_{bl} \frac{12 E_s \pi d_{bl}^4}{64 l_k^3} \Delta_d \leq n_{bl} f_{ye} \frac{d_{bl}^3}{3 l_k} \tag{5.4}$$

where n_{bl} is the number of longitudinal reinforcement bars, d_{bl} their diameter and f_{ye} is the effective steel yield stress defining the upper limit of the stress that contributes to dowel action. If there is no tensile stress in the bars f_{ye} equals the yield stress f_y, and if the bars are yielding in tension f_{ye} is zero. Generally, F_d is assumed to be relatively small compared to other components, especially as the longitudinal strain in the reinforcement increases towards the yield strain.

The transverse reinforcement is assumed to be activated in between this just mentioned wedge shaped piece of concrete and the critical loading zone. Its average strain over a base length of $0.9d$, ε_v, is calculated from the horizontal displacement components in the cracks below the main shear crack and that shear crack itself. The stress f_v is calculated from ε_v based on a bilinear stress-strain relationship with strain hardening. With this stress, the force in the transverse reinforcement, F_s, follows as:

$$F_s = \varrho_v b(d' \cot\theta - l_{k1} - 1.5 l_{b1e}) f_v \tag{5.5}$$

where l_{b1e} is the characteristic length of the CLZ which will be discussed in more detail in the following paragraphs and Section 5.6.

The reaction force of the critical loading zone F_{CLZ} is calculated from the concrete compression strain ε_{CLZ} in the CLZ. To calculate this strain, the displacement component in direction of F_{CLZ} is distributed over a base length of $3l_{b1e}\cos\alpha$. The average stress corresponding to ε_{CLZ} is calculated based on a modification of Popovics stress-strain relation [58]. With this average stress $f_{c,avg}$, the resulting force F_{CLZ} follows as:

$$F_{CLZ} = \alpha l_{b1e} b f_{c,avg}(\varepsilon_{CLZ}) \tag{5.6}$$

The vertical force component of the longitudinal reinforcement in the CLZ which is in compression, F_{sc}, is calculated from the vertical strain component of the CLZ. Depending on the displacements and rotation of the rigid body, the CLZ might be pushed against the bottom face of the shear crack. In this case the force F_{cf} develops, which is the resultant of the contact force perpendicular to the crack and the corresponding friction force. To compute the friction component, a friction coefficient of $\mu = 0.7$ is used.

The compression strains and stresses in the cracked part under the shear crack are calculated based on a section analysis in which the curvature is determined by equilibrium and the strain of the longitudinal reinforcement tie. Despite the use of this simple analysis procedure to calculate the stresses, sections are not assumed to remain plane. As mentioned previously, the region under the shear crack is assumed to be cracked radially and the cracks are hence all directed towards the compression zone. Therefore, the force in the compression zone F_c is not assumed vertical, but its inclination is obtained from equilibrium.

Because of the mechanism underlying the 3PKT, the theory is only applicable if the transverse reinforcement tie is predicted to yield before the longitudinal tie. If the longitudinal reinforcement tie is the one that yields first, the behavior is of a more flexural type with significant deformations in the fan below the shear crack and little opening of the shear crack itself. This means that in the corresponding physical pier predominantly flexural cracking is expected while shear cracks, if they develop, are expected to open little. One needs to keep in mind that the longitudinal reinforcement tie in the 3PKT represents half the total longitudinal reinforcement and yielding of this tie thus corresponds to a state in which the strain of half the reinforcement on average exceeds yield strain. This is not to be confused with the first or nominal yield used in the plastic hinge model, which refers to the strain of the outer reinforcement bars only.

5.2.3 Failure mechanism

Looking at the assumed kinematics and force components also helps understanding the failure mechanism generally predicted by the 3PKT. Initially, cracks develop and open grad-

ually with increasing elongation of the transverse and longitudinal reinforcement. With increasing transversal load and reinforcement stresses, the reaction force of the CLZ increases as well. Thus, some part of the applied shear force is resisted directly by the CLZ, i.e. by a mechanism comparable to direct strut action. When the CLZ enters the post-peak range the resistance degrades but the deformations continue to grow. This leads to an increasing sliding deformation along the shear crack which causes an increased aggregate interlock force. At first, this increase of aggregate interlock force compensates for the loss of resistance of the CLZ. However, as displacements and rotations get larger the shear crack opens further. With growing crack width and sliding deformations the aggregate interlock component eventually decreases as well, which causes failure of the wall. Even though the mechanism is generally similar for all walls failing in shear, the ratio of the force resisted by the CLZ depends strongly on the wall geometry, for instance. Squad walls transfer a much larger portion of the shear load directly through the CLZ than slender walls, which in turn develop higher aggregate interlock forces.

A completely different failure mechanism might develop if the walls have sufficient reinforcement which limits damage at the crack and in the CLZ. In this case, the compression zone under the shear crack might crush in compression, which causes a rather brittle failure of the wall.

5.3 Experimental database for comparison

The 3PKT was validated against a database of large-scale, single curvature tests on cantilever RC walls with rectangular cross section. As the 3PKT is based on the kinematics resulting from the formation of a shear crack, a test series had to contain at least one test unit failing along such a crack, i.e. exhibit tensile shear failure. Seven test series comprising 36 tests met the required criteria. The 3PKT was applicable to 28 out of those 36 tests, meaning that in those cases the transverse reinforcement tie was predicted to yield before the longitudinal reinforcement tie.

The maximum aspect ratio L_s/h included in the database corresponds to the upper limit of 3.0 which is set for application of the 3PKT. If walls have higher aspect ratios, they are expected to exhibit more flexural behavior and thus develop different kinematics than those assumed in the 3PKT. With regards to the longitudinal reinforcement layout, both walls with reinforcement that was evenly distributed or concentrated in the boundaries are included in the database. In the latter case, they usually contain some confining reinforcement in the boundary as well. Longitudinal reinforcement ratios ranged from $\varrho_l = 0.8\%$ to 3.33% in the database. The reinforcement ratio was calculated as $\varrho_l = 0.5A_s/(0.5bh)$ where $0.5A_s$ is the sum of the longitudinal reinforcement in half the cross section. Except for wall S10 [88], which was tested monotonically and had a larger amount of reinforcement at the tension side, this corresponds to the longitudinal reinforcement ratio calculated as $\varrho_l = A_s/(bh)$. If this total reinforcement ratio differs from the longitudinal reinforcement ratio in the web $\varrho_{l,web}$ according to Table 5.1, reinforcement is concentrated at the boundaries. The transverse reinforcement ratios in the database vary between $\varrho_v = 0\%$ and 1.04%. With regard to the material properties, normal strength concrete with compression strengths between 14 MPa and 56 MPa and reinforcing steel with yield strengths between 384 MPa and 719 MPa were used. Table 5.1 summarizes the tests included in the database.

Table 5.1: *Database for validation of the 3PKT.*

	Geometry			Concrete and reinforcement						
Test unit	b [mm]	h [mm]	L_s/h [-]	ϱ_l [%]	$\varrho_{l,web}$ [%]	f_{yl} [MPa]	ϱ_v [%]	f_{yv} [MPa]	f_c [MPa]	$n = P/(bh)$ [-]
[1]										
VK1	350	1500	2.20	0.82	0.82	515	0.08	518	35	0.07
VK3	350	1500	2.20	1.23	1.23	515	0.08	518	34	0.07
[3]										
VK6	350	1500	3.00	1.23	1.23	521	0.08	528	44.4	0.06
VK7	350	1500	2.20	1.23	1.23	521	0.22	528	30	0.08
[90]										
WS2	80	500	2.40	3.33	0.42	536	0.3	719	36	0.00
WS4	80	500	2.40	3.33	0.42	536	0.3	719	36	0.00
[88]										
S4	100	1180	1.12	1.05	1.05	574	1.03	574	32.9	0.07
S9	100	1180	1.12	0.99	0.99	560	0		29.2	0.08
S10	100	1180	1.12	2.91	1.00	513	0.98	496	31.0	0.07
[91]										
Wall1	100	2000	0.58	0.80	0.704	435	0.369	425	25.0	0.00
Wall2	100	2000	0.33	0.80	0.704	435	0.369	425	22.0	0.00
[14]										
72	160	1700	1.00	1.54	0.5	384	0.26	427	17.6	0.11
73	160	1700	1.00	1.54	0.5	384	0.26	427	21.2	0.09
74	160	1700	1.00	1.54	0.5	384	0.52	430	21.2	0.09
75	160	1700	1.00	1.54	0.5	384	0.52	430	14.0	0.14
76	160	1700	1.00	1.54	0.5	384	1.04	423	15.0	0.13
77	160	1700	1.00	1.54	0.5	384	1.04	423	18.7	0.11
78	160	1700	1.00	0.91	0.5	390	0.52	429	21.2	0.09
79	160	1700	1.00	0.91	0.5	390	0.52	429	14.0	0.14
80	160	1700	1.00	0.91	0.5	390	1.04	423	15.0	0.13
81	160	1700	1.00	0.91	0.5	390	1.04	423	18.7	0.11
82	160	850	2.00	2.31	0.4	388	0.52	430	21.2	0.09
83	160	850	2.00	2.31	0.4	388	0.52	430	18.2	0.11
84	160	850	2.00	2.01	0.4	385	0.52	423	18.2	0.11
85	160	850	2.00	2.01	0.4	385	0.52	423	21.2	0.09
[92]										
SW4	60	600	2.10	2.82	0.31	500	0.39	545	36.9	0.00
SW5	60	600	2.10	3.01	0.47	535	0.31	400	31.8	0.00
SW6	60	600	2.10	2.82	0.31	500	0.31	400	38.6	0.00
SW7	60	600	2.10	3.01	0.47	535	0.39	545	32.0	0.00
SW8	60	600	2.10	2.93	0.31	430	0.42	400	45.8	0.00
SW9	60	600	2.10	2.93	0.31	430	0.56	400	38.9	0.00
[89]										
RW1	150	1220	2.00	1.29	0.27	470	0.27	515	48.0	0.07
RW2	150	1220	2.00	2.89	0.62	470	0.62	440	48.0	0.07
RW3	150	1220	1.50	1.32	0.33	469	0.33	515	48.0	0.08
RW4	150	1220	1.50	2.59	0.74	469	0.74	440	56.0	0.06
RW5	150	1220	1.50	2.51	0.62	470	0.62	440	56.0	0.02

continued on next page...

Table 5.1: *Continued from previous page*

	Geometry			Concrete and reinforcement						$n =$
	b	h	L_s/h	ϱ_l	$\varrho_{l,web}$	f_{yl}	ϱ_v	f_{yv}	f_c	$P/(bh)$
	[mm]	[mm]	[-]	[%]	[%]	[MPa]	[%]	[MPa]	[MPa]	[-]
Max.	350	2000	3.0	3.33	1.23	574	1.04	719	56	0.14
Min	60	500	0.33	0.80	0.27	384	0	400	14	0

Note: The names of the walls tested by [89] correspond to the original names as follows: RW1: RW-A20-P10-S38, RW2: RW-A20-P10-S63, RW3: RW-A15-P10-S51, RW4: RW-A15-P10-S78, RW5: RW-A15-P2.5-S64

The first four test units VK1-VK7 [1, 3] listed in the table are the same ones as previously used for the study on plastic hinge modeling in Chapter 3. Only the four test units with continuous reinforcement will be considered for the comparison with the 3PKT, as the test units with lap-splices develop different kinematics. Several failure modes were observed in these four tests. VK1 and VK3 both failed in shear and VK3 did so in a relatively brittle manner at a significantly lower drift than VK1. The more slender VK6 generally showed a more flexural behavior and eventually failed in a shear-flexural mode characterized by a loss of compression zone and significant deterioration in the lower part of the inclined cracks. VK7 on the contrary failed in flexural compression. Due to the higher transverse reinforcement ratio, which was sufficient to resist the shear force corresponding to the moment capacity, the diagonal cracks opened relatively little during the test.

Walls WS2 and WS4 [90] were not capacity designed either, but the longitudinal reinforcement was concentrated at the boundaries and not evenly distributed. Both tests were run in 1:3 scale with equal wall layout. The difference in the tests was the loading velocity: WS2 was loaded with displacement velocities of up to 5mm/min and WS4 was subjected to faster loading rates of up to 24mm/min. Both walls eventually failed in shear along a diagonal crack at approximately the same top displacement.

Different failure modes were observed for the three monotonically tested rectangular walls of the test series conducted by [88]. Walls S4 and S9 developed a shear crack pattern but the failure clearly concentrated in one crack only in wall S9, which had no transverse reinforcement at all, while several cracks opened in S4. Test unit S10 had a high longitudinal reinforcement ratio in the boundary element in tension and could thus develop high forces at the tension side. Yielding of this reinforcement only started right before diagonal compression failure occurred.

Two very short walls with aspect ratios $L_s/h \leq 1.0$ and very long cross sections ($h/b = 20$) were tested by [91]. Web reinforcement was relatively low also in this case and the boundaries were confined. Both walls were subjected to cyclic loading. For the more slender Wall1 a significant movement of the triangular part above the shear crack is reported before failure, which is caused by crushing of the concrete at both corners of this triangle and significant displacements along the shear crack. However, yielding of half the vertical reinforcement and significant opening of the basecrack were already observed at less than $1/3$ of the displacement at failure. Wall2 first developed some diagonal cracks and eventually also slid significantly along the construction joint at the base.

Some wall tests with varying slenderness and reinforcement layouts were summarized by [14]. All of the ones with rectangular cross section, that were hence considered in the database, had longitudinal reinforcement that was concentrated in the boundary regions of the walls. Two walls with the same layout were tested each time which means that the part of the test series that was considered herein comprises 14 tests with seven different

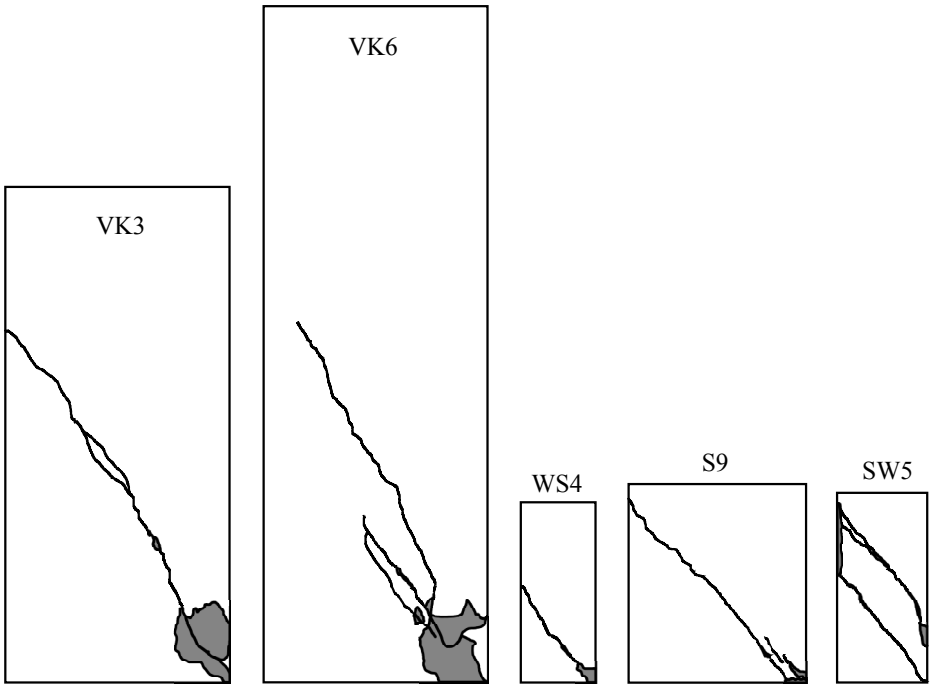

Figure 5.2: *Illustration of shear cracks which cause failure of test units VK3 [1], VK6 [3], WS4 [93], S9 [88] and SW5 [92] drawn to scale 1:50.*

layouts. According to the plots of the crack pattern provided in the report [14], some walls showed a failure that concentrated in one diagonal crack (tests no. 72 & 73) while others also showed some damage in compression at the base of the pier (test no. 82). Other series of walls with confined boundary elements were tested in cyclic loading by [92] and [89] which showed failure modes that were similar to those that were previously described.

To illustrate how the crack formation and damage in the physical test corresponds to the idealized deformation assumed in the 3PKT; as well as to show the different dimensions of the test units in this database, the shear crack which eventually caused failure is drawn to 1:50 scale in Figure 5.2 for five out of the 28 test units.

5.4 Validation of the 3PKT

The database introduced in the previous section is used to validate the 3PKT. As outlined in Section 5.2, a key parameter of the 3PKT is the so-called “critical loading zone” at the tip of the rigid body above the shear crack. So far, the size of this critical loading zone is a free parameter for which a relation needs to be established. For a first validation of the 3PKT this parameter was chosen so that the measured load-deformation responses of the test units were captured best. That means this one parameter was determined according to the available experimental results, while all other relations for the remaining force components, as well as all the corresponding strains and displacements were calculated according to equations and assumptions presented in Section 5.2. As the length l_{b1e}, which determines the size of the critical loading zone, usually turned out to be very similar for all specimen of one test series, the same length l_{b1e} was used for all of them in another step of the

validation. The data in the graphs presented in this and the following section stem from the second step of the validation procedure.

Table 5.2: *Experimental results and 3PKT predictions.*

	Experiment					3PKT				
Test	V_{max}	V_{ult} [1]	δ_{ult} [1]	$l_{b1e,TU}$ [2]	l_{b1e} [2]	V_{max}	V_{ult} [3]	δ_{ult} [3]	$\frac{V_{max}}{3PKT}^{Exp}$	$\frac{\delta_{ult}}{3PKT}^{Exp}$
unit	[kN]	[kN]	[%]	[mm]	[mm]	[kN]	[kN]	[%]	[-]	[-]
[1]										
VK1	729	583	1.90	320	320	698	558	1.91	1.04	1.00
VK3	879	703	1.35	300	320	868	694	1.74	1.01	0.77
[3]										
VK6	666	533	2.24	320	320	655	524	2.33	1.02	0.96
VK7	877	701	2.25	320	320	881	705	2.19	1.02	1.03
[90]										
WS2	137	109	2.14	180	180	136	109	2.23	1.00	0.96
WS4	130	104	2.24	180	180	136	109	2.23	0.96	1.00
[88]										
S4	392	314	-	3PKT not applicable						
S9	342	292*	0.80*	250	250	334	292*	0.94*	1.02	0.85
S10	670	643*	0.92*	250	250	673	643*	0.92*	1.00	1.00
[91]										
Wall1	540	432	1.50	3PKT not applicable						
Wall2	684	547	1.48	280	280	693	554	1.34	0.99	1.11
[14]										
72	825	660	-	300	220	714	571	0.67	1.16	-
73	740	592	-	200	220	756	605	0.64	0.98	-
74	830	664	0.89	200	220	878	702	0.75	0.95	1.18
75	825	660	-	220	220	788	630	0.88	1.05	-
76	820	656	1.25	3PKT not applicable						
77	930	744	-	3PKT not applicable						
78	700	560	-	3PKT not applicable						
79	630	504	-	200	220	626	501	1.14	1.01	-
80	720	576	-	3PKT not applicable						
81	775	620	-	3PKT not applicable						
82	328	262	-	200	220	349	-	-	0.94	-
83	340	272	-	200	220	346	-	-	0.98	-
84	330	264	-	220	220	312	-	-	1.06	-
85	375	300	-	200	220	316	-	-	1.19	-
[92]										
SW4	107	102**	1.73**	150	130	105	99**	1.82**	1.02	0.95
SW5	113	90	0.95	90	130	121	97	1.12	0.93	0.85
SW6	113	90	1.67	130	130	104	83	1.78	1.08	0.94
SW7	127	102	1.77	180	130	123	113**	1.39**	1.03	1.27
SW8	94	90**	2.00**	100	130	104	102**	2.46**	0.90	0.82
SW9	103	82	2.04	125	130	103	102**	2.02**	1.00	1.01
[89]										
RW1	459	367	3.14	3PKT not applicable						
RW2	730	584	2.99	350	300	722	578	1.64	1.01	1.83
RW3	589	471	3.30	300	300	605	484	3.50	0.97	0.94

continued on next page...

Table 5.2: *Continued from previous page*

	Experiment					3PKT			$\frac{V_{max}}{\frac{Exp}{3PKT}}$	$\frac{\delta_{ult}}{\frac{Exp}{3PKT}}$
	V_{max} [kN]	V_{ult}[1] [kN]	δ_{ult}[1] [%]	$l_{b1e,TU}$[2] [mm]	l_{b1e}[2] [mm]	V_{max} [kN]	V_{ult}[3] [kN]	δ_{ult}[3] [%]	[-]	[-]
RW4	841	673	2.97	270	300	865	793	1.61	0.97	1.84
RW5	665	532	2.42	300	300	746	746	2.16	0.89	1.12
Max.	930	744	3.30	350	320	881	793	3.50	1.19	1.84
Min	94	82	0.80	90	130	103	83	0.64	0.89	0.77
								Avg.	1.01	1.07
								COV	6.41%	26.8%

Note: The names of the walls tested by [89] correspond to the original names as follows: RW1: RW-A20-P10-S38, RW2: RW-A20-P10-S63, RW3: RW-A15-P10-S51, RW4: RW-A15-P10-S78, RW5: RW-A15-P2.5-S64

[1] Generally $V_{ult} = 0.8V_{max}$. If sudden failure occurred at a higher load or a higher load ratio was defined as ultimate state, this value and the corresponding drift are given instead.

[2] $l_{b1e,TU}$ is the value that provided the best results for this test unit, l_{b1e} the one with the best results for the series.

[3] In accordance with the experiments, 80% of the force or the load at sudden failure and the corresponding drifts are provided.

* A residual load $V > 80\%V_{max}$ was defined as failure and the provided drift corresponds to this failure load.

** Load and corresponding drift at which sudden failure occurred.

Table 5.2 gives an overview over the 3PKT predictions. It summarizes the measured and predicted peak loads and drifts corresponding to a 20% drop of load. The latter is here referred to as ultimate state or displacement capacity in accordance with e.g. most drift capacity models introduced in Section 4.2.2. If the test was stopped before the load had dropped by 20% or if a sudden failure occurred, the corresponding drift value is marked in the table with one or two asterisks, respectively. Also indicated are the test units for which the 3PKT was not applicable because the longitudinal reinforcement tie was predicted to yield first. In most cases, the included drift values were obtained from the hysteresis plots in the corresponding reference. In [1, 3] they are corrected for the rotation of the foundation. The drift values of [88] were corrected for foundation rotation according to the procedure outlined in [88]. For all other test units, either no specific information is provided regarding the rotation of the foundation or it was not measured. If the test was stopped without any further explanation before the load had dropped by 20%, i.e. if it is unknown whether failure occurred or the test was stopped for another reason, the ultimate drift is not reported in Table 5.2 (indicated with a dash).

Figure 5.3 compares the predicted load-deformation relationships of some of the test units listed in Table 5.2 with the measured ones. Figure 5.3a shows the envelopes of the positive loading direction of the four test units with continuous reinforcement reported in [1, 3] compared to the corresponding predictions. One can see that the peak load as well as the degrading branch are captured very well in most cases. Only the drift capacity of VK3 is slightly overestimated because the CLZ size that matched the entire test series best is a bit larger than the optimum fit for VK3. All 3PKT predictions are plotted up to δ_{ult}, i.e. the drift corresponding to a 20% drop of shear capacity.

Figure 5.3b contains only two test units of the series by [88], because the 3PKT was not applicable to the third one of the series. For the third test unit, the longitudinal reinforcement was predicted to yield before the transverse reinforcement. For each test unit, two

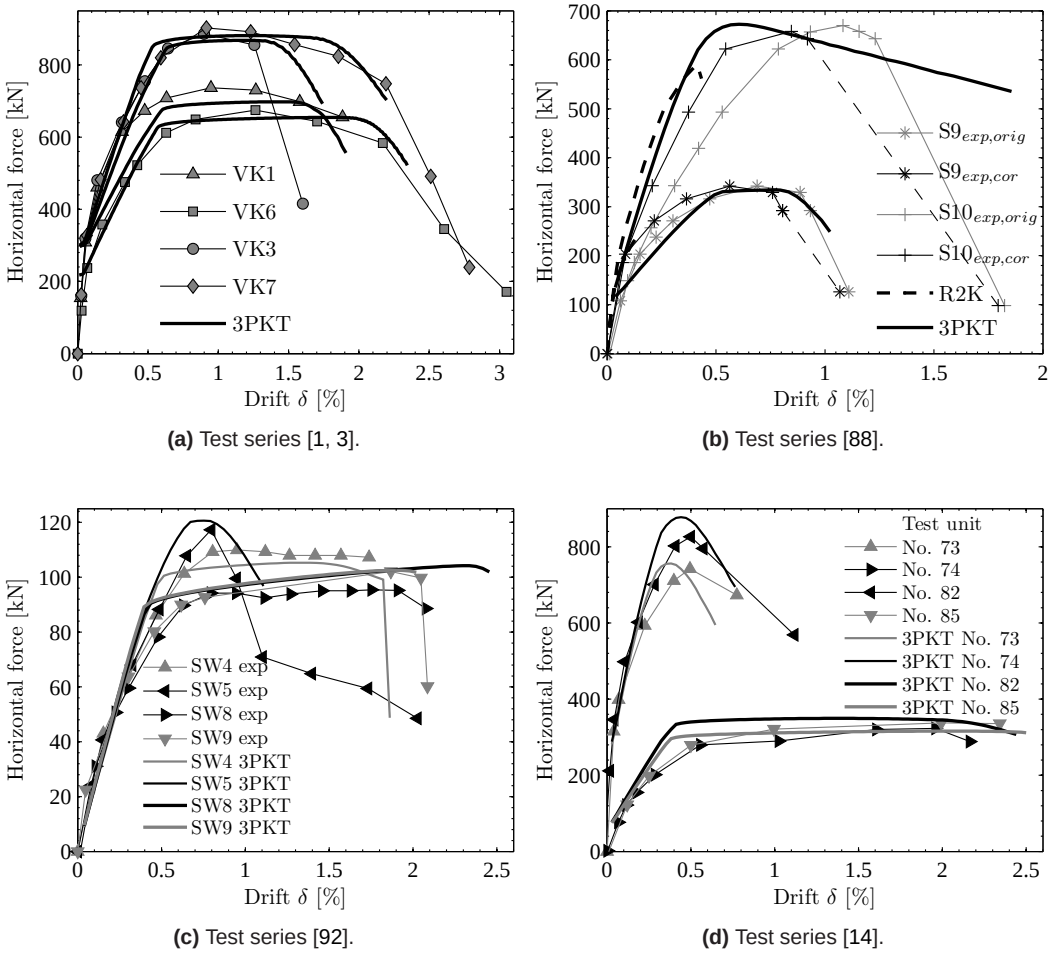

(a) Test series [1, 3]. **(b)** Test series [88].

(c) Test series [92]. **(d)** Test series [14].

Figure 5.3: *Comparison of load-deformation relationships predicted with the 3PKT and experimental data.*

experimental envelopes are shown: One original envelope (index *exp,orig*), which uses the deformations provided in the report and one envelope corrected for the rotation of the foundation as explained previously (index *exp,cor*). In the test report [88], data plots were provided up to the point at which the force dropped by about 10%, which was defined as failure in Table 5.2. However, the descriptions of the testing provide force and displacement values measured after failure. As the measurements that are necessary to correct for the rotation were not provided after failure, only an approximate correction using the data from the ascending branch was made and the graphs are plotted with dashed lines. Again, one can note that force and deformation capacity are well predicted by the 3PKT. The drift capacity of S10, corresponding to 96% of the peak load, is predicted very well, whereas the drift capacity of S9 is overestimated by 19%. Besides the prediction according to the 3PKT, this plot also contains predictions made with Response-2000 [94], annotated with “R2K”. The latter may be used to better estimate the pre-peak part of the response, as the 3PKT may underestimate the stiffness at this stage due to the underlying kinematics based on the fully developed shear crack. In the other plots, this prediction of the initial response has not been included to improve readability of the graphs containing the results of four test units.

Figure 5.3c shows the results for some of the test units by [92]. Crushing of the core concrete is reported for test unit SW4 during the cycles with peak displacement $\Delta = 24$mm $\rightarrow$ $\delta = 1.9\%$ and the hysteresis is provided up to a drift of $\delta = 1.74\%$, which indicates that the displacement amplitude $\delta = 1.9\%$ had not been reached in the cycle in which failure occurred. The 3PKT predicts a different failure mechanism with rupture of the transverse reinforcement at $\delta = 1.82\%$, which corresponds well to the measured drift capacity. Tests SW8 and SW9 were stopped due to considerable concrete damage. Also the 3PKT predicts failure due to flexural crushing. Test unit SW5 developed large shear cracks which eventually caused failure and the crack plots also show significant deterioration around the crack tips. According to the 3PKT, degradation initiates with degradation of the CLZ, which is immediately followed by decrease of the V_{ci} component. Hence, also in this case, the failure mode and the displacement capacity are well captured.

No description of failure modes is available for the tests summarized by [14]. However, the crack plots indicate a concentration of damage in one shear crack for test unit no. 73 and distribution of damage over several cracks for test unit no. 74. The more slender units no. 82 and no. 85 both developed shear cracks and showed crushing of the concrete at the base. Degradation along the shear crack is also predicted for test units no. 73 and 74, which is again triggered by a decrease of capacity of the CLZ. A similar failure mode is predicted for test unit no. 82. However, the shear resistance of the CLZ, V_{CLZ}, is much higher than V_{ci} in this case, whereas it was similar to V_{ci} for the two more slender test units. Also for test unit no. 85, the ratio of the load resisted by V_{CLZ} is predicted to be rather large whereas V_{ci} is almost negligible and failure is predicted to occur due to flexural crushing of the concrete at the base section.

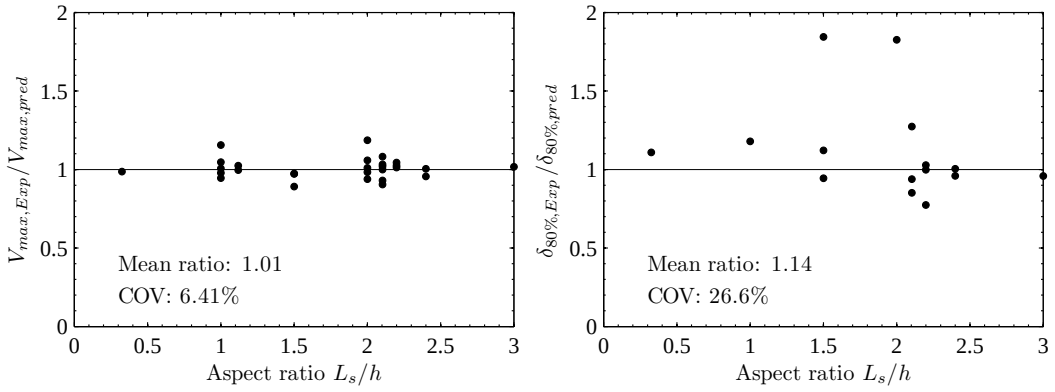

(a) Ratio of experimental to predicted peak load.

(b) Ratio of experimental to predicted drift corresponding to 20% drop of resistance.

Figure 5.4: *Comparison of 3PKT prediction with experimental data.*

Figure 5.4 shows the ratio of the experimental to the predicted peak load and drift capacity of all test units. As before, the drift corresponding to a 20% drop of shear resistance was defined as drift capacity. To have a clear definition and not include different criteria and failure modes in one plot, only test units for which such a degradation occurred are included. This means that sudden failures due to concrete crushing (i.e. SW4, SW8, SW9 [92]), which may also be well predicted, as shown in Figure 5.3, are not included. Furthermore, tests S9 and S10 [88], for which failure was reported but the provided hysteresis plots ended at residual loads that were larger than 90% of the peak load, are not included.

Note that in two cases, namely walls RW-A15-P10-S78 and RW-A15-P2.5-S64 [89], the 20% drop occurred in the experiment but was not predicted by the 3PKT. However, RW-A15-

P10-S78 did not degrade slowly but lost its capacity very rapidly. The 3PKT predicts failure due to flexural crushing at about half the drift at which failure actually occurred, hence this is one of the outliers in Figure 5.4b. Flexural crushing is also predicted for RW-A15-P2.5-S64 at about the drift at which the test unit did start to degrade in the experiment. For this test series, only a conference paper is available at present and no detailed measurement data. Hence, further investigations to find the source of these discrepancies could not be made. As not all values listed in the table are included in the plot, the mean value and coefficient of variation of the drift capacity is different than that provided in Table 5.2.

5.5 Influence of pier characteristics on response

5.5.1 Introduction

In the following sections, the influence of several structural characteristics on the behavior of walls is examined. The focus therein lies on examining the influence of each parameter on the deformation capacity, as this is the key value for displacement-based assessment. Furthermore, potential effects on the shear strength and failure modes will be investigated using the 3PKT.

5.5.2 Transverse reinforcement ratio

An important characteristic for the shear behavior of walls is their transverse reinforcement content ϱ_v, which influences especially the deformation capacity. To investigate the effect of ϱ_v on the behavior of walls, some of the tests reported by [14] as well as VK3 [1] and VK7 [3] are considered.

Tests no. 72 to 77 had different transverse reinforcement ratios but were otherwise identical. Two walls of each layout were tested in this campaign and walls no. 73 ($\varrho_v = 0.26\%$), no. 74 ($\varrho_v = 0.52\%$) and no. 77 ($\varrho_v = 1.04\%$) will be considered for further comparison. Some influence of ϱ_v is visible even in the crack patterns: While the damage of the test unit with the lowest ϱ_v concentrates in one crack, more evenly distributed cracks are observed in the other four cases. Generally, more compression damage of the concrete was observed with higher ϱ_v. Very similar observations were made for test units VK3 and VK7. Failure concentrated in one shear crack of VK3, whereas the shear cracks of VK7 opened only little and the test unit finally failed in compression.

To study the influence of the transverse reinforcement content according to the 3PKT, several analysis with varying ϱ_v were run for the considered piers with average material properties. Figure 5.5 shows the results of these analyses. As expected, the drift capacity is strongly influenced by the transverse reinforcement ratio in each case. Especially the drift capacity of the more slender test units (VK3 & VK7: $L_s/h = 2.2$) is predicted to increase significantly if the transverse reinforcement ratio is increased. This is also supported by the experimental data. On the contrary, the force capacity is not affected as much. Only at very low transverse reinforcement ratios (from $\varrho_v = 0.0\%$ to $\varrho_v = 0.08\%$) an increase in shear resistance is observed for this wall layout. With very low ratios of ϱ_v the flexural capacity of the wall can already be reached and hence no further increase of the force is possible.

The shorter test units No. 73, 74 and 77, on the other hand, typically fail before their flexural capacity is reached. In Figure 5.5, the flexural capacity is attained only with the

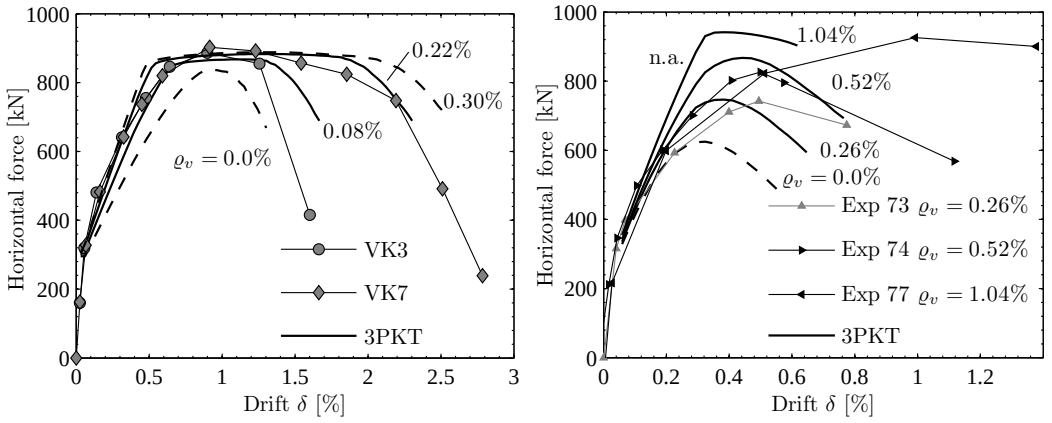

(a) VK3 and VK7 [1, 3]. **(b)** Tests No. 73, 74 & 77 [14].

Figure 5.5: *3PKT analyses with varying transverse reinforcement ratios compared to experimental data.*

highest reinforcement ratio of $\varrho_v = 1.04\%$, but the 3PKT is not applicable for this ϱ_v because the longitudinal reinforcement tie yields first. As the shear capacity is hence not limited by the flexural capacity but by the shear capacity and thus the transverse reinforcement ratio, an increase in ϱ_v does not only lead to an increased drift, but also to an increased force capacity for these walls. Figure 5.6a shows the predicted development of crack width and slip for the transverse reinforcement ratios that are also included in Figure 5.5. With increasing transverse reinforcement ratio the opening of the crack and also the downwards sliding, which eventually causes failure, are delayed. The highest transverse reinforcement ratio prohibits almost any sliding and only permits limited crack opening.

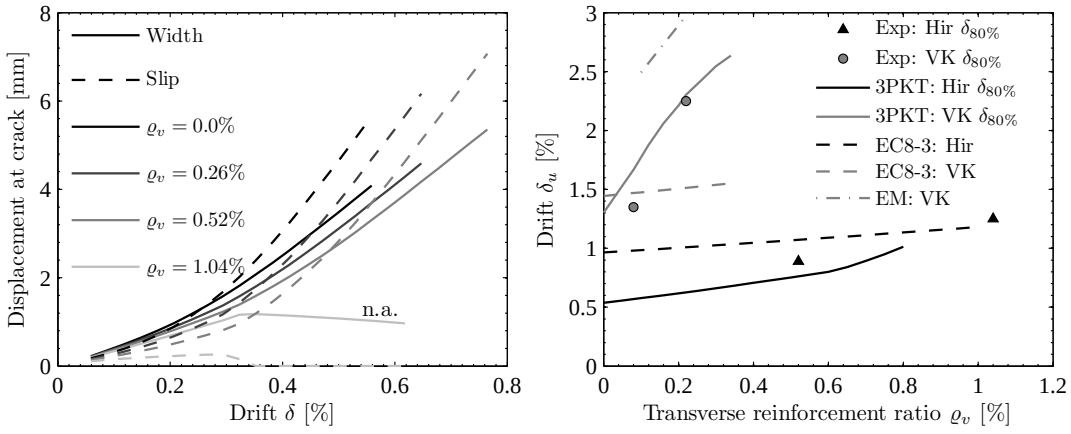

(a) Crack width and slip of tests by [14]. **(b)** Drift capacity.

Figure 5.6: *Crack development and drift capacity depending on transverse reinforcement content.*

Figure 5.6b shows the drift capacity of the two considered wall layouts in dependence of the transverse reinforcement ratio. For comparison, the drift capacity estimates according to Equations (2.40) [24] and (4.11) [75] are also included in this figure. The drift capacity according to Equation (4.10) [76] was derived using test data of columns with higher aspect and axial load ratio and could hence not be applied. The applied Equations (2.40)

and (4.11) were originally developed to predict the deformation capacity corresponding to a 20% drop of lateral load. According to the boundary values defined for certain characteristics [75] is neither applicable to the short walls ("Hir") nor to walls with $\varrho_v < 1.0\%$ ("VK"). Even though the criteria of application are formally met for higher ϱ_v, one has to keep in mind that the equation was derived from experimental data of columns and not of walls. However, the trend of the drift capacity is well predicted with this model and similar to that obtained with the 3PKT, but the drift capacities are about 30-40% larger than those calculated using the 3PKT. The drift capacity according to [24] matches well the experimental data of the squat walls, but not that of the slender walls. It has been evaluated using a confinement effectiveness factor of $k_{con} = 0.3$ for the squat walls, as detailed drawings of the reinforcement layout were not available for these. For the walls with higher aspect ratio, the factor turned out to be $k_{con} = 0.4$ according to the provided reinforcement. In both cases, the mechanical reinforcement content in compression was assumed equal to that in tension and the first term in brackets hence evaluated as $f_c^{0.225}$. Furthermore, the average material properties of the two tests of each set were used and the members were regarded to be primary elements without seismic detailing. The different characteristics of the two wall layouts, such as the distribution of the longitudinal reinforcement (equally distributed or concentrated at the boundaries) and the slenderness, are not sufficiently taken into account with this model, as evident in Figure 5.6. The 3PKT predictions agree well with the experimental data of both test series on the other hand. Predictions are shown for all transverse reinforcement ratios for which the 3PKT was applicable and the load eventually dropped by 20%. As indicated in the previous paragraph, the 3PKT distinguishes between shear failure before and after reaching the flexural capacity and thus takes into account the behavior of the walls in a more detailed way than the drift capacity models. It is therefore able to better capture the different behavior of the two test series and thus also the difference in the drift limits.

5.5.3 Aspect ratio

Besides the transverse reinforcement content, the aspect ratio L_s/h significantly influences the behavior of walls. Both strength and deformation capacity are affected by changes of L_s/h. This is due to a transition from a predominantly shear controlled behavior towards a flexural behavior with increasing aspect ratio. To visualize the effect of a varying slenderness, three test units will be considered in the following: Test units VK3 [1] and VK6 [3] for which the aspect ratio was the varied experimental parameter and test unit SW6 [92]. The first two test units (called VK in the following plots) had evenly distributed reinforcement, low transverse reinforcement and an axial load ratio of $n \approx 0.07$. The aspect ratio has not been the only varied parameter in any other test series, hence only an analytical investigation could be made using any other wall layout as basis. Wall SW6 was chosen because, contrary to VK3 and VK6, it does not have an axial load and has its longitudinal reinforcement concentrated in the boundaries.

Figure 5.7 shows the influence of the aspect ratio on the force-deformation response for the selected test units. The increasing aspect ratio leads to a transition from a rather brittle to a more ductile response. While the lateral load resistance decreases, the drift capacity increases. The experimental data of VK3 and VK6 does not only support the predicted trend but also the absolute values. One has to keep in mind, however, that the average material properties were used which causes some variation in the predicted and measured drift capacities. The measured envelope of SW6 is also well predicted and the predicted trend due to a change in aspect ratio is similar as for VK3 & VK6.

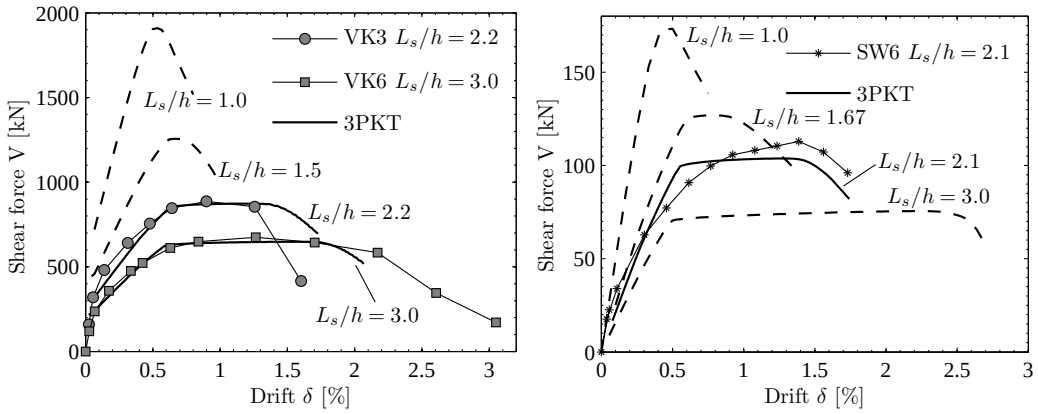

(a) VK3 and VK6 [1, 3]. **(b)** SW6 [92].

Figure 5.7: *3PKT analyses with varying aspect ratio compared to experimental data.*

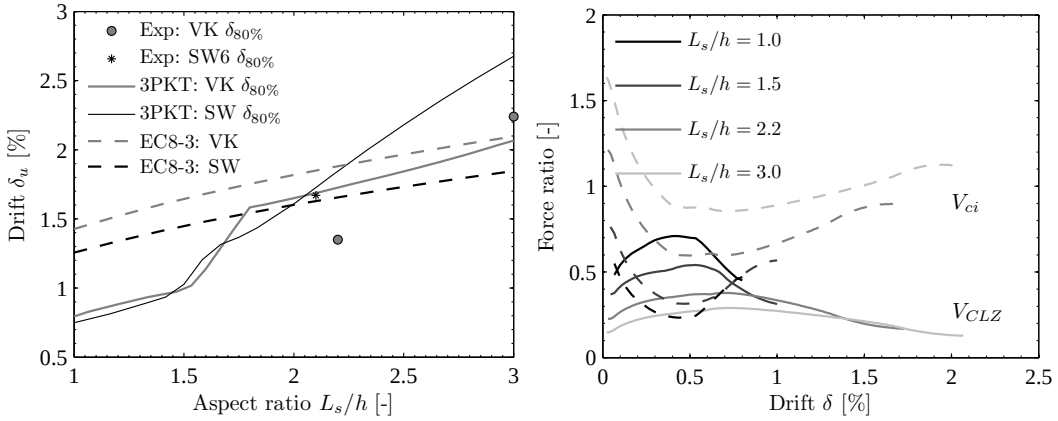

(a) Drift capacity. **(b)** Force component ratios VK.

Figure 5.8: *Drift capacity and force components depending on aspect ratio.*

However, as Figure 5.8a shows, the influence of L_s/h on the drift capacity differs for the two layouts. The drift capacity is approximately the same up to an aspect ratio of about 1.5. Between $L_s/h = 1.5$ and 2.0, there is a transition towards a more flexural behavior with a significant increase of drift capacity in both cases. But while the drift capacity of the VK3 & VK6 layout increases with about the same gradient as it did for $L_s/h < 1.5$, the gradient with which the capacity of SW6 increases is larger than before. These three test units, and comparison with other test unit layouts not included in this section, show that the effect of the aspect ratio on the drift capacity strongly depends also on other characteristics, such as the distribution of the reinforcement. Contrary to the 3PKT, the equation of [24] predicts a more steady increase of drift capacity over the entire range of considered aspect ratios. All material values to evaluate this equation were taken from Table 5.1, the same assumptions as in the previous Section 5.5.2 were made regarding the reinforcement ratios in tension and compression and k_{con} was evaluated according to the reinforcement layout as 0.4 and 0.04 for VK3 & VK6 and SW6, respectively. Furthermore, the equation was evaluated for primary elements without seismic detailing. Other drift capacity estimates introduced in Section 4.2.2 are not included, as they are not applicable for the low aspect ratios.

The change in the behavior with increasing aspect ratio can also be illustrated with the force components predicted by the 3PKT. If the aspect ratio is low, the ratio of the load that is carried by the critical loading zone V_{CLZ}/V is relatively high for the layout of VK3 & VK6, see Figure 5.8b. This indicates a high direct load transfer through the rigid body. As the aspect ratio increases, the direct load transfer through the CLZ becomes less important and a larger ratio of the force is transferred along the crack. Not only the aggregate interlock force, which is included in Figure 5.8b, but also the friction force at the crack tip increases significantly with L_s/h. This friction force does not occur in test unit SW6 as it is not subjected to axial load. Concerning the aggregate interlock force and the resistance of the CLZ, the trends are similar to that of VK3 & VK6 though. If the test unit is short, a high ratio of the load is transferred directly through the critical loading zone, but with increasing aspect ratio an increasing ratio of the force is transferred at the crack through aggregate interlock.

5.5.4 Axial load ratio

Similarly to the study on the influence of the aspect ratio using SW6 [92], the influence of the axial load ratio could only be studied analytically because none of the included test series included the axial load ratio as a parameter. The rather slender test unit VK6 [3] is chosen for the analytical study, because it illustrates well the effect that the axial load ratio may have on the internal force distribution and the drift capacity. For comparison, the influence of the axial load is also shown based on test unit S9, which has an aspect ratio of only $L_s/h = 1.12$ and no stirrups.

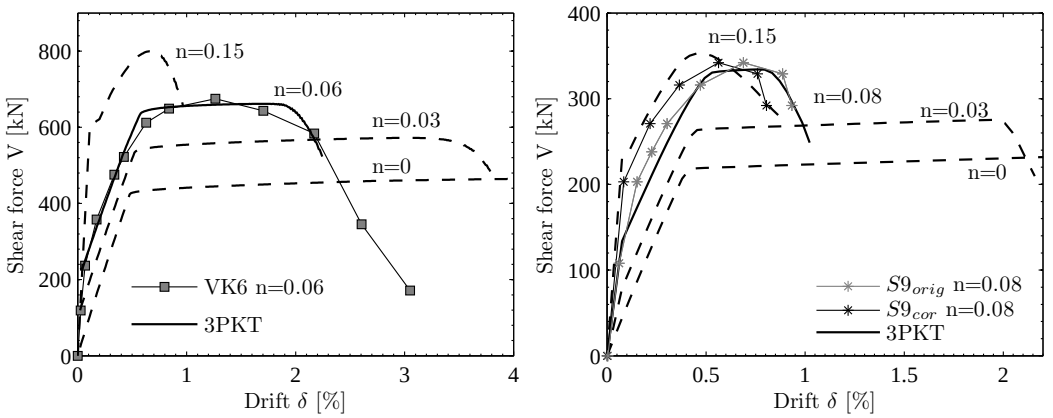

(a) VK6 [3]. **(b)** S9 [88].

Figure 5.9: *3PKT analyses with varying axial load ratio compared to experimental data.*

Figure 5.9 shows the influence of the axial load ratio on the force-deformation response of test units VK6 and S9. In both cases, a similar behavior is observed: With increasing axial load, the shear force capacity increases whereas the deformation capacity decreases. Within the investigated range of axial loads, an asymptotic behavior is observed towards the highest ratio $n = 0.15$. Figure 5.10 shows that the drift capacity only changes very little for axial load ratios that are higher than about 0.1. Also the shear force resistance increases at a much lower rate than before from approximately this axial load ratio on.

Initially, an increasing axial load causes a strong decrease of drift capacity, except for $n \leq\sim 0.02$ for VK6, which does not influence the drift capacity much, see Figure 5.10. Towards

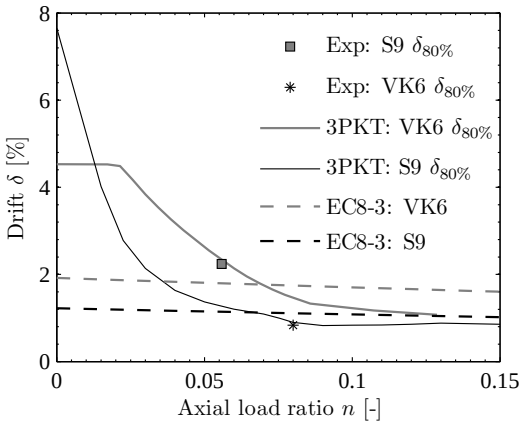

Figure 5.10: *Drift capacity depending on axial load ratio.*

an axial load ratio of $n \approx 0.1$, the influence of the axial load reduces and the drift capacity approaches a kind of lower bound value. From about this load ratio on (VK6: $n = 0.11$, S9: $n = 0.09$), the yield strain of the longitudinal reinforcement is no longer reached and the behavior thus more shear controlled. Also the crack angle does no longer change from then on. While the crack angle has been controlled by the wall geometry in the case of S9, it has been getting steeper with increasing load in the case of VK6 up to $n = 0.11$ when it reached its final value of $\theta = 29°$. Figure 5.11 shows that along with this steepening of the crack angle goes an earlier increase of crack width and slip.

As evident in Figure 5.10, the 3PKT predicts a much stronger dependence of the drift capacity on the axial load than Equation 2.40 of EC8-Part 3 [24] does. The latter estimates a more steady decrease of drift capacity with increasing axial load. At low axial load ratios, the drift capacity according to [24] is much lower than that according to the 3PKT, but from around $n = 0.08$ onwards, they are similar. Equation (2.40) is again evaluated for primary seismic elements, assuming that no seismic detailing is provided. The confinement effectiveness factor of VK6 was calculated as $k_{con} = 0.4$ whereas S9 did not have any transverse reinforcement and hence the corresponding exponent is zero.

As mentioned previously, failure of the test units is initiated when the concrete in the CLZ crushes and the rigid body starts sliding down the crack. With increasing axial load ratio, this mechanism initiates at lower drifts. This trend can be well illustrated by looking at the force components and the development of the displacements – width and slip – at the crack of VK6. Figure 5.11 shows these for the axial load ratios that mark significant points in Figure 5.10. One can see that with increasing axial load the shear resistance due to aggregate interlock V_{ci} and friction V_{cf} become more important. The aggregate interlock component increases because the sliding displacement grows faster than the crack width with increasing *n*. The increase of the friction component hints at an increasing contact force between the tip of the rigid body and the fan below the crack. Besides the force components acting at the crack, the behavior of the CLZ is also strongly influenced by *n*. With increasing axial load, the peak of the CLZ is reached earlier and thus also the decrease of V_{CLZ} starts earlier. Similar trends concerning V_{CLZ} are observed for S9. However, as this test unit does not have any stirrups and is rather short, V_s and V_{cf} are almost zero. Therefore, the CLZ carries almost the entire load at low axial load ratios. With increasing axial load, the slip increases faster than the width which causes an increasing aggregate interlock force.

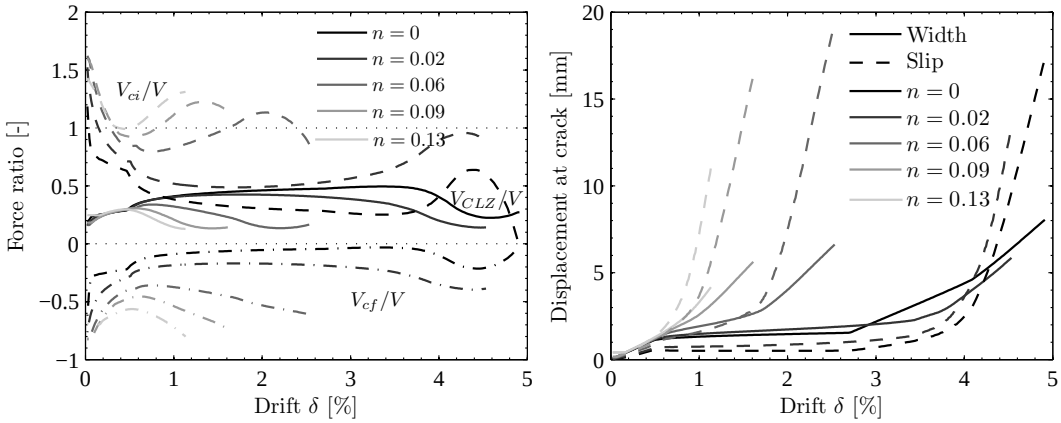

(a) Force ratios

(b) Crack width and slip

Figure 5.11: *Force ratios and development of displacements at the crack for VK6 with varying axial load ratio.*

5.5.5 Longitudinal reinforcement ratio

The effect of the longitudinal reinforcement ratio ϱ_l is examined based on test units VK1 & VK3 [1, 3] and SW5 & SW6 [92]. For the former pair of test units, ϱ_l was the only varied parameter. The longitudinal reinforcement was evenly distributed around the cross section and hence the location of the reinforcement tie in the 3PKT, merely varied slightly. Contrary to this, the distribution of the reinforcement was changed besides the reinforcement content in walls SW5 and SW6. In test unit SW6, a large portion of the longitudinal reinforcement was concentrated in the boundary elements and hence its static height *d* was larger than that of SW5. Furthermore, the concrete strengths of SW5 & SW6 were subject to larger variation ($f_{c,SW5} = 31.8$ MPa, $f_{c,SW6} = 38.6$ MPa) than that of VK1 & VK3 ($f_{c,VK1} = 35$ MPa, $f_{c,VK3} = 34$ MPa). These differences need to be kept in mind when interpreting the results, which are consequently influenced by several parameters. Despite this, the test units were deemed suitable to qualitatively illustrate potential effects of changing longitudinal reinforcement contents. All 3PKT calculations were made with average material properties and average static height d of each pair of test units.

Figure 5.12 shows the predicted responses for selected reinforcement contents compared to the measured force-deformation envelopes. Comparison to Figure 5.9 shows that the effect of varying longitudinal reinforcement contents on the envelope is similar to that of varying axial load: With increasing ϱ_l the resistance of the test unit increases and the deformation capacity decreases. This effect seems straightforward considering the forces acting on the rigid body, see Figure 5.1b. An increased reinforcement content leads to an increased vertical force acting on the rigid body, but with a line of action which is shifted with relation to that of the axial load.

The effect of ϱ_l on the internal force distribution is nevertheless slightly different than that of *n*. An increased reinforcement content does not cause any additional contact force at the tip of the rigid body, and V_{cf} is hence not affected as much as it was the case for an increasing axial load. But, similarly to what was observed for an increasing axial load, the peak load of the CLZ is attained at lower drifts with increasing ϱ_l. Thus, with increasing ϱ_l the downwards sliding of the rigid body and the increase of V_{ci} initiate earlier. The higher shear capacity with higher ϱ_l is due to an increased aggregate interlock component for

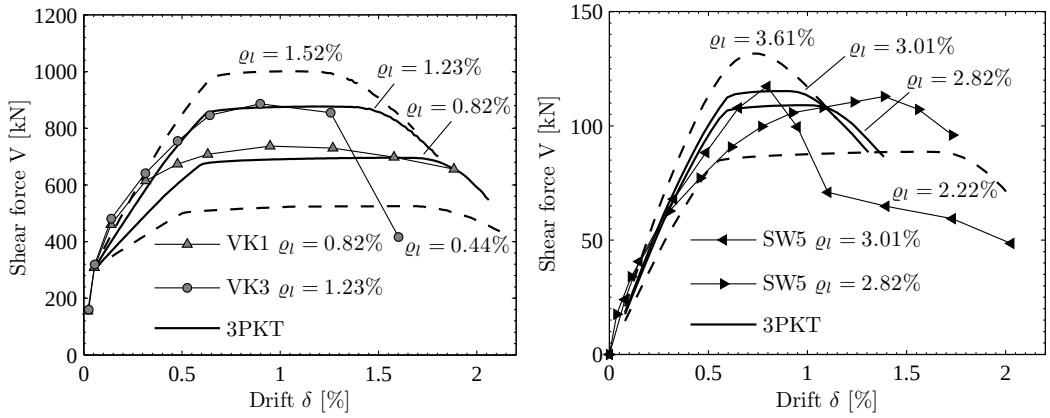

(a) VK1 & VK3 [1, 3] **(b)** SW5 & SW6 [92]

Figure 5.12: *3PKT analyses with varying longitudinal reinforcement ratio compared to experimental data.*

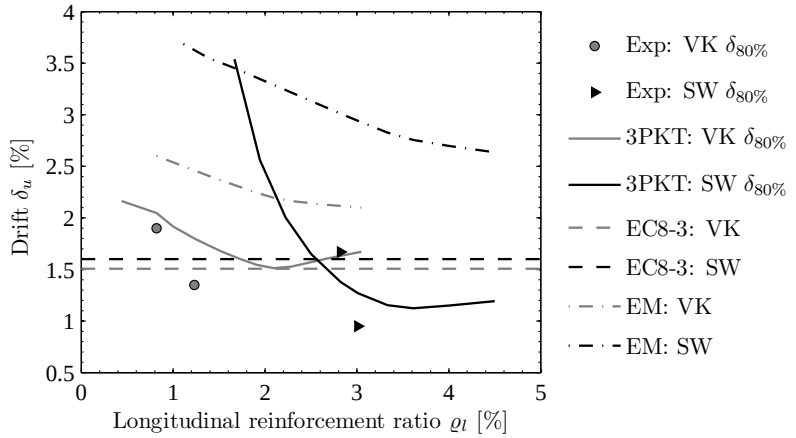

Figure 5.13: *Drift capacity depending on longitudinal reinforcement ratio*

both test unit layouts, which was also observed for *n*. While the magnitude of V_{ci} as well as its relative contribution to the resistance V_{ci}/V increase significantly, its degradation also starts at lower drift ratios. As failure of the test unit is typically triggered by the degradation of aggregate interlock, the drift capacity is thus reduced.

Figure 5.13 shows the drift capacity of the walls in function of ϱ_l according to the 3PKT. Initially, there is a relatively strong decrease of drift capacity with increasing ϱ_l. For reinforcement ratios lower than about 1.7%, no degradation of shear resistance was predicted for the wall layout by [92] but the analysis suddenly stopped due to rupture of the longitudinal reinforcement. The displacement corresponding to this failure is also very dependent on the ultimate strain of the steel and is therefore not included in the plot. With increasing ratios a significant drop of drift capacity is observed initially before the effect of ϱ_l on δ weakens with a further increase of ϱ_l. According to the 3PKT, there is even a slight reverse in the trend for very high reinforcement ratios. This phenomenon occurs because crack width and slip develop in such a way that the aggregate interlock component decreases more slowly than for lower ϱ_l. This trend cannot be validated by experimental data, but also the drift capacity estimate according to Equation (4.11) predicts a slight change in the trend

from around the same ϱ_l as the 3PKT. However, one needs to keep in mind that the high ratios for which this reverse in trend occurs are relatively rare and these are thus rather theoretical examples. The drift capacity according to Equation (4.11) does not directly include an influence of ϱ_l but accounts for the shear stress applied to a section. It was here evaluated using the maximum resistance as predicted by the 3PKT for each ϱ_l. The trend predicted with this formulation is somewhat similar to that of the 3PKT, especially for the VK1 & VK3 layout, but the predicted capacities themselves are higher. The drift capacity according to EC8 Part 3, Equation (2.40), does not account for any influence of the longitudinal reinforcement ratio and is included in Figure 5.13 using the average properties of the considered test units.

The experimental data supports the trends predicted with the 3PKT. According to this data, the effect of the longitudinal reinforcement is even a bit stronger than predicted. However, one needs to keep in mind that predictions were made based on average values of the material properties and of the static height. While the drift ratio of VK1 ($\varrho_l = 0.82\%$) is well captured, that of VK3 ($\varrho_l = 1.23\%$) is a bit overestimated. The data of SW5 and SW6 seems to imply a much stronger influence of ϱ_l than predicted. However, as mentioned also the static height *d* and the concrete strength vary significantly between the two test units. According to the 3PKT, the concrete strength has a considerable influence on the drift capacity, as the strength of the critical loading zone and consequently the drift at which it enters the post-peak range depend on f_c. Due to these changes between the two test units, the behavior is influenced by more than one parameter and while the included data illustrates a trend, the absolute values cannot be compared with the predictions. Comparison of the experimental data with the drift estimates according to Equation (2.40) and (4.11) shows that with the former, which does not account for ϱ_l, drift capacities in between the actual ones are predicted. The latter does predict a decreasing trend with increasing ϱ_l but overestimates the capacity of all the test units.

5.6 Critical loading zone CLZ

5.6.1 Influence of size of the CLZ on the response

As outlined in Section 5.2.3, the behavior of the critical loading zone influences the behavior of walls especially with regards to their failure mechanism. The degradation of the CLZ and thus of the degradation of what can be considered a direct strut mechanism leads to sliding of the rigid body down the crack. As the CLZ and the aggregate interlock are the main load bearing components in vertical direction, the degradation of these equals the degradation of axial load bearing capacity, which can be considered a total failure of the structure.

This far, the size of the CLZ was a parameter which was determined from the available experimental responses of the walls. Generally, two observations can be made regarding the choice of the size of the CLZ: For relatively squat walls ($L_s/h \leq\sim 1$) the direct load transfer via the CLZ constitutes a significant part of the total load transfer. An underestimation of the actual size of the critical loading zone thus leads to an underestimation of the shear resistance of the structure, see Figure 5.14a. The 3PKT model would in this case start to degrade at drifts at which in reality the peak load is not yet reached. Thus, both the shear strength and the drift capacity are likely to be underestimated.

On the contrary, if the wall is slender ($L_s/h \geq\sim 2$), the contribution of the CLZ to the shear resistance constitutes a smaller part than for squat walls whereas the aggregate interlock gains in importance. If the CLZ is chosen too small in this case, its degradation might

initiate at smaller drifts which does not yet trigger failure, but an increase in aggregate interlock force. However, while the aggregate interlock initially compensates for a lower force capacity of the CLZ, an earlier activation of the aggregate interlock mechanisms also causes an earlier degradation of F_{ci}. In other words, if the downward sliding of the rigid body commences earlier, it will also grow too large and cause failure earlier. Hence, for slender walls, the choice of the size of the CLZ influences mainly the drift at which the total shear resistance of the structure starts to degrade and not so much the shear strength, see Figure 5.14b.

5.6.2 Relation of the size of the CLZ to various parameters

a Experimental observations

If the 3PKT shall be used for predicting the load-deformation response of bridge piers, a formulation to predict the size of the CLZ based on the characteristics of the pier must be found. To obtain a relation for the characteristic length l_{b1e} which defines the size of the CLZ, potential influences of some pier characteristics on the development of the size of the CLZ were examined. Figure 5.15 shows the compression zone of test unit VK6 [3] in the first, i.e. positive, loading direction. The extent of the critical loading zone, as it is obtained by fitting of the test results, is shaded in Figure 5.15a and the shear crack leading to failure is indicated as well. One can note that in this case, the angle of the crack is predicted very well and the size of the CLZ corresponds approximately to the area over which compression cracks are distributed.

Even though not all test units develop such a clearly visible triangular damage area, the CLZ can generally be regarded as the volume in which the damage of the part of the wall above the shear crack eventually concentrates. The following sections give an overview over the parameters that were estimated to potentially influence the size of the CLZ and show their relation to the actual characteristic length l_{b1e} determined from the experimental load-deformation response. Note that, to have as little bias originating from other assumptions as possible, the length $l_{b1e,TU}$, which is individually determined for each test unit, is considered to find a relation for l_{b1e}. However, as previously indicated, l_{b1e} is relatively constant for all

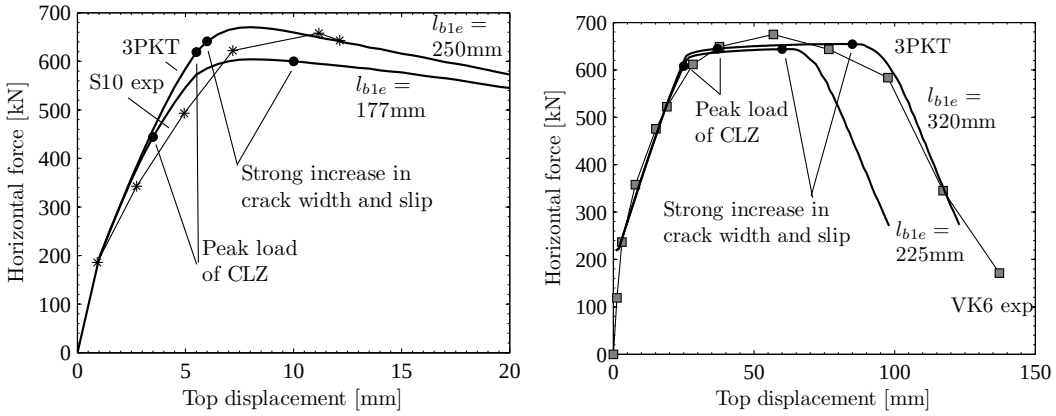

(a) S10: $L_s/h = 1.12$ **(b)** VK6: $L_s/h = 3.0$

Figure 5.14: *Influence of the size of the CLZ on the response of a slender and a squat wall.*

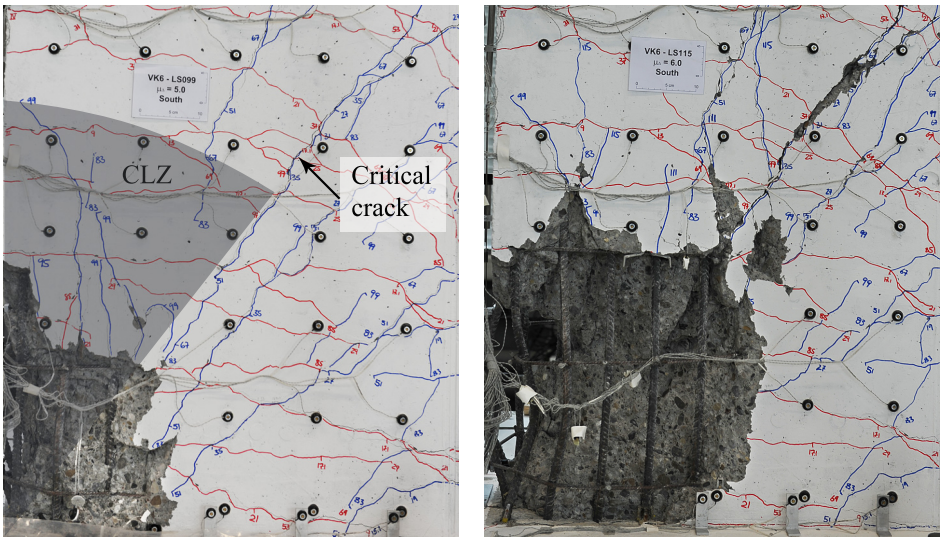

(a) Load step corresponding to drift $\delta = 2.2\,\%$

(b) Load step corresponding to drift $\delta = 2.6\,\%$

Figure 5.15: *Photos of the compression zone of of test unit VK6 [3] with shaded area indicating assumed critical loading zone CLZ.*

walls tested within one series, except for two test series ([92, 89]). For a better comparison, the l_{b1e} with which all results of a test series were captured best on average is included in all following plots as well.

b Reinforcement content and layout

The reinforcement in the CLZ was considered to be a potential influence for several reasons. Both the longitudinal and the transverse reinforcement may act as confinement and thus influence the distribution of damage in the compression zone. The transverse reinforcement may also anchor the CLZ in the fan underneath the shear crack and hence restrain the lateral movement of the CLZ. However, as Figure 5.16a clearly shows, no relation between the transverse reinforcement and the size of the critical loading zone, represented by l_{b1e}, can be observed in the test data. The situation is not different if the size of the CLZ is related to the longitudinal reinforcement content.

In analogy to the effect the loading plate has on the size of the CLZ of a deep beam, the effect of the bending stiffness of the longitudinal reinforcement was examined. The bars were regarded as cantilevers with a clamped bearing in the foundation that restrain the lateral movement of the tip of the CLZ. In this respect, they would resemble a bearing plate. The size of this virtual plate should be related to the bending stiffness of the bars. The bending stiffness EI of a bar with diameter d_{bl} is calculated as $EI = E\pi d_{bl}^4/64 = kd_{bl}^4$, with the constant value $k = E\pi/64$. Hence, if the size of the CLZ was related to EI, a relation between l_{b1e} and the stiffness of the reinforcement bars in the CLZ $n_{bl}kd^4$, where n_{bl} is the considered number of reinforcement bars, should be found. Generally, only the outer layer of reinforcement bars was assumed to contribute to the stiffness, if the boundary element was not confined by hoops. If there was confinement, it was assumed that the two reinforcement layers coupled by hoops could only deflect in parallel and hence both layers were considered. This was the case for Tran and Wallace's walls [89] as well as for some of Pilakoutas and Elnashai's [92]. But Figure 5.16b clearly shows that there is no relation between the lateral stiffness of the reinforcing bars and l_{b1e}.

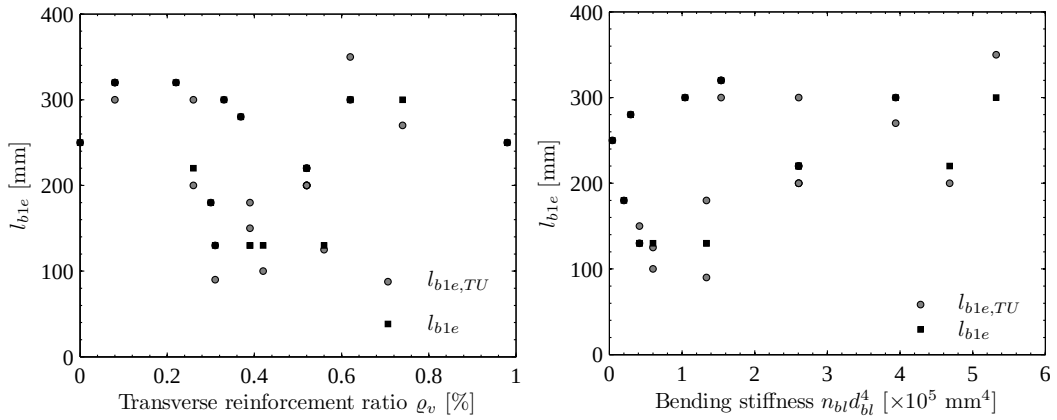

(a) l_{b1e} against transverse reinforcement ratio **(b)** l_{b1e} against bending stiffness $EI = kd_{bl}^4$

Figure 5.16: *Relation between the l_{b1e} determined from the experimental response and some reinforcement parameters.*

Other reinforcement characteristics, such as bar spacing and buckling lengths, which could influence the extend of the damaged area, were investigated as well and showed no correlation to the actual size of the CLZ. Therefore one can say that, considering the currently available data, no relation between any reinforcement parameters and the size of the critical loading zone can be established and the size of the critical loading zone must depend on other parameters.

c Height of the damaged zone in compression

Even though the CLZ also deforms in lateral direction and does not have a constant area throughout its height, it was considered that its damage could be compared to that of uniaxial compression tests. Similarly to the localization of damage that can be observed for some materials (e.g. steel) in tension, a concentration of damage has also previously been observed for concrete in compression. To describe the softening behavior of concrete in compression, [95] developed the “compressive damage zone model”, which is based on the assumption that damage spreads only over a certain height in slender specimen. A height of 2.5 times the width of the specimen was assumed for the damage zone. This corresponds to the observation of [96] that the failure crack of concrete compression tests tends to form at an angle of 22° ($= \arctan(1/2.5)$).

If the critical loading zone would, despite its complex loading condition and its triangular shape, form following the same rules, its size should be related to the width of the wall. Figure 5.17 shows that the correlation is better than for the previously examined relations, but still relatively weak. Hence, the assumption that the CLZ can be compared to the damaged area in compression tests seems too crude.

d Geometrical relations

The idea to check a potential dependence of l_{b1e} on the geometry of the walls is based on considerations similar to those presented in the previous section, where the influence of the width of the wall was looked at. Besides the two approaches mentioned in the previous section, models based on fracture mechanics occasionally include the hypothesis that the

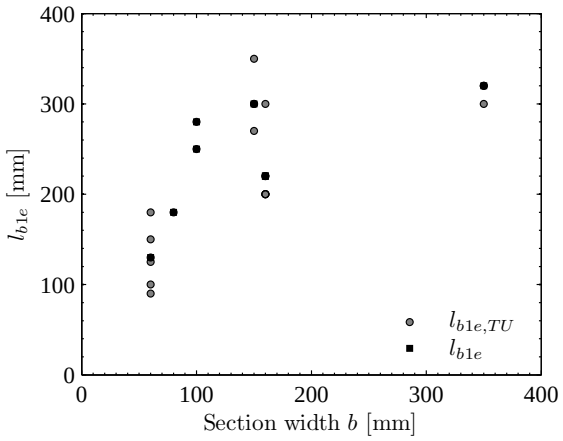

Figure 5.17: *l_{b1e} against section width b*

damage area is proportional to a specific dimension, e.g. [97]. Even though no fracture mechanics approach is chosen in the 3PKT or shall be included for the size of the critical loading zone, the treated problems resemble each other. Fracture mechanics approaches are sometimes employed if the concentration of damage within a larger volume has to be described. Also for the 3PKT the dimensions of a small zone (i.e. the CLZ), in which the damage of a larger volume (i.e. the rigid body) concentrates, are searched for. Besides, the observation that l_{b1e} usually turned out to be similar for test units of one test series supports the idea that the size of the CLZ could be related to the geometry. By and large, the dimensions of the test units within one series are the same provided the aspect ratio is not a test parameter.

Furthermore, one can also assume that stresses and strains will spread under certain angles and distribute over specific areas. This was already done for the 2PKT [12], where, based on an analytical model of the crack tip, it was found that the stresses at the crack tip concentrate over a length of $3l_{b1e}\cos\alpha$. Further up the crack the stresses in the rigid body were found to level at a constant value. Hence, the expression $3l_{b1e}\cos\alpha$ was chosen as length for the critical loading zone in the 2PKT and kept in the 3PKT [13].

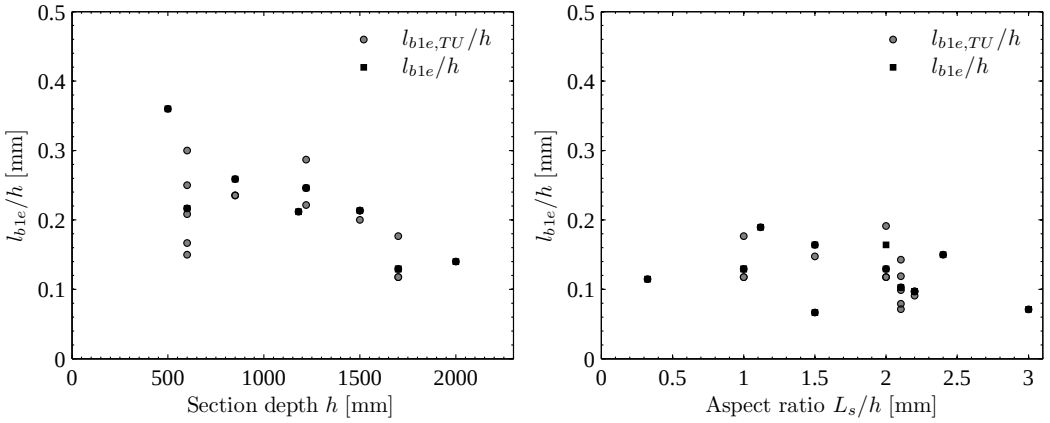

(a) l_{b1e}/h against section depth *h*

(b) l_{b1e}/h against aspect ratio L_s/h

Figure 5.18: *Relation between l_{b1e}/h and geometrical properties.*

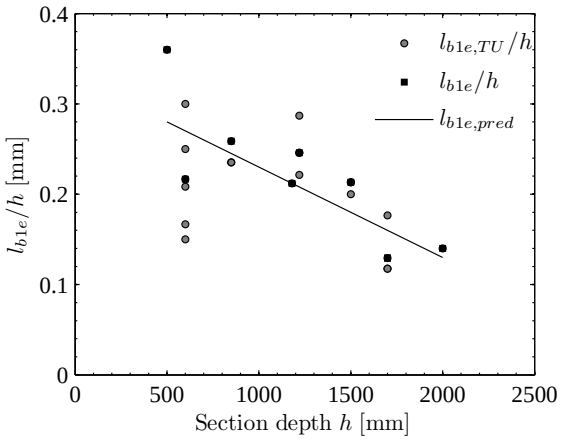

Figure 5.19: *Proposed linear relation between l_{b1e}/h and h.*

For these reasons, looking for a possible relation between l_{b1e} and values representing the geometry of the structure was deemed feasible. Figure 5.18 shows that the size of the critical loading zone does indeed seem to depend on the dimensions of the test unit. In both graphs, the dimensionless expression l_{b1e}/h was used to examine possible correlations. Both graphs indicate a linear relation for l_{b1e}/h in dependence of *h* or L_s/h. However, the graph showing l_{b1e}/h against L_s/h contains one clear outlier: the length of the CLZ of the shortest test unit in the database. Keeping also in mind that a larger ratio of the load is transferred directly through the CLZ if the walls are short, it seems well possible that l_{b1e}/h is not linearly dependent on L_s/h but has a larger gradient at low L_s/h. However, as there is only one data point below an aspect ratio of $L_s/h = 1.0$ it is hard to tell whether it is an outlier or whether it indicates a changing trend for squat walls with aspect ratios below 1.0. Also the relation between $l_{b1e,TU}/h$ and *h* shows some more scatter for smaller section heights *h*. However, all the walls with height $h = 600\,\text{mm}$ belong to the same test series [92] for which a larger variation with regards to the optimum l_{b1e} values was noticed than for most other test series. Whether that stems from scatter in the experimental results or whether the walls vary in some characteristics that influence the length l_{b1e} is difficult to tell. Only the reinforcement layout was varied between the different test units, but, as shown previously, no correlation between any reinforcement parameters and the development of the CLZ was found. Thus it is assumed that scatter in the experimental results might be the possible source of the variations at small *h* and that geometrical relations are, in light of the limited amount of experimental data, suited to establish a relation for l_{b1e}.

e Conclusions and proposed size of CLZ

As shown in the previous section, the dimensionless value l_{b1e}/h and the height of the section h seem to be linearly related, i.e. $l_{b1e} \propto h^2$. Even though there is some scatter associated to this relation, there is also reason to assume that at least some of that scatter is due to variations in the available experimental data, as already indicated in the previous paragraph. Generally, only hysteresis plots and photos or drawings of the crack patterns were available but no local deformation measurements, close-up photos and detailed descriptions of the tests. The latter was only available for the tests reported by [1, 3, 88]. Available experimental data of good quality is thus rather limited, which complicates a detailed analysis of the critical loading zone.

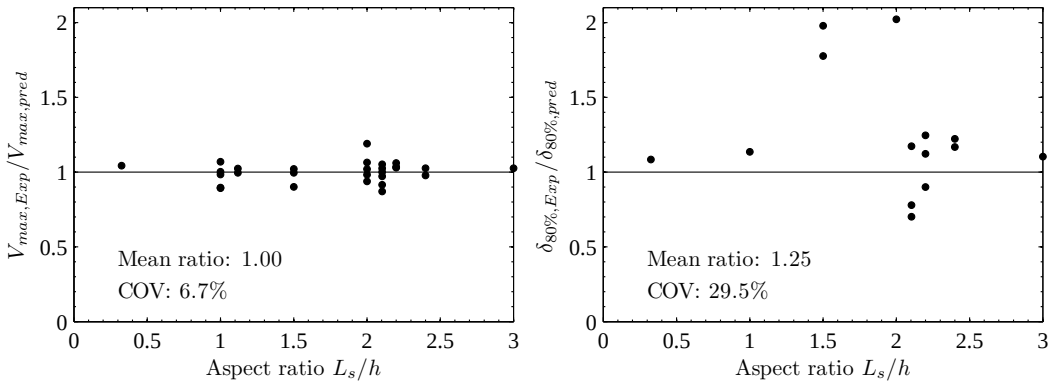

(a) Ratio of experimental to predicted peak load.

(b) Ratio of experimental to predicted drift corresponding to 20% drop of resistance.

Figure 5.20: *Comparison of 3PKT prediction using l_{b1e} according to Eq.* (5.7) *with experimental data.*

Given the limited extent of the database, it seems reasonable to establish a rather simple expression for l_{b1e} as the data is not sufficient to validate more elaborate approaches. Hence, the following linear approximation of l_{b1e}/h dependent on *h* is proposed:

$$\frac{l_{b1e}}{h} = 0.33 - 0.1h \qquad \text{for } 0.5\text{m} \leq h \leq 2.0\text{m} \quad \text{with } h \text{ in m} \tag{5.7}$$

As Figure 5.19 shows, especially the values of l_{b1e}, with which the responses of an entire test series are captured best, are approximated well with the linear relation. This relation should, as indicated in Equation (5.7), only be used for walls with depths between $h = 0.5$ m and $h = 2.0$ m which corresponds to the range included in the database.

If the size of the critical loading zone is estimated according to Equation (5.7), the shear strength of the walls is still very well predicted with an average ratio of experimental to predicted peak load of 1.00 and a coefficient of variation of 6.7%, see Figure 5.20. As expected, the agreement of the predicted drifts is worsened slightly with an average ratio $\delta_{80\%,exp}/\delta_{80\%,pred}$ of 1.25 and a coefficient of variation of 29.5%. However, as evident in Figure 5.20, the large scatter is mainly due to three test units whose drift capacity was underestimated by about 50%. Equally to what has been shown in Figure 5.4, a clear cut regarding the drift corresponding to a drop to 80% of the force resistance was also made for the data included in this plot. Thus, if the test was stopped before, the data was not included. The drift capacities of test units for which less than 20% degradation of shear force capacity was observed in the experiments, namely S9, S10 [88] and SW8, SW9 [92], were predicted with an average ratio of 0.82, i.e. the drifts were overestimated by about 20% on average, and a coefficient of variation of 18.7%.

Regarding the outliers in Figure 5.20 the observations are similar to those made when the optimum l_{b1e} was used. All outliers result from the predictions for the walls of [89]. There were two test units whose drop to 80% of the load and the according drift capacity was reached in the prediction: test units RW-A15-P10-S51 and RW-A15-P2.5-S64. RW-A15-P10-S51 was predicted to fail in flexural crushing just before the load had dropped 20% at about half the drift at which degradation started in the experiment, so the drift capacity was underestimated by 50%. Nevertheless, RW-A15-P2.5-S64 was predicted to also fail in flexural crushing at approximately the drift at which the test unit did actually degrade. However, the 3PKT does not capture the post-peak response if failure due to

flexural crushing occurs but rather stops the analysis. Shear degradation was predicted for another test unit, RW-A15-P10-S78, but at about half the drift at which it occurred in the experiment. As mentioned previously, the differences between the predictions and the experimental data could not be examined in detail, as sufficient measurement data to do so is not available at present.

5.7 Conclusions

The aim of this chapter was to validate a three parameter kinematic theory for shear critical walls, previously developed by [13], against a database of 28 rectangular reinforced concrete walls. This theory is based on the kinematics of walls exhibiting significant shear cracking which eventually leads to failure. Hence, only series that contained at least one test unit with such a failure mode were considered for validation. This led to a total number of 36 walls with varying characteristics that were initially considered. The transverse reinforcement ratios of these walls ranged from 0% to 1.04%, normal force ratios from 0 to 0.14 and the aspect ratio from 0.33 to 3.0, which marks an upper bound for application of the 3PKT. Yielding of the longitudinal reinforcement was predicted to occur before yielding of the transverse reinforcement for eight of the walls, which results in a flexural mechanism and renders the 3PKT inapplicable. The force-displacement response of the remaining 28 walls was predicted very well on average. Especially the prediction of the force capacity agrees well with the experimental data with an average ratio of measured to predicted peak load of 1.01 and a COV of 6.4%. Slightly more scatter is associated to the prediction of the drift capacity corresponding to a 20% drop of lateral load bearing capacity with an average ratio of 1.14 and a COV of 26.6%. However, especially in light of the scatter associated with the experimental data itself, which is displayed in differences between drifts in positive and negative loading direction or between two tests with the same layout, these drift capacity predictions are still good.

Furthermore, the effect several characteristics have on the response of walls was studied especially with regard to the displacement capacity. To this end, the influence of the transverse and longitudinal reinforcement ratios, aspect ratio and axial load ratio on the behavior of the walls was investigated. Experimental data against which the predictions could be verified was only available for variations of the aspect and transverse reinforcement ratios. In both cases, this data agrees well with the predictions of the 3PKT. Generally, the 3PKT shows that, as expected, each of the examined characteristics has a strong influence on the displacement capacity. The strength of the 3PKT lies in explicitly taking into account the load bearing mechanism developing in a wall. The drift capacity formulations which the 3PKT predictions were compared to primarily predict a general trend due to a change of a certain parameter, e.g. an increasing drift capacity with increasing aspect ratio. These predictions may differ slightly for different wall layouts, but the gradients typically do not change much, as evident in the graphs in this chapter. Contrarily to the drift capacity models, the 3PKT is able to capture changes in the load bearing mechanisms, which may have a significant influence on the drift capacity. An example for this is the prediction of the transverse reinforcement ratio that marks the transition from brittle to ductile behavior and thus the transition towards a larger gradient of the drift capacity prediction for a given wall layout.

Finally, the behavior of the critical loading zone, which especially influences at which drift degradation initiates, was studied in more detail. However, this study was restricted by a lack of detailed experimental data for this zone. The correlation of the size of the CLZ with several characteristics was studied. Based on the currently available experimental data, a simple empirical expression, which is a function of the geometry of the wall, is

proposed. If the size of the CLZ is determined with this expression, the prediction of the displacement capacity is slightly worse than before but still satisfactory, with an average ratio of experimental to predicted drift of 1.25 and a COV of 29.5%. The prediction of the peak force is almost equally good as before with an average ratio of 1.0 and a COV of 6.7%. The empirical expression for the size of the CLZ should only be used for walls with characteristics within the range of characteristics included in the database.

6 Summary, Conclusions and Outlook

6.1 Summary

The study presented here aims at contributing to the modeling of the inelastic response of rectangular, reinforced concrete wall-type bridge piers, which are not detailed in a way that ensures a ductile response. Models to predict the inelastic force-deformation relationship are necessary for the displacement-based assessment of existing structures. As this assessment needs to be done by practicing engineers, the aim of the study was to develop models that are easily applicable but which yield reliable results nevertheless. A test series of seven large-scale bridge piers with detailing that is representative of existing structures was used for the validation of the models.

Chapter 2 gives a review of existing plastic hinge models that are applicable to wall-type structures. Besides a summary of plastic hinge length proposals, this chapter includes equations to calculate the flexural response of a structural member as well as strain and curvature limits, which are used to define the deformation capacity. Due to the geometry of the piers and their detailing deficiencies, two further aspects need to be considered in the plastic hinge model: shear deformations and the influence of lap-splices in the potential plastic hinge region on the behavior of the pier. Three different modeling approaches for predicting the shear deformations that can be used in combination with plastic hinge modeling are reviewed. As investigating the behavior of lap-splices in detail is outside the scope of this study, only some models for predicting the strength of lap-splices and for estimating failure strain limits are reviewed.

In the following Chapter 3 the models that were introduced in the previous chapter are applied to predict the force-deformation response of the seven experimentally tested piers. Based on the comparison with the experimental data, an approach with which the flexural response is well predicted is identified. Furthermore, it is shown that by using strain limits for the moment curvature analysis relatively conservative estimates of the deformation capacities corresponding to a point shortly after peak load are obtained. The results of the approaches to predict the shear deformations are compared to the experimental data and modifications to better capture the shear response are examined. Based on the failure mode observed in the experiments and comparison with the experimental data, a concrete strain limit is established with which the onset of degradation of the test units with lap-splices is well captured. It is assumed that the lateral strength of the test unit then reduces immediately to its residual value which is related to the maximum eccentricity of the axial load.

Shear strength degradation models are reviewed in Chapter 4, which could provide a less conservative estimate of the drift capacity. The first part of the chapter introduces several types of shear degradation models which were mostly developed for columns and beams, such as ductility dependent models and drift capacity models. The second part compares the prediction of the models to the experimental data. It is shown that no reliable estimates of the drift capacity can be obtained with these types of models.

Chapter 5 treats a different modeling approach based on the kinematics of shear critical piers which allows for predicting the onset of shear and axial failure. At the beginning of the chapter, a brief introduction to this modeling approach, developed by [13], is given. This introduction is followed by a validation of the approach against a database of 28 wall-type

piers. The model is shown to yield good predictions of the shear force and deformation capacity of the walls included in the database. Subsequently, the influence of some important characteristics on the behavior of piers, particularly on their drift capacity, is examined with the kinematic model. Finally, one characteristic parameter of this model, the size of the "critical loading zone" which primarily influences the drift at which degradation initiates, is discussed and an equation for estimating this length is proposed.

6.2 Conclusions

The aim of this study was to identify and develop easily applicable models that can be used by practicing engineers for the displacement-based assessment of existing bridges. The focus of the study was to predict the behavior of rectangular, wall-type bridge piers with detailing deficiencies such as lap-splices in potential plastic hinge regions and low transverse reinforcement ratios. Two types of models were investigated to this end: plastic hinge models and a kinematic model. Regarding the plastic hinge modeling approach, several conclusions can be drawn from this study. Despite the fact that plastic hinge models are intended to predict the response of flexure-controlled members, good results were obtained for the potentially shear critical wall-type piers that were investigated in this study. Based on a comparison with the experimental data of seven bridge pier tests, a plastic hinge length and formulations for the response, with which good estimates of the flexural response were obtained, could be identified. The effect of strain penetration was neither explicitly accounted for in the formulation of the plastic hinge nor the one of the flexural response, as no detailed conclusion on how to incorporate it in the inelastic range could be drawn from the experimental data. Furthermore, comparison with the experimental data showed that it appears to be small enough to be neglected.

With the identified plastic hinge modeling procedure, good agreement was obtained not only on a global, but also on a local level, which means that the deformation predicted for a certain limit strain in the plastic hinge agreed well with the deformation at which that limit strain is reached in the tests. Within the scope of plastic hinge modeling, strain or curvature limits are used to define upper bounds for the curvature in the plastic hinge and thus define the deformation capacity of the structure. With these curvature limits, relatively conservative estimates of the deformation capacity are obtained. However, for a less conservative limit the onset of shear degradation needed to be taken into account. This is difficult within the scope of plastic hinge modeling, as shear failure is based on a different mechanism than that assumed in plastic hinge modeling. Hence, models such as the kinematic model should be applied for less conservative estimates of the deformation capacity.

With regard to the influence of lap-splices at the base of the pier it was shown that a good estimate of the onset of failure could be obtained, using a simple limit for the concrete strain. This strain governs failure if the splice is not well confined and long enough to sustain the maximum tension forces that could occur. The experimental data showed that a slow degradation towards the residual shear force capacity, which is determined by the eccentricity of the axial load, is not guaranteed. Predicting the rate of decay appears difficult, however, as it may depend on material properties with considerable scatter, such as the concrete tensile strength, or the actual concrete cover of the reinforcement. Hence, it should be assumed that the capacity drops to the residual level as soon as the strain that triggers lap-splice failure is exceeded.

A more extensive study proved to be necessary to capture the shear deformations in combination with the plastic hinge modeling approach. Existing shear deformation models have

been developed based on experimental results of mainly capacity designed and hence flexure-controlled walls. For this type of walls, the shear deformation in the inelastic range can be expressed as a constant ratio of the flexural deformation. While this constant ratio was observed for the slender and thus more flexure-controlled walls of this study, the assumption of a constant ratio did not hold for the more shear critical walls. Nevertheless, a satisfactory prediction of the shear deformation was obtained by modification of an approach which relates the shear strain to the axial strain. Instead of assuming a constant ratio of shear to flexural deformation, the ratio was computed from the axial strain and curvature obtained from the moment-curvature analysis at each displacement. Furthermore, a correction factor accounting for the increased shear deformations of piers with low shear force resistance needed to be taken into account. Concerning the applicability of ductility-dependent shear degradation models or drift capacity models, which are sometimes used in combination with plastic hinge models to estimate the displacement capacity of a member, comparison with the experimental data showed that good results could not be obtained with any of the existing approaches. This is due to the fact that most of them were developed for beams or columns and contain simplifications that are reasonable for this type of structural components, but invalid for wall-type piers. With these models, it is possible to predict general trends in the development of the drift capacity based on certain characteristics of the walls but not actual drift capacity estimates for a specific wall-type pier.

To obtain a reliable estimate of the deformation capacity of a pier, its main characteristics need to be taken into account. Doing so in a simplified manner yields results that are significantly better than those obtained with the models mentioned in the previous paragraph, as shown with the validation of a kinematic model. Application of this model revealed that while the influence of a certain characteristic, such as the transverse reinforcement ratio, on the drift capacity may qualitatively be the same for varying pier layouts, there may be significant quantitative differences. The shear force and the drift capacity predictions obtained with the kinematic model for shear critical, rectangular wall-type piers were found to be in very good agreement with the data of 28 tests subjected to single curvature loading. Hence, this model is suitable to predict the deformation capacity that is defined by the degradation of both the shear and the axial load bearing mechanisms. Based on the currently available test data, a simple empirical expression that relates the size of the “critical loading zone”, a parameter that primarily influences the drift capacity at the onset of shear degradation, to the section depth of the wall is proposed. With this estimate, the agreement of the shear force prediction with the experimental data remains very good whereas the agreement of the drift capacity prediction is slightly decreased, but still good.

6.3 Outlook

Several topics on which further research is necessary can be defined based on this study. Regarding the plastic hinge modeling approach, two topics that constituted an important part of this study still leave room for further research: the influence of lap-splices and the shear deformations. The proposed concrete strain might be regarded as an upper bound limit for the failure of the splice. The behavior of splices under reversed cyclic loading needs to be better understood to examine whether a lower limit that initiates failure before the concrete is crushed in compression is necessary. One of the three test units with lap-splices considered in this study exhibited such a splitting failure before significant concrete damage was observed, even though the splice was sufficiently long to transfer the maximum tension

force. However, based on the experimental data of the large scale tests, no limits to predict this failure could be derived.

With regard to the shear deformations, an approach relating the shear deformation to the axial elongation of the test unit was investigated. Preliminary results indicated that good predictions may be possible with this approach. However, only the contribution of one out of two mechanisms, which contributed to approximately half the shear deformation, could be expressed as a closed form solution. Such a solution also needs to be established for the second mechanism.

Generally, one needs to keep in mind that even though the results obtained for the flexural deformation of the wall-type piers was good, the plastic hinge modeling approach has been validated against a very small database. Therefore, it needs to be validated, and improved where necessary, against a larger database to reduce uncertainties regarding the choice of e.g. the plastic hinge length and the limit strains that are applied.

Regarding the kinematic theory, the main field of research that remains is the estimate of the size of the “critical loading zone”. The experimental data that was available to investigate the development of this zone is, at present, very limited. Detailed measurements of the area in which that zone forms would be desirable to study the development of this zone in more detail.

Based on the experimental results and the review of models it seems recommendable to not use the same models for different cross sections or different types of structures without verifying the model for each type of structure. If models are applied without verification, the predictions can be unreliable. This was evident in the drift capacity predictions made with the beam and column models, for instance. Hence, the applicability of the models used in this report should be verified for different types of cross section (e.g. flanged sections, T-sections or hollow-core sections) and modified were necessary.

Notation and Abbreviations

Capital Latin letters

A	Cross sectional area
A_c	Cross sectional area of core
A_g	(Concrete) gross section
A_s	Longitudinal reinforcement area
A_{sb}	Area of one longitudinal reinforcement bar
A_v	Transverse reinforcement area
E	Modulus of elasticity
I	Moment of inertia
EI_{eff}	Effective flexural stiffness
EI_g	Uncracked, gross flexural stiffness
G	Shear modulus
K_{sh}	Shear stiffness
L_b	Base length (of an LVDT)
L_p	Plastic hinge length
L'_p	Plastic hinge length without influence due to strain penetration
L_{pr}	Length over which plasticity spreads ($\sim 2L'_p$)
L_s	Shear span
L_{sp}	Strain penetration component of the plastic hinge length
M	Bending moment
M_y	First yield moment
M_N	Nominal yield moment
P	Normal force
T	Tension force
V	Shear force
V_r	Shear capacity
V_c	Shear capacity provided by concrete
V_s	Shear capacity provided by transverse steel
V_p	Shear capacity provided by axial load
V_{ci}	Shear capacity due to aggregate interlock
V_{cr}	Shear cracking load

Small Latin letters

b	Section width (i.e. parallel to axis around which bending occurs)
b_c	Core section width
b_{con}	Confined section width

c	Concrete cover to center of stirrup
d	Effective section depth
d_{bl}	Longitudinal reinforcement bar diameter
d_{bv}	Transverse reinforcement bar diameter
f_b	Bond stress
f_c	Concrete compression strength
f_{cc}	Compression strength of confined concrete
f_{ct}	Concrete tension strength
$f_{cx,y}$	Concrete stress in x- or y-direction, respectively
$f_{sx,y}$	Steel stress in x- or y-direction, respectively
f_y	Yield strength of steel
f_{yv}	Yield strength of transverse reinforcement
f_u	Ultimate strength of steel
h	Total section depth
h_c	Core section depth
h_{con}	Confined section depth
k	Correction factor
k_{con}	Confinement effectiveness factor
l_{cr}	Length along which cracks develop
l_d	Development length of reinforcement bar
l_s	Lap-splice length
n	Normal force ratio
n_{bl}	Number of longitudinal reinforcement bars
n_{st}	Number of stirrups
s	Transverse reinforcement spacing
s_l	Spacing of longitudinal reinforcement
s_x	Crack spacing in x-direction (uniaxial tension)
s_y	Crack spacing in y-direction (uniaxial tension)
s_θ	Crack spacing perpendicular to crack
$s_{\theta,x}$	X-component of s_θ
$s_{\theta,y}$	Y-component of s_θ
v	Shear stress
x_c	Compression zone depth
x_N	Neutral axis depth
z	Internal lever arm

Capital Greek letters

Δ'_y	First yield displacement
Δ_y	Nominal yield displacement
Δ_{fl}	Flexural displacement
Δ_s	Shear displacement
Δ_{sp}	Strain penetration displacement

Small Greek letters

β	Compression softening factor
δ_s	Reinforcement bar slip
ε	Strain
ε_{c0}	Concrete strain under peak stress
ε_{cc}	Confined concrete strain under peak stress
ε_{cu}	Ultimate concrete strain
ε_h	Hardening strain of steel
ε_y	Yield strain of steel
ε_{su}	Ultimate strain of steel
ϕ	Curvature
ϕ_y	Nominal yield curvature
ϕ'_y	First yield curvature
ϕ_u	Ultimate curvature
γ	Shear strain
γ_{el}	Safety factor
μ_Δ	Displacement ductility
μ_ϕ	Curvature ductility
θ	Crack angle
θ_{sp}	Rotation due to strain penetration
θ_y	Yield rotation
θ_u	Ultimate rotation
ϱ_l	Longitudinal reinforcement ratio
$\varrho_{l,web}$	Longitudinal reinforcement ratio of the web
ϱ_v	Transverse reinforcement ratio
σ	Stress
τ_b	Bond stress
ω	Mechanical reinforcement ratio

Abbreviations

ASFI	Axial – Shear – Flexure Interaction method
MCFT	Modified Compression Field Theory
RC	Reinforced Concrete
USFM	Uniaxial – Shear – Flexure Model
VK	Test Unit (= *V*ersuchs*k*örper)

Bibliography

[1] M. Bimschas, *Displacement-Based Seismic Assessment of Existing Bridges in Regions of Moderate Seismicity*. PhD thesis, Swiss Federal Institute of Technology ETH Zurich, 2010.

[2] A. Dazio and M. Bimschas, "Erdbebensicherheit bestehender brücken, sia dokumentation d0234 - neues aus der brückenforschung," tech. rep., Schweizerischer ingenieur und Architektenverein, November 2010.

[3] P. Hannewald, M. Bimschas, and A. Dazio, "Quasi-static cyclic tests on RC bridge piers with detailing deficiencies," IBK Report xx, Institute of Structural Engineering, Swiss Federal Institute of Technology ETH, 2013. to be published.

[4] A. Bohl and P. Adebar, "Plastic hinge lengths in high-rise concrete shear walls," *ACI Structural Journal*, vol. 108, no. 2, 2011.

[5] J. B. Mander, M. Priestley, and R. Park, "Theoretical stress-strain model for confined concrete," *ASCE Journal of Structural Engineering*, vol. 114, no. 8, pp. 1804–1826, 1988.

[6] D. Biskinis and M. N. Fardis, "Flexure-controlled ultimate deformations of members with continuous or lap-spliced bars," *Structural concrete*, vol. 11, no. 2, 2010.

[7] M. J. N. Priestley, G. M. Calvi, and M. J. Kowalsky, *Displacement based seismic design of structures*. IUSS Press Pavia Italy, 2007.

[8] K. Beyer, A. Dazio, and M. J. N. Priestley, "Shear deformations of slender RC walls under seismic loading," *ACI Structural Journal*, vol. 108, no. 2, 2011.

[9] L. Hagsten, L. Hestbech, and J. Fisker, "Energiprincipper - del 3: Betonkonstruktioner. Teori," 2011. Lecture Notes.

[10] M. J. Kowalsky and M. J. N. Priestley, "Improved analytical model for shear strength of circular reinforced concrete columns in seismic regions," *ACI Structural Journal*, vol. 97, no. 3, pp. 388–396, 2000.

[11] CEN, "Eurocode 2: Design of concrete structures: Part 1-1: General rules and rules for buildings," building code, European Committee for Standardization, 2004.

[12] B. I. Mihaylov, E. C. Bentz, and M. P. Collins, "Two parameter kinematic theory for shear behavior of deep beams," *ACI Structural Journal*, vol. 110, no. 3, pp. 447–456, 2013.

[13] B. I. Mihaylov, P. Hannewald, and K. Beyer, "A three parameter kinematic theory for shear-critical reinforced concrete piers," *ASCE Journal of Structural Engineering*, 2013. submitted.

[14] M. Hirosawa, "Past experimental results on reinforced concrete shear walls and analysis on them," Tech. Rep. 6, Kenchiku Kenkyu Shiryo, Building Research Institute, Ministry of Construction, 1975.

[15] SIA, "SIA261: Actions on structures," building code, Swiss Society of Engineers and Architects, 2003.

[16] SIA, “SIA160: Norm fr die belastungsannahmen, die Inbetriebnahme und die überwachung der bauten,” building code, Swiss Society of Engineers and Architects, 1970.

[17] T. Wenk, “Beurteilung der Erdbebensicherheit bestehender Strassenbrücken (assessment of earthquake safety of existing road bridges),” documentation, Federal roads office FEDRO, 2005.

[18] M. Bimschas, “Seismic safety of existing bridges in regions of moderate seismicity,” in *6th International PhD Symposium in Civil Engineering*, (Zurich, Switzerland), August 2006.

[19] M. Bimschas and A. Dazio, “Bridge assessment in regions of moderate seismicity - a case study,” in *First European Conference on Earthquake Engineering and Seismology*, (Geneva, Switzerland), September 2006. paper number 1256.

[20] E. M. Hines, *Seismic performance of hollow rectangular reinforced concrete bridge piers with confined corner elements*. PhD thesis, University of California, San Diego, 2002.

[21] M. Priestley and F. Seible, eds., *Seismic assessment and retrofit of bridges*. Structural systems research project, University of California at San Diego, 1991. Report No. SSRP-91/103.

[22] T. B. Panagiotakos and M. N. Fardis, “Deformations of reinforced concrete members at yielding and ultimate,” *ACI Structural Journal*, vol. 98, no. 2, 2001.

[23] M. N. Fardis, ed., *Guidelines for Displacement-based Design of Buildings and Bridges*. No. 05 in LESSLOSS Reports, IUSS Press, Pavia Italy, 2007.

[24] CEN, “Eurocode 8: Design of structures for earthquake resistance - part 3: Assessment and retrofitting of buildings,” building code, European Committee for Standardization, 2005.

[25] P. S. Wong and F. J. Vecchio, *Vector2 & Formworks user’s manual*, 2002.

[26] A. Baker and A. Amarakone, “Inelastic hyperstatic frames analysis,” *ACI special publication*, vol. 12, pp. 85–142, 1965.

[27] İlker Kazaz, “An analytical study on the plastic hinge length of structural walls,” *ASCE Journal of Structural Engineering*, 2013.

[28] E. M. Hines, J. I. Restrepo, and F. Seible, “Force-displacement characterization of well-confined bridge piers,” *ACI Structural Journal*, vol. 101, no. 4, 2004.

[29] H. Shima, L.-L. Chou, and H. Okamura, “Micro and macro models for bond in reinforced concrete,” *Journal of the Faculty of Engineering*, vol. 39, no. 2, pp. 133–194, 1987.

[30] H. Sezen and E. J. Setzler, “Reinforcement slip in reinforced concrete columns,” *ACI Structural Journal*, vol. 105, no. 3, p. 280, 2008.

[31] D. Biskinis and M. N. Fardis, “Deformations at flexural yielding of members with continuous or lap-spliced bars,” *Structural concrete*, vol. 11, no. 3, 2010.

[32] V. Sigrist, *Zum Verformungsvermögen von Stahlbetonträgern*. PhD thesis, Swiss Federal Institute of Technology ETH Zurich, 1995.

[33] J. Zhao and S. Sritharan, “Modeling of strain penetration effects in fiber-based analysis of reinforced concrete structures,” *ACI Structural Journal*, vol. 104, no. 2, pp. 133–141, 2007.

[34] S. A. Sheikh and S. Uzumeri, “Analytical model for concrete confinement in tied columns,” *Journal of the Structural Division*, vol. 108, no. 12, pp. 2703–2722, 1982.

[35] İlker Kazaz, P. Gülkan, and A. Yakut, “Deformation limits for structural walls with confined boundaries,” *Earthquake Spectra*, vol. 28, no. 3, pp. 1019 – 1046, 2012.

[36] T. Paulay and M. Priestley, “Stability of ductile structural walls,” *ACI Structural Journal*, vol. 90, no. 4, pp. 385–392, 1993.

[37] R. Y. Chai and D. Elayer, “Lateral stability of reinforced concrete columns under axial reversed cyclic tension and compression,” *ACI Structural Journal*, vol. 96, no. 5, pp. 780–789, 1999.

[38] V. G. Bardakis and M. N. Fardis, “A displacement-based seismic design procedure for concrete bridges having deck integral with the piers,” *Bulletin of Earthquake Engineering*, vol. 9, pp. 1–24, 2011.

[39] M. P. Collins and D. Mitchell, *Prestressed concrete structures*. Prentice Hall (Englewood Cliffs, NJ), 1997 Response Publications ed., 1991.

[40] E. Bentz, F. J. Vecchio, and M. P. Collins, “Simplified modified compression field theory for calculating shear strength of reinforced concrete elements,” *ACI Structural Journal*, vol. 103, no. 4, pp. 614–624, 2006.

[41] E. C. Bentz and M. P. Collins, *Membrane-2000*. ecf.utoronto.ca/ bentz/m2k.htm, 2000. Version 1.0.0.

[42] H. Sezen and C. Patwardhan, “Shear displacement model for reinforced concrete columns,” in *Structures Congress*, ASCE, 2006.

[43] ACI-ASCE Committee 408, “Report on bond of steel reinforcing bars under cyclic loads,” ACI Committee report ACI.2R-12, American Concrete Institute, Farmington Hills, MI, 2012.

[44] J. D. Aristizábal-Ochoa, A. E. Fiorato, and W. G. Corley, “Tension lap splices under severe load reversals,” *Research and development bulletin*, vol. RD077.01D, 1982.

[45] B. Sivakumar, P. Gergely, and R. White, “Suggestions for the design of r/c lapped splices for seismic loading,” *Concrete International*, vol. 5, no. 2, pp. 46–50, 1983.

[46] B. Sparling and T. Rezansoff, “The effect of confinement on lap splices in reversed cyclic loading,” *Canadian Journal of Civil Engineering*, vol. 13, pp. 681–692, 1986.

[47] T. Rezansoff, J. A. Zacaruk, and R. Topping, “Tensile lap splices in reinforced concrete beams under inelastic cyclic loading,” *ACI Structural Journal*, vol. 85, no. 1, pp. 46–52, 1988.

[48] D. Darwin, M. L. Tholen, E. K. Idun, and J. Zuo, “Splice strength of high relative rib area reinforcing bars,” *ACI Structural Journal*, vol. 93, no. 1, 1996.

[49] T. Paulay, “Lapped splices in earthquake-resisting columns,” *ACI Journal proceedings*, vol. 79, no. 6, pp. 485–469, 1982.

[50] M. Priestley, F. Seible, and G. M. Calvi, *Seismic design and retrofit of bridges*. New York, NY: John Wiley & Sons, Inc., 1996.

[51] E. Canbay and R. J. Frosch, “Bond strength of lap-spliced bars,” *ACI Structural Journal*, vol. 102, no. 4, pp. 605–614, 2005.

[52] FIB, “Model code 2010 - final draft, volume 1,” Tech. Rep. fib bulletin 65, International Federation for Structural Concrete, 2012.

[53] A. Dazio, K. Beyer, and H. Bachmann, “Quasi-static cyclic tests and plastic hinge analysis of RC structural walls,” *Engineering Structures*, vol. 31, no. 7, 2009.

[54] K. Beyer, A. Dazio, and M. N. Priestley, “Seismic design of torsionally eccentric buildings with U-shaped RC walls,” Research Report ROSE - 2008/03, ROSE school, 2008.

[55] C. Goodnight, M. Kowalsky, and J. Nau, “Effect of load history and design variables on the behavior of circular bridge columns.” ACI Fall Convention, Session: Forming a Framework for Performance Based Seismic Design of Concrete Bridges, 2012.

[56] A. Dazio, T. Wenk, and H. Bachmann, “Versuche an Stahlbetontragwänden unter zyklisch-statischer Einwirkung,” Test report IBK Report 239, Swiss Federal Institute of Technology ETH Zurich, 1999. Birkhäuser Verlag.

[57] MathWorks, *Matlab*. mathworks.com, 2010. Version 7.11.0.584 R2010b.

[58] S. Popovics, “A review of stress-strain relationships for concrete,” *ACI Journal proceedings*, vol. 67, no. 3, pp. 243 – 248, 1970.

[59] E. Thorenfeldt, A. Tomaszewicz, and J. Jensen, “Mechanical properties of high-strength concrete and application in design,” in *Proceedings of the Symposium “Utilization of High Strength Concrete”*, (Stavanger, Norway), pp. 149–159, 1987.

[60] J. F. Stanton and H. M. McNiven, “The development of a mathematical model to predict the flexural response of reinforced concrete beams to cyclic loads, using system identification,” Report UCB/EERC 2, College of Engineering, University of California Berkeley, 1979.

[61] S.-Y. M. Ma, V. V. Bertero, and E. P. Popov, “Experimental and analytical studies on hysteretic behavior of reinforced concrete rectangular and T-beams,” Report EERC 2, College of Engineering, University of California Berkeley, 1976.

[62] F. C. Filipou, E. P. Popov, and V. V. Bertero, “Effects of bond deterioration on hysteretic behavior of reinforced concrete joints,” Report UCB/EERC 19, College of Engineering, University of California Berkeley, 1983.

[63] FIB, “Model code 2010 - first complete draft, vol. 1,” Tech. Rep. fib bulletin 55, International Federation for Structural Concrete, 2010.

[64] G. Angeli, P. Hannewald, and K. Beyer, “Behaviour of poorly detailed lap-splices under cyclic loading,” in *Vienna Congress on Recent Advances in Earthquake Engineering and Structural Dynamics VEESD* (W. L. Christoph Adam, Rudolf Heuer and C. Schranz, eds.), 2013. Paper No. 197.

[65] ATC, “Seismic Retrofitting Guidelines for Highway Bridges,” Tech. Rep. ATC-06-2, Applied Technology Council, Redwood City, California, 1983.

[66] D. E. Biskinis, G. K. Roupakias, and M. N. Fardis, “Degradation of shear strength of reinforced concrete members with inelastic cyclic displacements,” *ACI Structural Journal*, vol. 101, no. 6, 2004.

[67] M. Aschheim and J. P. Moehle, “Shear strength and deformability of rc bridge columns subjected to inelastic cyclic displacements,” Report UCB/EERC 92/04, College of Engineering, University of California at Berkeley, 1992.

[68] M. N. Priestley, R. Verma, and Y. Xiao, “Seismic shear strength of reinforced concrete columns,” *ASCE Journal of Structural Engineering*, vol. 120, no. 8, pp. 2310 – 2329, 1994.

[69] H. Sezen and J. P. Moehle, “Shear strength model for lightly reinforced concrete columns,” *ASCE Journal of Structural Engineering*, vol. 130, no. 11, 2004.

[70] Y.-L. Wong, T. Paulay, and M. N. Priestley, “Response of circular reinforced concrete columns to multi-directional seismic attack,” *ACI Structural Journal*, vol. 90, no. 2, pp. 180 – 191, 1993.

[71] M. N. Priestley, R. Verma, and Y. Xiao, “Discussion on seismic shear strength of reinforced concrete columns by Mark Aschheim, Jack P. Moehle and Julio A. Ramirez and closure of discussion,” *ASCE Journal of Structural Engineering*, vol. 122, no. 4, pp. 461 – 467, 1996.

[72] S. Pujol, M. Sozen, and J. Ramírez, “Transverse reinforcement for columns of rc frames to resist earthquakes,” *ASCE Journal of Structural Engineering*, vol. 126, no. 4, 2000.

[73] D. Kato and K. Ohnishi, “Axial load carrying capacity of r/c columns under lateral load reversals,” in *The Third U.S.-Japan Workshop on Performance-Based Earthquake Engineering Methodology for Reinforced Concrete Building Structures*, (University of California, Berkeley), pp. 247 –255, Pacific Earthquake Engineering Research Center, College of Engineering, 2002. PEER Report 2002/02.

[74] K. J. Elwood and J. P. Moehle, “Shake table tests and analytical studies on the gravity load collapse of reinforced concrete frames,” PEER Report 2003/01, Pacific Earthquake Engineering Research Center, College of Engineering University of California, Berkeley, November 2003.

[75] K. J. Elwood and J. P. Moehle, “Drift capacity of reinforced concrete columns with light transverse reinforcement,” *Earthquake Spectra*, vol. 21, no. 1, pp. 71 – 89, 2005.

[76] S. S. E. Lam, B. Wu, Y. L. Wong, Z. Y. Wang, Z. Q. Liu, and C. S. Li, “Drift capacity of rectangular reinforced concrete columns with low lateral confinement and high-axial load,” *ASCE Journal of Structural Engineering*, vol. 129, no. 6, 2003.

[77] H.-G. Park, E.-J. Yu, and K.-K. Choi, “Shear-strength degradation model for rc columns subjected to cyclic loading,” *Engineering Structures*, vol. 34, pp. 187 – 197, 2011.

[78] K. J. Elwood and M. O. Eberhard, “Effective stiffness of reinforced concrete columns,” *ACI Structural Journal*, vol. 106, no. 4, pp. 476 –484, 2009.

[79] H. Mostafaei, *Axial - shear - flexure interaction approach for displacement-based evaluation of reinforced concrete elements*. PhD thesis, University of Tokyo, Graduate School of Engineering, 2006.

[80] H. Mostafaei and T. Kabeyasawa, “Axial-shear-flexure interaction approach for reinforced concrete columns,” *ACI Structural Journal*, vol. 104, no. 2, pp. 218–226, 2007.

[81] H. Mostafaei and F. J. Vecchio, “Uniaxial shear-flexure model for reinforced concrete elements,” *Journal of Structural Engineering*, vol. 134, no. 9, pp. 1538–1547, 2008.

[82] H. Mostafaei and J. K. Hum, “Response simulation of reinforced concrete columns under lateral loads,” Research Report RR-No.294, Institute for Research in Construction, National Research Council Canada, 2010.

[83] H. Mostafaei, F. J. Vecchio, and T. Kabeyasawa, “Deformation capacity of reinforced concrete columns,” *ACI structural journal*, vol. 106, no. 2, pp. 187 – 195, 2009.

[84] A. C. Lynn, *Seismic evaluation of existing reinforced concrete building columns*. PhD thesis, University of California, Berkeley, 2001.

[85] H. Sezen, *Seismic Behavior and Modeling of Reinforced Concrete Building Columns*. PhD thesis, University of California, Berkeley, 2002.

[86] CSA, “A23.3-04 (R2010) - Design of concrete structures,” standard, Canadian Standards Association, 2004.

[87] B. Li, K. Maekawa, and H. Okamura, “Contact density model for stress transfer across cracks in concrete,” *Journal of the Faculty of Engineering*, vol. 40, no. 1, pp. 9–52, 1989. The University of Tokyo.

[88] J. Maier and B. Thürlimann, “Bruchversuche an Stahlbetonscheiben,” test report, Swiss Federal Institute of Technology ETH, Zurich, Switzerland, 1985.

[89] T. A. Tran and J. W. Wallace, “Experimental study of nonlinear flexural and shear deformations of reinforced concrete structural walls,” in *Proceedings of the 15th WCEE*, 2012.

[90] A. Dazio, T. Wenk, and H. Bachmann, “Vorversuche an Stahlbetontragwänden unter zyklisch-statischer Einwirkung,” test report, Swiss Federal Institute of Technology ETH Zurich, 1995.

[91] S. Wiradinata, “Behaviour of squat walls subjected to load reversals,” Master’s thesis, Department of Civil Engineering, University of Toronto, 1985.

[92] K. Pilakoutas and A. Elnashai, “Cyclic behavior of reinforced concrete cantilever walls, Part I: Experimental results,” *ACI Structural Journal*, vol. 92, no. 3, pp. 271–281, 1995.

[93] H. Bachmann, T. Wenk, A. Dazio, M. Baumann, K. Bucher, M. Neujahr, and H. Riemer, “Erdbebensicherung von Bauwerken, Demonstrationsversuche,” tech. rep., Swiss Federal Institute of Technology ETH Zurich, 1995. Fortbildungskurs für Bauingenieure.

[94] E. C. Bentz and M. P. Collins, *Response-2000*. ecf.utoronto.ca/ bentz/r2k.htm, 2000. Version 1.0.5.

[95] G. Markeset and A. Hillerborg, “Softening of concrete in compression - localization and size effects,” *Cement and concrete research*, vol. 25, no. 4, pp. 702 – 708, 1995.

[96] J. G. van Mier, *Concrete Fracture: a multiscale approach*. CRC Press Taylor & Francis Group, 2012.

[97] Z. P. Bazant, “Fracturing truss model: Size effect in shear failure of reinforced concrete,” *Journal of engineering mechanics*, vol. 123, no. 12, pp. 1276–1288, 1997.

Projektabschluss

Schweizerische Eidgenossenschaft
Confédération suisse
Confederazione Svizzera
Confederaziun svizra

Eidgenössisches Departement für
Umwelt, Verkehr, Energie und Kommunikation UVEK
Bundesamt für Strassen ASTRA

FORSCHUNG IM STRASSENWESEN DES UVEK

Version vom 09.10.2013

Formular Nr. 3: Projektabschluss

erstellt / geändert am: 13.2.2014

Grunddaten

Projekt-Nr.:	AGB 2008/001
Projekttitel:	„Erdbebensicherheit bestehender Brücken – Zyklisch inelastisches Verhalten von Brückenstützen"
Enddatum:	31.12.2013

Texte

Zusammenfassung der Projektresultate:

Bestehende Brücken können gemäss Normen ohne Vorgaben zur Bemessung für Erdbebenlasten konstruiert sein. Besonders in Ländern wie der Schweiz, in denen die Seismizität moderat ist, sind moderne Erdbebennormen oft erst vor wenigen Jahren eingeführt worden, da die Erdbebengefahr lange unterschätzt wurde. Existierende Brücken haben daher möglicherweise eine geringe Verformungskapazität aufgrund ihrer Bauart und ihrer konstruktiven Details. Um dies zu beurteilen wurde ein zweiteiliges Forschungsvorhaben initiiert. Der erste Teil dieses Projektes [1], [2] wurde an der ETHZ ausgeführt und diente der Abschätzung des Verformungsbedarfs. Er befasste sich eingehend mit der Modellierung von Brücken sowie der Identifizierung kritischer Stützenkonfigurationen. Zu den dabei identifizierten kritischen Details gehören Bewehrungsstösse in der potenziellen plastischen Region über dem Fundament, geringe Querbewehrungsgrade und das Fehlen von Umschnürungsbewehrung. Für die Überprüfung dieser Brücken können verformensbasierte Methoden, welche die bei einem Erdbeben aufgebrachten Verformungen mit der Verformungskapazität vergleichen, verwendet werden [1], [2].

Das Projekt „Erdbebensicherheit bestehender Brücken – Zyklisch inelastisches Verhalten von Brückenstützen" ist der zweite Teil des Forschungsvorhabens. Es befasst sich mit der Abschätzung der Verformungskapazität von typischen Schweizer Brückenstützen. Da die verformensbasierte Überprüfung von praktisch tätigen Ingenieuren durchgeführt wird und eine grosse Anzahl Brücken zu überprüfen ist, sollten die Modelle zur Abschätzung des Verformungsvermögens relativ einfach anwendbar sein und gleichzeitig gute und nicht zu konservative Resultate liefern. Mit dieser Arbeit soll zur Entwicklung solcher Modelle beigetragen werden. Versuche an Stützen mit den genannten Konstruktionsdefiziten, die im Rahmen beider Teile des Forschungsprojektes an der ETHZ durchgeführt wurden [1], [3], dienen als experimentelle Datenbasis zur Überprüfung und Validierung. Zwei Ansätze wurden auf Basis der genannten Kriterien zum vertieften Studium ausgewählt: die Modellierung mit plastischem Gelenk sowie ein kinematisches Modell für schubkritische Wände.

Als erstes wird die Modellierung mit plastischem Gelenk untersucht. Es wird ein Überblick über Gleichungen zur Bestimmung der Länge des plastischen Gelenkes, zur Ermittlung der Biege- und Schubverformung sowie zur Berechnung der Dehnungslimite die den Versagenszustand definieren gegeben. Durch Überprüfung mit den experimentellen Daten wird ein Verfahren identifiziert, mit dem die Last-Verformungskurve der Stützen ermittelt werden kann. Der Einfluss der Bewehrungsstösse auf das Verhalten sowie die Schubverformungen werden dabei in einfacher Weise berücksichtigt.

Das zweite Modell ist ein kinematisches Modell welches sich insbesondere eignet, das Verhalten von rechteckigen, schubkritischen Stützen nach Erreichen der Maximallast vorherzusagen. Das Modell basiert auf der bei Schubrissbildung einsetzenden Kinematik und wurde andernorts entwickelt. In diesem Bericht wird es mit Hilfe einer erweiterten Datenbank validiert. Ausserdem wird der Einfluss einiger wichtigen Charakteristiken, wie zum Beispiel der Bewehrungsgehalte und der Schlankheit, insbesondere im Hinblick auf die Verformungskapazität anhand dieses Modells dargestellt.

Der Vergleich der Vorhersagen mit den experimentellen Daten zeigte, dass die Modellierung mit plastischem Gelenk trotz ihrer Einfachheit gute Ergebnisse für die hier betrachteten nur teilweise biegebestimmten Wände lieferte. Dieser Modellierungsansatz resultiert in einer eher konservativen Abschätzung der Verformungskapazität, die in etwa der Verformung bei Maximallast entspricht. Um auch den zum degradierenden Ast gehörenden Teil der Antwort zu berücksichtigen, sollte das kinematische Modell, mit dem sowohl Querkraft- als auch Axiallastversagen erfasst werden können, verwendet werden.

[1] M. Bimschas, «Displacement-Based Seismic Assessment of Existing Bridges in regions of Moderate Seismicity,» Swiss Federal Institute of Technology ETH, Zurich, 2010.
[2] A. Dazio und M. Bimschas, «Erdbebensicherheit bestehender Brücken,» SIA Dokumentation D0234 - Neues aus der Brückenforschung, pp. 15-36, November 2010.
[3] P. Hannewald, M. Bimschas und A. Dazio, „Quasi-static cyclic tests on RC bridge piers with detailing deficiencies," Swiss Federal Institute of Technology ETH, Zurich, 2013.

Schweizerische Eidgenossenschaft
Confédération suisse
Confederazione Svizzera
Confederaziun svizra

Eidgenössisches Departement für
Umwelt, Verkehr, Energie und Kommunikation UVEK
Bundesamt für Strassen ASTRA

Zielerreichung:

Alle Meilensteine im von Herrn Dr. Alessandro Dazio verfassten Forschungsantrag wurden erreicht. Diese waren (Tabelle 3 im Antrag):

1) Literaturstudie und Einarbeitung.
2) Parametrische Studie zum Verformungsverhalten von konventionell bemessenen wandartigen Stahlbetonbrückenstützen.
3) Planung der Versuchsserie.
4) Konstruktion der Versuchskörper.
5) Vorbereitung und Durchführung der Versuche.
6) Analyse der Versuchsdaten und Verfassung des Versuchsberichts.
7) Überprüfung bzw. Entwicklung von Modellen, um das Verformungsverhalten von konventionell bemessenen wandartigen Stahlbetonbrückenstützen realitätsnahe zu erfassen.
8) Verfassung des Schlussberichts.

Die Arbeiten zu den Meilensteine 1-5 und der erste Teil der Arbeiten zu Meilenstein 6 wurden von Frau Hannewald an der ETHZ durchgeführt. Ab März 2011 arbeitete Frau Hannewald an der EPFL. In dieser Zeit wurden die Arbeiten zu Meilenstein 6-8 abgeschlossen.

Folgerungen und Empfehlungen:

Im Rahmen dieses Forschungsprojektes wurde ein anwendungsfähiges Ingenieursmodell zur Beurteilung der Verformungskapazität von typischen Schweizer Brückenstützen entwickelt. Zur Verfeinerung dieses Modells sollten die folgenden Fragestellungen behandelt werden:

1) Verhalten von Bewehrungsstössen bei zyklischer Beanspruchung

2) Entwicklung eines einfachen kinematischen Modells, das erlaubt, im Rahmen der Modellierung mit plastischem Gelenk die Schubverformungen besser abzuschätzen. Erste Ansätze und Ideen wurden dazu in diesem Projekt entwickelt, die zwar vielversprechend aussehen, aber um zur Anwendungsreife gelangen zu können noch deutlich weiter entwickelt werden müssen.

3) Aufbauend auf Punkt 2 könnte ein nicht-lineares Stabelement für Finite Element Berechnungen entwickelt werden, das Biege- und Schubverformungen berücksichtigt. Heutige Stabelemente sind sehr fortgeschritten hinsichtlich der Modellierung von Biegeverformungen. Der Modellierung von Schubverformungen unterliegt aber in der Regel noch ein linear-elastisches Modell und die Interaktion von Biege- und Schubverformungen wird vernachlässigt.

4) Die jetzigen Modelle für das Verformungsverhalten von Brückenstützen wurden für moderate Axiallasten entwickelt. Um sie zu veraligemeinern, sollte das Verhalten unter höheren Axiallasten untersucht werden. Höhere Axialkräfte können zu einer deutlich reduzierten Verformungskapazität infolge grösserer Betonstauchungen und einer kleineren Länge des plastischen Gelenkes führen.

5) Bis jetzt wurden wandartige Stützenquerschnitte angeschaut. Die Modelle könnten auf weitere Querschnitte ausgedehnt werden, z. B. runde Querschnitte oder Hohlquerschnitte.

Publikationen:

An der ETHZ:
Hannewald P, Bimschas M, Dazio A (2013) Quasi-static cyclic tests on RC bridge piers with detailing deficiencies, Swiss Federal Institute of Technology ETH, Zurich, Switzerland.

An der EPFL:
Hannewald P, Beyer K (2014) Seismic safety of existing bridges – Cyclic inelastic behaviour of bridge piers, ASTRA Forschungsbericht AGB 2008/001.
Hannewald P (2013) Seismic behavior of poorly detailed RC bridge piers, PhD Thesis No 5894, EPFL, Lausanne, Switzerland.
Hannewald P, Mihaylov B, Beyer K (2013) Validation and discussion of a three parameter kinematic theory for reinforced concrete piers, submitted to ASCE Journal of Structural Engineering.
Angeli G, Hannewald P, Beyer K (2013) Behaviour of poorly detailed lap-splices under cyclic loading, Proc. of the Vienna Congress on Recent Advances in Earthquake Engineering and Structural Dynamics, Vienna, Austria.
Hannewald P, Beyer K. (2013) Plastic hinge models for the displacement-based assessment of wall-type bridge piers with poor detailing, Proc. of the Vienna Congress on Recent Advances in Earthquake Engineering and Structural Dynamics, Vienna, Austria.

Der Projektleiter/die Projektleiterin:

Name: Beyer Vorname: Katrin

Amt, Firma, Institut: Earthquake Engineering & Structural Dynamics laboratory, ENAC, EPFL

Unterschrift des Projektleiters/der Projektleiterin:

Katrin Beyer

Forschung im Strassenwesen des UVEK: Formular 3 **Seite 2 / 3**

Schweizerische Eidgenossenschaft
Confédération suisse
Confederazione Svizzera
Confederaziun svizra

Eidgenössisches Departement für
Umwelt, Verkehr, Energie und Kommunikation UVEK
Bundesamt für Strassen ASTRA

FORSCHUNG IM STRASSENWESEN DES UVEK

Formular Nr. 3: Projektabschluss

Beurteilung der Begleitkommission:

Beurteilung:

90% aller Brücken in der Schweiz wurden vor der Einführung der neuen Normgeneration von 1989 erstellt. Sie wurden mit wesentlich tieferen Erdbebenlasten bemessen, als es die heutigen Normen erfordern. Besonders mehrfeldrige Brücken (ca. 40% der schweizerischen Brückenpopulation) mit in Querrichtung gedrungenen Pfeilern sind anfällig auf seismische Beanspruchungen. Diese sollten deshalb näher auf ihre Erdbebensicherheit untersucht werden. Kraftbasierte Bemessungsmethoden führen meist zu ungenügenden Erfüllungsgraden, welche unter Umständen aufwändige Instandsetzungsmassnahmen nach sich ziehen. Mit verformungsbasierten Bemessungsmethoden können hingegen in vielen Fällen dank des vorhandenen Verformungsvermögens ausreichende Erfüllungsgrade nachgewiesen werden. Dies ist vor allem in Ländern wie der Schweiz mit mässiger Seismizität der Fall, wo der Verformungsbedarf relativ klein ist. Die zuverlässige Ermittlung des Verformungsvermögens eines Pfeilers ist damit von zentraler Bedeutung bei der Erdbebenbemessung. Dahingehend ist die vorliegende Arbeit von grosser Bedeutung, da das Verformungsvermögen von gedrungenen Stützen untersucht wird, bei welchen ein plastisches Biegegelenk oder ein Schubversagen eintreten kann.

Umsetzung:

Im Rahmen der Forschung am Institut für Baustatik und Konstruktion an der ETHZ wurde festgestellt, dass gedrungene Stützen in Querrichtung besonders anfällig auf Schäden bei seismischer Beanspruchung sind. Es wurden deshalb vier repräsentative Versuchskörper hergestellt und unter zyklischer Belastung geprüft. Zwei Versuchskörper wiesen Bewehrungsstösse oberhalb des Fundamentes auf, was einer üblichen Bewehrungsanordnung entsprach.

Die sorgfältige Durchführung der Versuche und die gewonnenen Erkenntnisse über die Versagensart, im Speziellen der Druckzone an der Einspannstelle, erlauben es, die vorgeschlagenen Bemessungsmodelle zu validieren. Ein wichtiger Aspekt ist dabei die getrennte Erfassung der Biege- und Schubverformungen an den Versuchskörpern, um die entsprechenden Anteile zu erkennen und auseinander zu halten.

Bekannte Abschätzungsverfahren zur Ermittlung des Biegeverformungsvermögens werden mit den eigenen Ergebnissen, denjenigen des vorhergehenden Projekts sowie mit der Literatur verglichen. Daraus wird eine bekannte Näherungsformel mit einem neuen Ansatz für die Bestimmung der Länge des plastischen Gelenkes kombiniert, welche sehr zuverlässige Ergebnisse liefert.

Im Weiteren werden bekannte Ansätze zur Vorhersage des Schubverformungsanteils verglichen und es wird ein Ansatz gewählt, welcher den meisten Anforderungen genügt. Der Einfluss der Bewehrungsstösse konnte ebenfalls durch eine Begrenzung der Betondehnungen des angrenzenden Betons erfasst werden. Wird diese Grenze überschritten, so setzt der Schubwiderstand schlagartig.

Analog zum bekannten kinematischen Zweiparametermodell für Schubwände wird ein kinematisches Dreiparametermodell entwickelt und validiert. Bei der sorgfältigen Analyse aller Einflussparameter durch Sensitivitätsanalysen werden die Hauptparameter ermittelt und diskutiert. Das Modell mit dem vorgeschlagenen Ansatz zur Bestimmung der Grösse der kritischen Belastungszone am Fuss der Schubwand vermag die maximale Schubkraft bis zum Bruch sehr gut zu erfassen. Für das Verformungsvermögen gelingt dies leider weniger gut. Dies hängt aber auch mit der Reproduzierbarkeit der Versuche (Unterschied zwischen positivem und negativem Belastungszyklus) zusammen.

weitergehender Forschungsbedarf:

Im Rahmen der vorliegenden Arbeit zeigte sich der Bedarf einer Vertiefung der Modelle für plastische Gelenke wobei folgende Einflüsse zu berücksichtigen wären:

- Einfluss von Bewehrungsstössen bei zyklischer Beanspruchung
- Einfluss der achsialen Verlängerung der Versuchskörper auf das Schubverformungsvermögen

Basierend auf vertieften Untersuchungen sollten die vorgeschlagenen Modelle an einer grösseren Anzahl von Versuchen geeicht werden.

Einfluss auf Normenwerk:

Die Arbeit leistet einen Beitrag zur zuverlässigeren Erfassung des Verformungsverhaltens von Brückenstützen unter Beachtung der Bildung von plastischen Gelenken am Stützenfuss und von Schubverformungen. Die in der Norm dargelegte, verformungsbasierte Erdbebenbemessung kann damit auch für mehrfeldrige Brücken mit in Querrichtung gedrungenen Pfeilern angewandt werden.

Der Präsident/die Präsidentin der Begleitkommission:

Name: Fürst Vorname: Armand

Amt, Firma, Institut: Fürst Laffranchi Bauingenieure GmbH

Unterschrift des Präsidenten/der Präsidentin der Begleitkommission:

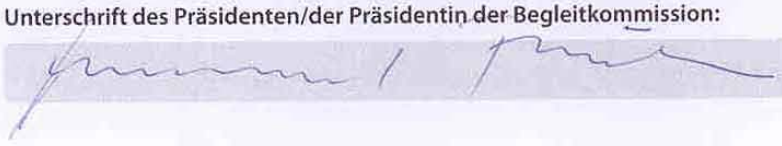

Verzeichnis der Berichte der Forschung im Strassenwesen

Stand: 31.10.2013

Bericht-Nr.	Projekt Nr.	Titel	Jahr
1422	ASTRA 2011/006_OBF	Fracture processes and in-situ fracture observations in Gipskeuper	2013
1421	VSS 2009/901	Experimenteller Nachweis des vorgeschlagenen Raum- und Topologiemodells für die VM-Anwendungen in der Schweiz (MDATrafo)	2013
1420	SVI 2008/003	Projektierungsfreiräume bei Strassen und Plätzen	2013
1419	VSS 2001/452	Stabilität der Polymere beim Heisseinbau von PmB-haltigen Strassenbelägen	2013
1416	FGU 2010/001	Sulfatwiderstand von Beton: verbessertes Verfahren basierend auf der Prüfung nach SIA 262/1, Anhang D	2013
1415	VSS 2010/A01	Wissenslücken im Infrastrukturmanagementprozess "Strasse" im Siedlungsgebiet	2013
1414	VSS 2010/201	Passive Sicherheit von Tragkonstruktionen der Strassenausstattung	2013
1413	SVI 2009/003	Güterverkehrsintensive Branchen und Güterverkehrsströme in der Schweiz Forschungspaket UVEK/ASTRA Strategien zum wesensgerechten Einsatz der Verkehrsmittel im Güterverkehr der Schweiz Teilprojekt B1	2013
1412	ASTRA 2010/020	Werkzeug zur aktuellen Gangliniennorm	2013
1411	VSS 2009/902	Verkehrstelematik für die Unterstützung des Verkehrsmanagements in ausserordentlichen Lagen	2013
1410	VSS 2010/202_OBF	Reduktion von Unfallfolgen bei Bränden in Strassentunneln durch Abschnittsbildung	2013
1409	ASTRA 2010/017_OBF	Regelung der Luftströmung in Strassentunneln im Brandfall	2013
1408	VSS 2000/434	Vieillissement thermique des enrobés bitumineux en laboratoire	2012
1407	ASTRA 2006/014	Fusion des indicateurs de sécurité routière : FUSAIN	2012
1406	ASTRA 2004/015	Amélioration du modèle de comportement individuell du Conducteur pour évaluer la sécurité d'un flux de trafic par simulation	2012
1405	ASTRA 2010/009	Potential von Photovoltaik an Schallschutzmassnahmen entlang der Nationalstrassen	2012
1404	VSS 2009/707	Validierung der Kosten-Nutzen-Bewertung von Fahrbahn-Erhaltungsmassnahmen	2012
1403	SVI 2007/018	Vernetzung von HLS- und HVS-Steuerungen	2012
1402	VSS 2008/403	Witterungsbeständigkeit und Durchdrückverhalten von Geokunststoffen	2012
1401	SVI 2006/003	Akzeptanz von Verkehrsmanagementmassnahmen-Vorstudie	2012
1400	VSS 2009/601	Begrünte Stützgitterböschungssysteme	2012
1399	VSS 2011/901	Erhöhung der Verkehrssicherheit durch Incentivierung	2012
1398	ASTRA 2010/019	Environmental Footprint of Heavy Vehicles Phase III: Comparison of Footprint and Heavy Vehicle Fee (LSVA) Criteria	2012
1397	FGU 2008/003_OBF	Brandschutz im Tunnel: Schutzziele und Brandbemessung Phase 1: Stand der Technik	2012
1396	VSS 1999/128	Einfluss des Umhüllungsgrades der Mineralstoffe auf die mechanischen Eigenschaften von Mischgut	2012
1395	FGU 2009/003	KarstALEA: Wegleitung zur Prognose von karstspezifischen Gefahren im Untertagbau	2012
1394	VSS 2010/102	Grundlagen Betriebskonzepte	2012
1393	VSS 2010/702	Aktualisierung SN 640 907, Kostengrundlage im Erhaltungsmanagement	2012
1392	ASTRA	FEHRL Institutes WIM Initiative (Fiwi)	2012

Bericht-Nr.	Projekt Nr.	Titel	Jahr
	2008/008_009		
1391	ASTRA 2011/003	Leitbild ITS-CH Landverkehr 2025/30	2012
1390	FGU 2008/004_OBF	Einfluss der Grundwasserströmung auf das Quellverhalten des Gipskeupers im Belchentunnel	2012
1389	FGU 2003/002	Long Term Behaviour of the Swiss National Road Tunnels	2012
1388	SVI 2007/022	Möglichkeiten und Grenzen von elektronischen Busspuren	2012
1387	VSS 2010/205_OBF	Ablage der Prozessdaten bei Tunnel-Prozessleitsystemen	2012
1386	VSS 2006/204	Schallreflexionen an Kunstbauten im Strassenbereich	2012
1385	VSS 2004/703	Bases pour la révision des normes sur la mesure et l'évaluation de la planéité des chaussées	2012
1384	VSS 1999/249	Konzeptuelle Schnittstellen zwischen der Basisdatenbank und EMF-, EMK- und EMT-DB	2012
1383	FGU 2008/005	Einfluss der Grundwasserströmung auf das Quellverhalten des Gipskeupers im Chienbergtunnel	2012
1382	VSS 2001/504	Optimierung der statischen Eindringtiefe zur Beurteilung von harten Gussasphaltsorten	2012
1381	SVI 2004/055	Nutzen von Reisezeiteinsparungen im Personenverkehr	2012
1380	ASTRA 2007/009	Wirkungsweise und Potential von kombinierter Mobilität	2012
1379	VSS 2010/206_OBF	Harmonisierung der Abläufe und Benutzeroberflächen bei Tunnel-Prozessleitsystemen	2012
1378	SVI 2004/053	Mehr Sicherheit dank Kernfahrbahnen?	2012
1377	VSS 2009/302	Verkehrssicherheitsbeurteilung bestehender Verkehrsanlagen (Road Safety Inspection)	2012
1376	ASTRA 2011/008_004	Erfahrungen im Schweizer Betonbrückenbau	2012
1375	VSS 2008/304	Dynamische Signalisierungen auf Hauptverkehrsstrassen	2012
1374	FGU 2004/003	Entwicklung eines zerstörungsfreien Prüfverfahrens für Schweissnähte von KDB	2012
1373	VSS 2008/204	Vereinheitlichung der Tunnelbeleuchtung	2012
1372	SVI 2011/001	Verkehrssicherheitsgewinne aus Erkenntnissen aus Datapooling und strukturierten Datenanalysen	2012
1371	ASTRA 2008/017	Potenzial von Fahrgemeinschaften	2011
1370	VSS 2008/404	Dauerhaftigkeit von Betonfahrbahnen aus Betongranulat	2011
1369	VSS 2003/204	Rétention et traitement des eaux de chaussée	2012
1368	FGU 2008/002	Soll sich der Mensch dem Tunnel anpassen oder der Tunnel dem Menschen?	2011
1367	VSS 2005/801	Grundlagen betreffend Projektierung, Bau und Nachhaltigkeit von Anschlussgleisen	2011
1366	VSS 2005/702	Überprüfung des Bewertungshintergrundes zur Beurteilung der Strassengriffigkeit	2010
1365	SVI 2004/014	Neue Erkenntnisse zum Mobilitätsverhalten dank Data Mining?	2011
1364	SVI 2009/004	Regulierung des Güterverkehrs Auswirkungen auf die Transportwirtschaft Forschungspaket UVEK/ASTRA Strategien zum wesensgerechten Einsatz der Verkehrsmittel im Güterverkehr der Schweiz TP D	2012
1363	VSS 2007/905	Verkehrsprognosen mit Online -Daten	2011
1362	SVI 2004/012	Aktivitätenorientierte Analyse des Neuverkehrs	2012
1361	SVI 2004/043	Innovative Ansätze der Parkraumbewirtschaftung	2012
1360	VSS 2010/203	Akustische Führung im Strassentunnel	2012
1359	SVI 2004/003	Wissens- und Technologientransfer im Verkehrsbereich	2012
1358	SVI 2004/079	Verkehrsanbindung von Freizeitanlagen	2012
1357	SVI 2007/007	Unaufmerksamkeit und Ablenkung: Was macht der Mensch am Steuer?	2012
1356	SVI 2007/014	Kooperation an Bahnhöfen und Haltestellen	2011

Bericht-Nr.	Projekt Nr.	Titel	Jahr
1355	FGU 2007/002	Prüfung des Sulfatwiderstandes von Beton nach SIA 262/1, Anhang D: Anwendbarkeit und Relevanz für die Praxis	2011
1354	VSS 2003/203	Anordnung, Gestaltung und Ausführung von Treppen, Rampen und Treppenwegen	2011
1353	VSS 2000/368	Grundlagen für den Fussverkehr	2011
1352	VSS 2008/302	Fussgängerstreifen (Grundlagen)	2011
1351	ASTRA 2009/001	Development of a best practice methodology for risk assessment in road tunnels	2011
1350	VSS 2007/904	IT-Security im Bereich Verkehrstelematik	2011
1349	VSS 2003/205	In-Situ-Abflussversuche zur Untersuchung der Entwässerung von Autobahnen	2011
1348	VSS 2008/801	Sicherheit bei Parallelführung und Zusammentreffen von Strassen mit der Schiene	2011
1347	VSS 2000/455	Leistungsfähigkeit von Parkierungsanlagen	2010
1346	ASTRA 2007/004	Quantifizierung von Leckagen in Abluftkanälen bei Strassentunneln mit konzentrierter Rauchabsaugung	2010
1345	SVI 2004/039	Einsatzbereiche verschiedener Verkehrsmittel in Agglomerationen	2011
1344	VSS 2009/709	Initialprojekt für das Forschungspaket "Nutzensteigerung für die Anwender des SIS"	2011
1343	VSS 2009/903	Basistechnologien für die intermodale Nutzungserfassung im Personenverkehr	2011
1342	FGU 2005/003	Untersuchungen zur Frostkörperbildung und Frosthebung beim Gefrierverfahren	2010
1341	FGU 2007/005	Design aids for the planning of TBM drives in squeezing ground	2011
1340	SVI 2004/051	Aggressionen im Verkehr	2011
1339	SVI 2005/001	Widerstandsfunktionen für Innerorts-Strassenabschnitte ausserhalb des Einflussbereiches von Knoten	2010
1338	VSS 2006/902	Wirkungsmodelle für fahrzeugseitige Einrichtungen zur Steigerung der Verkehrssicherheit	2009
1337	ASTRA 2006/015	Development of urban network travel time estimation methodology	2011
1336	ASTRA 2007/006	SPIN-ALP: Scanning the Potential of Intermodal Transport on Alpine Corridors	2010
1335	VSS 2007/502	Stripping bei lärmmindernden Deckschichten unter Überrollbeanspruchung im Labormassstab	2011
1334	ASTRA 2009/009	Was treibt uns an? Antriebe und Treibstoffe für die Mobilität von Morgen	2011
1333	SVI 2007/001	Standards für die Mobilitätsversorgung im peripheren Raum	2011
1332	VSS 2006/905	Standardisierte Verkehrsdaten für das verkehrsträgerübergreifende Verkehrsmanagement	2011
1331	VSS 2005/501	Rückrechnung im Strassenbau	2011
1330	FGU 2008/006	Energiegewinnung aus städtischen Tunneln: Systemeevaluation	2010
1329	SVI 2004/073	Alternativen zu Fussgängerstreifen in Tempo-30-Zonen	2010
1328	VSS 2005/302	Grundlagen zur Quantifizierung der Auswirkungen von Sicherheitsdefiziten	2011
1327	VSS 2006/601	Vorhersage von Frost und Nebel für Strassen	2010
1326	VSS 2006/207	Erfolgskontrolle Fahrzeugrückhaltesysteme	2011
1325	SVI 2000/557	Indices caractéristiques d'une cité-vélo. Méthode d'évaluation des politiques cyclables en 8 indices pour les petites et moyennes communes.	2010
1324	VSS 2004/702	Eigenheiten und Konsequenzen für die Erhaltung der Strassenverkehrsanlagen im überbauten Gebiet	2009
1323	VSS 2008/205	Ereignisdetektion im Strassentunnel	2011
1322	SVI 2005/007	Zeitwerte im Personenverkehr: Wahrnehmungs- und Distanzabhängigkeit	2008
1321	VSS 2008/501	Validation de l'oedomètre CRS sur des échantillons intacts	2010

Bericht-Nr.	Projekt Nr.	Titel	Jahr
1320	VSS 2007/303	Funktionale Anforderungen an Verkehrserfassungssysteme im Zusammenhang mit Lichtsignalanlagen	2010
1319	VSS 2000/467	Auswirkungen von Verkehrsberuhigungsmassnahmen auf die Lärmimmissionen	2010
1318	FGU 2006/001	Langzeitquellversuche an anhydritführenden Gesteinen	2010
1317	VSS 2000/469	Geometrisches Normalprofil für alle Fahrzeugtypen	2010
1316	VSS 2001/701	Objektorientierte Modellierung von Strasseninformationen	2010
1315	VSS 2006/904	Abstimmung zwischen individueller Verkehrsinformation und Verkehrsmanagement	2010
1314	VSS 2005/203	Datenbank für Verkehrsaufkommensraten	2008
1313	VSS 2001/201	Kosten-/Nutzenbetrachtung von Strassenentwässerungssystemen, Ökobilanzierung	2010
1312	SVI 2004/006	Der Verkehr aus Sicht der Kinder: Schulwege von Primarschulkindern in der Schweiz	2010
1311	VSS 2000/543	VIABILITE DES PROJETS ET DES INSTALLATIONS ANNEXES	2010
1310	ASTRA 2007/002	Beeinflussung der Luftströmung in Strassentunneln im Brandfall	2010
1309	VSS 2008/303	Verkehrsregelungssysteme - Modernisierung von Lichtsignalanlagen	2010
1308	VSS 2008/201	Hindernisfreier Verkehrsraum - Anforderungen aus Sicht von Menschen mit Behinderung	2010
1307	ASTRA 2006/002	Entwicklung optimaler Mischgüter und Auswahl geeigneter Bindemittel; D-A-CH - Initialprojekt	2008
1306	ASTRA 2008/002	Strassenglätte-Prognosesystem (SGPS)	2010
1305	VSS 2000/457	Verkehrserzeugung durch Parkierungsanlagen	2009
1304	VSS 2004/716	Massnahmenplanung im Erhaltungsmanagement von Fahrbahnen	2008
1303	ASTRA 2009/010	Geschwindigkeiten in Steigungen und Gefällen; Überprüfung	2010
1302	VSS 1999/131	Zusammenhang zwischen Bindemitteleigenschaften und Schadensbildern des Belages?	2010
1301	SVI 2007/006	Optimierung der Strassenverkehrsunfallstatistik durch Berücksichtigung von Daten aus dem Gesundheitswesen	2009
1300	VSS 2003/903	SATELROU Perspectives et applications des méthodes de navigation pour la télématique des transports routiers et pour le système d'information de la route	2010
1299	VSS 2008/502	Projet initial - Enrobés bitumineux à faibles impacts énergétiques et écologiques	2009
1298	ASTRA 2007/012	Griffigkeit auf winterlichen Fahrbahnen	2010
1297	VSS 2007/702	Einsatz von Asphaltbewehrungen (Asphalteinlagen) im Erhaltungsmanagement	2009
1296	ASTRA 2007/008	Swiss contribution to the Heavy-Duty Particle Measurement Programme (HD-PMP)	2010
1295	VSS 2005/305	Entwurfsgrundlagen für Lichtsignalanlagen und Leitfaden	2010
1294	VSS 2007/405	Wiederhol- und Vergleichspräzision der Druckfestigkeit von Gesteinskörnungen am Haufwerk	2010
1293	VSS 2005/402	Détermination de la présence et de l'efficacité de dope dans les bétons bitumineux	2010
1292	ASTRA 2006/004	Entwicklung eines Pflanzenöl-Blockheizkraftwerkes mit eigener Ölmühle	2010
1291	ASTRA 2009/005	Fahrmuster auf überlasteten Autobahnen Simultanes Berechnungsmodell für das Fahrverhalten auf Autobahnen als Grundlage für die Berechnung von Schadstoffemissionen und Fahrzeitgewinnen	2010
1290	VSS 1999/209	Conception et aménagement de passages inférieurs et supérieurs pour piétons et deux-roues légers	2008
1289	VSS 2005/505	Affinität von Gesteinskörnungen und Bitumen, nationale Umsetzung der	2010

Bericht-Nr.	Projekt Nr.	Titel	Jahr
		EN	
1288	ASTRA 2006/020	Footprint II - Long Term Pavement Performance and Environmental Monitoring on A1	2010
1287	VSS 2008/301	Verkehrsqualität und Leistungsfähigkeit von komplexen ungesteuerten Knoten: Analytisches Schätzverfahren	2009
1286	VSS 2000/338	Verkehrsqualität und Leistungsfähigkeit auf Strassen ohne Richtungstrennung	2010
1285	VSS 2002/202	In-situ Messung der akustischen Leistungsfähigkeit von Schallschirmen	2009
1284	VSS 2004/203	Evacuation des eaux de chaussée par les bas-cotés	2010
1283	VSS 2000/339	Grundlagen für eine differenzierte Bemessung von Verkehrsanlagen	2008
1282	VSS 2004/715	Massnahmenplanung im Erhaltungsmanagement von Fahrbahnen: Zusatzkosten infolge Vor- und Aufschub von Erhaltungsmassnahmen	2010
1281	SVI 2004/002	Systematische Wirkungsanalysen von kleinen und mittleren Verkehrsvorhaben	2009
1280	ASTRA 2004/016	Auswirkungen von fahrzeuginternen Informationssystemen auf das Fahrverhalten und die Verkehrssicherheit Verkehrspsychologischer Teilbericht	2010
1279	VSS 2005/301	Leistungsfähigkeit zweistreifiger Kreisel	2009
1278	ASTRA 2004/016	Auswirkungen von fahrzeuginternen Informationssystemen auf das Fahrverhalten und die Verkehrssicherheit - Verkehrstechnischer Teilbericht	2009
1277	SVI 2007/005	Multimodale Verkehrsqualitätsstufen für den Strassenverkehr - Vorstudie	2010
1276	VSS 2006/201	Überprüfung der schweizerischen Ganglinien	2008
1275	ASTRA 2006/016	Dynamic Urban Origin - Destination Matrix - Estimation Methodology	2009
1274	SVI 2004/088	Einsatz von Simulationswerkzeugen in der Güterverkehrs- und Transportplanung	2009
1273	ASTRA 2008/006	UNTERHALT 2000 - Massnahme M17, FORSCHUNG: Dauerhafte Materialien und Verfahren SYNTHESE - BERICHT zum Gesamtprojekt "Dauerhafte Beläge" mit den Einzelnen Forschungsprojekten: - ASTRA 200/419: Verhaltensbilanz der Beläge auf Nationalstrassen - ASTRA 2000/420: Dauerhafte Komponenten auf der Basis erfolgreicher Strecken - ASTRA 2000/421: Durabilité des enrobés - ASTRA 2000/422: Dauerhafte Beläge, Rundlaufversuch - ASTRA 2000/423: Griffigkeit der Beläge auf Autobahnen, Vergleich zwischen den Messergebnissen von SRM und SCRIM - ASTRA 2008/005: Vergleichsstrecken mit unterschiedlichen oberen Tragschichten auf einer Nationalstrasse	2008
1272	VSS 2007/304	Verkehrsregelungssysteme - behinderte und ältere Menschen an Lichtsignalanlagen	2010
1271	VSS 2004/201	Unterhalt von Lärmschirmen	2009
1270	VSS 2005/502	Interaktion Strasse Hangstabilität: Monitoring und Rückwärtsrechnung	2009
1269	VSS 2005/201	Evaluation von Fahrzeugrückhaltesystemen im Mittelstreifen von Autobahnen	2009
1268	ASTRA 2005/007	PM10-Emissionsfaktoren von Abriebspartikeln des Strassenverkehrs (APART)	2009
1267	VSS 2007/902	MDAinSVT Einsatz modellbasierter Datentransfernormen (INTERLIS) in der Strassenverkehrstelematik	2009
1266	VSS 2000/343	Unfall- und Unfallkostenraten im Strassenverkehr	2009
1265	VSS 2005/701	Zusammenhang zwischen dielektrischen Eigenschaften und Zustandsmerkmalen von bitumenhaltigen Fahrbahnbelägen (Pilotuntersuchung)	2009
1264	SVI 2004/004	Verkehrspolitische Entscheidfindung in der Verkehrsplanung	2009

Bericht-Nr.	Projekt Nr.	Titel	Jahr
1263	VSS 2001/503	Phénomène du dégel des sols gélifs dans les infrastructures des voies de communication et les pergélisols alpins	2006
1262	VSS 2003/503	Lärmverhalten von Deckschichten im Vergleich zu Gussasphalt mit strukturierter Oberfläche	2009
1261	ASTRA 2004/018	Pilotstudie zur Evaluation einer mobilen Grossversuchsanlage für beschleunigte Verkehrslastsimulation auf Strassenbelägen	2009
1260	FGU 2005/001	Testeinsatz der Methodik "Indirekte Vorauserkundung von wasserführenden Zonen mittels Temperaturdaten anhand der Messdaten des Lötschberg-Basistunnels	2009
1259	VSS 2004/710	Massnahmenplanung im Erhaltungsmanagement von Fahrbahnen - Synthesebericht	2008
1258	VSS 2005/802	Kaphaltestellen Anforderungen und Auswirkungen	2009
1257	SVI 2004/057	Wie Strassenraumbilder den Verkehr beeinflussen Der Durchfahrtswiderstand als Arbeitsinstrument bei der städtebaulichen Gestaltung von Strassenräumen	2009
1256	VSS 2006/903	Qualitätsanforderungen an die digitale Videobild-Bearbeitung zur Verkehrsüberwachung	2009
1255	VSS 2006/901	Neue Methoden zur Erkennung und Durchsetzung der zulässigen Höchstgeschwindigkeit	2009
1254	VSS 2006/502	Drains verticaux préfabriqués thermiques pour la consolidation in-situ des sols	2009
1253	VSS 2001/203	Rétention des polluants des eaux de chausées selon le système "infilitrations sur les talus". Vérification in situ et optimisation	2009
1252	SVI 2003/001	Nettoverkehr von verkehrsintensiven Einrichtungen (VE)	2009
1251	ASTRA 2002/405	Incidence des granulats arrondis ou partiellement arrondis sur les propriétés d'ahérence des bétons bitumineux	2008
1250	VSS 2005/202	Strassenabwasser Filterschacht	2007
1249	FGU 2003/004	Einflussfaktoren auf den Brandwiderstand von Betonkonstruktionen	2009
1248	VSS 2000/433	Dynamische Eindringtiefe zur Beurteilung von Gussasphalt	2008
1247	VSS 2000/348	Anforderungen an die strassenseitige Ausrüstung bei der Umwidmung von Standstreifen	2009
1246	VSS 2004/713	Massnahmenplanung im Erhaltungsmanagement von Fahrbahnen: Bedeutung Oberflächenzustand und Tragfähigkeit sowie gegenseitige Beziehung für Gebrauchs- und Substanzwert	2009
1245	VSS 2004/701	Verfahren zur Bestimmung des Erhaltungsbedarfs in kommunalen Strassennetzen	2009
1244	VSS 2004/714	Massnahmenplanung im Erhaltungsmanagement von Fahrbahnen - Gesamtnutzen und Nutzen-Kosten-Verhältnis von standardisierten Erhaltungsmassnahmen	2008
1243	VSS 2000/463	Kosten des betrieblichen Unterhalts von Strassenanlagen	2008
1242	VSS 2005/451	Recycling von Ausbauasphalt in Heissmischgut	2007
1241	ASTRA 2001/052	Erhöhung der Aussagekraft des LCPC Spurbildungstests	2009
1240	ASTRA 2002/010	L'acceptabilité du péage de congestion : Résultats et analyse de l'enquête en Suisse	2009
1239	VSS 2000/450	Bemessungsgrundlagen für das Bewehren mit Geokunststoffen	2009
1238	VSS 2005/303	Verkehrssicherheit an Tagesbaustellen und bei Anschlüssen im Baustellenbereich von Hochleistungsstrassen	2008
1237	VSS 2007/903	Grundlagen für eCall in der Schweiz	2009
1236	ASTRA 2008/008_07	Analytische Gegenüberstellung der Strategie- und Tätigkeitsschwerpunkte ASTRA-AIPCR	2008
1235	VSS 2004/711	Forschungspaket Massnahmenplanung im EM von Fahrbahnen - Standardisierte Erhaltungsmassnahmen	2008
1234	VSS 2006/504	Expérimentation in situ du nouveau drainomètre européen	2008

Bericht-Nr.	Projekt Nr.	Titel	Jahr
1233	ASTRA 2000/420	Unterhalt 2000 Forschungsprojekt FP2 Dauerhafte Komponenten bitumenhaltiger Belagsschichten	2009
651	AGB 2006/006_OBF	Instandsetzung und Monitoring von AAR-geschädigten Stützmauern und Brücken	2013
650	AGB 2005/010	Korrosionsbeständigkeit von nichtrostenden Betonstählen	2012
649	AGB 2008/012	Anforderungen an den Karbonatisierungswiderstand von Betonen	2012
648	AGB 2005/023 + AGB 2006/003	Validierung der AAR-Prüfungen für Neubau und Instandsetzung	2011
647	AGB 2004/010	Quality Control and Monitoring of electrically isolated post- tensioning tendons in bridges	2011
646	AGB 2005/018	Interactin sol-structure : ponts à culées intégrales	2010
645	AGB 2005/021	Grundlagen für die Verwendung von Recyclingbeton aus Betongranulat	2010
644	AGB 2005/004	Hochleistungsfähiger Faserfeinkornbeton zur Effizienzsteigerung bei der Erhaltung von Kunstbauten aus Stahlbeton	2010
643	AGB 2005/014	Akustische Überwachung einer stark geschädigten Spannbetonbrücke und Zustandserfassung beim Abbruch	2010
642	AGB 2002/006	Verbund von Spanngliedern	2009
641	AGB 2007/007	Empfehlungen zur Qualitätskontrolle von Beton mit Luftpermeabilitätsmessungen	2009
640	AGB 2003/011	Nouvelle méthode de vérification des ponts mixtes à âme pleine	2010
639	AGB 2008/003	RiskNow-Falling Rocks Excel-basiertes Werkzeug zur Risikoermittlung bei Steinschlagschutzgalerien	2010
638	AGB2003/003	Ursachen der Rissbildung in Stahlbetonbauwerken aus Hochleistungsbeton und neue Wege zu deren Vermeidung	2008
637	AGB 2005/009	Détermination de la présence de chlorures à l'aide du Géoradar	2009
636	AGB 2002/028	Dimensionnement et vérification des dalles de roulement de ponts routiers	2009
635	AGB 2004/002	Applicabilité de l'enrobé drainant sur les ouvrages d'art du réseau des routes nationales	2008
634	AGB 2002/007	Untersuchungen zur Potenzialfeldmessung an Stahlbetonbauten	2008
633	AGB 2002/014	Oberflächenschutzsysteme für Betontragwerke	2008
632	AGB 2008/201	Sicherheit des Verkehrssystem Strasse und dessen Kunstbauten Testregion - Methoden zur Risikobeurteilung Schlussbericht	2010
631	AGB 2000/555	Applications structurales du Béton Fibré à Ultra-hautes Performances aux ponts	2008
630	AGB 2002/016	Korrosionsinhibitoren für die Instandsetzung chloridverseuchter Stahlbetonbauten	2010
629	AGB 2003/001 + AGB 2005/019	Integrale Brücken - Sachstandsbericht	2008
628	AGB 2005/026	Massnahmen gegen chlorid-induzierte Korrosion und zur Erhöhung der Dauerhaftigkeit	2008
627	AGB 2002/002	Eigenschaften von normalbreiten und überbreiten Fahrbahnübergängen aus Polymerbitumen nach starker Verkehrsbelastung	2008
626	AGB 2005/110	Sicherheit des Verkehrssystems Strasse und dessen Kunstbauten: Baustellensicherheit bei Kunstbauten	2009
625	AGB 2005/109	Sicherheit des Verkehrssystems Strasse und dessen Kunstbauten: Effektivität und Effizienz von Massnahmen bei Kunstbauten	2009
624	AGB 2005/108	Sicherheit des Verkehrssystems / Strasse und dessen Kunstbauten / Risikobeurteilung für Kunstbauten	2010
623	AGB 2005/107	Sicherheit des Verkehrssystems Strasse und dessen Kunstbauten: Tragsicherheit der bestehenden Kunstbauten	2009
622	AGB 2005/106	Rechtliche Aspekte eines risiko- und effizienzbasierten Sicherheitskonzepts	2009

Bericht-Nr.	Projekt Nr.	Titel	Jahr
621	AGB 2005/105	Sicherheit des Verkehrssystems Strasse und dessen Kunstbauten Szenarien der Gefahrenentwicklung	2009
620	AGB 2005/104	Sicherheit des Verkehrssystems Strasse und dessen Kunstbauten: Effektivität und Effizienz von Massnahmen	2009
619	AGB 2005/103	Sicherheit des Verkehrssystems / Strasse und dessen Kunstbauten / Ermittlung des Netzrisikos	2010
618	AGB 2005/102	Sicherheit des Verkehrssystems Strasse und dessen Kunstbauten: Methodik zur vergleichenden Risikobeurteilung	2009
617	AGB 2005/100	Sicherheit des Verkehrssystems Strasse und dessen Kunstbauten Synthesebericht	2010
616	AGB 2002/020	Beurteilung von Risiken und Kriterien zur Festlegung akzeptierter Risiken in Folge aussergewöhnlicher Einwirkungen bei Kunstbauten	2009